QUANTUM-MECHANICAL APPROACH TO COLLISION-INDUCED RADIATIVE EMISSIONS

Anthony Leung

A Dissertation Submitted to the Faculty of Graduate Studies
in Partial Fulfilment of the Requirements
for the Degree of
Doctor of Philosophy

Graduate Program in Physics and Astronomy
York University
Toronto, Ontario

April 2018

Abstract

Charge exchange is a process that occurs in an atomic collision where an electron from one of the colliding particles is transferred to the other; typically from a neutral atom or molecule to an ion. Electrons transferred into an excited energy state then decay into a lower-energy state and emit photons during this process. This phenomenon of collision-induced radiative emissions is of great interest in astrophysics and experimental x-ray spectroscopy research since it helps understand the production of x-rays in astrophysical settings. On the theoretical side, obtaining a description of these radiative emissions involves numerical work since a closed-form solution is not possible. Using standard numerical approaches, one needs to rely on models and approximations, especially in collision problems involving many-electron systems. Consequently, results obtained in this way can be at odds with experimental observations and/or results from different theoretical methods. In this dissertation, the main method is the two-centre basis generator method performed within the independent electron model. It is a dynamical approach to solving atomic collision problems and has shown to be reliable in describing charge exchange and other electronic processes. This work gives an extensive view on the applicability of this approach in the context of collision-induced radiative emissions where present results from a variety of ion-atom and ion-molecule collisions are benchmarked with results from previous studies.

To my parents, for their unconditional love and support

Acknowledgements

The research presented in this dissertation was conducted between 2014 and 2018 at York University (Canada). Funding of this research was mainly provided by three Ontario Graduate Scholarships (2014, 2015, 2016), an award jointly funded by York University and the Province of Ontario. The Provost Dissertation Scholarship (2017), an award funded by York University, supported the completion of this dissertation. High-performance computing resources for this research were provided by the facilities of the Shared Hierarchical Academic Research Computing Network (SHARCNET) and Compute/Calcul Canada. I gratefully acknowledge the support of these agencies.

First and foremost, I am very grateful for the guidance, patience, and support provided by my supervisor, Prof. Tom Kirchner. His knowledge in atomic physics knows no bounds and I am grateful for his willingness to share his expertise to enrich this work and my own learning experience.

I must also express my gratitude towards the other members of the supervisory committee, Prof. Marko Horbatsch and Prof. Michael Haslam, whose suggestions and feedback have added great value to my work.

My sincere thanks also goes to the examining committee: Prof. Randy Lewis for being the chair, Prof. Gino Lavoie despite his expertise lies in inorganic chemistry, and most important of all, the commitment of Prof. Allison Harris for travelling to York University to make this exam possible.

I fully appreciate the administrative assistance from the wonderful staffs in our department: Marlene Caplan and Janaki De Camillis.

Last but not least, my deepest gratitude goes to my family.

Anthony Cheun-Kit Leung
York University
April 3, 2018

Contents

List of Tables

List of Figures

List of Acronyms

ADC	autoionizing double-capture
AO	atomic orbital
AOCC	atomic-orbital close-coupling
BGM	basis generator method
CBM	classical over-barrier model
COLTRIMS	cold-target recoil ion momentum spectroscopy
CTMC	classical trajectory Monte Carlo
DEC	double-electron capture
HSCC	hyperspherical close-coupling
IEM	independent electron model
IEVM	independent event model
MO	molecular orbital
MOCC	molecular-orbital close-coupling
OPM	optimized potential method
TC	two-centre
TDDFT	time-dependent density functional theory
TDL	time-dependent lattice
TDSE	time-dependent Schrödinger equation
TEC	triple-electron capture
SEC	single-electron capture
SWCX	solar-wind charge-exchange

CHAPTER 1

General introduction

This dissertation presents a theoretical study of radiative emissions from ion-atom and ion-molecule collisions. Throughout the dissertation, equations and physical quantities are expressed in atomic units ($\hbar = e = m_e = 4\pi\epsilon_0 = 1$) unless stated otherwise. This is specified with the 'a.u.' suffix. Impact energy is often expressed in keV divided by the projectile ion mass in atomic mass units (u) and is denoted by E_P.

1.1 CONTEXTUAL BACKGROUND

Atomic collision studies have a long tradition in atomic physics and are deemed important for understanding matter interactions at the fundamental level. These studies also have an important role in other research fields such as plasma diagnostics, radiation therapy, and astrophysics. A particular example of the latter is the cometary x-ray emission phenomenon.

In 1996, the Röntgen astronomy satellite unexpectedly detected strong x-ray emissions from the comet C/Hyakutake 1996 B2 [1]. It was initially speculated that these x-rays were a result of thermal bremsstrahlung from collisions of cometary gases with hot solar wind electrons but the predicted luminosities by this mechanism are too small by a few orders of magnitude compared to the observed emissions due to the weak flux of these electrons [2]. Moreover, a typical temperature in thermal bremsstrahlung of approximately 10^6 K is needed for the production of x-ray photons, which cannot occur in the extremely cold comas with temperatures around 50 K [3]. It was later established that collisions of comet gases with solar-wind ions by *charge exchange* is the main mechanism for the observed emissions [4–6]; a process that can be understood at the atomic level. In the context of astrophysical settings, this phenomenon has been often referred to as *solar-wind charge-exchange* (SWCX) since solar-wind ions can also collide with other gaseous media such as planetary atmospheres [4] and heliospheres [7, 8]. Charge exchange is one of the few electronic processes that commonly occur in atomic collisions.

1.2 ELECTRON DYNAMICS IN ATOMIC COLLISIONS

In our atomic collision system, the following entities are involved: the target core, active electron(s) in the target, and the projectile ion. The possibility of active projectile electrons is not considered in this work. The collision dynamics that are of interest in the present work all happen on the femto-second timescale such that the target, being an atom or a molecule, can be treated fixed-in-space while the projectile is assumed to move with constant velocity. In the context of the SWCX problem, the gaseous species are treated as targets and the highly-charged solar wind ions are treated as projectiles. There are a few electronic processes that can occur in a collision: excitation, ionization to the continuum, and the aforementioned charge-exchange. These processes can be quantified with cross sections. Specifically, charge exchange is a process where an electron from the neutral target is captured into a bound state of the projectile ion. Such a process is also referred to as *electron capture* or *charge transfer*.

Suppose a projectile (denoted by A) with charge q is in collision with a neutral target in the ground state (denoted by B). By restricting to single-electron transitions for simplicity, the target electron has initial quantum numbers (n, l, m) before the collision and final quantum numbers (n', l', m') after the collision. Namely, n, l, m are the principal, angular momentum, and magnetic substate quantum numbers, respectively. The electronic processes can be summarized as follows

$$\begin{aligned}
A^{q+} + B(nlm) &\rightarrow A^{q+} + B^*(n'l'm'), && \text{Target excitation,} && (1.1)\\
A^{q+} + B(nlm) &\rightarrow A^{q+} + B^+ + e, && \text{Ionization,} && (1.2)\\
A^{q+} + B(nlm) &\rightarrow A^{(q-1)+}(n'l'm') + B^+, && \text{Electron capture.} && (1.3)
\end{aligned}$$

Contributions of these electronic processes can vary depending on the projectile velocity or impact energy.

Atomic collision problems can be separated into the following nonrelativistic projectile impact-energy regimes: ultra-low, low, intermediate, and high. The classification of these regimes is based on the comparison of the projectile speed v_P to the classical orbital speed of the target's valence electron v_e. In the nonrelativistic high-energy regime ($v_{\mathrm{P}} \gg v_e$), which corresponds to impact energies from approximately a few to tens of MeV/u, ionization and excitation are dominant. In the intermediate regime ($v_{\mathrm{P}} \approx v_e$), all three processes have their fair share of contribution in the collision. Finally in the low energy regimes ($v_{\mathrm{P}} \ll v_e$), corresponding to impact energies below approximately 10 keV/u, electron capture is dominant.

The regime that is relevant to the SWCX collisions is the low-energy regime. Velocities of solar wind ions in the heliosphere can be between 200 and 800 km/s [9], which correspond to energies between 0.2 and 3 keV/u. Collisions in this regime are also described as *slow*. Furthermore, the captured electron can populate an excited state of the projectile which then undergoes radiative stabilization, emitting photon(s) in the process. Since radiative emissions are involved in single-electron capture, the next step of reaction (1.3) is

$$A^{q+} + B(nlm) \;\rightarrow\; A^{(q-1)+}(n'l'm') + B^{+} \;\rightarrow A^{(q-1)+} + B^{+} + \gamma, \tag{1.4}$$

where γ represents a photon emitted from the excited projectile.

In the case of many-electron systems and multiple-capture events, electrons captured into excited states can undergo Auger decay (also called autoionization) where some electrons are ejected from the projectile while others transition into lower bound states due to electron-electron interaction. Auger processes do occur before radiative decay since Auger decay rates tend to be higher than radiative rates. This means that an electron that has undergone an Auger process and still occupies an excited state proceeds with radiative decay, contributing to the overall emission spectrum. For example, suppose two electrons are captured into the projectile which then undergo Auger decay resulting in one electron remaining. The entire process of this example is

$$\begin{array}{l} A^{q+} + B \longrightarrow \underbrace{A^{(q-2)+}(n'l'm', n''l''m'') + B^{2+}} \\ \qquad\qquad\qquad\qquad \Big\downarrow \text{autoionization} \\ \qquad\qquad A^{(q-1)+}(nlm) + e + B^{2+} \longrightarrow A^{(q-1)+} + B^{+} + \gamma + e. \end{array} \tag{1.5}$$

Such a capture event is referred to as *apparent* capture in this dissertation. In this example of initial double-capture resulting in one remaining electron after Auger decay, it is called *apparent single-capture*.

In slow collisions, the populated bound state is known to be selective [10] and this state can be predicted from potential curve crossings in energy correlation diagrams. This captured state can also be predicted in a more intuitive, albeit simple, treatment in terms of classical models.

1.2.1 Classical over-barrier model

Classical approaches have often been used for estimating capture cross sections as long as quantum effects are not pronounced. For charge transfer, the classical over-barrier model (CBM) is one such example. The CBM was initially proposed by Ryufuku *et al.* [11] for single-electron transfer and later extended for multiple-electron transfer by Bárány *et al.* [12]. In the work by Niehaus [13], the CBM is further extended to include recapture events.

The CBM can be a very useful tool for gauging the magnitude of capture cross sections obtained from more detailed methods such as the quantum-mechanical basis-set expansion method. However, the CBM is only appropriate in the low energy regime since it does not consider ionization and it is independent of the collision velocity, but this is adequate for the SWCX collision problems considered in the present work. To aid the discussion of this dissertation, the main ideas of the CBM are summarized in the following.

In the CBM, electron transfer is to take place when the electron has sufficient energy to overcome the potential barrier between the projectile ion with charge q and the target nucleus. This is illustrated in Fig. 1.1. Also shown in the figure are the radiative decay transitions of the captured electron in the projectile where photons of different frequencies are emitted. The purpose of including the radiative processes in the figure is to illustrate the overall goal of the present study.

In the simplest case of a bare projectile ion with charge q, removing the first electron results in a superimposed Coulomb potential

$$V = -\frac{1}{r} - \frac{q}{|R - r|} \tag{1.6}$$

where r is the distance between the electron and the target core and R is the internuclear distance between the target and projectile cores. Equation (1.6) is the starting point to find the crossing distance R_C where electron transfer takes place. Since the

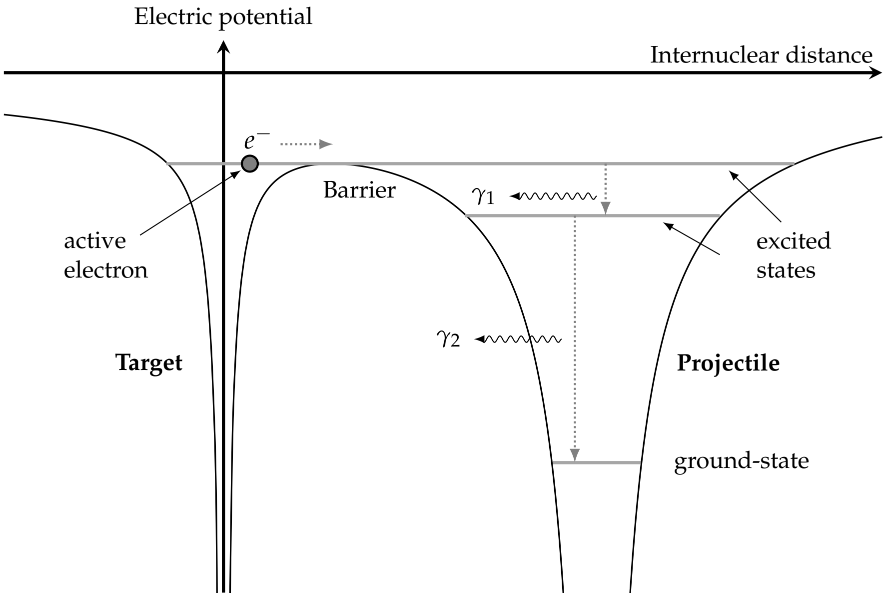

FIG. 1.1: Simple illustration of electron transfer in the classical over-barrier model. The figure shows the instant when the electron has sufficient energy to pass over the barrier and transfers into the bare projectile ion and subsequently decays radiatively. The electronic potential is plotted with respect to the internuclear distance between the target and projectile. The projectile is treated as a bare ion.

incoming projectile is a bare ion then the captured electron occupies a Rydberg state. One can then derive the principal quantum number n of the captured bound state that satisfies (1.6). This is determined to be [11, 14]

$$n \leq q \left[2I_{\mathrm{T}} \left(1 + \frac{q-1}{2\sqrt{q}+1} \right) \right]^{-1/2} \tag{1.7}$$

where I_{T} is the target ionization potential of the electron. The upper bound in relation (1.7) is the *main* capture n-state. Relation (1.7) implies that the higher the charge of the projectile ion, the higher the n-state that the electron is captured into. The corresponding *crossing distance* is [11, 14]

$$R_{\mathrm{C}}(n) = \frac{q-1}{(q^2/2n^2) - I_{\mathrm{T}}} \tag{1.8}$$

which one can use to compute capture cross sections $\sigma_{\mathrm{cap}} = \pi R_{\mathrm{C}}^2$. For example, consider the C^{6+}-He system. Given the first ionization potential of helium is 0.904 a.u. then the main capture state is $n = 3$ with a crossing distance of $R_{\mathrm{cap}} = 4.63$ a.u. which gives a cross section of about 18.8×10^{-16} cm^2. According to the recommended values by Janev and Winter [10], a slow collision of 4 keV/u for the C^{6+}-He system corresponds to a cross section of about $(10 \pm 4) \times 10^{-16}$ cm^2. This recommended value is a close match of the CBM prediction.

1.3 RESEARCH PROBLEM

The discovery of the SWCX phenomenon in comets led to a new pathway in atomic collision research where more emphasis is placed on post-collision processes. For cometary emissions, with the composition of comet gases [15] and solar-wind ions [16] deduced from satellite spectrometer measurements, one can reproduce and study these radiative emissions in the laboratory and/or theoretically in greater detail. For example, the x-ray emission spectra from these interactions are used for determining the speed of solar-wind ions [9]. More recently, experimental results are used as benchmarks for other satellite measurements such as solar-wind ion abundances [17].

Experimental and theoretical data always have uncertainties and sometimes significant differences between them. Even comparing results produced from different theoretical methods can show significant discrepancies due to limitations of the methods used [18]. In the case of SWCX studies, this can be problematic for understanding properties and features of interstellar media [19]. Therefore, it is imperative that the model can reliably describe the electronic processes of these systems in a consistent manner.

There are several approaches to performing a theoretical calculation on charge-exchange collisions. As discussed earlier, the CBM is one example to determine capture cross sections but the model is independent of impact energies. It also does not give nl-subshell populations directly, which are important for radiative cascade analyses, which then need to rely on presupposed nl-distribution models [10]. Another classical approach is the classical-trajectory Monte Carlo (CTMC) [20] method which uses classical statistical mechanics to simulate atomic collisions.

The CTMC method is essentially a computer experiment where the total cross section for a process is determined by $\sigma_R = (N_R/N_{\text{total}})\pi b_{\text{max}}^2$ where N_R is the number of successful reactions out of a total of N_{total} trajectories and b_{max} is the maximum impact parameter. This method can be quite useful in describing state-selective charge-exchange and excitation of high-lying energy states [21] that are not easily accessible with quantum-mechanical approaches since high computational resources are required. It is also appropriate to use CTMC in such a case due to the classical correspondence principle (i.e., the classical limit). On the other hand, CTMC is not necessarily robust to describe multiple-capture events at solar-wind speeds since quantum effects such as tunnelling and/or quasi-molecular couplings between the projectile and the target can affect the electron dynamics. Another challenge working with multi-electron systems using the CTMC is the issue of classically unstable electrons that are bound to the same nucleus, causing artificial autoionization when the trajectory is followed long enough [22]. Regardless, many research groups studying SWCX collisions continue to perform CTMC calculations to benchmark experimental results due to their feasibility. There are some successes with CTMC in describing radiative emissions from charge-exchange collisions such as in Ref. [23] but in other works such as in Refs. [24, 25] the experimental results do not at all agree with CTMC results. Although quantum-mechanical approaches would, in principle, resolve these inconsistencies, they are often a challenge to implement.

In formal scattering theory, the starting point for the nonrelativistic collision problem are the Lippmann-Schwinger equations [26], which are obtained when appropriate boundary conditions are applied to the Schrödinger equation [27]. However, a complete quantum-mechanical description from solving the Lippmann-Schwinger equations, even for the simplest proton-hydrogen scattering problem, has been a challenge for a long time and it is only recently that significant progress has been made on this problem by using the so-called quantum-mechanical two-centre convergent close-coupling method [28].

If the collision of interest is sufficiently fast (i.e., $E_{\mathrm{P}} \geq 0.5$ keV/u) it is possible to treat the motion of the heavy particles classically. The motion of the electrons is then governed by the *time-dependent* Schrödinger equation (TDSE). Such a treatment is referred to as the *semi-classical impact parameter* treatment (or simply *semi-classical approximation*) [29]. Even with this treatment, solving the many-electron TDSE analytically is impossible and one needs to rely on numerical methods. The various computational approaches to solving the TDSE include the lattice method [30] and the close-coupling method [29].

The lattice method solves the TDSE directly by means of the standard finite-difference technique. Although in principle this approach can be applied to atomic collisions in any impact-energy regime, obtaining the full three-dimensional solution requires large computational resources due to the large lattice size required for the long-range Coulomb potential. In fact, obtaining the full three-dimenensional lattice solution for the antiproton-hydrogen collision problem was made possible only in the late 1990s when computing power has advanced far enough to handle such a demanding task [30]. Because of such high demand in computational resources, the lattice approach has been limited to excitation or target ionization since these processes are localized near the target [30, 31] and the target is assumed to be fixed-in-space in practice. It is also possible to describe electron-capture for the SWCX problem [32] using this approach but this may be restricted to low-lying bound capture states where the electron clouds do not extend to the lattice edge.

The close-coupling method is based on the ansatz that the electronic solution is expressed as a linear combination of basis states. Two variants of this approach are often used: atomic orbital close-coupling (AOCC) and molecular orbital close-coupling (MOCC) where an atomic basis set and a molecular basis set are used to represent the problem, respectively. The motivation to use a molecular basis set comes from the consideration that a transient molecule is formed in slow collisions.

The computational requirements of the close-coupling method can also be demanding since, depending on the collision system, a large basis set is needed to properly represent the problem, and obviously necessary to achieve convergence of the solution. This is generally true even for describing single-electron processes. Nevertheless, many groups have successfully performed cross section calculations using the close-coupling approach for ion-hydrogen and a few ion-alkali collisions where results have displayed good agreement with experimental data for single-electron transitions [10, 33]. There were also studies that attempted to describe two-electron processes in ion-helium collisions [33], but the required basis size is considerably greater than that of single-electron processes in order to properly represent the two-electron wavefunction.

In working with many-electron targets in an atomic collision problem, the standard approach is the *independent electron model* (IEM) [34]. The basic idea of the IEM is to reduce the many-electron problem into single-electron problems by approximating the electron-electron Coulomb interactions as an effective potential term. Because of this assumption, the success in describing multiple-electron processes can vary across different collision systems, which depends on the significance of electron correlation effects. Once the single-electron problems are solved yielding single-electron probabilities, they can then be combined statistically to obtain many-electron quantities. The IEM can also be utilized in the CTMC approach.

It was mentioned in the review by Smith and Brickhouse [35] that theoretical calculations on SWCX problems using quantum-mechanical approaches, such as the close-coupling method, remain scarce with only works on simple ion-atom slow collisions having been reported recently, for example, O^{6+}-H collisions [36]. This scarcity of quantum-mechanical calculations was also mentioned in other reviews [37–39]. With the few approaches briefly discussed so far and their respective practical challenges, it is not surprising that this is the case. However, despite the challenges that the standard close-coupling method exhibits in slow atomic collision problems, there is at least one variant that shows some promises.

1.4 MOTIVATION

A more modern approach to solving atomic collision problems is the basis generator method (BGM) performed within the IEM framework using the semi-classical approximation. Pioneered by Lüdde *et al.* [40, 41] and later extended to the two-centre BGM (TC-BGM) [42], this approach is also based on the close-coupling method but its main feature is the use of a *dynamic* basis set to represent the problem. This allows for a more economical approach compared to AOCC and MOCC without compromising on the accuracy of the results.

The TC-BGM has been used to describe a variety of ion-atom collision systems in the intermediate and high impact-energy regimes [43–46] and in the low energy regime as low as 0.1 keV/u [47, 48]. In recent years, this method has been adapted to ion-molecule collisions with H_2O [49–51] and CH_4 [52] but limited to the intermediate and high energy regimes. As for studies using the TC-BGM to study collision-induced radiative emissions, only one analysis [53] had been carried out so far.

From a theoretical perspective, collision-induced radiative emission spectra provide a good benchmark on the accuracy of subshell capture population calculations. With the wealth of experimental data on the SWCX problems that are available, it is worthwhile to explore the TC-BGM by assessing its applicability on these collision problems.

1.5 COLLISION SYSTEMS OF INTEREST

In this dissertation, a series of radiative emission analyses from collision systems related to the SWCX phenomenon are carried out. Given the vast chemical compositions of both solar wind and interstellar gases, only a selected number of collision systems were investigated. The selection of these systems is mainly based on: (i) availability of experimental data, and (ii) complexity of the collision system. The investigation focuses on collisions involving highly-charged projectiles ($q \geq 6$) and targets of various complexity such as atomic hydrogen, noble gases (e.g., He, Ne), and the aforementioned H_2O and CH_4 molecules. Experimental data on all these collision problems were used as benchmarks. The following lists the collision studies that were carried out during this research period along with a brief synopsis:

1. *Ne^{10+} collisions with helium, neon, and argon* [54]

   Ali *et al.* [24] reported experimental and CTMC capture cross sections and radiative emission spectra of the Lyman series from Ne^{10+}-He, -Ne, and -Ar collisions at $E_P = 4.54$ keV/u. Another work by Liu *et al.* [55] also studied these collisions using the TC-AOCC method but the agreement with Ali *et al.* [24] appeared inconsistent. The present analysis examines both studies by comparing with present results using the TC-BGM.

2. *C^{6+} collisions with helium and molecular hydrogen* [56]

   This study examines the experimental works by Defay *et al.* [57] and Fogle *et al.* [25] where radiative emissions from C^{6+}-He and C^{6+}-H_2 collisions were reported, respectively. Here, emission spectra of the Lyman series were examined from collisions over a range of impact energies between 0.5 and 40 keV/u. This study also explores the role of autoionizing double-capture events on the emission spectra.

3. *O^{6+} collisions with argon, water, and methane* [58]

   Machacek *et al.* [59] reported experimental and CTMC total capture cross sections from O^{6+} collisions with Ar and a variety of molecules at 1.17 and 2.33 keV/u. Cross sections from CTMC calculations were used to produce radiative emission spectra from these collisions. The present analysis focuses on collisions with Ar, H_2O, and CH_4 targets. It offers a first look on the applicability of the TC-BGM to slow collisions with H_2O and CH_4 targets.

4. *Collisions of C^{6+} and O^{8+} ions with hydrogen and krypton atoms*

   This analysis is a first attempt of using the TC-BGM to describe electron capture in collisions with a Kr target. Electron capture from Kr is compared with collisions with atomic hydrogen over impact energies between 0.5 and 40 keV/u. Subsequent radiative emissions from these collisions were also calculated and results are compared with experimental measurements by Andrianarijaona *et al.* [60] and Seely *et al.* [61].

From the above list, much of the work presented in this dissertation is adapted from published and peer-reviewed articles with the exception of the last item. However, certain details and results that were originally prepared have been left out from these publications. This dissertation serves as an excellent opportunity to re-purpose these details.

1.6 DISSERTATION OUTLINE

In the next chapters, many points on the framework and methodology of collision calculations that were briefly discussed so far are further expanded. The organization of this dissertation is as follows. Chapter 2 discusses the collision framework and the motivation to use the single-electron picture of the IEM along with choices of effective potentials for the present research. In Chapter 3, details of the TC-BGM are discussed and how this method is applied to ion-atom and ion-molecule collisions along with methods for final-state analyses and the post-collision processes are discussed. Following Chapter 3, results and findings for all collision studies mentioned in the above list are given as individual chapters. Lastly, a summary and outlook outlining various possible future studies are given in the last chapter.

CHAPTER 2

Collision framework

2.1 OVERVIEW

The exact treatment of the many-particle collision problem is a challenging task. As briefly discussed in Ch. 1, numerical calculations in the exact treatment for the simplest case of the proton-hydrogen collision system has only been reported recently [28]. Nevertheless, if one works with nonrelativistic collisions that are considered fast enough, specifically comparable with the orbital speed of the target valence electron, models and approximations can be employed to make the problem feasible to solve.

The purpose of this chapter is to establish the framework in which the collision calculations are performed. The discussion begins with the topic of the separation of the nucleus and electron problems in the semi-classical approximation. For the many-electron problem, one can then separate this into effective single-electron problems via the IEM. The approximation made in the IEM can be understood from the perspective of time-dependent density functional theory (TDDFT). Furthermore, an effective potential that describes the electron-electron interaction is required within the single-electron picture. Two variants were used in this work and the choices of these potentials are also discussed.

2.2 TREATMENT OF HEAVY-PARTICLE MOTION

Electrons and nuclei have masses with different orders of magnitude. For example in a hydrogen atom, the proton has a mass of about 1836 a.u. which is much heavier than an electron with a mass of 1 a.u.. If the magnitude of the force exerted on both the electrons and nuclei are the same, then the change in momentum as a result of this force must also be the same. For the nuclei, this corresponds to small changes in velocity. For this reason, it can be assumed that the total wavefunction can be expressed as a product of the electronic and nuclear wavefunctions. This separation of the electronic and nuclear problems is known as the *Born-Oppenheimer approximation* [62].

2.2.1 The semi-classical approximation

With the separation of the nuclear and electronic dynamics, one can employ the semi-classical approximation where the nuclei are treated classically and the electrons quantum-mechanically. In collision problems, the validity of this treatment can be shown with the de Broglie wavelength that is associated with the heavy projectile. For a projectile with mass M travelling with speed v_{p}, the associated de Broglie wavelength λ is

$$\lambda = \frac{2\pi}{M v_{\mathrm{p}}}. \tag{2.1}$$

For example, if the projectile is a proton with a mass of 1836 a.u. and $E_{\mathrm{P}} = 100$ eV/u, corresponding to a speed of ≈ 0.07 a.u., the associated de Broglie wavelength is $\lambda \approx 0.05$ a.u., which is short compared to the interaction region on the order of the Bohr radius (1 a.u.). For such small wavelengths (i.e., $\lambda < 1$) a localized wave packet can be formed where the centre of which follows a classical trajectory [29].

The impact energies of the collision problems considered here are $E_{\mathrm{P}} \geq 0.5$ keV/u, high enough to employ the semi-classical approximation based on the above condition. Moreover, the projectile nucleus is assumed to travel in a pre-determined straight-line path, which is also valid at these impact energies. However, in the case of energies well below 0.5 keV/u, one would need to resort to a full quantum-mechanical treatment for an accurate description of the collision dynamics.

Under the semi-classical approximation, electrons in the target are governed by the time-dependent Schrödinger equation (TDSE)

$$i\frac{\partial \Psi(t)}{\partial t} = \hat{H}(t)\Psi(t), \tag{2.2}$$

where Ψ is the many-electron wavefunction and $\hat{H}$ is the electronic Hamiltonian. In a collision problem, the goal is to solve the TDSE subject to some initial condition

$\Psi(t = t_0)$ to extract the electronic transition amplitudes by propagating in time until the projectile and target no longer interact, i.e.,

$$a_f = \lim_{t \to \infty} \langle \phi_f(t) | \Psi(t) \rangle \, . \tag{2.3}$$

The corresponding transition probability that the system is found in ϕ_f is $p_f = |a_f|^2$.

With the framework discussed so far, it is helpful to visualize the setup of the collision problem in Cartesian space. Figure 2.1 shows the setup of a collision system, which is known as the *impact parameter model* [29]. For simplicity, the figure shows a target with only one electron and the projectile is assumed to be a bare ion. In addition, the xz-plane is chosen as the scattering plane with the target nucleus fixed at the origin and the projectile moving in a straight path at $x > 0$. The internuclear distance can then be described as $\mathbf{R}(t) = (b, 0, v_{\mathrm{P}} t)$ where b is the impact parameter.

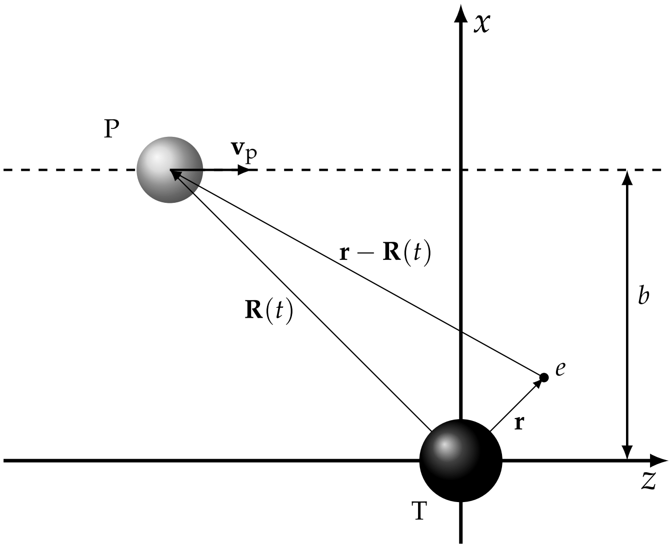

FIG. 2.1: Setup of the collision problem in the impact parameter model. The xz-plane is chosen to be the scattering plane. The target (T) core is fixed at the origin while the projectile (P) core assumes a predetermined straight-line path at constant velocity.

With the collision system in a coordinate representation (e.g., Fig. 2.1) the general many-electron Hamiltonian $\hat{H}$ is expressed as

$$\begin{aligned} \hat{H}(t) &= \hat{T} + \hat{V}_{ee} + \hat{V}_{\mathrm{ext}}(t) \\ &= -\frac{1}{2} \sum_{j=1}^{N} \nabla_j^2 + \sum_{i<j}^{N} \frac{1}{|\mathbf{r}_i - \mathbf{r}_j|} + \sum_{j=1}^{N} \left(\frac{-Z_{\mathrm{T}}}{r_j} + \frac{-Z_{\mathrm{P}}}{|\mathbf{r}_j - \mathbf{R}(t)|} \right) \end{aligned} \tag{2.4}$$

where $\hat{T}$ is the kinetic energy, $\hat{V}_{ee}$ is the electron-electron interaction potential, and $\hat{V}_{\text{ext}}$ is an external single-electron potential. In Eq. (2.4), $\hat{V}_{\text{ext}}$ is the potential of the target and projectile nuclei with charges Z_{T} and Z_{P}, respectively but in general can include other external interactions such as a laser field. Electron spin-dependent interactions, which are intrinsic in quantum systems, are neglected in the Hamiltonian (2.4) but it should be noted that spin-statistics is included in the IEM framework as a requirement that the many-electron wavefunction be antisymmetric. As mentioned earlier, the many-electron TDSE cannot be solved analytically and this can now be understood from the Hamiltonian (2.4) where the interaction terms prevent the equation from being separable. At this stage, numerical methods are still not tractable enough to efficiently solve the collision problem. While there have been studies on collision calculations that solve the full many-electron TDSE, most of these studies were only done with helium as the target [33]. In other words, solving the full TDSE has only been successful with, at most, two-electron transitions.

2.3 EFFECTIVE SINGLE-ELECTRON PICTURE

An approach to work with collision systems involving many active electrons is the effective single-electron picture. This approach can be based on TDDFT, an important theory in quantum mechanics.

The basic idea of TDDFT is to take a complicated interacting many-particle problem and express it as a much simpler system of independent particles. The Runge–Gross theorem [63], which serves as the foundation of TDDFT, shows that there is a one-to-one mapping (correspondence) between the external potential $\hat{V}_{\text{ext}}(t)$ and the electronic one-particle density $n(\mathbf{r}, t)$. This powerful theorem implies that, in principle, the complete properties contained in the many-electron wavefunction can be reconstructed from the one-particle density.

In the Kohn–Sham scheme [64], the one-particle density takes the form

$$n(\mathbf{r}, t) = \sum_{j=1}^{N} |\psi_j(\mathbf{r}, t)|^2 \tag{2.5}$$

where the set $\{\psi_j, j = 1, ..., N\}$ consists of solutions of the time-dependent Kohn–Sham equations

$$i\frac{\partial \psi_j(\mathbf{r},t)}{\partial t} = \hat{h}(t)\psi_j(\mathbf{r},t), \quad j = 1, ..., N \tag{2.6}$$

with the single-electron Hamiltonian $\hat{h}(t)$

$$\hat{h}(t) = -\frac{1}{2}\nabla^2 + v_{\mathrm{KS}}(\mathbf{r},t). \tag{2.7}$$

The effective Kohn–Sham potential v_{KS} is, in fact, a functional that is uniquely determined by $n(\mathbf{r},t)$ as a consequence of the Runge–Gross theorem. The Kohn–Sham potential can be decomposed into the external Coulomb interaction v_{ext} and the effective electron-electron interaction v_{ee}

$$v_{\mathrm{KS}}[n](\mathbf{r},t) = v_{\mathrm{ext}}(\mathbf{r}) + v_{ee}(\mathbf{r},t). \tag{2.8}$$

It is important to note that the Runge–Gross theorem only proves the correspondence of v_{ee}, meaning it does not provide a prescription of how v_{ee} is to be constructed. Therefore, v_{ee} is modelled in practice. To this end, v_{ee} can be decomposed as

$$v_{ee}[n](\mathbf{r},t) = v_{\mathrm{H}}[n](\mathbf{r},t) + v_{\mathrm{xc}}[n](\mathbf{r},t), \tag{2.9}$$

where

$$v_{\mathrm{H}}[n](\mathbf{r},t) = \int \frac{n(r',t)}{|\mathbf{r}-\mathbf{r}'|}d^3r' \tag{2.10}$$

is the Hartree potential that accounts for the screening due the presence of all electrons and v_{xc} is the effective exchange-correlation potential. The correlation part of v_{xc} remains out of reach in this work, which means the collision systems studied here are restricted to the exchange-only level. This no-correlation limit corresponds to an analysis on the level of the IEM.

The IEM starts with the assumption that the many-electron wavefunction Ψ is expressed as products of the single-electron wavefunctions ψ. However, this itself does not satisfy the antisymmetry property of the Pauli exclusion principle, which states that two electrons (or fermions) under exchange must lead to a sign reversal in the wavefunction. Another way to state this principle is to say that no two electrons can have the same quantum numbers. To satisfy this requirement, the many-electron wavefunction should at all times be expressed as a Slater determinant

$$\Psi(\mathbf{r}_1, ..., \mathbf{r}_N, \sigma_1, ..., \sigma_N, t) = \frac{1}{\sqrt{N!}} \begin{vmatrix} \psi_{1\sigma_1}(\mathbf{r}_1, t) & \psi_{2\sigma_2}(\mathbf{r}_1, t) & ... & \psi_{N\sigma_N}(\mathbf{r}_1, t) \\ \psi_{1\sigma_1}(\mathbf{r}_2, t) & \psi_{2\sigma_2}(\mathbf{r}_2, t) & ... & \psi_{N\sigma_N}(\mathbf{r}_2, t) \\ \vdots & \vdots & \ddots & \vdots \\ \psi_{1\sigma_1}(\mathbf{r}_N, t) & \psi_{2\sigma_2}(\mathbf{r}_N, t) & ... & \psi_{N\sigma_N}(\mathbf{r}_N, t) \end{vmatrix}, \tag{2.11}$$

where $\psi_{i\sigma_i}$ denote the spin orbitals and the index σ_i is the z-component of the spin. This serves as a starting point for the well-known time-dependent Hartree-Fock method to variationally solve the many-electron problem. Unlike the Hartree-Fock method, the Kohn–Sham scheme of TDDFT that the present calculations are based on requires that the exchange potential be local. For the collision problem, the single-electron TDSEs are summarized as

$$\boxed{i\frac{\partial \psi_j(\mathbf{r}, t)}{\partial t} = \left[-\frac{1}{2}\nabla^2 + V_\mathrm{T} + V_\mathrm{P}\right] \psi_j(\mathbf{r}, t), \quad j = 1, ..., N. \tag{2.12}}$$

where V_T and V_P are effective potentials of the target and projectile, respectively.

2.4 EFFECTIVE GROUND-STATE POTENTIALS

Several representations of target and projectiles ground-state potentials in the single-electron TDSEs (2.12) were used in this work. The projectiles that are involved are mostly bare ions, meaning that V_P is simply a Coulomb potential. When electrons are present on the incoming projectile, there are various ways one can represent the associated potential within the IEM framework. One approach is to include a Hartree term (2.10) to account for the electron screening. Alternatively, effective potentials can also be used for describing electrons moving outside an inner closed-shell projectile core. In this approach, electrons in the inner-shell structure are assumed to be frozen (i.e., time-independent), which is valid for collisions that are sufficiently fast (i.e., impact energies in the intermediate regime or higher). This assumption can also be made with the Hartree approach (2.10) by dropping the time-dependence.

The simplest approach in obtaining a frozen, effective ground-state potential is the approximate screened Coulomb potential $-Z_\mathrm{eff}/r$ where Z_eff is an effective nuclear charge. A more elaborate approach is to start with a charged cloud density and solve Poisson's equation subject to appropriate boundary conditions and asymptotic behaviours. In the work by Daniele [65, 66], a general expression of the effective potential of the valence electron in alkali atoms and alkali-like ions was obtained

$$V_{\text{eff}}(r) = -\left(\frac{Z - \sum_s z_s}{r}\right) + \sum_s \sum_{k=0}^{n_s+1} -\frac{z_s(\gamma_s r)^k (n_s + 2 - k)}{r(n_s + 2)k!} \exp(-\gamma_s r) \tag{2.13}$$

where n_s is the principal quantum number of the s-th inner shell and z_s is the corresponding number of electrons. Eq. (2.13) also contains the free parameters γ_s which are chosen such that one obtains the minimal energy eigenvalue of the stationary Hamiltonian $-\frac{1}{2}\nabla^2 + V_{\text{eff}}$.

The effective ground-state potential of Eq. (2.13) has been used to study single-electron transitions in collision systems with a few electrons in the target (e.g., lithium [67]). Furthermore, the form of Eq. (2.13) has also been adapted to *model* the potential of the hydrogen molecule target [68, 69], dressed projectiles (e.g., O^{6+} [70]), and noble gas atoms [55]. Despite the successes of model potentials, they may not be sufficient for a realistic description when exchange effects are important.

A more systematic approach to frozen effective ground-state potentials, which is often used in this work, is the optimized potential method (OPM). Within a Hartree-Fock (self-consistent) framework, the OPM applied to atoms was developed by Talman and Shadwick [71][1]. It is an iterative numerical process where the effective potential is determined variationally by minimizing the expectation value of the stationary Hamiltonian with respect to a Slater determinant. With the constraint that the potential be local, the Slater determinant is formed from single-electron orbitals and variations are with respect to the effective potential. This results in a linear integral equation (OPM integral equation) for the effective potential, which is solved numerically. Interestingly, this self-consistent approach to the OPM [71] was later recognized as the exchange-only limit of the Kohn–Sham scheme of density functional theory [74]. Specifically, the OPM integral equation can be derived starting from the effective exchange-correlation potential [75]

$$v_{\text{xc}}[n](\mathbf{r}) = \frac{\delta E_{\text{xc}}[n]}{\delta n(\mathbf{r})}. \tag{2.14}$$

For exchange-only, E_{x} corresponds to the standard Fock expression. Furthermore, it is important to note that approximate treatments of exchange effects such as the local-

---

[1] J. Slater [72] laid out the ground work and later R. Sharp and G. Horton [73] developed the formalism of the OPM. The latter apparently remained unnoticed for quite some time.

density approximation [64] or the Hartree-Fock-Slater potential [72] can lead to large discrepancies in collision calculations due to an incorrect asymptotic behaviour of v_{x}, particularly in the low impact energy regime [76]. This makes the OPM potential, which is free of these limitations, an appealing choice.

2.4.1 Time-dependent screening effect

In a many-electron system, removal of an electron can cause a decrease in screening due to a change in the electronic distribution, and should correspond to a change in the effective potential. Up until now, the discussion regarding the usage of an effective target potential in a many-electron system assumes that it is frozen. This assumption is reasonable for fast collisions where the spatial electronic distribution does not change at those time scales. However, this would not hold if one works in the low-energy regime [76, 77].

Going for a microscopic treatment of the time-dependent screening effects poses two major problems: (i) increase in computational cost, and (ii) loss of linearity of the single-electron Hamiltonian. For these reasons, a simplified model of this time-dependent screening effect, which is referred to as the *target-response model* (or *response model*), was introduced for ion-atom collisions [78]. This model has been applied to various collision systems with many-electron targets, mainly within TC-BGM calculations [42, 79, 80], which showed improved total cross sections compared to the frozen potential approximation in the low and intermediate energy regimes. However, its effects on radiative cascades was only explored in one study [53], and therefore, calculations in this work on ion-atom collisions were performed with and without this model for comparison. The important aspects of the formulation of the time-dependent screening model from Ref. [78] are given in the following.

Starting with the effective potential of the atomic target defined as

$$v_{\mathrm{eff}}^{\mathrm{T}}(\mathbf{r},t) = -\frac{Z_{\mathrm{T}}}{r} + v_{ee}(\mathbf{r},t), \tag{2.15}$$

the effective electron-electron potential v_{ee} is separated into static (v_{ee}^{0}) and dynamic (δv_{ee}) parts,

$$v_{ee}(\mathbf{r},t) = v_{ee}^{0}(r) + \delta v_{ee}(\mathbf{r},t), \tag{2.16}$$

such that

$$v_{\text{eff}}^{\text{T}}(\mathbf{r},t) = -\frac{Z_{\text{T}}}{r} + v_{ee}^{0}(r) + \delta v_{ee}(\mathbf{r},t). \tag{2.17}$$

More precisely, v_{ee}^{0} is the undisturbed atomic target ground-state potential before the collision. As mentioned above, v_{ee}^{0} is represented by the exchange-only version of the OPM potential in this work. By setting $\delta v_{\text{eff}} = 0$ this corresponds to the frozen potential approximation. In this work, this treatment is referred to as the *no-response approximation*.

The formulation of a simplified time-dependent variation of the electron screening δv_{eff} [78] starts with the assumption that $v_{\text{eff}}^{\text{T}}$ can be approximated as a linear combination of ionic ground-state central potentials $v_q(r)$ weighted with time-dependent q-fold electron-loss (removal) probabilities P_q^{loss}

$$v_{\text{eff}}^{\text{T}}(\mathbf{r},t) \approx v_{\text{eff}}^{\text{T}}(r,t) = \sum_{q=0}^{N} P_q^{\text{loss}}(t) v_q(r). \tag{2.18}$$

Starting with $q = 0$ (i.e., no electron removed), v_q is defined as

$$v_q(r) = v_0(r) = -\frac{Z_{\text{T}}}{r} + v_{ee}^{0}(r). \tag{2.19}$$

For $q \geq 1$, v_q is assumed to scale in the following way,

$$v_q(r) = v_0(r) - \frac{q-1}{N-1} v_{ee}^{0}(r), \tag{2.20}$$

such that v_{eff} reduces to $-Z_{\text{T}}/r$ for a fully ionized target (i.e., $q = N$). It is important to note that the case for $q = 1$ simply reduces to the $q = 0$ case of Eq. (2.19). This is because the active electron in single removal has to be subject to an effective potential that approaches $-1/r$ asymptotically but does not reduce the screening due to removal of other electrons.

The task now is to relate the ansatz of Eq. (2.18) to the individual potentials in the general definition of $v_{\text{eff}}^{\text{T}}$ (2.17). By using Eqs. (2.19) and (2.20), it follows that

$$
\begin{aligned}
v_{\text{eff}}^{\text{T}}(r,t) &= \sum_{q=0}^{N} P_q^{\text{loss}}(t) v_q(r) \\
&= P_0^{\text{loss}}(t) v_0(r) + \sum_{q=1}^{N} P_q^{\text{loss}}(t) v_q(r) \\
&= \left(1 - \sum_{q=1}^{N} P_q^{\text{loss}}(t)\right) v_0(r) + \sum_{q=1}^{N} P_q^{\text{loss}}(t) \left[v_0(r) - \frac{q-1}{N-1} v_{ee}^0(r)\right] \\
&= v_0(r) - \frac{1}{N-1} \sum_{q=1}^{N} (q-1) P_q^{\text{loss}}(t) v_{ee}^0(r).
\end{aligned} \tag{2.21}
$$

Comparing the last line of Eq. (2.21) with Eq. (2.17), the time-dependent variation in the effective potential is

$$
\delta v_{ee}(\mathbf{r},t) = -\frac{1}{N-1} \sum_{q=1}^{N} (q-1) P_q^{\text{loss}}(t) v_{ee}^0(r). \tag{2.22}
$$

What remains is to relate P_q^{loss} with solutions of the single-electron TDSEs (2.12). This is done using the so-called *net numbers* which correspond to the average number of electrons undergoing a certain process (e.g., capture) [77]. Net electron loss is expressed as

$$
P_{\text{net}}^{\text{loss}}(t) = \sum_{q=1}^{N} q P_q^{\text{loss}}(t). \tag{2.23}
$$

It is explicitly calculated according to

$$
P_{\text{net}}^{\text{loss}}(t) = N - \sum_{i=1}^{N} \sum_{v=1}^{V} |\langle \phi_v | \psi_i(t) \rangle|^2, \tag{2.24}
$$

where a finite set of bound target states $\{\phi_v\}$ are projected onto the single-electron solutions during the collision. With these defined, working out the details of Eq. (2.22) gives

$$\begin{aligned}\delta v_{ee}(\mathbf{r},t) &= -\frac{1}{N-1}\sum_{q=1}^{N}(q-1)P_q^{\text{loss}}(t)v_{ee}^0(r)\\ &= -\frac{1}{N-1}\left[\sum_{q=1}^{N} qP_q^{\text{loss}}(t) - \sum_{q=1}^{N} P_q^{\text{loss}}(t)\right] v_{ee}^0(r)\\ &= -\frac{1}{N-1}\left[P_{\text{net}}^{\text{loss}}(t) + P_0^{\text{loss}}(t) - 1\right] v_{ee}^0(r)\end{aligned}$$

and by defining $Q_s(t) = P_{\text{net}}^{\text{loss}}(t) + P_0^{\text{loss}}(t) - 1$ as the *screening function*, $\delta v_{ee}(\mathbf{r},t)$ can be expressed as

$$\boxed{\delta v_{ee}(\mathbf{r},t) = -\frac{Q_s(t)}{N-1}v_{ee}^0(r). \qquad (2.25)}$$

Furthermore, $P_{\text{net}}^{\text{loss}}/N$ can be interpreted as the average probability for a single electron that is lost from the target. Therefore, P_0^{loss} can also be related to $P_{\text{net}}^{\text{loss}}$ by the binomial formula such that

$$P_0^{\text{loss}}(t) = \left[1 - \frac{P_{\text{net}}^{\text{loss}}(t)}{N}\right]^N . \qquad (2.26)$$

Having established the collision framework for the present study the discussion can now proceed towards the calculation of transition amplitudes of the single-electron TDSEs.

CHAPTER 3

Theoretical methods: Collision and post-collision analyses

3.1 OVERVIEW

In this chapter, the methods of collision and post-collision calculations used in the present work are presented. The analyses of these calculations are performed separately. Although the present work involves collisions in the low-energy regime, they take place on the femto-second timescale (10^{-15} s) while the post-collision Auger ($\approx 10^{-12}$ s) and radiative ($\approx 10^{-9}$ s) processes occur on longer timescales.

There are two main goals in solving the collision problem in the present work: (i) calculating capture cross sections, and (ii) obtaining radiative spectra from single-electron capture events. The approach to the collision problem, which is represented by a set of single-electron TDSEs, is the close-coupling approach. Specifically, the present work uses the TC-BGM. This chapter discusses the features of the TC-BGM and its applicability to ion-atom and ion-molecule systems. The chapter also delves into final-state analyses and how these methods are used in the post-collision Auger and radiative calculations.

3.2 COLLISION ANALYSIS: THE CLOSE-COUPLING METHOD

The close-coupling method is considered a standard theoretical approach to describe electronic transitions in a fully non-perturbative framework. In this approach, the electron motion is constrained to a configuration space which is represented by a finite set of basis states $\{\psi_j, j = 1, ..., N\}$. Within the semi-classical approximation, the time-dependent electronic wavefunction is expressed as a linear combination of these basis states,

$$\Psi(\mathbf{r}, t) = \sum_{j=1}^{N} a_j(t)\varphi_j(\mathbf{r}, t), \tag{3.1}$$

When the electronic wavefunction is expanded in this way, it is only required to determine a *finite* set of transition amplitudes a_j. By assuming the wavefunction (3.1) obeys the TDSE within the space of a finite basis set, then

$$\langle\varphi_k| \left[i\frac{\partial}{\partial t} - \hat{H}(t) \right] |\Psi(t)\rangle = 0. \tag{3.2}$$

This leads to a set of N-coupled equations,

$$i\sum_{j=1}^{N} \langle\varphi_k|\varphi_j\rangle \frac{da_j(t)}{dt} = \sum_{j=1}^{N} \langle\varphi_k| \hat{H}(t) - i\frac{\partial}{\partial t} |\varphi_j\rangle a_j(t), \qquad k = 1, ..., N. \tag{3.3}$$

For an orthonormal basis set, Eqs. (3.3) reduce to

$$i\frac{da_k(t)}{dt} = \sum_{j=1}^{N} a_j(t) \langle\varphi_k| \hat{H}(t) - i\frac{\partial}{\partial t} |\varphi_j\rangle, \qquad k = 1, ..., N. \tag{3.4}$$

Although the close-coupling approach is shown for the full TDSE, it applies in the same way for single-electron TDSEs.

Traditionally, two types of electronic basis sets have been used to represent bound states – atomic-orbital (AO) sets and/or a molecular-orbital (MO) sets. The review by Fritsch and Lin [33] extensively discusses these basis sets and their various ways of construction. Additionally, finite numbers of pseudostates are also included in the basis set in practice as they are useful to obtain ionization cross sections. They are also used for representing the united-atom orbitals for describing the molecular character of the electronic wavefunction at small internuclear distances and impact parameters [81, 82]. Pseudostates in an atomic basis set can be constructed using Sturmian, Gaussian, or Hylleraas functions [33] by diagonalizing the Hamiltonian matrix. For calculations using a molecular basis set, pseudostates have been constructed using Gaussian-type orbitals [69].

In an atomic collision problem, the natural approach to the close-coupling method is the two-centre basis-set expansion. Although collision problems had been carried out using a one-centre basis due to practical reasons, it is not sufficient when electron capture is important [33]. To include pseudostates, they may be centred either on the projectile or the target. One could also choose to centre pseudostates at some point between the target and the projectile, which constitute to a three-centre basis set expansion [33], but obviously at a price of a difficult three-centre integral calculation.

The general strategy of close-coupling calculations using an AO basis is to include as many states as possible. The basis should contain, at the minimum, the initially populated states of the target and some final bound states of the projectile. If the objective is to describe target excitation, then it is expected that some excited states are included as well. Excited states, as well as pseudostates, are also considered as intermediate states that may be populated and de-populated during the collision.

Due to the computational demand, the AO close-coupling method was applied to one-electron transitions for quite some time [10, 33]. These studies have also been limited to ion-hydrogen and ion-alkali collision systems with lowly-charged projectiles (e.g., H^+, He^{2+}) since highly-charged projectile ions results in bound capture states of high n, which requires a large basis set. However, as computational power has increased over time it has become quite feasible to handle a large basis set in close-coupling calculations.

3.3 THE BASIS GENERATOR METHOD IN ION-ATOM COLLISIONS

The BGM [40], based on the close-coupling method, was designed as an alternative approach to solve the single-electron TDSEs

$$i\frac{\partial\psi_i(\mathbf{r},t)}{\partial t} = \hat{h}(t)\psi_i(\mathbf{r},t), \quad i = 1, ..., N. \tag{3.5}$$

It rests on the idea that convergence can be achieved without resorting to a very large basis set through the use of a dynamical basis which is adapted to the problem at hand.

In the formal setting, the BGM starts with the definition of a *generating basis*, which is a finite set of bound eigenstates of the undisturbed Hamiltonian $\hat{h}_0$

$$\hat{h}_0 \left|\phi_v^0\right\rangle = \epsilon_v \left|\phi_v^0\right\rangle, \quad v = 1, ..., V \tag{3.6}$$

$$\hat{h}(t) = \hat{h}_0 + v(t). \tag{3.7}$$

A hierarchy of V-dimensional subspaces of the Hilbert space is then generated by successive application of the Schödinger operator $\hat{O} = \hat{h}(t) - i\partial_t$

$$\begin{aligned} |\phi_v^u(t)\rangle &= \hat{O}\,|\phi_v^{u-1}(t)\rangle \\ &= \hat{O}^u\,|\phi_v^0\rangle\,, \qquad v = 1, ..., V, \;\; u = 1, ..., U. \end{aligned} \tag{3.8}$$

While the states of Eq. (3.8) are not orthonormal they were shown to be linearly independent [40]. It was also shown that only states of the highest order in the hierarchy couple to the part of the Hilbert space that is not included in the basis (i.e., the infinite complementary space) [40]. In principle, this BGM scheme can be applied for different Hamiltonians.

The construction of the hierarchy of states $|\phi_v^u\rangle$ through repeated application of the Schrödinger operator leads to complicated high-order gradient terms. Therefore, the so-called *BGM strategy* was established [41] in order to provide a more practical implementation of the BGM. This involves introducing an alternative set of states $\{|\chi_\nu^\mu\rangle\}$ with a simpler basis generation such that each state $|\phi_v^u\rangle$ can be represented as a linear combination of the former. Specifically, it was shown [41] that for a collision system described by the Hamiltonian

$$\hat{h}(t) = -\frac{1}{2}\nabla^2 - \frac{Z_\mathrm{T}}{r} - \frac{Z_\mathrm{P}}{|\mathbf{r} - \mathbf{R}(t)|}, \tag{3.9}$$

the alternative hierarchy can include only a regularized Coulomb potential $\hat{W}(t)$ where states in this hierarchy takes the form

$$|\chi_\nu^\mu(t)\rangle = [\hat{W}(t)]^\mu\,|\chi_\nu^0\rangle\,, \quad \nu = 1, ..., K, \;\; \mu = 1, ..., M_\nu \tag{3.10}$$

with χ_ν^0 resembling spherical Slater-type orbitals[1] by assumption. The set of M_ν is referred to as the *BGM hierarchy*, which determines the size and structure of the BGM basis. In the earliest work of the BGM [40], which details a two-centre geometry collision problem using a one-centre generating basis, it has been shown that good convergence and reliable results are obtained by approximating these orbitals (3.10) using the eigenstates of the undisturbed atomic Hamiltonian (3.9)

$$\chi_\nu^\mu(\mathbf{r}, t) = [\hat{W}_\mathrm{P}(t;\alpha)]^\mu \phi_\nu^0(\mathbf{r}), \tag{3.11}$$

---

[1] Unlike Slater-type orbitals, χ_ν^0 allows for negative powers of r [41].

with the Yukawa-like regularization of the projectile

$$\hat{W}_{\mathrm{P}}(t) = \frac{1 - \exp(-\alpha|\mathbf{r} - \mathbf{R}(t)|)}{|\mathbf{r} - \mathbf{R}(t)|} \tag{3.12}$$

using a regularization parameter of $\alpha = 1$. The vectors $\mathbf{r}$ and $\mathbf{R}(t)$ are the same as those in Fig. 2.1. The states χ_ν^μ for $\mu > 0$ are the *BGM pseudostates* and when orthogonalized [41] to the generating basis, they account for quasimolecular effects at low impact velocities and ionization channels. This hierarchy scheme has been successfully used in various collision problems [77, 78, 80, 83, 84]. However, the use of a one-centre generating basis limits the applicability of the BGM to describe electron capture since bound projectile states are not explicitly included in the set.

An extension of the BGM based on a two-centre basis (i.e., TC-BGM) was introduced [42] to allow for a more detailed description of electron capture. It is the main method used for collision calculations in the present work. Naturally, the collision calculations in the TC-BGM are performed in the centre-of-mass frame. The basis is now generated from a finite set of K_{T} target and $K - K_{\mathrm{T}}$ projectile states taking into account Galilean invariance by the appropriate choice of electron translation factors

$$\phi_\nu^0(\mathbf{r}) = \begin{cases} \phi_\nu(\mathbf{r}_{\mathrm{T}}) \exp\left(i\mathbf{v}_{\mathrm{T}} \cdot \mathbf{r}\right), & \nu \le K_{\mathrm{T}} \\ \phi_\nu(\mathbf{r}_{\mathrm{P}}) \exp\left(i\mathbf{v}_{\mathrm{P}} \cdot \mathbf{r}\right), & \text{otherwise,} \end{cases} \tag{3.13}$$

where $\mathbf{r}$, $\mathbf{r}_{\mathrm{T}}$, and $\mathbf{r}_{\mathrm{P}}$ are the position vectors with respect to the centre-of-mass, target, and projectile frames, respectively. The vectors $\mathbf{v}_{\mathrm{T}}$ and $\mathbf{v}_{\mathrm{P}}$ are the constant velocities of the atomic target and projectile in the centre-of-mass frame, respectively. Basis generation in the TC-BGM is also produced by repeated application of the regularized projectile potential (3.12) onto the generating basis of Eq. (3.13). Similar to the one-centre BGM, basis generation in the TC-BGM by using only target states can achieve good convergence and reliable results [42–44, 48].

In the present work, single-electron TDSEs (3.5) are solved by expansion of the single-electron solution in terms of the TC-BGM basis states (3.13) and hierarchy (3.11). For the j-th active electron, the single-electron solution is given as

$$\psi_j(\mathbf{r}, t) = \sum_{\mu=0}^{M_\nu} \sum_{\nu=1}^{K} a_{\mu\nu}^j(t) \chi_\nu^\mu(\mathbf{r}, t). \tag{3.14}$$

The coupled-channel equations expressed in these basis states are then

$$i \sum_{\mu=0}^{M_\nu} \sum_{\nu=1}^{K} \langle \chi_{\nu'}^{\mu'} | \chi_\nu^\mu \rangle \frac{d a_{\mu\nu}^j(t)}{dt} = \sum_{\mu=0}^{M_\nu} \sum_{\nu=1}^{K} \langle \chi_{\nu'}^{\mu'} | \, \hat{h} - i \frac{\partial}{\partial t} \, | \chi_\nu^\mu \rangle \, a_{\mu\nu}^j, \tag{3.15}$$

which can also be expressed in matrix-vector form

$$iS\dot{\mathbf{a}}_j = M\mathbf{a}_j \tag{3.16}$$

where S is the overlap matrix containing elements of $\langle \chi_{\nu'}^{\mu'} | \chi_\nu^\mu \rangle$, M is the interaction matrix containing matrix elements of $\langle \chi_{\nu'}^{\mu'} | \, \hat{h} - i\partial_t \, | \chi_\nu^\mu \rangle$, and $\mathbf{a}_j$ is a vector with the expansion coefficients $a_{\mu\nu}^j$ as components. In practice, parts of the interaction matrix elements are expressed in terms of overlap matrix elements such that the explicit gradient terms are avoided in the computation. The details of these transformations are found in the Appendices of Refs. [40, 41, 50].

3.3.1 Convergence and numerical accuracy

Convergence of the numerical solutions to the coupled-channel equations (3.15) is largely based on the BGM hierarchy $\{M_\nu\}$. Selection of M_ν relies on a few simple rules based on experiences from previous TC-BGM calculations. First, the same value of M_ν is assigned for all ν corresponding to orbitals with identical n and l quantum numbers. Second, a monotonous increment of M_ν is preferred but one should avoid large steps. However, numerical instabilities can limit the size of M_ν. For convergence testing, one should perform calculations using different hierarchies and compare results by relative differences. The selection of the BGM hierarchies shown throughout are based on this approach. As a demonstration, Table 3.1 shows three different hierarchies used to check convergence on collision calculations of the C^{6+}-He system. The hierarchy labelled 'H-1' has the fewest BGM pseudostates while the hierarchy labelled 'H-3' has the most.

Figure 3.1 shows the time development of the total capture probability based on the hierarchies in Table 3.1. These calculations are done using the no-response approximation in the effective potential. While all three curves in the figure are very similar in magnitude for $z < 0$, the curve of H-1 begins to deviate at around $z = 2$. When the projectile is sufficiently far, for example at $z = 40$, one can check that the rela-

TABLE 3.1: BGM hierarchies $\{M_\nu\}$ used for convergence testing on C^{6+}-He collision calculations at impact parameter $b = 4$ a.u. and $E_P = 25$ keV/u.

State:	$1s$	$2s$	$2p$	$3s$	$3p$	$3d$	$4s$	$4p$	$4d$	$4f$
H-1:	0	0	0	0	0	0	1	1	1	1
H-2:	0	1	1	2	2	2	3	3	3	3
H-3:	0	1	2	2	3	3	3	3	4	4

tive difference of p_{cap} from using H-1 with respect to using H-3 is $\approx 5\%$. Comparing the H-3 calculation to the result from using H-2, the relative difference is $\approx 0.2\%$. In this case, since these relative differences are very similar at larger z distances, one can choose to terminate the propagation at $z = 40$ in further calculations. Although very similar results can be obtained if either H-2 or H-3 is used one should be mindful of the difference in calculation time between basis sets of very different sizes. In this case, using H-2 took about half the time in completing this calculation compared to using H-3. This makes H-2 an optimal choice for further calculations.

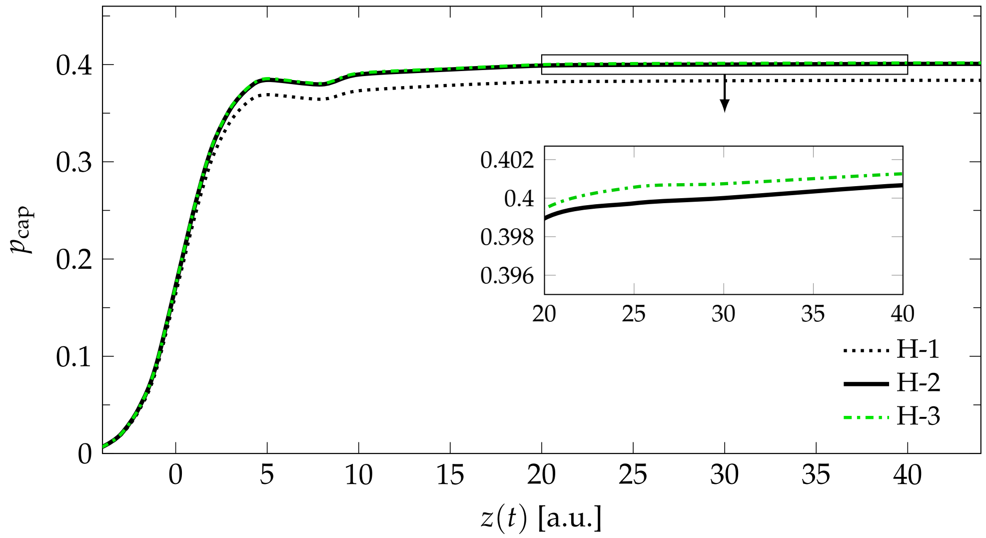

FIG. 3.1: Time development of the total capture probability in C^{6+}-He collisions at impact parameter $b = 4$ a.u. and $E_P = 25$ keV/u based on different BGM hierarchies. The hierarchy sets correspond to those in Table 3.1. Total capture probability is plotted with respect to the projectile position $z(t)$ based on the straight-line trajectory model [i.e., $z(t) = v_P t$]. The inset gives a closer view on curves based on calculations using the H-2 and H-3 hierarchies.

3.4 THE BASIS GENERATOR METHOD IN ION-MOLECULE COLLISIONS

Collision problems involving molecules introduce an additional layer of complexity in the computation due their multi-centre[2] nature. In Refs. [49, 50], a technique was developed that separates the molecular geometry and collision dynamics which allows the use of the TC-BGM for ion-molecule collision problems.

Figure 3.2 shows the setup of the ion-molecule problem in the straight-line semi-classical treatment using H_2O as an example target. The ion-molecule collisions considered in the present work are sufficiently fast (with projectile impact energies of 1 keV/amu and above) to ensure that the molecule neither rotates or vibrates while it interacts with the projectile. In the ion-molecule collision problem, the single-electron equation is

$$i\frac{\partial}{\partial t}\left|\psi^{\Gamma}_{\alpha\beta\gamma}(t)\right\rangle = \left[\hat{h}^{\mathrm{MO}}_{\alpha\beta\gamma} + V_{\mathrm{P}}(t)\right]\left|\psi^{\Gamma}_{\alpha\beta\gamma}(t)\right\rangle, \tag{3.17}$$

with

$$\hat{h}^{\mathrm{MO}}_{\alpha\beta\gamma} = -\frac{1}{2}\nabla^2 + V^{\mathrm{MO}}_{\alpha\beta\gamma}, \tag{3.18}$$

where α, β, γ are the Euler angles[3] (in degrees) which describe the orientation of the molecule in the initial state $|\psi^{\Gamma}_{\alpha\beta\gamma}(t_i)\rangle = |\Gamma_{\alpha\beta\gamma}\rangle$. To be consistent with Refs. [49, 50], capital Greek letters are used to label the MOs. The single-electron Hamiltonian of the system (3.17) is decomposed into the projectile part, V_{P}, and the molecular target part $\hat{h}^{\mathrm{MO}}_{\alpha\beta\gamma}$ (3.18). The Hamiltonian of the target molecule $\hat{h}^{\mathrm{MO}}_{\alpha\beta\gamma}$ consists of the kinetic energy and an effective ground-state potential.

Assuming that the solutions of Eq. (3.17) can be expanded in terms of a time-dependent, non-orthogonal basis

$$\left|\psi^{\Gamma}_{\alpha\beta\gamma}(t)\right\rangle = \sum_{j=1} a^{\Gamma}_{j,\alpha\beta\gamma}(t)\left|\chi_j(t)\right\rangle, \tag{3.19}$$

the following set of coupled-channel equations is obtained

$$i\sum_{j=1}\langle\chi_k(t)|\chi_j(t)\rangle\frac{d}{dt}a^{\Gamma}_{j,\alpha\beta\gamma}(t) = \sum_{j=1}\langle\chi_k(t)|\,\hat{h}^{\mathrm{MO}}_{\alpha\beta\gamma} + V_{\mathrm{P}}(t) - i\frac{\partial}{dt}\,|\chi_j(t)\rangle\, a^{\Gamma}_{j,\alpha\beta\gamma}(t). \tag{3.20}$$

The multi-centre nature of molecules give rise to multi-centre matrix elements, which constitute the main bottleneck of this type of collision problem. This is seen in the in-

---

[2] The term ‘multi-centre’ in the present work refers to more than two centres.

[3] The present work uses the *z*-*y*-*z* convention.

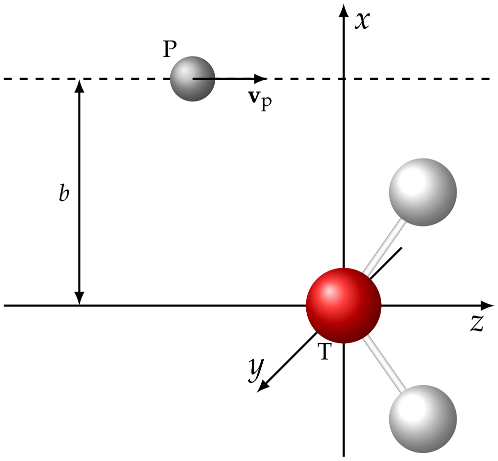

FIG. 3.2: Collision setup for the ion-molecule problem using H_2O as the target. The oxygen atom of the molecule is placed at the origin and the two hydrogen atoms lie in the xz scattering plane where the projectile assumes a straight-line path with constant velocity.

teraction matrix element [i.e., rhs of Eq. (3.20)], specifically, the integrals $\langle \chi_k | V^{\mathrm{MO}}_{\alpha\beta\gamma} | \chi_j \rangle$.

The technique developed in Refs. [49, 50] provides a way to avoid the multi-centre integrals in the coupled-channel equations for the molecular collision problem. It is based on the following strategy:

1. Express the molecular Hamiltonian in the spectral representation

$$\hat{h}^{\mathrm{MO}}_{\alpha\beta\gamma} = \sum_{\Lambda} \epsilon_\Lambda \left| \Lambda_{\alpha\beta\gamma} \right\rangle \left\langle \Lambda_{\alpha\beta\gamma} \right| , \tag{3.21}$$

   where ϵ_Λ is the energy eigenvalue of the MO labeled Λ. While in principle this is equivalent to Eq. (3.18), in practice the summation in the spectral representation is finite, and thus, not exact. The present work considers only the initially occupied MOs.

2. Expand the MOs $|\Lambda\rangle$ for each orientation considered in an orthonormal, single-centre basis. This expansion can only be a decent approximation for molecules with compact geometries. In this work, only molecules of H_2O and CH_4 are considered.

As a result, the collision calculation is effectively separated into two parts: (i) the molecular geometry problem where the expansion coefficients for the initial conditions are determined for different orientations with respect to the ion beam axis, and (ii) the collision dynamics where the transition amplitudes are propagated in time.

3.4.1 Expansion of the initial molecular orbitals

The starting point of the MO expansion of H_2O and CH_4 is based on the minimal-basis-set Hartree-Fock calculations performed by R. Pitzer and co-workers (Ref. [85] and Ref. [86], respectively). The MOs are expanded in terms of the Slater-type orbitals $|q\rangle$

$$|\bar{\Lambda}\rangle = \sum_q C_q^{\bar{\Lambda}} |q\rangle . \tag{3.22}$$

The coordinate system used in those works is the starting orientation of the molecules in the present work [i.e., $(\alpha, \beta, \gamma) = (0, 0, 0)$] and the MOs denoted without the $\alpha\beta\gamma$ indices refer to this particular orientation. They are shown in Fig. 3.3 for H_2O and CH_4.

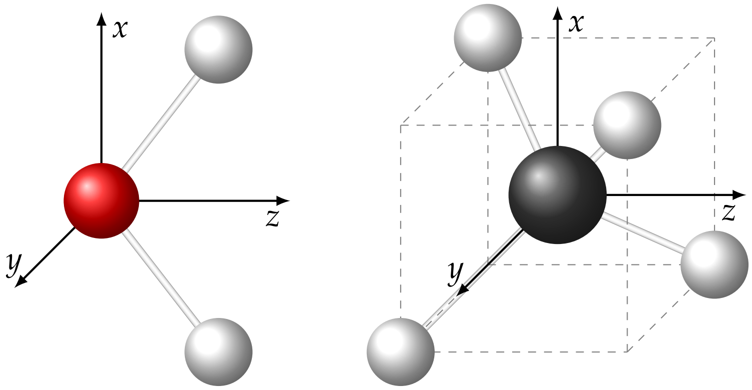

FIG. 3.3: Original orientation $(\alpha, \beta, \gamma) = (0, 0, 0)$ of the molecules considered: (a) H_2O , where the oxygen atom is centred at the origin with the two hydrogen atoms placed in the collision xz-plane, and (b) CH_4 , where the carbon atom is centred at the origin. The cube drawn with dashed lines and centred at the origin helps visualize the geometry of CH_4 .

As suggested in Fig. 3.3, the single-centre states used for expanding the MOs are states that are centred at the origin. Specifically, the MOs are expanded in terms of basis states of the oxygen and carbon atoms for H_2O and CH_4, respectively. This is accomplished by projecting Eq. (3.22) onto said basis $\{|\phi_s\rangle\}$

$$|\Lambda\rangle \equiv \hat{P} |\bar{\Lambda}\rangle = \left(\sum_s |\varphi_s\rangle \langle\varphi_s| \right) |\bar{\Lambda}\rangle = \sum_s \langle\varphi_s|\bar{\Lambda}\rangle |\varphi_s\rangle = \sum_s d_s^{\Lambda} |\varphi_s\rangle . \tag{3.23}$$

The atomic orbitals $|\varphi_s\rangle$ used here are obtained from the OPM. Note that the index s is a multi-index in practice, in other words, the nlm quantum numbers of the atomic states. The expansion coefficients $d_s^{\Lambda} = \langle\varphi_s|\bar{\Lambda}\rangle$ are obtained by computing the overlap integrals between the OPM orbitals and the Slater-type orbitals. These overlap integrals contain no more than two centres. This expansion is first done on the original orientation. To obtain expansion coefficients corresponding to a different molecular orientation, a rotated basis with states $|\tilde{\varphi}_s\rangle$ is used by applying a rotation operator $\hat{R}$ onto the original basis $\{|\varphi_s\rangle\}$

$$|\tilde{\varphi}_s\rangle = \hat{R}(\alpha,\beta,\gamma)\,|\varphi_s\rangle \tag{3.24}$$

such that

$$|\Lambda_{\alpha\beta\gamma}\rangle = \sum_s d^{\Lambda}_{s,\alpha\beta\gamma}\,|\tilde{\varphi}_s\rangle = \sum_s d^{\Lambda}_{s,\alpha\beta\gamma}\,|s\rangle\,, \tag{3.25}$$

where

$$d^{\Lambda}_{s,000} = d^{\Lambda}_{s}. \tag{3.26}$$

Here, the shorthand notation $|\tilde{\varphi}_s\rangle = |s\rangle$ is now used to denote the atomic states. For practical purposes, a mirror symmetry with respect to the xz-plane is exploited in the matrix element calculations. Consequently, this restricts the number of orientations that can be considered. The orientations used in this work are shown in Fig. 3.4 for H_2O and Fig. 3.5 for CH_4. Although other orientations for H_2O can be considered, it has been shown in Ref. [49] through symmetry arguments [50] that this restriction is not a serious limitation for total capture and ionization cross section calculations. Similar results have also been explicitly shown for CH_4 collisions [52]. Although the focus of these studies was for proton collisions in the intermediate and fast regimes, the same restriction is also applicable in slow collisions. This is shown in Ch. 6.

Another practical aspect to note is the accuracy of this single-centred expansion of the MOs. In the present work, all orbitals of the KLM shells are included to re-expand the minimal-basis set of the MOs of Refs. [85, 86]. This yields total norm integrals of

$$0.9 \leq \sum_s^{KLM} |\,\langle s|\tilde{\Gamma}_{\alpha\beta\gamma}\rangle\,|^2 < 1, \tag{3.27}$$

which shows that the expansion technique is not perfect but since the total norms are reasonably close to 1, this is deemed acceptable. Because of this imperfection, the normalization of the approximated MOs is re-adjusted for a standard statistical interpretation of the propagated states.

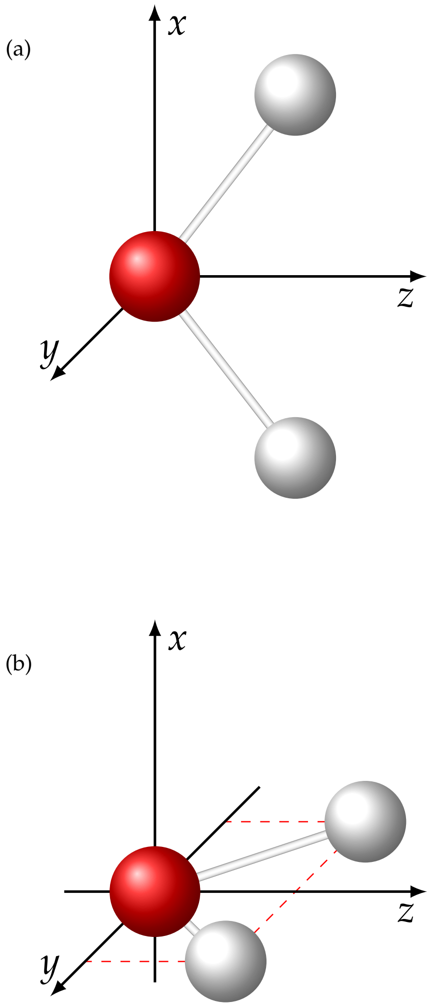

FIG. 3.4: Orientations of H_2O considered in molecular collision calculations: (a) $(0, 0, 0)$, (b) $(90, 0, 0)$.

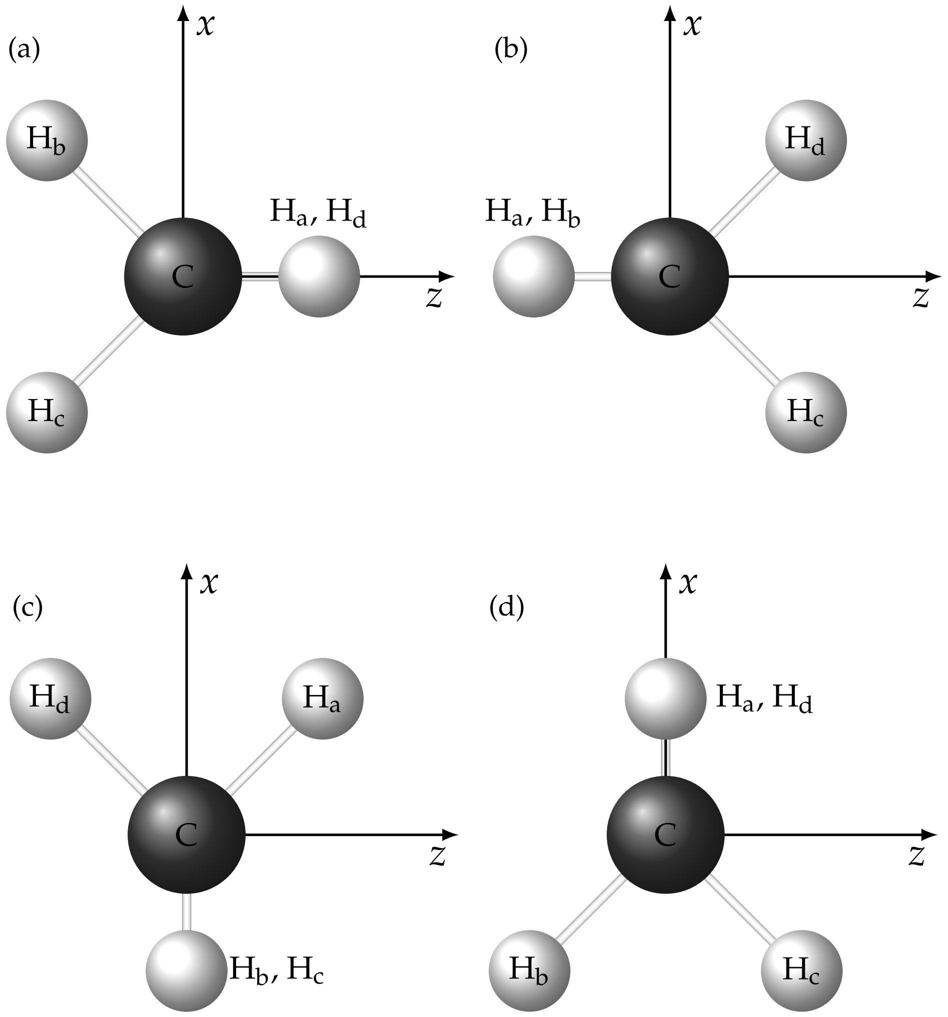

FIG. 3.5: Orientations of CH_4 considered in molecular collision calculations: (a) $(0, 0, -45)$, (b) $(0, -90, -45)$, (c) $(45, 90, 180)$, and (d) $(-45, -90, 0)$. Each diagram of CH_4 shows two hydrogen atoms in the collision plane while the other two hydrogen atoms are in the azimuthal plane.

3.4.2 Collision dynamics

With $h^{\mathrm{MO}}_{\alpha\beta\gamma}$ expressed in the spectral representation and the MOs expanded in terms of a single-centre, orthonormal basis, the matrix element $\langle\chi_k|\hat{h}^{\mathrm{MO}}_{\alpha\beta\gamma}|\chi_j\rangle$ becomes

$$\langle\chi_k(t)|\hat{h}^{\mathrm{MO}}_{\alpha\beta\gamma}|\chi_j(t)\rangle = \sum_{\Lambda}\sum_{s,s'}\epsilon_\Lambda \langle\chi_k(t)|s\rangle\, d^{\Lambda}_{s,\alpha\beta\gamma} d^{\Lambda}_{s',\alpha\beta\gamma} \langle s'|\chi_j(t)\rangle \tag{3.28}$$

in which multi-centre terms no longer appear explicitly. These matrix elements now consist of molecular energy eigenvalues ϵ_Λ, overlap matrix elements $\langle\chi_k|s\rangle$ of basis states and expansion coefficients d^{Λ}_{s} which characterize the linear combinations of single-center states used to represent the MOs.

The strategy of bypassing the multi-centre terms is complete by making use of the linearity of the single-electron TDSE to propagate the single-centre basis states $|s\rangle$ rather than the MOs. With the states of $\{|s\rangle\}$ as initial conditions to solve the set of coupled-channel equations, the following solution is obtained

$$|\psi^{s}_{\alpha\beta\gamma}(t)\rangle = \sum_{j} a^{s}_{j,\alpha\beta\gamma}(t)\,|\chi_j(t)\rangle\,. \tag{3.29}$$

Afterwards, they are combined to reconstruct the molecular solutions

$$|\psi^{\Gamma}_{\alpha\beta\gamma}(t)\rangle = \sum_{s} d^{\Gamma}_{s,\alpha\beta\gamma}\,|\psi^{s}_{\alpha\beta\gamma}(t)\rangle = \sum_{s,j} d^{\Gamma}_{s,\alpha\beta\gamma} a^{s}_{j,\alpha\beta\gamma}(t)\,|\chi_j(t)\rangle\,. \tag{3.30}$$

Through this strategy, it can be seen that the coupled-channel equations for the ion-molecule problem are similar to those of an ion-atom problem. In fact, the states $|\chi_j\rangle$ for the molecular problem are represented by the TC-BGM states of Eqs. (3.10) and (3.13) in practice. Interested readers should refer to the appendix section of Ref. [50] for a detailed discussion on the practical implementation of the TC-BGM in ion-molecule problems.

3.5 FINAL-STATE ANALYSIS: EXTRACTION OF MEASURABLE CROSS SECTIONS

The objective is to generate observables that can be compared with experimental cross sections. The present work focuses on total cross sections given as

$$\sigma = \int P(\mathbf{b}) d\mathbf{b}. \tag{3.31}$$

While not explicitly stated, these cross sections are in fact dependent on the projectile velocity. For the purpose of post-collision Auger and radiative analyses, the cross sections generated should be state-selective. For example, σ_{nl} is the state-selective cross section describing an electronic process for a single electron occupying some final bound nl-state.

In a many-electron system, solving the TDSE within the IEM framework does not immediately yield useful quantities that describe many-electron processes. One way to reinstate the many-electron aspects within the IEM is to combine the single-electron probabilities statistically. The method of multinomial analysis is the main approach in the present work.

The basis set used in the present work is divided into three subspaces for electronic processes: capture, excitation, and ionization. Note that the TC-BGM explicitly yields single-electron capture p^{cap}, target excitation p^{ex} (including the elastic channel), and ionization probabilities p^{ion} such that it satisfies the unitarity criterion, $p^{\text{cap}} + p^{\text{ex}} + p^{\text{ion}} = 1$. From here, one can utilize a multinomial model that combines these single-electron probabilities. These models can differ depending on the level of sophistication.

In one model, there is the probability of shell-specific, simultaneous k-fold capture and l-fold ionization which is given as [83, 87]

$$\begin{aligned} P_{kl} = \sum_{k_1,\ldots,k_m}^{N_1,\ldots,N_m} \sum_{l_1,\ldots,l_m}^{N_1,\ldots,N_m} \prod_{i=1}^{m} \binom{N_i}{k_i + l_i} \binom{k_i + l_i}{l_i} (p_i^{\text{cap}})^{k_i} (p_i^{\text{ion}})^{l_i} \\ \times (1 - p_i^{\text{cap}} - p_i^{\text{ion}})^{N_i - k_i - l_i} \delta_{k,\sum_i k_i} \delta_{l,\sum_i l_i}, \end{aligned} \tag{3.32}$$

where m is the number of electron shells, N_i is the number of electrons in the i-th shell, and δ is the Kronecker delta that ensures only k-fold capture and l-fold ionization events are summed up. The computation of this model can be quite involved for a large number of active electrons and target shells along with high multiplicities of k and l.

For the present study the focus is capture with no ionization ($l = 0$). The general P_{kl} then reduces to

$$P_{k0} = \sum_{k_1,\ldots,k_m}^{N_1,\ldots,N_m} \prod_{i=1}^{m} \binom{N_i}{k_i} (p_i^{\text{cap}})^{k_i} (1 - p_i^{\text{cap}} - p_i^{\text{ion}})^{N_i - k_i} \delta_{k,\sum_i k_i}, \tag{3.33}$$

To obtain state-selective cross sections for post-collision analyses, it is necessary that these probabilities are computed at the nl-subshell level.

3.6 POST-COLLISION ANALYSES: AUGER AND RADIATIVE DECAY

When an electron is captured into an excited state of the projectile, it subsequently transits to the lowest unoccupied bound state. Two decay processes are considered in the present work: Auger and radiative decay. Although one objective is to produce radiative emission spectra from single-electron capture (SEC) events, it is known [88–91] that multiple-capture events followed by autoionization can contribute to the overall SEC cross sections, and thus, the radiative spectral counts. In Ch. 1 this was referred to as *apparent capture*. Therefore in experiments where apparent capture events are not differentiated from *pure* capture, contributions from the former must be taken into account.

In a first-principles approach, the treatment of Auger and radiative processes starts from the standard rate (master) equation which describes the time-evolution of a level population. For some primary level p its population $N_p(t)$ is governed by [92]

$$\frac{dN_p(t)}{dt} = \sum_{i=p+1}^{m} N_i(t) A_{i\to p} - N_p(t) \sum_{f=1}^{p-1} A_{p\to f}, \tag{3.34}$$

where A is a transition probability per unit time. The first summation on the rhs of Eq. (3.34) is the rate of re-population of level p from a cascade in higher levels i and the second sum is the rate of de-population into lower levels f. The population level index is a multi-index in practice, since transitions can occur through intermediate states dictated by radiative and non-radiative selection rules. Moreover, it is common practice to define the *decay constant* α of level p as

$$\alpha_p = \sum_{f=1}^{p-1} A_{p\to f}. \tag{3.35}$$

Computation of an electron transition rate starts from Fermi's Golden Rule [93]

$$A_{i\to f} = \frac{2\pi}{\hbar}|M_{fi}|^2\rho(\epsilon_f)\Big|_{\epsilon_f=\epsilon_i\pm\hbar\omega}, \tag{3.36}$$

where M_{fi} is the interaction matrix element between the initial state $|i\rangle$ and final state $|f\rangle$, and $\rho(\epsilon_f)$ is the density of states in the energy interval $[\epsilon_f-\Delta\epsilon, \epsilon_f+\Delta\epsilon]$. In dipole approximation, the *spontaneous (radiative) emission rate* from initial level i to final level f is [94]

$$A^{\text{dip.}}_{i\to f} = \frac{4}{3}\left(\frac{\omega_{fi}}{c}\right)^3|\mathbf{r}_{fi}|^2, \tag{3.37}$$

with

$$\mathbf{r}_{fi} = \langle\varphi_f|\mathbf{r}|\varphi_i\rangle\,, \tag{3.38}$$

and ω_{if} is the transition frequency. The main focus for the radiative spectra are transitions according to the electric-dipole selection rule (i.e, $|l-l'|=1$) since transition rates based on other radiative selection rules (e.g., electric quadrupole, magnetic dipole) are comparatively small [95]. Because most projectiles considered in the present work are bare ions such that only radiative emissions from hydrogenlike n, l states are involved, the above equation can be worked out to arrive at

$$A^{\text{rad}}_{nl\to n'l'} = \frac{4}{3}\left(\frac{\omega_{nn'}}{c}\right)^3(2l'+1)\begin{pmatrix} l' & 1 & l \\ 0 & 0 & 0\end{pmatrix}^2\left(\int_0^\infty R_{nl}R_{n'l'}r^3dr\right)^2, \tag{3.39}$$

where the brackets with two rows denote the Wigner-3j symbol and R_{nl} is the (normalized) radial wavefunction for the hydrogenlike projectile,

$$R_{nl}(r) = \sqrt{\left(\frac{2Z}{n}\right)^3\frac{(n-l-1)!}{2n[(n+l)!]^3}}\exp\left(-\frac{Zr}{n}\right)\left(\frac{2Zr}{n}\right)^l\left[L^{2l+1}_{n-l-1}(2r/n)\right], \tag{3.40}$$

which is expressed in terms of an associated Laguerre polynomial $L^p_{q-p}(x)$.

The present work also considers radiative rates in lithium-like structures (e.g., O^{5+}). Seeking an analytical form representing states of these structures is not viable, and so in this situation the RATIP package [96] was utilized to numerically calculate these states and corresponding transition rates. In general, this suite of programs provides a platform to generate and evaluate atomic data for open-shell atoms. RATIP has been applied to a large number of case studies on the level structure and decay of atoms and ions with much success [97]. For radiative transition rates, one would utilize the EINSTEIN program, which also computes these rates starting from Fermi's Golden rule. Furthermore, the present work also relies on RATIP in obtaining Auger rates, which are computed using the AUGER program. Note that the interaction among the electrons in the calculation done in AUGER is described by the scalar operator [96]

$$V = V^{\text{Coulomb}} + V^{\text{Breit}} = \sum_{i<j} \left(\frac{1}{|r_i - r_j|} - b_{ij} \right) \tag{3.41}$$

which is simply the sum of static Coulomb repulsion and the Breit interaction (b_{ij}) for relativistic corrections. The latter can be neglected as an option provided in the program. For consistency with the IEM framework, calculations of these rates were restricted to single-configuration wavefunctions since RATIP allows for states produced using the multiconfiguration Dirac-Fock method [98, 99].

To obtain the populations, rate equations similar to Eq. (3.34) must be written for all other levels. This results in a system of coupled first-order differential equations

$$\frac{d}{dt} \begin{pmatrix} N_1 \\ N_2 \\ \vdots \\ N_{m-1} \\ N_m \end{pmatrix} = \begin{pmatrix} -\alpha_1 & A_{21} & A_{31} & \cdots & A_{m1} \\ 0 & -\alpha_2 & A_{32} & \cdots & A_{m2} \\ \vdots & \vdots & \ddots & & \vdots \\ 0 & 0 & & -\alpha_{m-1} & A_{m\ m-1} \\ 0 & 0 & \cdots & 0 & -\alpha_m \end{pmatrix} \begin{pmatrix} N_1 \\ N_2 \\ \vdots \\ N_{m-1} \\ N_m \end{pmatrix}, \tag{3.42}$$

which can be solved numerically using standard methods. With populations obtained by solving Eq. (3.42), the total photon count due to transitions from level p to f is [100]

$$(\text{count})_{p\to f} = A_{p\to f} \int_0^\infty N_p(t)dt. \tag{3.43}$$

As discussed further below, the analytical solution of N_p to Eq. (3.42) is of exponential form. In this work, the interest is integrating Eq. (3.43) with N_p that consists of a decaying factor [see Eq. (3.44)]. In practice then, the numerical integration of Eq. (3.43) is terminated once N_p approaches zero asymptotically, and this has been set to 10^{-5} in present calculations. Furthermore, the present work mainly examines the dominant emissions where the final state corresponds to the lowest energy state, and thus, it is not necessary to compute the total photon count from all possible transitions.

Instead of solving the system of equations (3.42) numerically, it is possible to obtain an analytical solution for N_p such that the total photon count (3.43) can be computed in a more direct fashion. An analytical solution of N_p is obtained by using the diagrammatic mnemonic developed by Curtis [92]. In this approach, the solution of a population level is constructed by grouping cascading processes according to increasing order of complexity. This is realized by examining the formal solution of the population [92]

$$N_p(t) = \exp\left(-\alpha_p t\right) \left[N_p(0) + \sum_{i=p+1}^{m} A_{i\to p} \int_0^t dt' \exp\left(\alpha_p t'\right) N_i(t') \right], \tag{3.44}$$

where the level population appears on both sides of the equation, and by successively iterating the rhs. This yields a (finite) series of nested sums and integrals

$$\begin{aligned} N_p(t) = \exp\left(-\alpha_p t\right) \Bigg\{ & N_p(0) + \sum_{i=p+1}^{m} N_i(0) A_{i\to p} \int_0^t dt' \exp\left[(\alpha_p - \alpha_i) t'\right] \\ & + \sum_{i=p+1}^{m-1} \sum_{j=i+1}^{m} N_j(0) A_{j\to i} A_{i\to p} \int_0^t dt' \exp\left[(\alpha_p - \alpha_i) t'\right] \\ & \times \int_0^{t'} dt'' \exp\left[(\alpha_i - \alpha_j) t''\right] + \ldots \Bigg\}. \end{aligned} \tag{3.45}$$

As Curtis [92] pointed out, there is a physical interpretation of each order of the series on the rhs of Eq. (3.45) which contains the cascades moving from initial levels to the level of interest p by the number of steps equal to the order of the term. By denoting each order by a sum of labelled diagrams that depict the corresponding cascade, Eq. (3.45) becomes

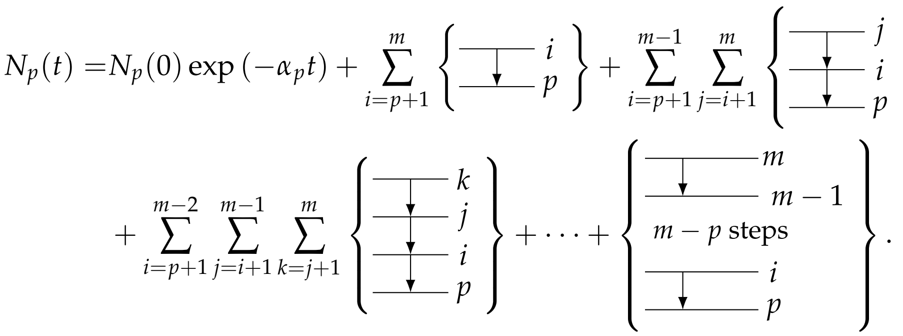

$$\begin{aligned} N_p(t) = {} & N_p(0)\exp\left(-\alpha_p t\right) + \sum_{i=p+1}^{m} \left\{ \begin{array}{cl} \rule{2em}{0.4pt} & i \\ \downarrow & \\ \rule{2em}{0.4pt} & p \end{array} \right\} + \sum_{i=p+1}^{m-1} \sum_{j=i+1}^{m} \left\{ \begin{array}{cl} \rule{2em}{0.4pt} & j \\ \downarrow & \\ \rule{2em}{0.4pt} & i \\ \downarrow & \\ \rule{2em}{0.4pt} & p \end{array} \right\} \\ & + \sum_{i=p+1}^{m-2} \sum_{j=i+1}^{m-1} \sum_{k=j+1}^{m} \left\{ \begin{array}{cl} \rule{2em}{0.4pt} & k \\ \downarrow & \\ \rule{2em}{0.4pt} & j \\ \downarrow & \\ \rule{2em}{0.4pt} & i \\ \downarrow & \\ \rule{2em}{0.4pt} & p \end{array} \right\} + \cdots + \left\{ \begin{array}{cl} \rule{4em}{0.4pt} & m \\ \downarrow & \\ \rule{4em}{0.4pt} & m-1 \\ m-p \text{ steps} & \\ \rule{4em}{0.4pt} & i \\ \downarrow & \\ \rule{4em}{0.4pt} & p \end{array} \right\}. \end{aligned} \tag{3.46}$$

Working out the integrals results in [92],

$$\{i \to n\} = N_i(0) A_{i\to n} \left[\frac{\exp\left(-\alpha_i t\right)}{(\alpha_n - \alpha_i)} + \frac{\exp\left(-\alpha_n t\right)}{(\alpha_i - \alpha_n)} \right], \tag{3.47}$$

$$\{j \to i \to n\} = N_j(0)A_{j\to i}A_{i\to n}\left[\frac{\exp(-\alpha_j t)}{(\alpha_i-\alpha_j)(\alpha_n-\alpha_j)} + \frac{\exp(-\alpha_i t)}{(\alpha_j-\alpha_i)(\alpha_n-\alpha_i)} + \frac{\exp(-\alpha_n t)}{(\alpha_j-\alpha_n)(\alpha_i-\alpha_n)}\right], \tag{3.48}$$

$$\{k \to j \to i \to n\} = N_k(0)A_{k\to j}A_{j\to i}A_{i\to n}\left[\frac{\exp(-\alpha_k t)}{(\alpha_j-\alpha_k)(\alpha_i-\alpha_k)(\alpha_n-\alpha_k)} + \frac{\exp(-\alpha_j t)}{(\alpha_k-\alpha_j)(\alpha_i-\alpha_j)(\alpha_n-\alpha_j)} + \frac{\exp(-\alpha_i t)}{(\alpha_k-\alpha_i)(\alpha_j-\alpha_i)(\alpha_n-\alpha_i)} + \frac{\exp(-\alpha_n t)}{(\alpha_k-\alpha_n)(\alpha_j-\alpha_n)(\alpha_i-\alpha_n)}\right], \tag{3.49}$$

$$\{m \to m-1 \to \cdots \to i \to p\} = N_m(0)\left(\prod_{i=p}^{m-1} A_{i+1\to i}\right)\sum_{j=p}^{m}\left[\exp(-\alpha_j t)\Big/\prod_{k\neq j}(\alpha_k-\alpha_j)\right]. \tag{3.50}$$

By Eq. (3.43), the total photon count due to transition from level p to f is

$$(\text{count})_{p\to f} = N_p(0)\frac{A_{p\to f}}{\alpha_p} + \sum_{i=p+1}^{m}\left[N_i(0)\frac{A_{i\to p}}{\alpha_i}\right]\frac{A_{p\to f}}{\alpha_p} + \sum_{i=p+1}^{m-1}\sum_{j=i+1}^{m}\left[N_j(0)\frac{A_{j\to i}A_{i\to p}}{\alpha_j\alpha_i}\right]\frac{A_{p\to f}}{\alpha_p} + \cdots. \tag{3.51}$$

In the context of this work, the initial populations $N_i(0)$ are represented by capture cross sections σ_i. This approach of computing the total photon count only requires initial populations of each state and the corresponding *branching ratios* $A_{i\to j}/\alpha_i$. Such an approach to cascade calculations has been used by many groups [25, 32, 101]. An obvious disadvantage is that Eq. (3.51) can get cumbersome if states with high-n quantum numbers are involved due to high multiplicities of l-substates. On the other hand, an advantage to this approach is that it allows one to gauge which cascade channels are dominant or negligible. Regardless, both approaches of numerically solving the system of differential equations (3.42) and directly computing Eq. (3.51) have been used in the present work. It has been verified in this work that results produced by these two types of calculations agree within approximately 10^{-4}.

As mentioned in the beginning of this section, apparent capture events can contribute to the overall radiative spectral counts. In this work, it was found that apparent SEC contributions are mainly from autoionizing double-capture (ADC). To quantify the ADC contribution, one can refer to the second term of Eq. (3.51) since all doubly-excited states that undergo an Auger process follow the first-order cascade. One can then separate the ADC contribution in the summation from all other contributions. Therefore, the contribution from all ADC towards some singly excited state p can be extracted from total double-electron capture (DEC) cross sections by

$$\sigma_p^{\mathrm{ADC}} = \sum_i^m \sigma_i^{\mathrm{DEC}} \frac{A_{i\to p}}{\alpha_i}. \tag{3.52}$$

One can then make useful comparisons of ADC with pure SEC in terms of cross sections and radiative emissions, which is a recurring analysis that is performed in this work where many-electron targets are involved.

With the main methodology laid out, the discussion can now delve into various collision problems. However, there are situations in this work, specifically in Ch. 6 working with molecular collisions, where the methods discussed in this chapter may not be ideal or even applicable, and so one needs to either suggest a modification to existing methods or resort to alternatives.

CHAPTER 4

Ne^{10+} collisions with helium, neon, and argon

This chapter has been adapted from:

> A. C. K. Leung and T. Kirchner, Independent-electron analysis of the x-ray spectra from single-electron capture in Ne^{10+} collisions with He, Ne, and Ar atoms, Phys. Rev. A **92,** 032712 (2015).

4.1 OVERVIEW AND BACKGROUND

In this chapter, results of the present analysis on radiative spectra from Ne^{10+}-He, -Ne, and -Ar collisions at the impact energy of 4.54 keV/u are discussed. Results of these calculations are compared with experimental measurements and CTMC calculations by Ali *et al.* [24] and also previous TC-AOCC calculations performed within the IEM by Liu *et al.* [55].

In brief, the experiment by Ali *et al.* [24] was performed using the cold-target recoil ion momentum spectroscopy (COLTRIMS) imaging technique [102] with simultaneous x-ray spectroscopy to obtain triple-coincident measurements of x-rays, scattered projectiles, and target recoil ions. An important advantage of these simultaneous measurements is that it is not only possible to separate x-rays originating in pure SEC events from those due to multiple-electron capture events, but it is also possible to obtain x-ray spectra corresponding to pure SEC into a specific *n*-state. In fact, the experimental x-ray results reported by Ali *et al.* [24] are from collisions due to only pure SEC. Furthermore, comparisons with CTMC calculations show some discrepancies with the experimental x-ray spectra and it was speculated that this could be due to the inaccuracy of the *nl* population distribution obtained from CTMC.

An independent theoretical study using the quantum-mechanical TC-AOCC method performed within the IEM to describe the experimental data of Ali *et al.* [24] was first reported by Liu *et al.* [55]. However, only calculations of cross sections and x-ray spectra for He and Ne targets were reported. Results from that study showed considerable discrepancies in the n-state relative cross sections with both measurements and CTMC results. As for the x-ray spectra, the agreement between the TC-AOCC predictions and experimental measurements is mixed. The x-ray spectra of interest are shown in Fig. 4.1 which displays the experimental and CTMC results from Ali *et al.* [24] along with the IEM TC-AOCC results [55]. Because of the resolution of the x-ray detector (126 to 133 eV full-width at half-maximum), emissions from $np \rightarrow 1s$ transitions for $n \geq 3$ cannot be resolved. Consequently, those emissions were grouped together and are referred to as the Ly-β+ peak in this analysis. For consistency, the calculated spectra were assumed to have Gaussian profiles with identical full-width at half-maximum as the resolution of the x-ray detector.

Liu *et al.* [55] speculated that the large discrepancies in relative cross sections may be due to the model potential used in the single-electron Hamiltonian. There was also speculation on the neglect of two- or multiple-electron capture undergoing autoionization as another source of discrepancy. However, this would contradict the experimental protocols of Ali *et al.* [24] where the measurements reported are from pure SEC events. Because of this misunderstanding, there is a need for another theoretical verification. Altogether, the TC-AOCC analysis performed within the IEM [55] presents an opportunity to assess the TC-BGM for these collision systems.

4.2 SETUP OF THE PROBLEM

The problem of interest is a bare Ne^{10+} projectile colliding with He, Ne, or Ar target at the impact energy $E_\mathrm{P} = 4.54$ keV/u (≈ 933 km/s). This impact energy is said to correspond to the higher end of the solar-wind ion velocities [24]. The single-electron Hamiltonian is

$$\hat{h}(t) = -\frac{1}{2}\nabla^2 + V_\mathrm{T} - \frac{10}{|\mathbf{r}_\mathrm{T} - \mathbf{R}(t)|} \tag{4.1}$$

where the effective ground-state potential of the target V_T (i.e., He, Ne, and Ar) was obtained using the OPM.

For the present calculation, the TC-BGM basis set includes all states of the *KLMN*

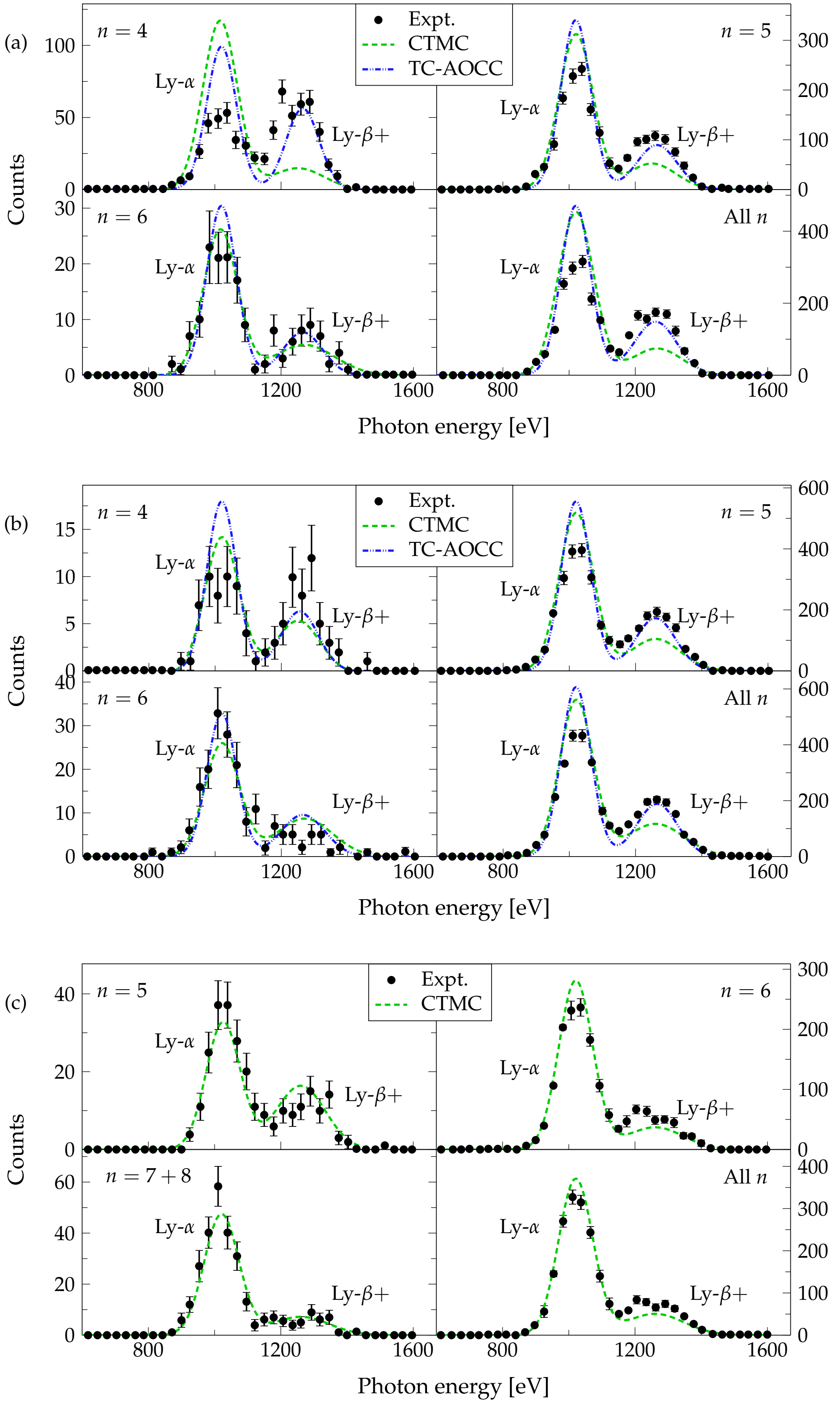

FIG. 4.1: X-ray spectra from collisions of Ne^{10+} with (a) He, (b) Ne, and (c) Ar. Experimental and CTMC results are by Ali *et al.* [24] and TC-AOCC results are by Liu *et al.* [55].

shells for He and Ne. For Ar, all states of the LMN shells were used since electron capture from the L shell was found to be negligible, and thus, electrons in the K shell were assumed to be passive. Additionally, the basis set also contains nlm hydrogen-like states from $n = 1$ to $n = 10$ on the projectile and a set of BGM pseudostates. The BGM hierarchy used for this analysis is shown in Table 4.1. The CBM predicts that the main capture channel on the projectile from slow collisions of Ne^{10+}-He and -Ne is expected to be $n = 5$ while collisions with Ar is expected to be $n = 6$, and thus, the set of projectile states is deemed sufficient for this analysis. The dominant capture channel for Ar differs from collisions with He and Ne due to a larger difference in the first ionization potential. More precisely, the orbital energy eigenvalues obtained using the OPM potential for He, Ne, and Ar obtained are 0.918, 0.851, and 0.591 a.u., respectively. The respective accepted ionization potentials are 0.904, 0.792, and 0.579 a.u. [103].

TABLE 4.1: BGM hierarchy used in present calculations for Ne^{10+}-He, -Ne, and -Ar collisions.

State	$1s$	$2s$	$2p$	$3s$	$3p$	$3d$	$4s$	$4p$	$4d$	$4f$
Target: He										
M_ν:	0	1	1	1	1	1	1	1	2	2
Target: Ne										
M_ν:	0	1	1	1	1	1	1	1	2	2
Target: Ar										
M_ν:	–	1	1	1	1	1	1	1	2	2

As discussed in Ch. 3, solutions of the single-electron TDSEs are to be combined via multinomial analyses for accurate representation of observables. For pure SEC, the multinomial analysis of Eq. (3.33) was used in this analysis. In the TC-AOCC report by Liu *et al.* [55], it is unclear how this was carried out. Another possible analysis of single-electron capture probabilities is *net capture*. As briefly introduced in Sec. 2.4.1, *net electron numbers* are the sum of the single-electron probabilities and can be interpreted as average electron numbers for a particular process [78, 104, 105]. For net capture, it is

$$P_{\mathrm{net}}^{\mathrm{cap}}(t) = \sum_{i=1}^{N} \sum_{v=1}^{K} |\langle \phi_v | \psi_i(t) \rangle|^2. \tag{4.2}$$

where $\{\phi_v\}$ is a set of bound projectile states. Net cross sections[1] have in fact measured and reported by Rudd *et al.* [106]. Furthermore, one can show that if the single-electron probabilities are small (on the order of 1% or less), the multinomial expressions of Eq. (3.33) reduces to the net capture for $k = 1$. For this reason, net capture is also considered as a possible analysis Liu *et al.* [55] might have used in their calculations.

4.3 CAPTURE PROBABILITIES AND CROSS SECTIONS

Starting with the present results using the pure SEC multinomial analysis, Fig. 4.2 shows the capture probability curves as a function of the impact parameter for each collision system. There are some differences between the no-response and the target-response results except at large impact parameters where the probabilities appear converged. Furthermore, the probabilities displayed are only from the dominant capture channel since probabilities of other channels are considerably smaller.

Next, the present pure SEC probabilities and net capture are compared. Fig. 4.3 shows the capture probability from the present TC-BGM calculations plotted with respect to the impact parameter. For simplicity, only results from the Ne^{10+}-Ne collision system in the no-response approximation are presented for this comparison since similar observations have been made for the other systems. The plots clearly show the stark differences in magnitude between the pure SEC probabilities and net capture. The latter is shown to be considerably larger than the former, which indicates that multi-electron capture is strong.

As discussed in previous chapters, electron capture tends to be selective to a particular n-state in slow collisions. This was also observed in the Q-value spectra by Ali *et al.* [24]. The plots in Fig. 4.3 for the Ne^{10+}-Ne collision system show that the area under the pure SEC profile at $n = 5$ is the largest. As for net capture, however, this does not appear to be the case. This is more apparent by computing the respective n-state cross sections.

The n-state relative cross section distribution for each system is shown in Fig. 4.4. Comparisons between the present calculations of net capture and pure SEC are shown separately. Figure 4.4(a) shows the present pure SEC results with the experimental and CTMC results [24] while Fig. 4.4(b) shows the present net capture with the experimental [24] and TC-AOCC [55] results. From the experimental results, the capture distribu-

---

[1] Also referred as *gross cross sections* in the literature.

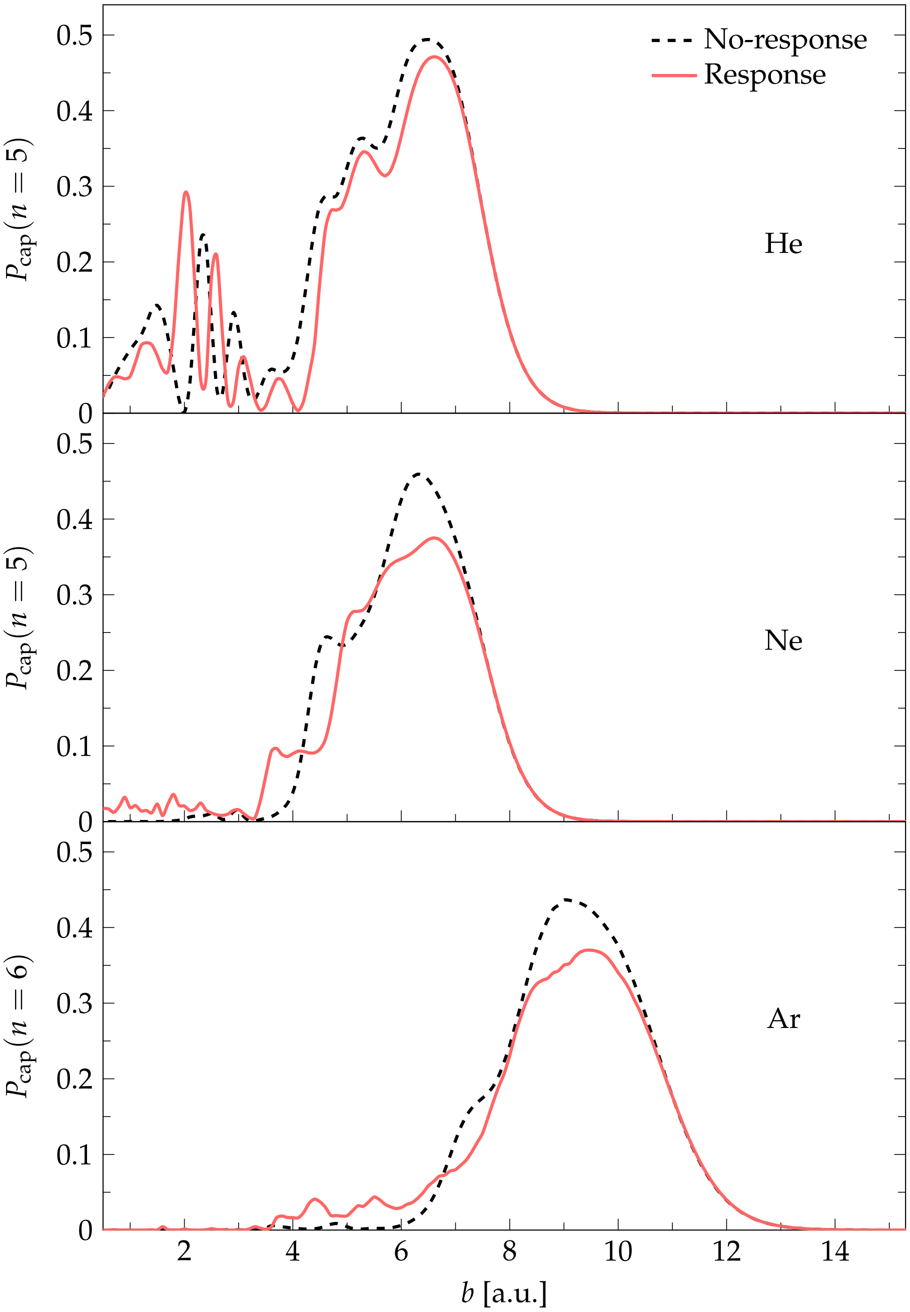

FIG. 4.2: TC-BGM pure SEC probabilities of the dominant capture state of Ne^{10+} collisions with He (top panel), Ne (middle panel), and Ar (bottom panel) at $E_{\mathrm{P}} = 4.54$ keV/u. Each panel shows both the present calculations using the no-response approximation and the target-response model.

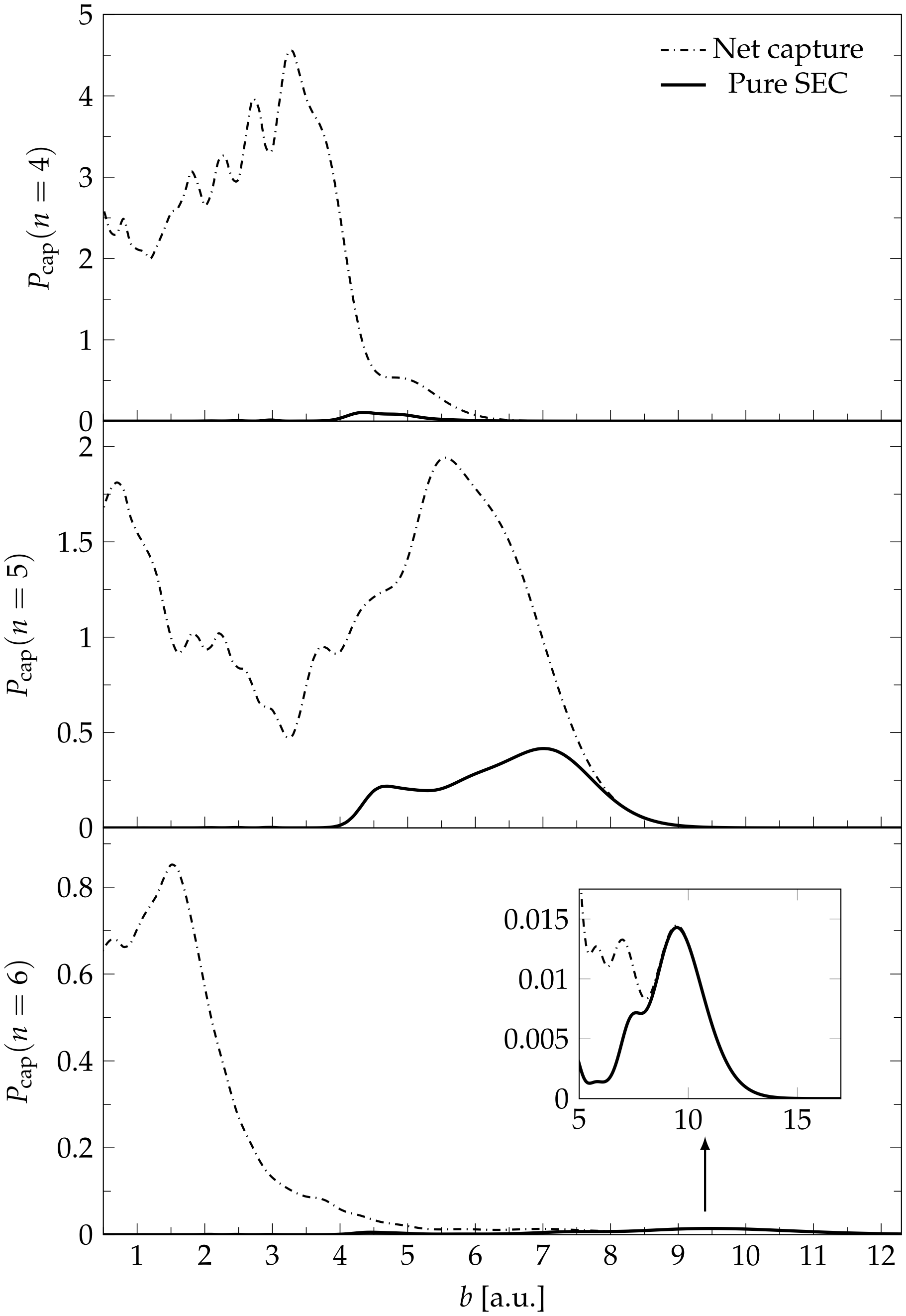

FIG. 4.3: TC-BGM pure SEC probabilities and net capture numbers to the $n = 4$ (top panel), $n = 5$ (middle panel), $n = 6$ (bottom panel) states of the projectile in Ne^{10+}-Ne collisions at $E_{\mathrm{P}} = 4.54$ keV/u. Calculations correspond to the no-response approximation.

tion exhibits a resonant profile, demonstrating the selective nature of capture in slow collisions [10]. Theoretical results that reflect this profile are the present pure SEC and CTMC results [Fig. 4.4(a)]. The capture distribution between the no-response and response calculations are mostly similar except for Ar where the disparity between them is slightly more pronounced. While the TC-AOCC distribution for Ne^{10+}-He collisions is similar to the experimental measurements, results for Ne^{10+}-Ne collisions show a broader distribution [Fig. 4.4(b)]. This broader profile is also seen in the present net capture, particularly calculations using the response model. In either case, whether it is the TC-AOCC or the present net capture results, they do not reflect the strong selectivity of capture shown by the experimental results.

In another comparison, Table 4.2 lists the nl partial capture cross sections for $n = 3$ up to $n = 7$ states from the present no-response approximation along with TC-AOCC results [55]. Present results using the response model are shown separately in Table A1 of Appendix A.. Focusing on Table 4.2, the only similarities between the pure SEC and TC-AOCC results are those for Ne^{10+}-He collisions corresponding to the $5l$ states. One can also draw the comparison that the TC-BGM net capture results for He collisions are roughly a factor of two greater than the TC-AOCC results, and this can be seen for all values. However, this does not appear to be the case for Ne collisions.

A possible explanation for the discrepancy shown in the TC-AOCC results for Ne collision could the choice of basis. Liu *et al.* [55] noted that they included in total four bound states on the Ne target in their calculation, namely the $2p$ and $3p$ states. This raises some concerns for the following reasons. First, the $2p$ and $3p$ subshells consist of three states each, either of the standard $p_{-1},\ p_0, p_1$ states corresponding to complex spherical harmonics, or of states that correspond to real spherical harmonics and preserve a mirror symmetry of the Hamiltonian, which makes them a popular choice in close-coupling scattering calculations [29]. Second, it appears problematic to exclude the s and d subshells, thereby blocking dipole-like excitations. By revisiting the present calculations for the Ne^{10+}-Ne collision system it was found that excluding the Ne $2s$ and $3s$ states yields substantial differences in capture cross sections compared to the original TC-BGM calculation with the full basis; for example, the cross sections for the dominant capture channel $n = 5$ do not appear as prominent as those in Table 4.2. It is clear at this point in the discussion that the TC-AOCC capture cross sections produced by Liu *et al.* [55] do not reflect the SEC events that occurred in the experiment [24]. However, this does not provide enough insight regarding the similarities of the x-ray

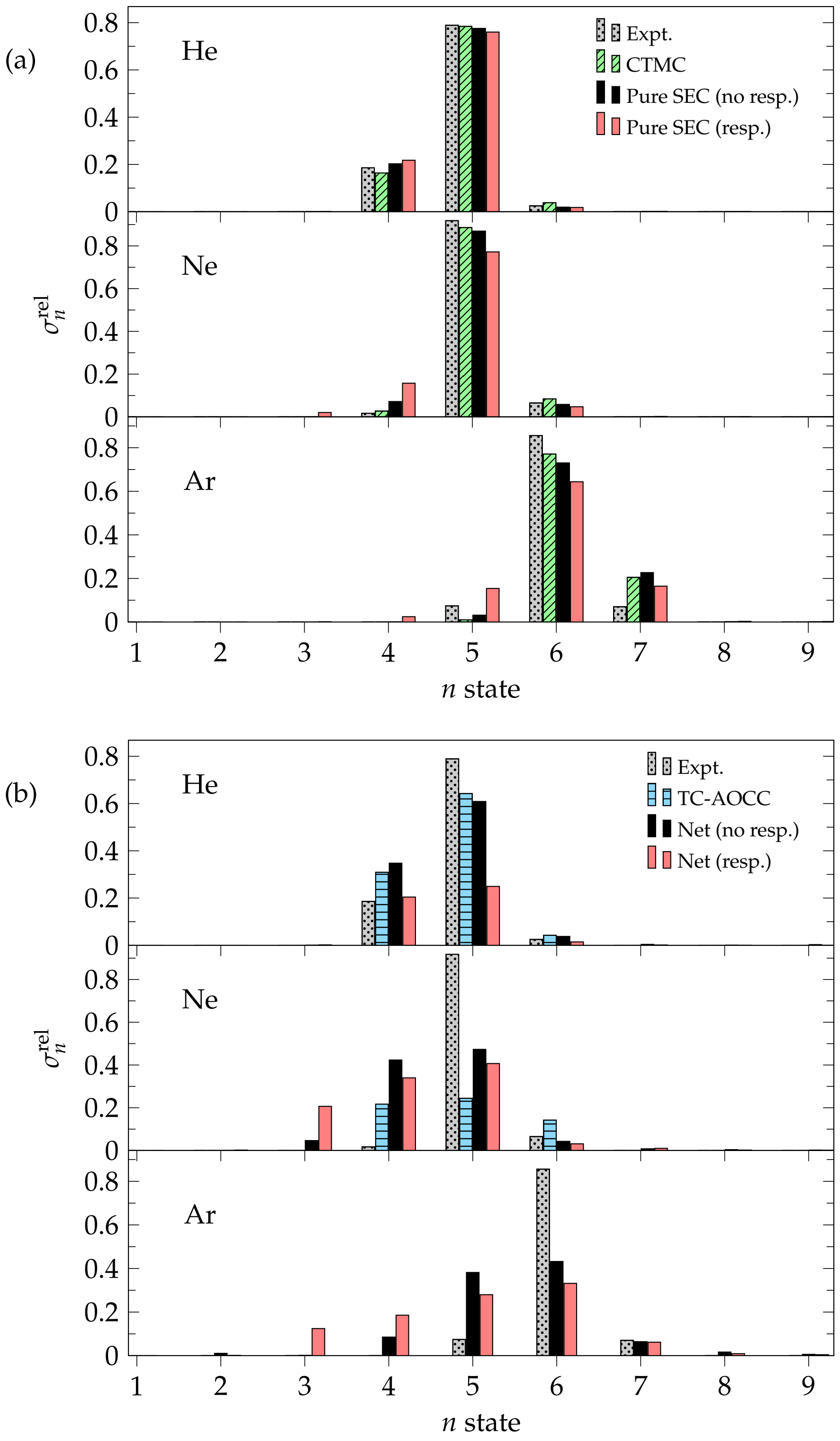

FIG. 4.4: n-state relative capture cross sections of Ne^{10+}-He, -Ne, and -Ar collisions at $E_\mathrm{P} = 4.54$ keV/u: (a) present TC-BGM pure SEC capture compared with experiment and CTMC [24]; (b) present TC-BGM net capture compared with TC-AOCC [55].

TABLE 4.2: *nl* capture cross sections (in 10^{-16} cm^2) from TC-BGM (no-response approximation) and TC-AOCC results [55].

TC-BGM IEM: No-response approximation								
States	Ne^{10+}-He			Ne^{10+}-Ne			Ne^{10+}-Ar	
(n, l)	Ref. [55]	Net	SEC	Ref. [55]	Net	SEC	Net	SEC
3, 0	0.00259	0.0060	0.0059	0.113	0.988	8.9×10^{-5}	0.0814	6.4×10^{-8}
3, 1	0.00497	0.013	0.00120	0.38767	2.580	0.000176	0.115	1.6×10^{-8}
3, 2	0.00555	0.014	0.00122	0.432	2.639	0.00018	0.164	7.1×10^{-9}
4, 0	1.280	2.702	0.655	0.619	4.080	0.121	3.254	0.00028
4, 1	2.50	5.31	1.42	1.548	12.337	0.261	7.918	0.00070
4, 2	2.366	5.074	1.316	2.2090	20.44	0.347	9.986	0.00068
4, 3	1.653	3.610	0.831	2.272	19.955	0.314	8.611	0.00046
5, 0	0.408	0.793	0.518	0.448	2.055	0.9694	7.106	0.090
5, 1	1.599	2.875	1.846	1.261	6.480	1.7530	20.021	0.195
5, 2	3.388	6.097	3.730	1.8989	12.969	3.0252	28.942	0.230
5, 3	5.193	9.352	5.097	2.062	19.746	3.789	40.350	0.205
5, 4	5.593	10.123	4.953	1.792	22.255	3.0958	37.188	0.123
6, 0	0.0187	0.032	0.005	0.0852	0.128	0.0131	3.013	0.989
6, 1	0.0655	0.116	0.018	0.834	0.291	0.0299	9.367	1.947
6, 2	0.1318	0.213	0.033	1.0724	0.808	0.0673	20.175	3.636
6, 3	0.161	0.269	0.047	1.0558	1.729	0.1311	31.090	5.001
6, 4	0.226	0.399	0.083	0.6593	1.050	0.2403	42.191	4.894
6, 5	0.4663	0.783	0.219	0.6337	1.725	0.3650	45.392	3.127
7, 0	0.00124	0.004	0.001	0.0862	0.019	0.0001	0.279	0.054
7, 1	0.0089	0.013	0.002	0.75998	0.080	0.0002	0.854	0.115
7, 2	0.01096	0.016	0.003	0.9482	0.103	0.0002	1.759	0.269
7, 3	0.01814	0.030	0.004	0.8596	0.145	0.0003	2.626	0.557
7, 4	0.04396	0.077	0.011	0.5730	0.271	0.0007	3.800	1.060
7, 5	0.03353	0.045	0.009	0.30936	0.276	0.0011	5.509	1.830
7, 6	0.00814	0.014	0.004	0.09185	0.165	0.0037	7.613	2.203

spectra between the experimental results and TC-AOCC (Fig. 4.1).

In a different perspective, Fig. 4.5 displays the relative *nl* partial capture cross sections $s_{nl} = \sigma_{nl}/\sigma_n$ for the dominant and subdominant capture channels in each collision system. Because the predicted x-ray spectra from CTMC and TC-AOCC calculations are normalized to the experimental data, it appears important to compare and examine these distributions. However, only results from TC-AOCC can be compared with present calculations since CTMC values were not reported. The distributions shown in Fig. 4.5 can be associated to various models that were studied extensively in the past, which have been reviewed by Janev and Winter [10]. In most cases, the relative *l*-distributions resemble the *statistical distribution* [10],

$$\sigma_{nl} = \frac{(2l+1)}{n^2}\sigma_n, \tag{4.3}$$

where electrons are mostly captured into the maximum *l* subshell. There are some instances where capture occurs preferentially in the lower *l*-state [e.g. Fig. 4.5(a) for $n = 4$] which resembles to the so-called *separable distribution* [10],

$$\sigma_{nl} = \frac{2l+1}{Z}\exp\left[\frac{-l(l+1)}{Z}\right]\sigma_n, \tag{4.4}$$

where Z is the charge of the projectile ion. Moreover, one notes the similar relative *l*-distributions between TC-AOCC [55] and the present TC-BGM results in the no-response approximation for the Ne^{10+}-He collision system. By comparing the various present TC-BGM calculations, it appears that the response model has a significant influence on the *l*-distribution where it tends to increase the population of subshells of high *l* numbers.

Despite the discrepancies shown between the TC-AOCC results of absolute *nl* cross section sections compared to present results (Table 4.2), they display similar relative *l*-distributions [Fig. 4.5(b)]. This may explain the reasonable agreement of the x-ray spectra (Fig. 4.1) between the TC-AOCC [55] and experimental results [24] regardless of the large discrepancies in the *n*-state cross section distribution [cf. Fig. 4.4(b)]. Because the TC-AOCC and the present net capture are not good representations of the experimental observations [24] it would be inappropriate to include these results further in the discussion of the x-ray spectra. Therefore, the x-ray spectra using the present net capture and TC-AOCC results of Liu *et al.* [55] are not considered further.

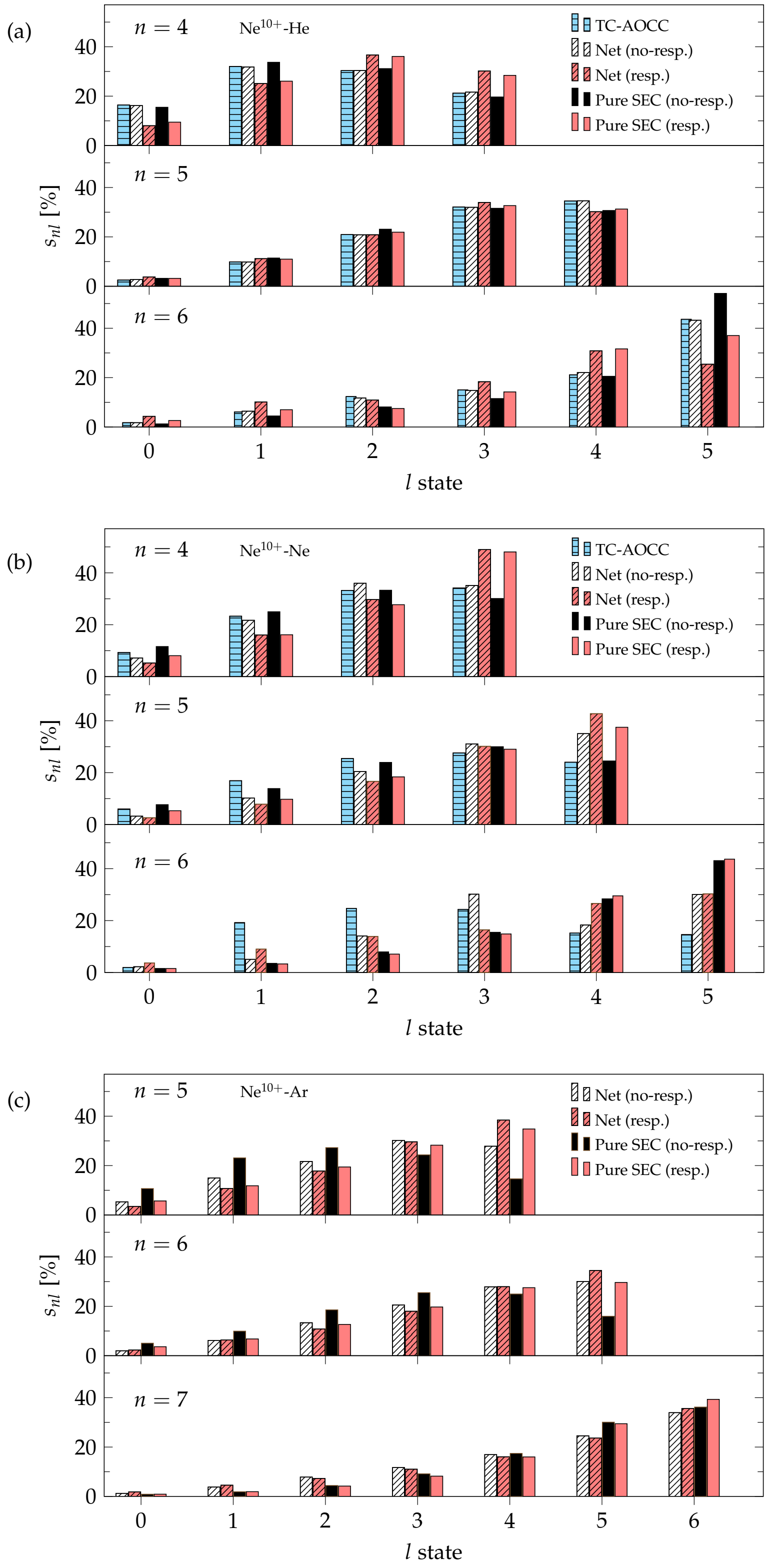

FIG. 4.5: *nl* relative pure SEC distributions s_{nl} for Ne^{10+} collisions with (a) He, (b) Ne, and (c) Ar.

4.4 X-RAY EMISSION SPECTRA

The n-state Ne^{9+} x-ray spectra from He, Ne, and Ar collisions are shown in Fig. 4.6. The present TC-BGM results using the pure SEC cross sections are compared with the experimental and CTMC results by Ali *et al.* [24]. Each group plot shows the x-ray spectra due to SEC into the dominant and two subdominant states along with the spectra as a result from capture into all states.

As mentioned in Sec. 4.1 the CTMC calculation of each emission line was assumed with a Gaussian profile that has a full-width at half-maximum of 126 eV, which is the resolution of the x-ray detector. Consequently, summing these profiles results in only two visible peaks: Ly-α ($2p \rightarrow 1s$) and Ly-$\beta+$ ($np \rightarrow 1s$, where $n \geq 3$). In the report by Ali *et al.* [24], the CTMC spectra profiles are normalized to the experimental areas. However, this normalization procedure may not be ideal and an alternative process is discussed further below. For now, the same convolution and normalization process was applied to the present results.

In most cases, the present spectra exhibit a slight overestimation of the Ly-α counts compared to the measured spectra while the Ly-$\beta+$ emissions are generally underestimated. This is most noticeable for He collisions [Fig. 4.6(a)]. This observation applies to the CTMC results as well. In a different case, the present spectra for Ar collisions [Fig. 4.6(c)] show the least amount of disparity with the experimental spectra where the profiles are generally within the experimental uncertainties.

Comparing between the no-response and target-response results, the latter generally do not lead to an improved agreement with the experimental spectra. In some cases, for example the $n = 6$ case in collisions with Ne [Fig. 4.6(b)], the response profile appears very similar to the no-response profile. These differences in the spectral peaks, or lack thereof, can be understood from looking at the relative l-distribution of Fig. 4.5(b). In the aforementioned case of Fig. 4.6(b), it is shown that the l-distributions of $n = 6$ in Fig. 4.5(b) precisely reflect the overlapping spectral profiles. Another scenario where, for example, the Ly-α emission count is enhanced in the response calculation can be understood by comparing the l-distribution at the maximum l-state. Electrons captured into this subshell can only follow the *yrast cascade chain* [100],

$$...4f \rightarrow 3d \rightarrow 2p \rightarrow 1s, \tag{4.5}$$

which directly contributes to Ly-α emissions.

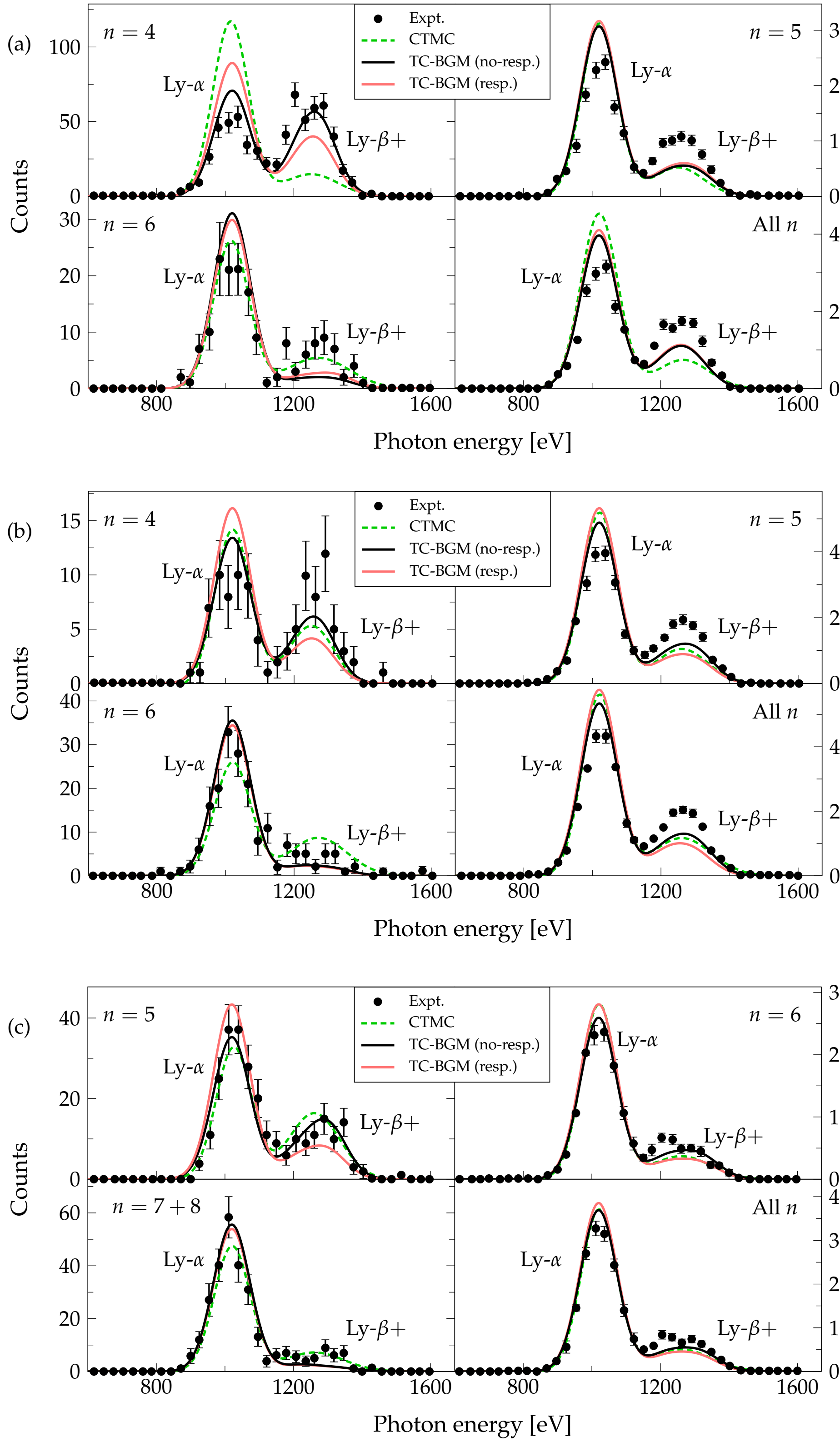

FIG. 4.6: X-ray spectra from pure SEC collisions of Ne^{10+} with (a) He, (b) Ne, and (c) Ar. Present TC-BGM results are shown with experimental and CTMC results by Ali *et al.* [24].

As briefly mentioned above, there is a misleading aspect of mutually normalizing the modelled spectral profiles to the experimental areas. Since this study differentiates the x-ray spectra based on the captured n-state, it is expected that the ratio of areas under two n-state spectral profiles be similar to the ratio of cross sections of the same n-states. Note that they may not be identical because of the convolution process. From the present relative σ_n distribution [Fig. 4.4(a)], the ratio between two n-state cross sections from the no-response results does not necessarily produce the same ratio as the response results. Consequently when each n-state spectral profile is normalized in this way, the ratio from all calculations are identical. As an example, consider the Ne^{10+}-Ne collision system. From Fig. 4.6(b), the ratio of areas under the calculated spectra profile between $n = 5$ and $n = 4$ is 31.1. Considering only the present calculations, the corresponding cross section ratios are $\sigma_5/\sigma_4 \approx 12.1$ and 5.13 for the no-response and response calculations, respectively. Clearly neither of these two cross section ratios are similar to the spectral area ratio.

One approach to preserve the σ_n ratios in the x-ray spectra is by first normalizing the 'All n' modelled spectra to the same experimental area and using its normalization factor to scale each individual n-state spectra profile. This procedure has been performed on the present results which are shown in Fig. 4.7. Whereas the modelled spectra for the dominant capture state are similar in appearance to the ones shown in Fig. 4.6, there are substantial differences in the subdominant states where the disparity between the two calculations is more pronounced, particularly for Ne and Ar.

Returning to the earlier example of Ne^{10+}-Ne collisions, the ratio of the spectral areas [Fig. 4.7(b)] between $n = 5$ and $n = 4$ is now 12.3 and 5.19 for the no-response and response results, respectively. Recall that the corresponding cross section ratios are 12.1 and 5.13, respectively. It is clear that these spectral area ratios are now consistent to the σ_n ratios produced by this alternative normalization process. Performing the same comparisons for the other collision systems reveals a similar consistency. Therefore, one may suspect that if Liu *et al.* [55] were to use this alternative normalization, the spectra reported would have appeared similar in counts as implied by their cross sections in Table 4.2; which would have led to different conclusions.

An important aspect to note regarding x-ray emissions from electron de-excitation is that they are known to be polarized [107] since magnetic m sublevels are not populated equally [108]. This can be problematic if one expects the x-ray emission to be isotropic and comparing calculations that correspond to orientation-integrated mea-

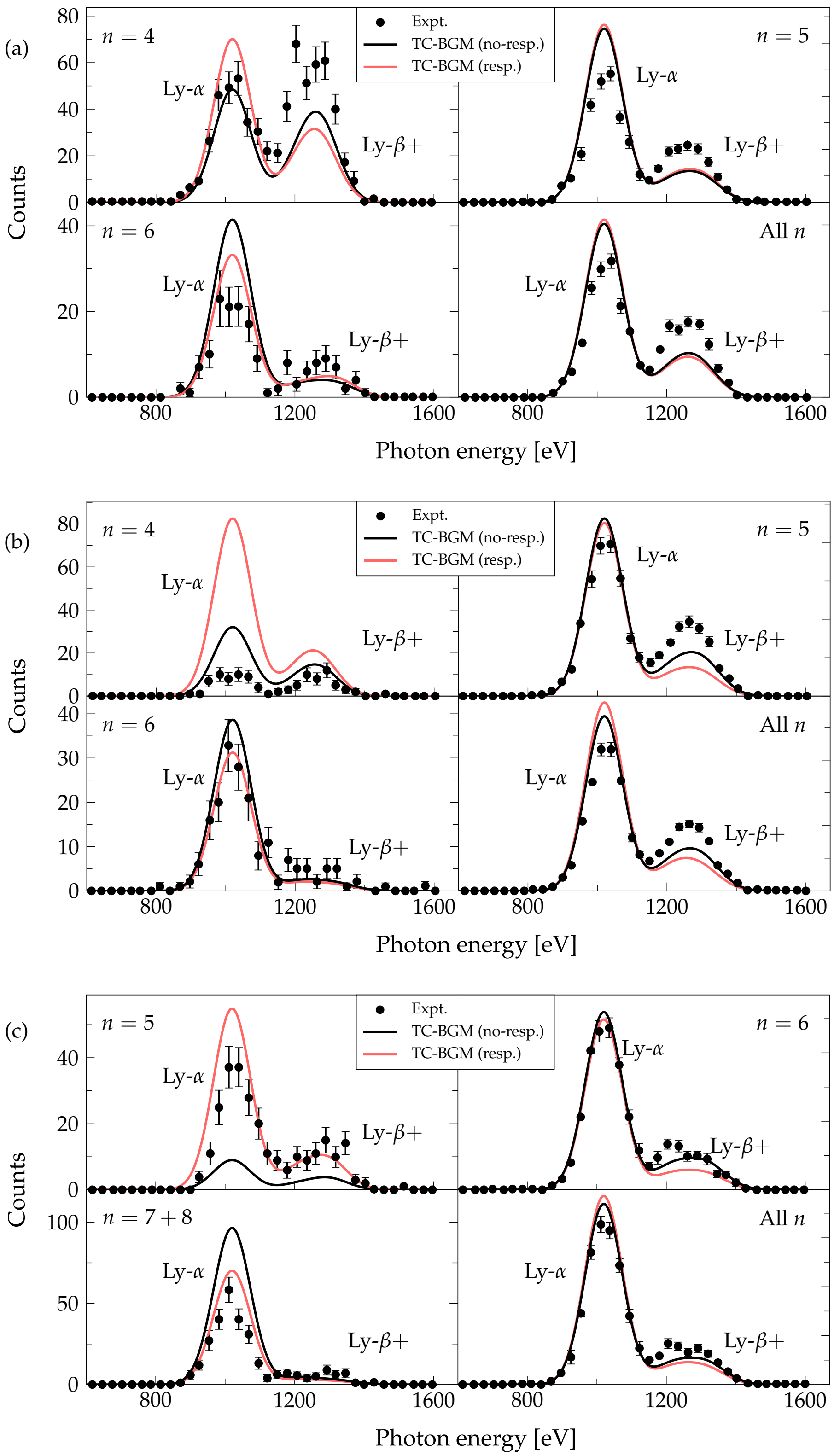

FIG. 4.7: X-ray spectra from pure SEC collisions of Ne^{10+} with (a) He, (b) Ne, and (c) Ar. Present n-state spectra are scaled with respect to the normalized 'All n' spectra.

surements with measurements performed at one given orientation, which was how the x-ray measurements considered here were carried out [24]. However, if x-rays are detected at 90° relative to the ion beam axis, as it was performed by Ali *et al.* [24], the discrepancy due to anisotropy can never be larger than 30%, assuming that the x-rays are fully polarized [107, 108]. In fact, previous experimental studies reported that discrepancies of 15% or lower are typically observed [101, 109]. Because the polarization rates of Ali *et al.* [24] are unknown, the upper limit of 15% due to anisotropy should be taken into account in addition to the reported experimental uncertainties. By considering the present results shown either in Fig. 4.6 or Fig. 4.7 with all these uncertainties, they are deemed to be satisfactory.

4.5 CONCLUSIONS

An analysis of SEC in Ne^{10+}-He, Ne, and Ar collisions at the impact energy $E_\mathrm{P} = 4.54$ keV/u was performed using the TC-BGM within the IEM. Capture cross sections obtained from the solution of the single-electron TDSE were used in a hydrogenic radiative cascade model to obtain x-ray emission spectra.

One objective of this study was to understand how the IEM TC-AOCC cross sections by Liu *et al.* [55] compared with the present analysis of net capture and the pure SEC multinomial calculations. Simultaneously, the present calculations were compared with the experimental and CTMC relative cross sections by Ali *et al.* [24]. While the nl cross sections from the TC-AOCC study for He collisions appeared to be related to the present net capture in the no-response approximation, no relation can be drawn for Ne collisions. Regardless, the present results based on the multinomial analysis representing pure SEC events showed satisfactory agreement with the experimental relative n-state cross sections [24]. This demonstrates that the use of an appropriate multinomial analysis is crucial for cross section calculations that are performed within the IEM.

The other objective of this study was to examine the x-ray spectra from pure SEC events for each collision system. By following the same convolution and mutual normalization procedure performed by Ali *et al.* [24], the present spectra showed no significant differences between the no-response and response calculations. However, this mutual normalization process led to questionable spectra count ratio, masking the deviations found in the present calculations on relative cross sections. It is perhaps through this procedure that led to the inconsistent agreement of cross sections and x-ray spectra by Liu *et al.* [55]. This misrepresentation of x-ray spectra was demonstrated for the present results by using a more consistent normalization process, unmasking these strong deviations. In either case, overall, the present x-ray result were found to be in satisfactory agreement with the experimental spectra [24].

CHAPTER 5

C^{6+} collisions with helium and molecular hydrogen

This chapter has been adapted from:

> A. C. K. Leung and T. Kirchner, Analysis of x-ray emission spectra in charge-exchange collisions of C^{6+} with He and H_2, Phys. Rev. A **93**, 052710 (2016).

5.1 OVERVIEW AND BACKGROUND

The analysis presented in this chapter focuses on two collaborative experiments performed at the Oak Ridge National Laboratory that were reported separately, one by Defay *et al.* [57] on C^{6+}-He collisions and the other by Fogle *et al.* [25] on C^{6+}-H_2 collisions. Measurements were performed at impact energies from 0.5 to 32 keV/u (correspond to velocities of approximately 300 to 2500 km/s). These two charge-exchange experiments were performed on the ion-atom merged-beam apparatus (described in Ref. [110] and references therein). For x-ray measurements, the x-ray microcalorimeter detector developed by a joint collaboration from the University of Wisconsin and Goddard Space Flight Center [111] was used. Designed for the purpose of measuring diffuse background x-rays, this x-ray microcalorimeter has a high resolution of no more than 10 eV full-width at half-maximum, which is sufficient to resolve the C VI Ly-α through Ly-γ line-emissions.

In these studies, x-ray emission counts were measured and ratios of these measurements were compared with theoretical calculations. These theoretical values include their own CTMC calculations and using previous reported AOCC [70] and MOCC

[112] *nl* partial capture cross sections to produce additional sets of Lyman emission counts using the diagrammatic method described in Sec. 3.6. Moreover, a separate analysis using the time-dependent lattice method (TDL) by Pindzola and Fogle [32] on C^{6+}-He collisions was also reported. These Lyman emission ratios for He and H_2 collisions are shown in Fig. 5.1 and Fig. 5.2, respectively. Through these comparisons, it was deduced that x-ray emissions from the C^{6+}-He experiment are mainly produced by SEC events while emissions from C^{6+}-H_2 collisions are produced by SEC and ADC events. Unlike the triple-coincident COLTRIMS experiment by Ali *et al.* [24], these experiments cannot differentiate the x-rays by capture events. Although satisfactory agreement is shown between the experimental and theoretical ratios at high impact energies, particularly with regard to the AOCC ratios, the agreement at the lower end is mixed. Therefore, the two collision problems presented by the Oak Ridge collaboration group [25, 57] serve as an excellent testing ground to further examine the applicability of the TC-BGM in explaining the observed x-ray emissions.

5.2 SETUP OF THE PROBLEM

The problem of interest is a bare C^{6+} projectile colliding with He or H_2 at impact energies from 0.5 to 40 keV/u. Within the IEM, the single-electron Hamiltonian is

$$\hat{h}(t) = -\frac{1}{2}\nabla^2 + V_{\mathrm{T}} - \frac{6}{|\mathbf{r}_{\mathrm{T}} - \mathbf{R}(t)|}, \tag{5.1}$$

where V_{T} is the effective ground-state potential of the target. For the He target, the effective ground-state potential obtained from the OPM was used. As for H_2, the single-centre, spherical model approach of Ref. [69] was employed

$$V_{\mathrm{H}_2} = -\frac{1}{r_{\mathrm{T}}} - \frac{1}{r_{\mathrm{T}}}(1 + \alpha r_{\mathrm{T}}) \exp\left(-2\alpha r_{\mathrm{T}}\right), \tag{5.2}$$

where $\alpha = 3.93$ is a parameter chosen such that the ground-state energy eigenvalue of the target Hamiltonian matches the correct first ionization energy of the molecule for the fixed internuclear distance (bond length) of 1.4 a.u.. It is important to note that in a previous C^{6+}-H_2 collision study [113], it was determined that capture mainly occurs at internuclear distances of about 8.5 a.u., which is reasonably far away from the molecule to justify the use of the spherical, single-centre model.

With regard to basis sets, all states of the *KLMN* shells of the target were included.

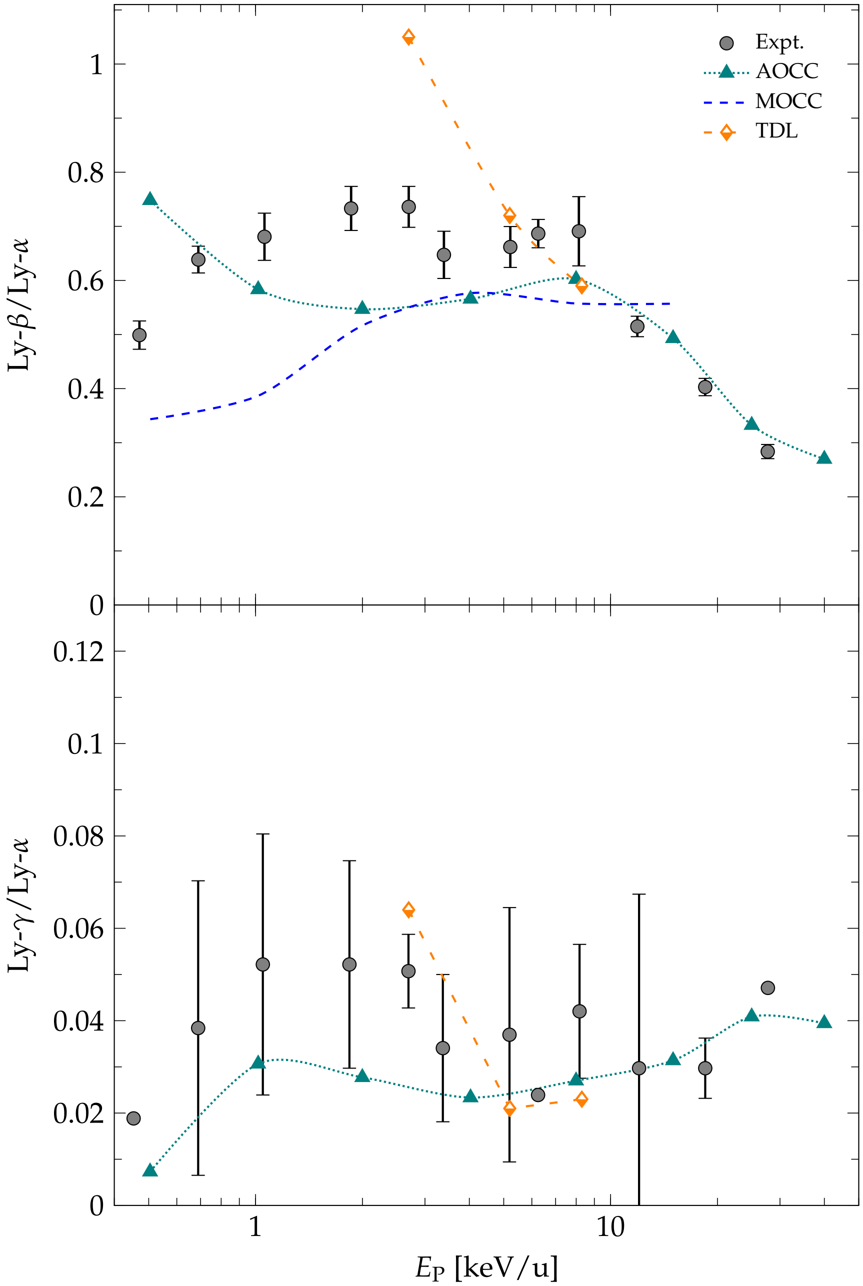

FIG. 5.1: Lyman line-emission ratios for C^{6+}-He collisions from previous studies: Ly-β/Ly-α ratios (top), and Ly-γ/Ly-α ratios (bottom). Experimental ratios are by Defay *et al.* [57] while calculated ratios are from AOCC [70], MOCC [112], and TDL [32].

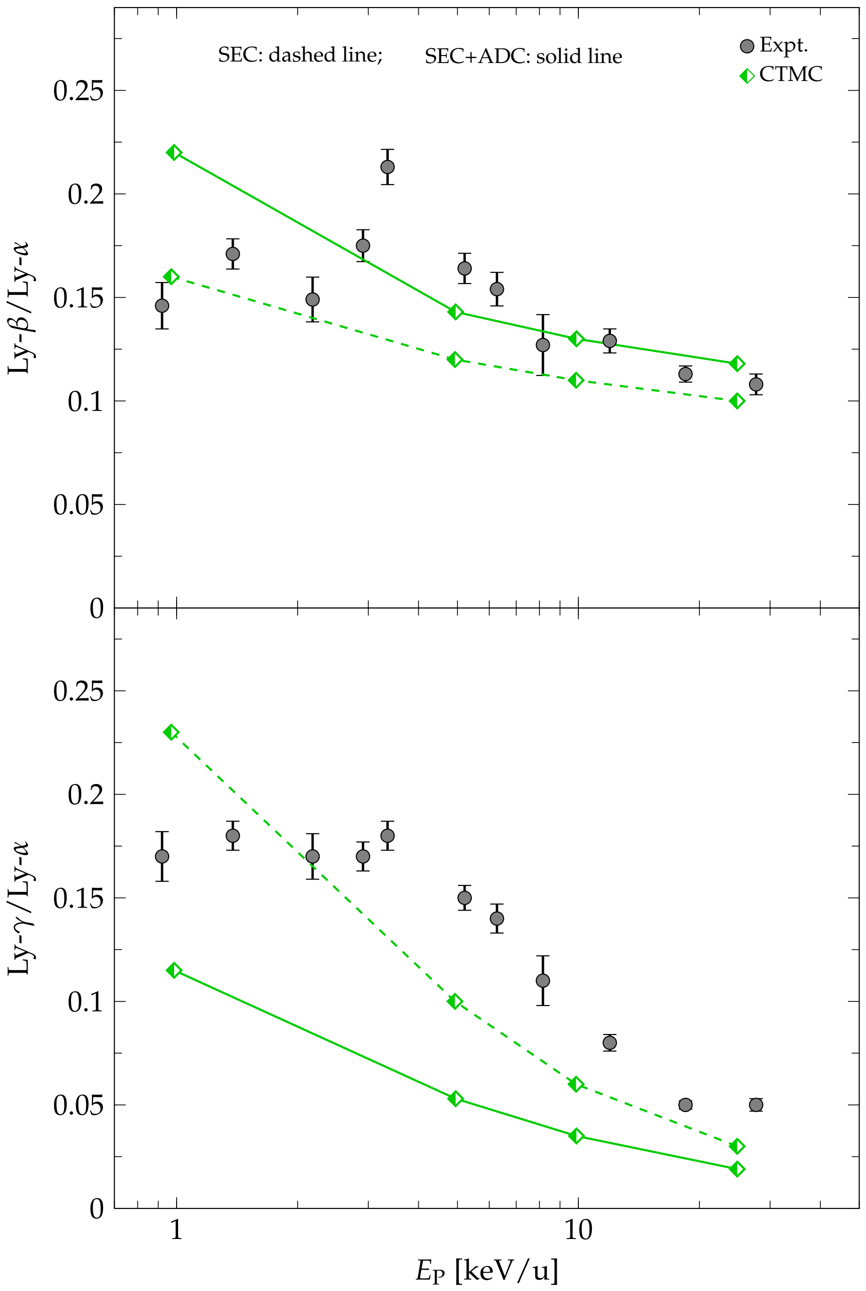

FIG. 5.2: Lyman line-emission ratios for C^{6+}-H_2 collisions from Fogle *et al.* [25]: Ly-β/Ly-α ratios (top), and Ly-γ/Ly-α (bottom). All calculated ratios which considered only pure SEC are shown with a dot-dashed line while those of SEC+ADC are shown with a solid line.

For the C^{6+} projectile, all hydrogenlike states from $n = 1$ to $n = 6$ were included since the CBM predicts the main capture channel to be $n = 3$ and $n = 4$ for He and H_2 collisions, respectively. Table 5.1 lists the BGM hierarchies that were used for the present analysis.

TABLE 5.1: BGM hierarchies used in present calculations for C^{6+}-He, and -H_2 collisions.

State	1*s*	2*s*	2*p*	3*s*	3*p*	3*d*	4*s*	4*p*	4*d*	4*f*
Impact energy: $0.5\ \text{keV/u} \leq E_P < 10\ \text{keV/u}$										
M_v:	0	1	1	1	2	2	2	2	2	2
Impact energy: $10\ \text{keV/u} \leq E_P \leq 40\ \text{keV/u}$										
M_v:	0	1	1	2	2	2	3	3	3	3

In order to provide a surveyable discussion, results of He and H_2 collisions are presented separately.

5.3 C^{6+}–He COLLISIONS

5.3.1 Capture probabilities and cross sections

Figure 5.3 shows the pure SEC capture probability profiles at $E_P = 1$ keV/u for the dominant capture channel of $n = 3$ and the subdominant channel of $n = 4$ using Eq. (3.33). Results of the present no-response and target-response calculations using the TC-BGM are compared. Probabilities for the other capture channels are not shown since they are negligible ($< 10^{-6}$). For $n = 3$ [Fig. 5.3(a)], the overall profile between the no-response and response results are similar and differences simply come down to the oscillations. Similar observations are also noted for the $n = 4$ profiles [Fig. 5.3(b)] but the differences are clearer as the area under the response profile is smaller than for the no-response calculation. Although somewhat subtle, the opposite behaviour is shown for the $n = 3$ profiles between $b = 0.5$ and $b = 2$. This can be understood from the decreased screening of the target core due to the response model, which leads to an increased binding of the electron, and so capture into a lower state is more probable with the response model.

To assess the present calculations, the capture cross sections are compared with values from previous studies. Figure 5.4 shows the total SEC cross sections for the C^{6+}-He

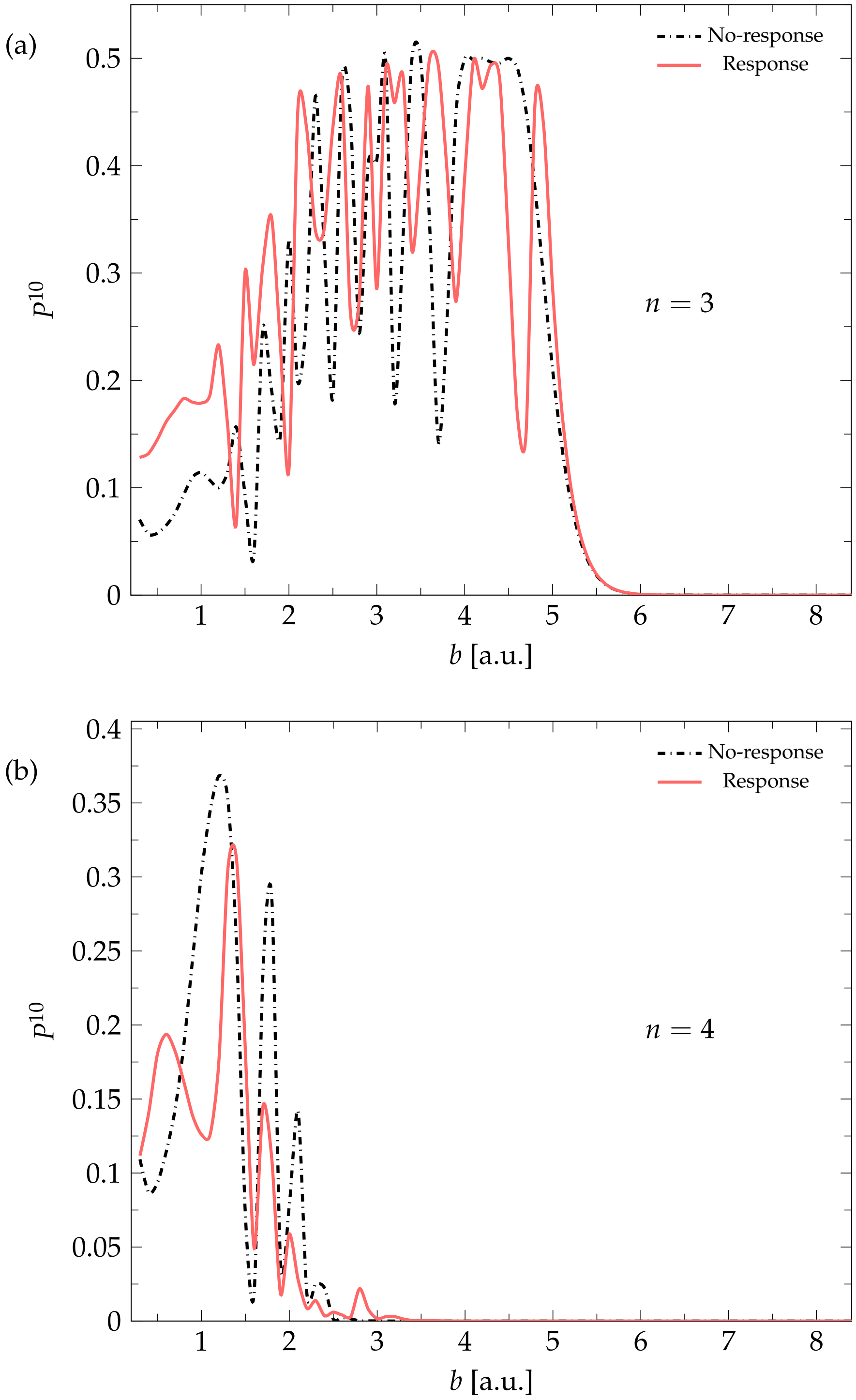

FIG. 5.3: TC-BGM pure SEC probabilities plotted with respect to impact parameter for C^{6+}-He collisions at $E_P = 1$ keV/u. Capture probabilities for: (a) $n = 3$, and; (b) $n = 4$.

collision system corresponding to impact energies from 0.5 to 40 keV/u. Cross sections from previous studies consist of calculations using the AOCC [70], MOCC [112], and the TDL [32] methods. Present values are also compared with the recommended set by Janev *et al.* [114]. These values were obtained from Chebyshev polynomial fits on data from various experimental and theoretical results and uncertainties are interpolated based on the reliability of the experiment and sophistication of the theoretical method.

As shown in Fig. 5.4, the present cross sections from both no-response and response calculations are well within the uncertainty range of the recommended values. They are fairly constant between 0.5 and 10 keV/u before starting to decrease at higher energies. The present values are also similar to MOCC values but the discrepancies between them are more apparent at low impact energies. In contrast, the TDL [32] are overestimated and lie outside the uncertainty range.

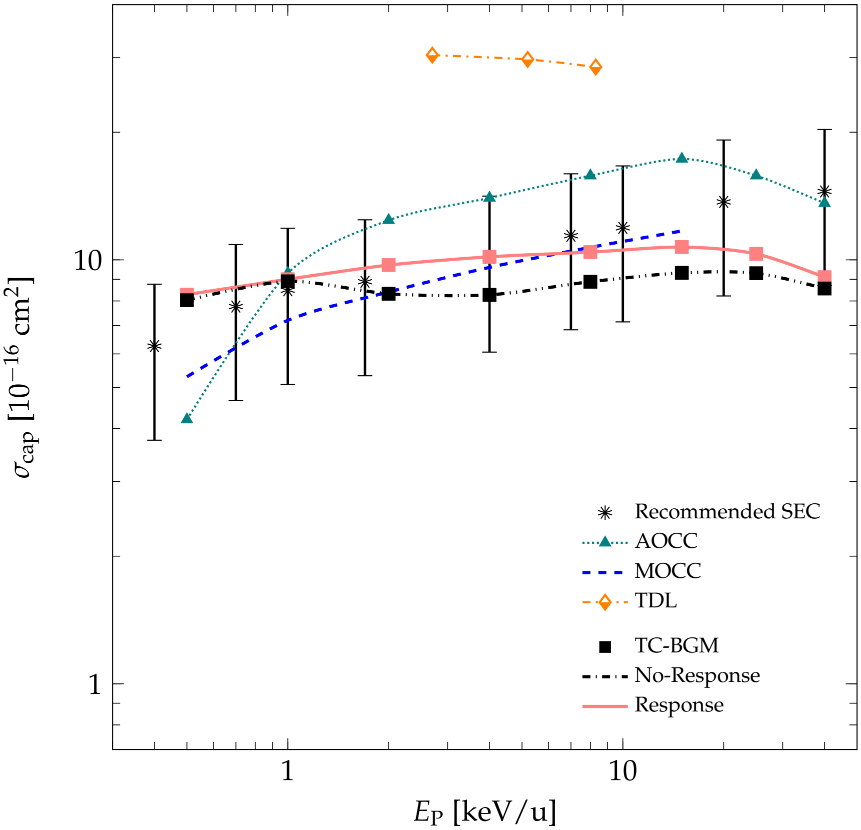

FIG. 5.4: Total SEC cross section plotted with respect to impact energy for C^{6+}-He collisions. Calculated SEC values are from AOCC [70], MOCC [112], TDL [32], and the present TC-BGM. Recommended SEC values were compiled by Janev *et al.* [114].

The discrepancies between the present cross sections and AOCC and MOCC may be due to several reasons. First, the AOCC and MOCC results that are shown in Fig. 5.4 were obtained using two-electron configurations in the wavefunction expansion scheme to explicitly describe the interelectronic interaction. This differs from the IEM used in the present TC-BGM calculations where the many-electron processes are described using a multinomial analysis of solutions of the single-electron TDSE. Another factor is the choice of basis. The AOCC calculations by Fritsch and Lin [70] contained only the ground state of He whereas the present calculations include all states from the $KLMN$ shells. The concern of having only the ground state in the target basis is that excitation transitions are blocked, thereby potentially affecting capture transition probabilities over the course of the collision. Similar remarks could also apply to the MOCC calculations by Kimura and Olson [112] where an additional $2p$ state was used in the target basis. Upon revisiting the present calculations, it was found that reducing the target basis to only the ground state resulted in larger cross sections.

The next aspect to discuss is the contribution to the Lyman line-emissions due to ADC. Defay *et al.* [57] did not consider ADC in the discussion of their x-ray emission measurements for the C^{6+}-He collision system. This is most likely due to the fact that DEC cross sections for this collision system are negligible compared to SEC. A survey of the literature (e.g., Refs. [88, 115–117]) confirms this aspect. However, results of DEC cross sections produced by the present method appear comparable in magnitude with SEC. For example in the no-response approximation, the total DEC cross section for the $3l3l'$ configuration at $E_P = 4$ keV/u is 10.8×10^{-16} cm^2, which is similar to the total SEC of 8.27×10^{-16} cm^2. Because of the similarity in magnitude between the two capture processes, one may be led to believe that ADC contributions should be included in the total SEC. As mentioned before, previous studies by other groups suggest otherwise. In one theoretical study by Harel *et al.* [115], calculations using the so-called one-electron diatomic molecule expansion scheme with two-electron configurations were carried out. It was reported, as an example, that this calculation yielded a DEC cross section for the $3l3l'$ state of 2.1×10^{-17} cm^2 at $E_P = 4.61$ keV/u. This is in good agreement with the Auger spectroscopy measurement by Stolterfoht *et al.* [116] of $(2.4 \pm 0.2) \times 10^{-17}$ cm^2. In another independent Auger spectroscopy experiment by Mack [88], the total ADC cross section was reported to be 2.2×10^{-17} cm^2 at a very similar impact energy. From these comparisons it is clear that the DEC cross section produced from the present calculations for this collision system is overestimated.

It is important to note that cross section calculations of two-electron processes performed within the IEM involving a helium target, more precisely using the multinomial analysis (3.32), are known to be erroneous [118–120]. As Shingal and Lin [118] suggested, this is because the effective potential of the helium atom used in the multinomial analysis does not correspond to the total ionization energy of 2.90 a.u. [103]. In the present analysis, the first ionization energy of helium is 0.92 a.u., thus, the total ionization energy is $2 \times 0.92 = 1.84$ a.u.. Furthermore, Shingal and Lin [118] have shown that IEM calculations that uses a modified effective potential where the binding energy of the electron is exactly half of the total ionization energy yields improved DEC cross sections. An alternative approach to working with double-electron processes within a similar framework is the *independent event model* (IEVM) [121]. In this approach, a given process is described by a sequence of independent events. Two sets of collision calculations of single-electron capture probabilities need to be carried out: one with neutral helium as the target ($p_{\text{cap}}^{\text{He}}$) and another one with the ground-state He$^+$ ion ($p_{\text{cap}}^{\text{He}^+}$). The total DEC probability in this model is

$$p_{\text{DEC}} = p_{\text{cap}}^{\text{He}} p_{\text{cap}}^{\text{He}^+} . \tag{5.3}$$

By revisiting the present calculation for the above example, using the IEVM yields a $3l3l'$ capture cross section of 2.2×10^{-17} cm^2 at 4 keV/u which is consistent with those from previous studies [115, 116]. Since all of these DEC results indicate that the ADC contributions to x-ray emissions should be negligible, there are no additional gains by including them in the present x-ray analysis. Therefore, DEC for the C^{6+}-He system is not considered further and contributions from pure SEC will be the main focus of discussion.

Figure 5.5 shows the n-state relative SEC cross section distributions at impact energies 1, 8, and 25 keV/u. As suggested from the measurements (Fig. 5.1), results at these energies are shown since they roughly represent where noticeable changes in the line-emission ratios occur. It is clear from the plots that the dominant capture channel is $n = 3$, which is consistent with previous findings from the analysis of AOCC [70], MOCC [112], and the CBM prediction. Also shown in Fig. 5.5 is the broadening of the population distribution as the impact energy increases, which is a consistent behaviour [10]. This can be understood from the quantized nature of the electronic states and, as Niehaus [13] has shown using classical arguments, from relating the energy-time uncertainty relation to the impact velocity, and thus, the impact energy.

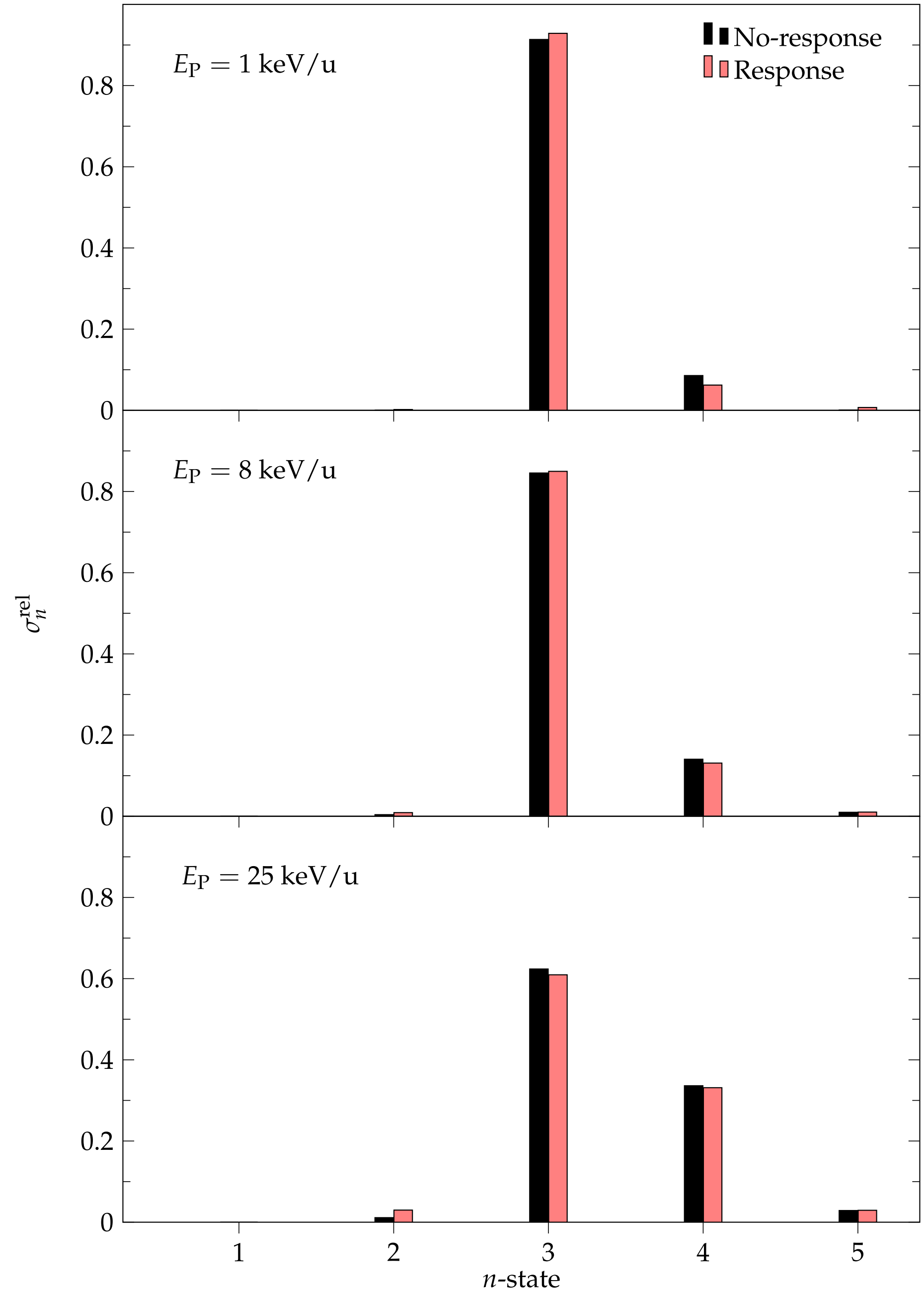

FIG. 5.5: n-state relative SEC cross sections for C^{6+}-He collisions at $E_P = 1$, 8, and 25 keV/u.

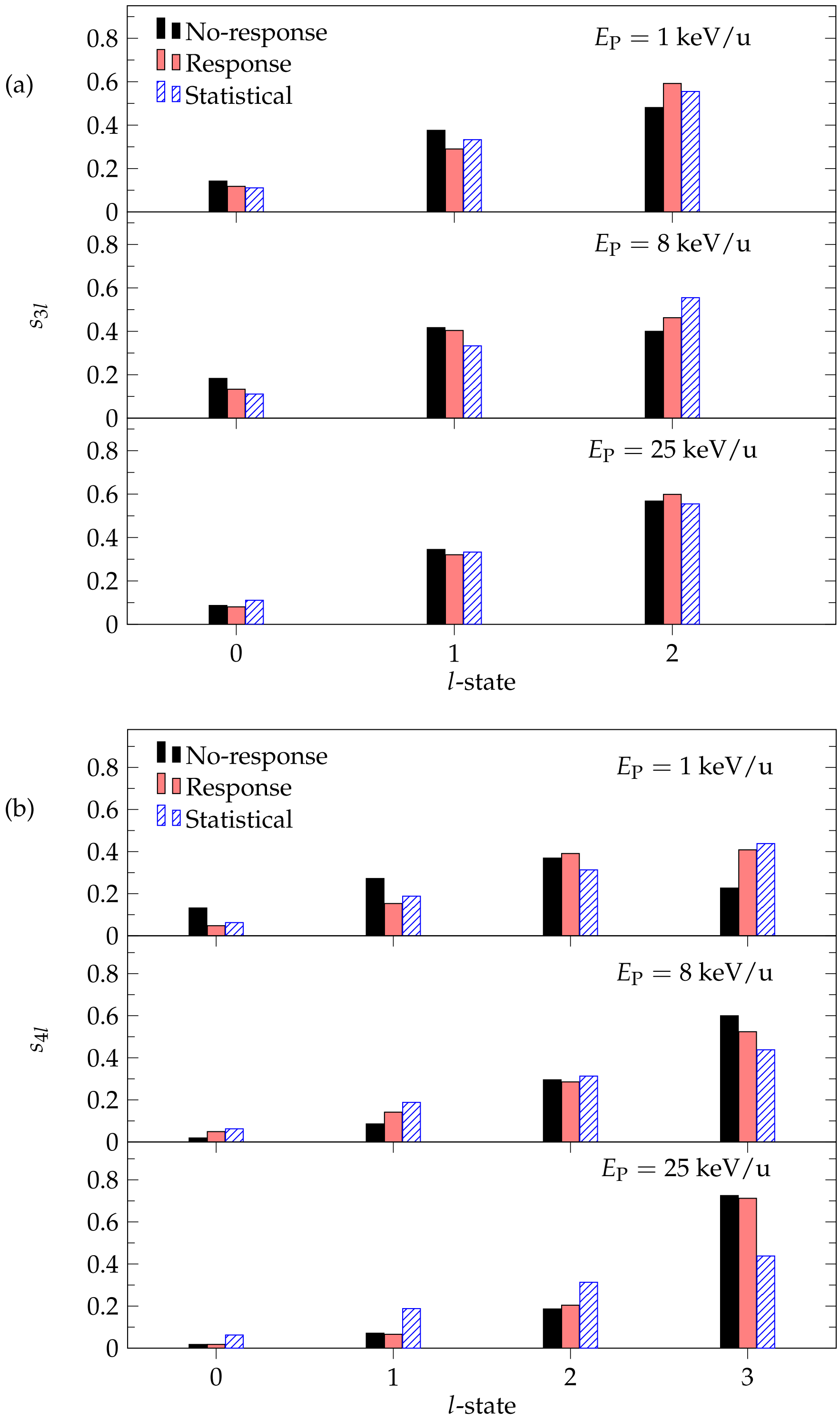

FIG. 5.6: nl relative SEC cross sections for C^{6+}-He collisions at 1, 6, and 25 keV/u: (a) $n = 3$ and (b) $n = 4$. TC-BGM results are compared with the presupposed statistical l-distribution.

Shown in Fig. 5.6 are the present relative nl partial cross-section distributions for $n = 3$ and $n = 4$ at $E_\mathrm{P} = 1$, 8, and 25 keV/u. The complete list of absolute 3l and 4l cross sections can be found in Appendix B.. Also shown alongside is the modelled statistical l-distribution (4.3). The l-selectivity in capture and its dependence on impact energy has been explored extensively (cf. Refs. [10, 122] and references therein), and so several comments are made here to assess the present results. Starting with the 3l-distributions [Fig. 5.6(a)], the no-response and response results appear similar to the statistical distribution, except at 8 keV/u where the relative population between $l = 1$ and $l = 2$ is fairly even. In other words, a small fluctuation occurs in the l-state populations as impact energy increases from 1 to 25 keV/u. A similar observation is made with the 4l-distributions [Fig. 5.6(b)] except that at 1 keV/u the no-response distribution does not resemble the statistical distribution. This is known to be a general feature in collisions in the low and intermediate energy regime where the l-selectivity in higher n-states corresponds to the same l-state of the dominant capture state [10] (in this case, $l = 2$). More precisely, this generally applies to collisions involving ions with charge states from $q = 2$ to $q = 6$. Furthermore, the figure also shows that capture into the maximum l-state is much preferred as the impact energy increases, which is also consistent with the behaviour seen previously [10]. It is clear that the statistical model is not appropriate to describe the l-distribution at these impact energies. In fact, no model exists in the literature to describe such a distribution which is often referred to as *over-statistical*.

5.3.2 Lyman line-emission ratios

Calculated results of the Lyman emission count ratios are presented in Fig. 5.7. The TC-BGM results are compared with the experimental data [57], AOCC [70], MOCC [112], and TDL ratios[32]. The 4l partial cross sections from MOCC [112] were not reported, and thus, Ly-γ/Ly-α ratios from MOCC are absent. The plots show that the present ratios follow a similar profile as the experimental ratios. The present profiles are also similar to other calculated ratios but with a few exceptions.

Starting with the Ly-β/Ly-α, the experimental ratios appear approximately constant from 0.5 to 10 keV/u and then decrease from 10 keV/u and onwards. Among the various calculated ratios that are shown, the present ratios calculated in the no-response approximation are most consistent with the experimental profile. Discrep-

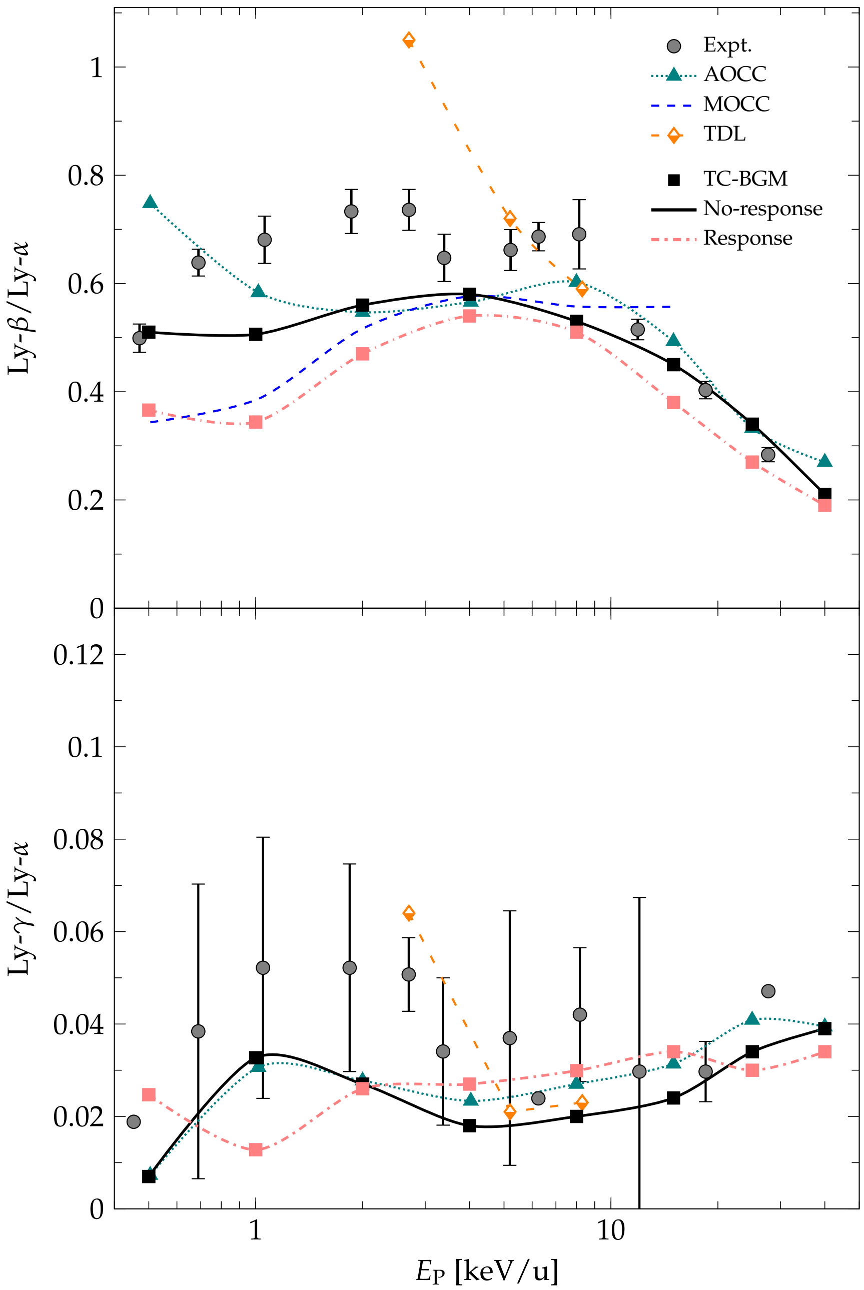

FIG. 5.7: Lyman line-emission ratios for C^{6+}-He collisions with present results compared with previous results: Ly-β/Ly-α ratios (top), and Ly-γ/Ly-α ratios (bottom).

ancies among the various calculations are clearly shown at low energies. One can speculate that the differences among the close-coupling results can be attributed to differences in basis sets as commented earlier regarding total cross sections. Between the present no-response and response results, the latter are consistently lower than the former and also the experimental ratios. Moreover, there is a noticeable outlier produced by the TDL at around 2 keV/u which is mainly due to differences in the $3l$ distribution. Comparing with the present results, population in the $3l$ distribution in both no-response and response calculations peaks in the $3d$ state while the $3l$ distribution produced by TDL calculations peaks in the $3p$ state, leading to a larger Ly-β count because of the $3p \rightarrow 1s$ transition. The decreasing behaviour at higher impact energies can be explained by the nl-distributions (Fig. 5.6) where capture preferentially occurs at the maximum l-state in that regime. As a result, an electron captured into this state can only decay radiatively by the yrast cascade (4.5), leading to a decrease in Ly-β counts and an increase in Ly-α counts.

For the Ly-γ/Ly-α ratios, the present results are overall in satisfactory agreement with the experimental data as they mostly fall within the experimental uncertainties. The present results, particularly the no-response calculation, are very similar to the AOCC profile as well. Note that these ratios are much smaller than the Ly-β/Ly-α ratios since, according to the present calculations, the cross section for $4p$ is much smaller than $3p$. Furthermore, there is also a slightly increasing behaviour as impact energy increases. This is mostly due to the increase in capture for higher n-states at these impact energies (see Fig. 5.5) as cascades from these states are populating the $4p$ state, which leads to an increase in Ly-γ counts.

5.4 C^{6+}–H_2 COLLISIONS

5.4.1 Capture probabilities and cross sections

In Fig. 5.8, probabilities of pure SEC into $n = 3$ and $n = 4$ of the projectile from C^{6+}-H_2 collisions at 1 keV/u are shown. As expected from the CBM, the dominant capture state is $n = 4$ for this collision system. As previously discussed for similar plots of the C^{6+}-He system (Fig. 5.3), there is an increase in capture at low impact parameters for the $n = 3$ state as a result of target response. It was noted that these effects were somewhat subtle in helium collisions but they are are more pronounced for H_2 collisions since $n = 3$ is not the dominant capture channel.

Moving on to total capture cross sections, the present results are assessed through comparisons with results from previous studies. Table 5.2 shows one such comparison with an experimental study by Hoekstra *et al.* [89] at the impact energy of 4 keV/u. Recall that ADC cross sections are extracted from DEC cross sections by Eq. (3.52). In general, the present SEC results are within the uncertainty range of the experimental results by Hoekstra *et al.* [89] with the exception of $n = 4$ from the response calculation, which is slightly underestimated. A similar comment also applies to the ADC results where the present results are similar to Hoekstra *et al.* [89]. Given that the experimental ADC result [89] is of the same order as $\sigma_{\text{SEC}}(n = 4)$, contributions from ADC towards the x-ray emissions are not negligible for this system.

TABLE 5.2: Total SEC cross sections (in 10^{-16} cm^2) from C^{6+}-H_2 collisions at $E_P = 4$ keV/u. Calculated values are from the present TC-BGM in the no-response approximation and response model; experimental data are from Hoekstra *et al.* [89].

	No-response	Response	Hoekstra *et al.* [89]
$\sigma_{\text{SEC}}(n = 3)$	2.67	3.73	3 ± 2
$\sigma_{\text{SEC}}(n = 4)$	25.99	22.58	32 ± 8
$\sigma_{\text{SEC}}(n = 5)$	1.56	0.94	1.5 ± 1
σ_{ADC}	15.58	15.09	11 ± 4

In another comparison, Fig. 5.9 shows several sets of total SEC cross sections plotted with respect to impact energy from 0.5 to 40 keV/u. Specifically, the present results, showing cross sections from pure SEC events and the combined SEC+ADC events, are compared with the total charge transfer measurements by Meyer *et al.* [123]. The plot shows that the inclusion of ADC events in the present calculations, whether in the no-response approximation or with the response model, results in good agreement with the experimental results. However, present calculations using the response model do show a much better agreement than the no-response results, particularly at low impact energies.

In the discussion of double-capture for the C^{6+}-He system (Sec. 5.3.1), it was shown through a sample calculation that the DEC cross section within the IEM using the present method was grossly overestimated compared to previous experimental results. It was also mentioned that an approach to alleviate this issue is to perform statistical analyses using the IEVM. Note that the present ADC calculations shown in Table 5.2

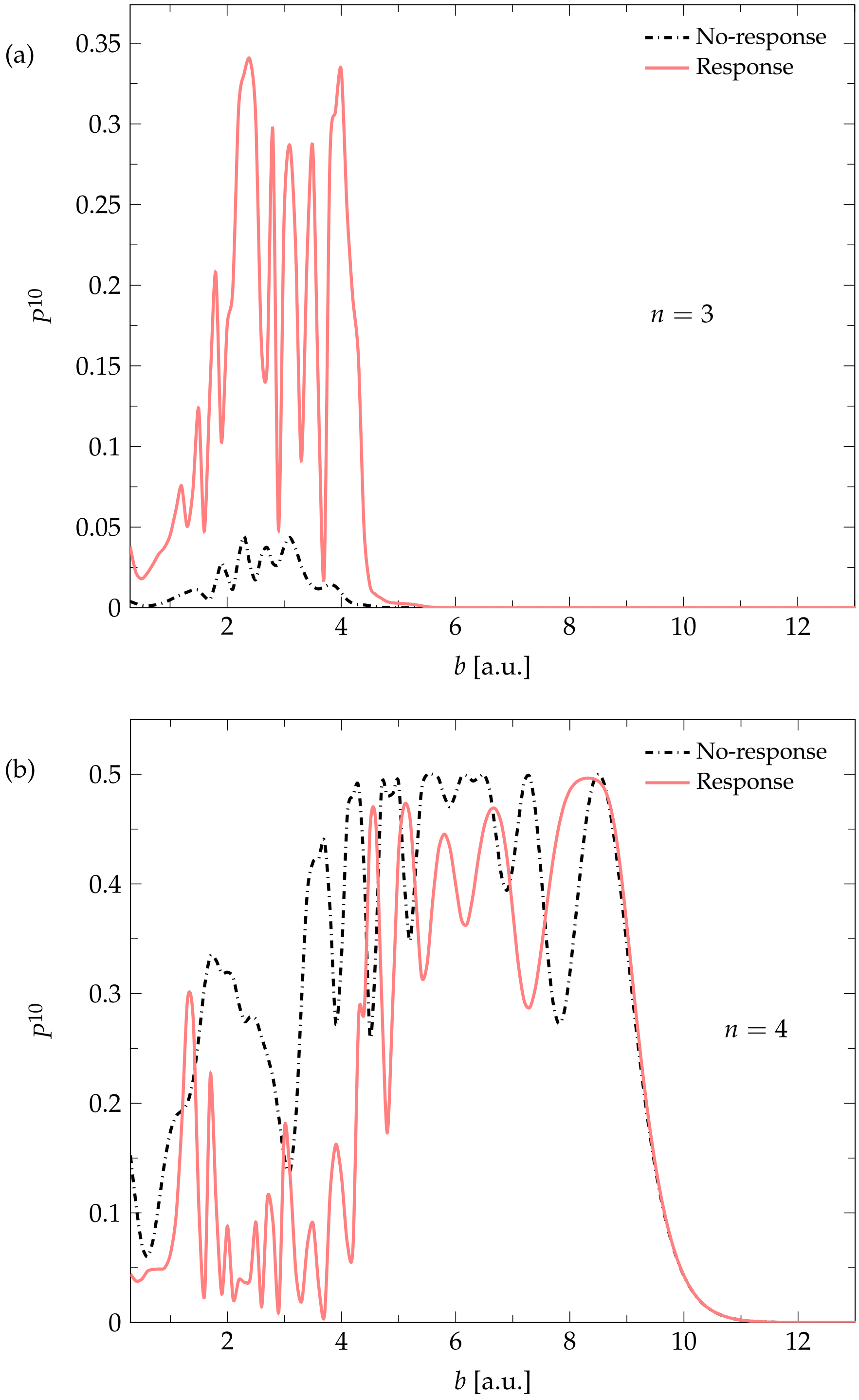

FIG. 5.8: TC-BGM pure SEC probabilities plotted with respect to impact parameter for C^{6+}-H_2 collisions at $E_P = 1$ keV/u. Capture probabilities for: (a) $n = 3$, and; (b) $n = 4$.

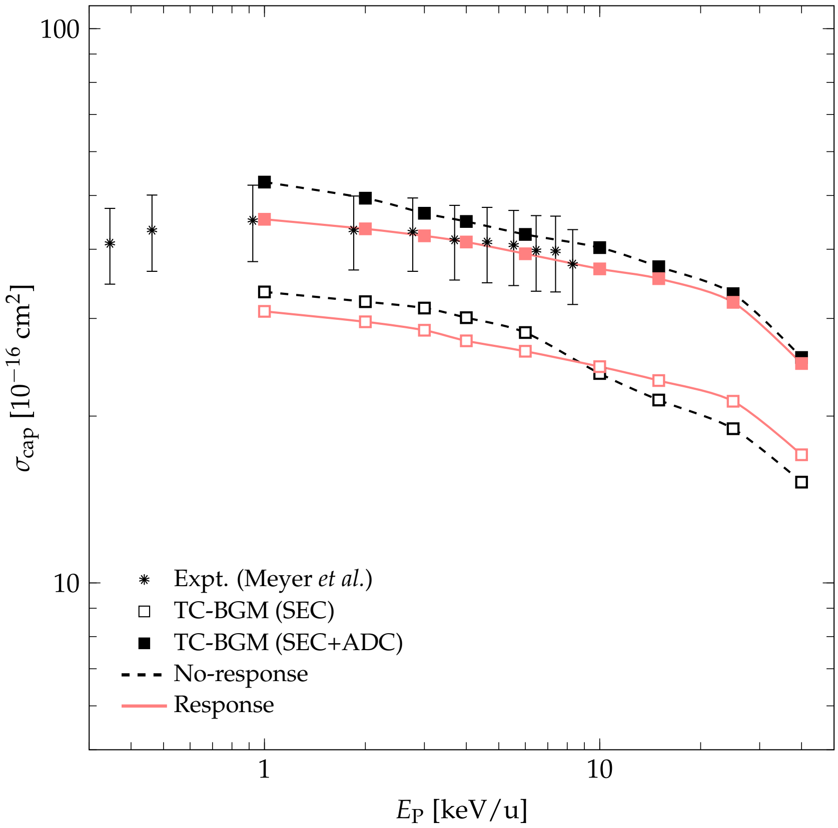

FIG. 5.9: Total SEC cross section plotted with respect to impact energy for C^{6+}-H_2 collisions. Calculated SEC values are from the present TC-BGM. Experimental total SEC values from Meyer *et al.* [123].

and Fig. 5.9 were, in fact, performed within the IEM.

The applicability of the multinomial analysis (3.32) to describe DEC for H_2 targets can be understood using the same argument relating to ionization potentials of the target as used for He. For H_2, the effective potential (5.2) used in the present calculation yields an energy eigenvalue of -0.60 a.u., whose magnitude is close to the accepted first ionization potential of 0.57 a.u. [103, 124]. In the perspective of the multinomial analysis, the total ionization energy is 1.2 a.u. which is close to the combined ionization energies of H_2 and H_2^+ (1.16 a.u.) [124]. This explains how calculations done using the multinomial analysis are more successful in describing DEC for H_2 than for helium. From this discussion and the comparisons made with previous results, there is enough confidence that the present ADC results can be considered further in the discussion.

Figure 5.10 shows the n-state relative capture distributions from the present calculations at impact energies 1, 6 and 25 keV/u. Not only does each plot compare the no-response and response results but also how the pure SEC distributions differ from the combined SEC+ADC distributions. Looking at the pure SEC distribution, it is found that $n = 4$ is the dominant capture state, which is consistent with the CBM. The distributions also show the population broadening as impact energy increases.

Adding contributions from ADC results in an increase of the $n = 2$ and $n = 3$ populations. In the correlation experiment by Mack *et al.* [125], results suggested that the principle double-capture states are of the form $3lnl'$ and $4lnl'$ with capture from the former being dominant. By the Auger analysis, this then suggests that there would only be substantial increase in the $2l$ state and that increase in the $3l$ state would be very minor. The magnitude of these changes is unclear and the only qualitative guide is from Hoekstra *et al.* [89] who suggested that, for example at 4.6 keV/u, the ADC cross section populating $n = 3$ is less than 1×10^{-16} cm^2. Based on the results of Table 5.2, this suggests that less than 10% of ADC contributes to the $n = 3$ population. The present results at 4 keV/u show a somewhat larger contribution of 38% and 22% from the no-response and target-response calculation, respectively. These discrepancies of the present results can be attributed to, as discussed previously, the fundamental problem of the IEM.

Examining the cross sections in further detail, Fig. 5.11 shows the nl-relative distribution at 1, 6, and 25 keV/u. Similar to Fig. 5.10, results of pure SEC and the combined SEC+ADC results are compared. However, this is only applicable for the $3l$-distributions. Absolute pure SEC cross section for the $2l$ states are omitted since they

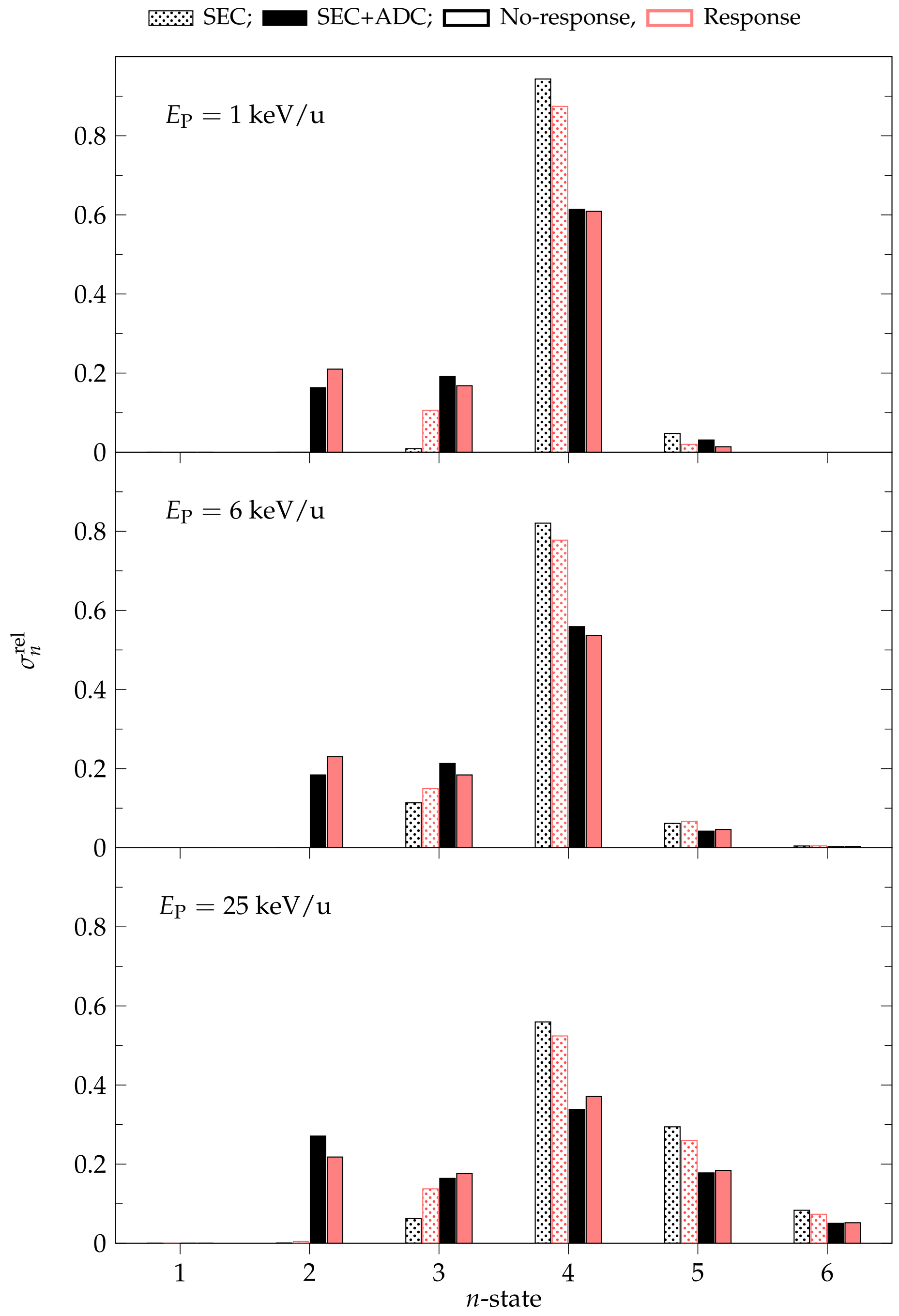

FIG. 5.10: n-state relative SEC cross sections for C^{6+}-H_2 collisions at $E_P = 1, 6$, and 25 keV/u.

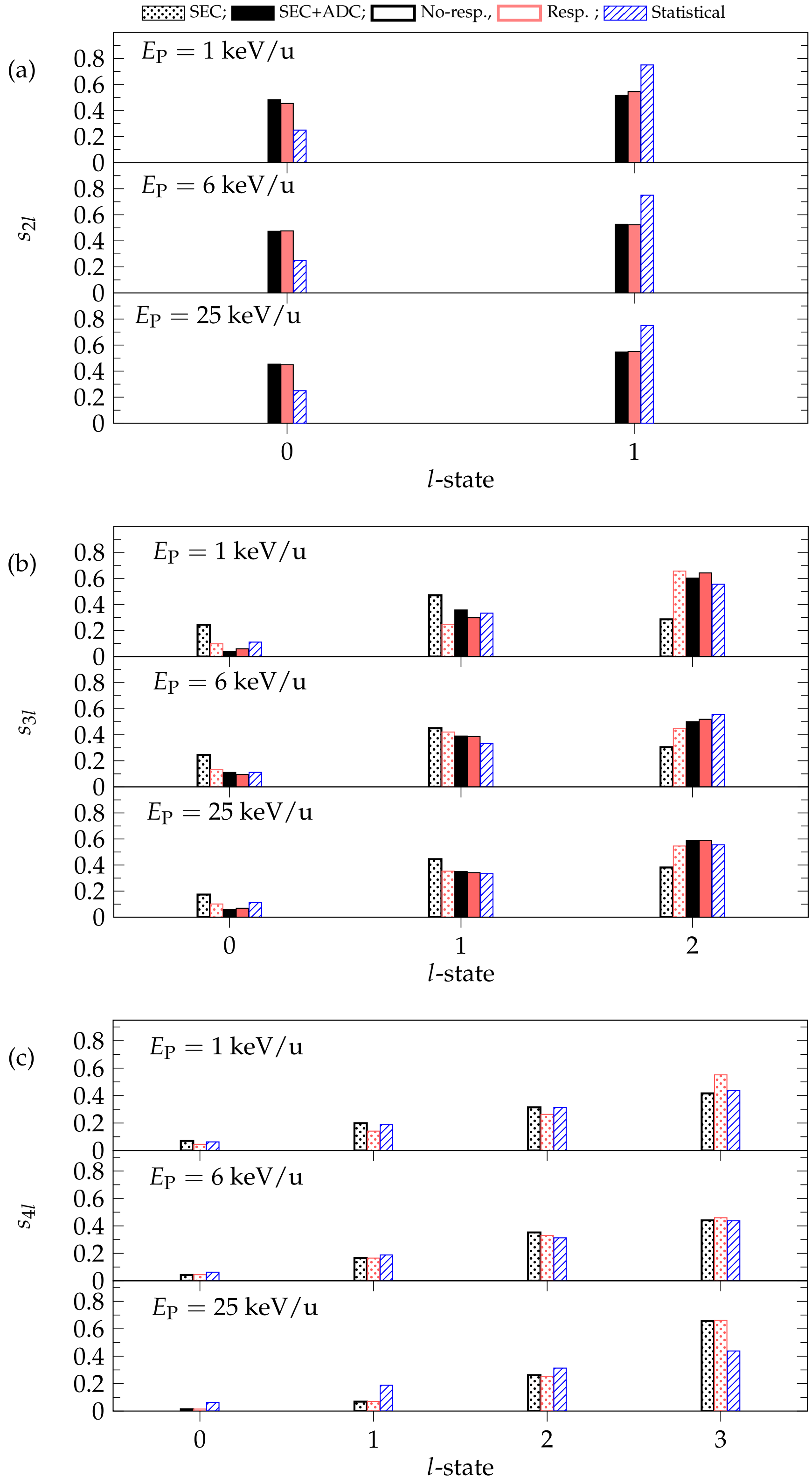

FIG. 5.11: nl relative SEC cross sections for C^{6+}-H_2 collisions at 1, 6, and 25 keV/u. Distributions correspond to (a) $n = 2$; (b) $n = 3$; (c) $n = 4$.

were found to be negligible (cf. Fig. 5.10), and thus, they serve no meaningful purpose for this comparison. Similarly, contributions from ADC into $n = 4$ were found to be negligible and so it suffices to show only pure SEC distributions for this shell. The complete list of the absolute pure SEC and ADC cross sections for the dominant capture nl states can be found in Appendix B..

In the CTMC analysis by Fogle *et al.* [25], it was deduced from their Lyman emission measurements that the statistical distribution (4.3) was the most suitable in describing the nl-distributions at energies below 25 keV/u. The present results support this except for the $2l$ states [Fig. 5.11(a)] which appear to be evenly populated instead. Moreover, the SEC+ADC profile of the $2l$ and $3l$ relative distributions exhibit minor changes as impact energy increases. For the $4l$ states, pure SEC into the maximum l-state becomes more dominant (i.e., over-statistical) as impact energy increases. Comparing the no-response and response calculations, the $3l$ and $4l$ pure SEC distributions are noticeably different at low energies but becomes similar at higher energies. As for SEC+ADC cross sections, the distributions produced from these two calculations are overall similar.

5.4.2 Lyman line-emission ratios

The present Lyman line emission ratios are shown in Fig. 5.12 alongside with CTMC and experimental ratios by Fogle *et al.* [25]. The label 'Pure SEC' only applies to the calculated ratios. The experimental ratios include both pure SEC and contributions from ADC [25].

Focusing on the present SEC+ADC line emission ratios, both no-response and the response results have very similar profiles as the experimental ratios. Between 1 and 6 keV/u, the no-response ratios are slightly larger than the response ratios. This is mostly because, at these energies, the response calculation predicts stronger capture in the maximum l-state than the no-response approximation (Fig. 5.11), which results in greater Ly-α emissions by the yrast cascade. In a related note, the nl-distributions also indicate strong capture into the maximum l-state as impact energy increases which explains the decreasing behaviour of these ratios due to increase of Ly-α counts by the yrast cascade (4.5). While the response Ly-β/Ly-α ratios show good agreement with the experiment the Ly-γ/Ly-α ratios are somewhat underestimated. The discrepancies between CTMC and the present calculations are at least partially due to the reliance on the presupposed l-distributions that Fogle *et al.* [25] used to estimate the nl cap-

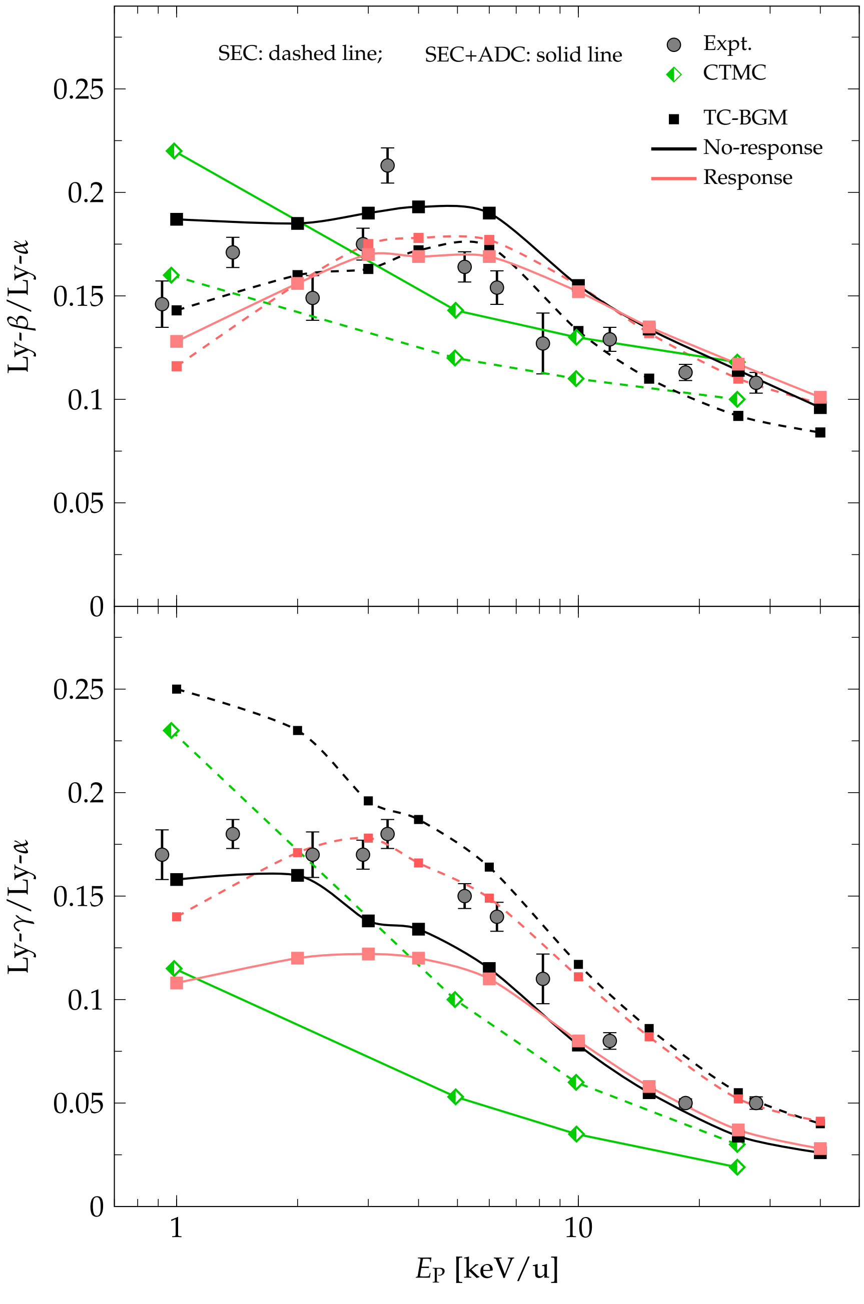

FIG. 5.12: Lyman line-emission ratios for C^{6+}-H_2 collisions from Fogle *et al.* [25] and present TC-BGM results: Ly-β/Ly-α ratios (top), and Ly-γ/Ly-α ratios (bottom). All calculated ratios which considered only pure SEC are shown with a dot-dashed line while those of SEC+ADC are shown with a solid line.

ture populations. Overall, the magnitude of the ratios from both present calculations appear to be more consistent with the experiment than CTMC.

By comparing the calculated ratios between SEC and the combined SEC+ADC processes, the present results for Ly-β/Ly-α do not differ significantly. The largest difference of approximately 0.04 can be seen from the no-response calculations at 1 keV/u. However, these differences are somewhat more pronounced in the Ly-γ/Ly-α ratios where a difference of about 0.1 is shown for the same calculation. Overall, by taking into account the uncertainties of the x-ray measurements due to polarization in addition to the reported experimental uncertainties, the present line-emission ratios are viewed as satisfactory.

5.5 CONCLUSIONS

In this analysis, Lyman line-emissions from C^{6+}-He and -H_2 collisions were examined for impact energies between 1 and 40 keV/u. Capture cross sections were obtained by solving the single-electron TDSEs and were used in the radiative cascade analysis. Several insights were gathered to understand the applicability of the TC-BGM performed within the IEM in describing radiative emissions in charge-exchange collisions involving two-electron targets over a range of impact energies in the low and intermediate energy regimes.

In the analysis of C^{6+}-He collisions, cross sections from pure SEC events were used in the radiative analysis. Results from previous studies which examined double-capture for this system [115, 116] suggest that contributions from ADC are negligible. Present results for Ly-β/Ly-α and Ly-γ/Ly-α ratios were found to be in satisfactory agreement with measurements by Defay *et al.* [57]. A brief analysis of double-capture for this system shows that cross sections produced from calculations using the IEM are grossly overestimated. This discrepancy can be alleviated if one perform calculations using the IEVM.

In the analysis of C^{6+}-H_2 collisions, a single-centre, spherical model potential was used to describe the molecular target in the single-electron TDSE calculations. From this approach, both SEC and ADC cross sections led to very good agreement with previous total SEC results by Meyer *et al.* [123] and Hoekstra *et al.* [89]. The result of using these cross sections for the radiative emission analysis showed satisfactory agreement with measurements of Fogle *et al.* [25]. Moreover, the present results showed that not all *nl*-populations strictly follow one particular *l*-distribution, which Fogle *et al.* [25] used in their CTMC calculations that may have resulted in certain discrepancies with the measured data. All of these results have demonstrated the applicability and reliability of the model potential approach for describing electron capture and the subsequent radiative decay process in collisions with H_2.

CHAPTER 6

O^{6+} collisions with argon, water, and methane

This chapter has been adapted from:

A. C. K. Leung and T. Kirchner, Radiative-emission analysis in charge-exchange collisions of O^{6+} with argon, water, and methane, Phys. Rev. A **95**, 042703 (2017).

6.1 OVERVIEW AND BACKGROUND

This chapter focuses on the charge-exchange analysis by Machacek *et al.* [59] where collisions of O^{6+} with Ar, H_2O, CH_4, and several other diatomic and triatomic molecules[1] were examined. In the context of radiative emissions in astrophysical settings, the O^{6+} ion is the most abundant solar wind heavy-ion [5, 126] while species of Ar, H_2O, and CH_4 are abundant in cometary coma and planetary atmospheres [59, 126].

The study by Machacek *et al.* [59] measured total capture cross sections from SEC, DEC, and TEC. For SEC, because the first ionization energy of Ar (0.58 a.u.) is rather close to that of H_2O (0.46 a.u.) and CH_4 (0.46 a.u.) [103], it is expected by the CBM that the main capture channel of the projectile is identical for all these targets (i.e., $n = 4$). Moreover, the sequential ionization potentials for Ar compared to these molecules are similar as well [59]. Because of this, Ar makes a reasonable "surrogate" for these molecules. For this analysis, one can then hypothesize that the SEC, DEC, and TEC cross sections would be similar across these targets. Furthermore, CTMC calculations of these cross sections were also carried out by Machacek *et al.* [59] and compared with the measurements. Results of CTMC calculations on radiative emissions from SEC in these collision systems were also reported.

---

[1] These include molecules of N_2, CO, CO_2, N_2O, and NO.

The analysis reported by Machacek *et al.* [59] revealed satisfactory agreement between CTMC calculations and measurements for total SEC and DEC cross sections. However, comparisons of TEC cross sections showed that CTMC results are underestimated by an order of magnitude. Not much can be said in regards to the radiative spectra produced from CTMC since measurements were not made. This presents an incentive to examine this series of collision problems, especially those involving complex molecules, using the TC-BGM.

6.2 SETUP OF THE PROBLEM

The present collision problem involves a highly-charged O^{6+} projectile ion scattering from Ar, H_2O, and CH_4 at impact energies of 1.17 and 2.33 keV/u. Results from the present calculations are mainly compared with Machacek *et al.* [59].

In the IEM framework, the interaction with the O^{6+} projectile in the single-electron Hamiltonian is represented by the model potential [70]

$$V_{O^{6+}}(r_P) = -\frac{6}{r_P} - \frac{2}{r_P}\exp\left(-2\alpha r_P\right)(1 + 2\alpha r_P + 2\alpha^2 r_P^2), \tag{6.1}$$

where r_P is the distance to the projectile core. The optimized value α was determined to be 8.4 [70]. As for the targets, the effective potential for Ar is identical to the one used in Ch. 4 and the present treatment of the molecular targets of H_2O and CH_4 has already been discussed in Sec. 3.4. The basis set used in this analysis includes all nlm states from $n = 2$ to $n = 6$ on the O^{5+} projectile, all states in the LMN shells of Ar, all states of the KLM shells of the atomic oxygen for H_2O and atomic carbon for CH_4, and a set of TC-BGM pseudeostates. Table 6.1 lists the BGM hierarchy used for this analysis.

An important part of this analysis is the calculation of total SEC, DEC, and TEC cross sections. The measurements by Machacek *et al.* [59] include contributions from higher multiple-capture events which undergo autoionization. The CTMC calculations reported by Machacek *et al.* [59] include these contributions up to sixfold capture. While the Auger analysis of DEC is feasible with the first-principles approach that was discussed in Sec. 3.6, inclusion of higher-multiple-capture events can lead to an exceedingly large rate matrix and large number of equations. In such a situation, one needs to resort to an alternative approach.

TABLE 6.1: BGM hierarchy used in present calculations for O^{6+}-Ar, -H_2O, and -CH_4 collisions. The hierarchy applies to 1.17 and 2.33 keV/u impact energies.

State	1*s*	2*s*	2*p*	3*s*	3*p*	3*d*	4*s*	4*p*	4*d*	4*f*
Target: Ar										
M_ν:	–	1	1	1	1	1	1	1	2	2
Target: atomic oxygen (for H_2O)										
M_ν:	0	0	1	1	1	1	–	–	–	–
Target: atomic carbon (for CH_4)										
M_ν:	0	0	1	1	1	1	–	–	–	–

6.2.1 *ad hoc* treatment of Auger dynamics

Calculations of apparent capture cross sections can be difficult to manage when the number of multiply-excited configurations is large. For this reason, an *ad hoc* Auger decay scheme was proposed by Ali *et al.* [91] to handle such calculations. This decay scheme is based on the cumulative knowledge available from studies of doubly-excited states and energy analyses of multiply-excited states. It consists of a simple set of criteria to determine the final configuration before undergoing radiative decay. These criteria are summarized as follows but the reader should refer to Ref. [91] for more details:

1. Only two-electron Auger processes are allowed.

2. For Auger decay to occur, the following condition must be met: $n_2 < 2n_1$, where n_2 is the energy state with a lower binding energy and n_1 is the energy state with a higher binding energy. Each Auger transition undergoes the nearest energetically allowed continuum limit with unit probability. The bound electrons are assumed to be hydrogen-like, and thus, final energy levels are determined by the Rydberg formula.

3. If more than one transition is allowed, they proceed in the following manner: (i) Electrons in the same shell interact first. (ii) If more than one shell holds two electrons, electrons in the shell with the higher binding energy interact first. (iii) If more than one transition with electrons in different shells is possible, then electrons with the smaller $\Delta n = n_2 - n_1$ (i.e., difference in n quantum numbers)

interact first. (iv) If more than one transition between electrons with the same Δn is possible, then electrons with the smaller *binding energy* difference interact first.

4. Each transition stated in Rule #3 gives rise to a new configuration and all above rules apply again. If the condition stated in Rule #2 is no longer met, the Auger process ends.

As a simple example, consider one electron captured into the $n = 3$ shell and two electrons into $n = 5$. The Auger transitions based on the rules above are illustrated in a simple energy diagram in Fig. 6.1 where transitions occur in the order from left to right. This particular example illustrates apparent single-capture since only one electron remains after the Auger process.

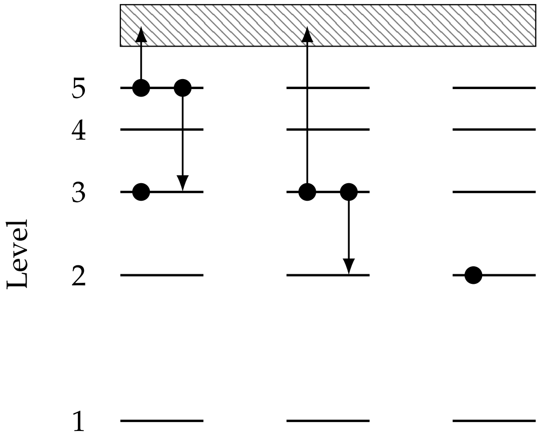

FIG. 6.1: Example illustrating the *ad hoc* Auger decay scheme. Transitions occur in the order from left to right. The cross-hatched box represents the continuum regime.

For cross section calculation using this Auger decay scheme in the IEM, one first calculates $P_{k_1,\ldots,k_M}$ [53] where

$$P_{k_1,\ldots,k_M} = \binom{K}{k_1 + \ldots + k_M}\binom{k_1 + \ldots + k_M}{k_1 + \ldots + k_{M-1}} \ldots \binom{k_1 + k_2}{k_1} (p_1)^{k_1} \ldots (p_M)^{k_M} (\bar{p})^{\bar{K}} \quad (6.2)$$

with

$$\bar{p} = 1 - \sum_n p_n, \quad (6.3)$$

$$\bar{K} = K - k_1 - k_2 - \ldots - k_M \quad (6.4)$$

is the probability of finding k_1 electrons captured in the $n = 1$ state of the projectile, k_2 electrons captured in the $n = 2$ state, and so forth up to the M-th state. The capture probabilities p_n are averaged over the initially occupied shells of the target. The parameter K is the number of active electrons in the target and k_n is the number of electrons captured into the n-th state of the projectile. Note that in this study, the lowest O^{6+} state that an electron can be captured into is the $n = 2$ state, and thus, one instead calculates $P_{k_2,\ldots,k_M}$. After performing this multinomial analysis, the corresponding cross section can be calculated in the usual manner (3.31).

One downside of this *ad hoc* Auger decay scheme is that any information on the angular momentum l-distribution is lost due to the summation of nlm probabilities over m and l states for Eq. (6.2). This information is essential for the radiative cascade analysis. It is possible to reinstate this information using presupposed distributions such as the statistical (4.3) or the separable (4.4) model, as it was done in Ref. [53]. However, it would be impossible to assess the TC-BGM in terms of how well it predicts the l-distributions, which is one of the main objectives in this work. As it turns out from the total capture cross section analysis (to be discussed in the next section), the main contributor to apparent SEC is double-capture and contributions from higher-multiple capture events can be safely neglected. In other words, the use of a presupposed l-distribution is not needed for the radiative cascade analysis since the first principles method is feasible in this situation.

6.3 CAPTURE CROSS SECTIONS

6.3.1 Preliminary results and the closure approximation

The initial results from the present molecular collision calculations based on the method outlined in Sec. 3.4 showed substantial differences from previous experimental data. For instance at $E_{\mathrm{P}} = 1.17$ keV/u, the total pure SEC cross section from collisions with H_2O was 69.3×10^{-16} cm^2, which is larger than the measurement by Machacek *et al.* [59] of $(49.8 \pm 3.4) \times 10^{-16}$ cm^2 which includes autoionizing multiple-capture events. A similar discrepancy with Machacek *et al.* [59] was also found for results of CH_4 collisions. Clearly if contributions from autoionizing multiple-capture were included the discrepancy would be even larger. Furthermore, Bodewits and Hoekstra [127] carried out a photon emission spectroscopy experiment for O^{6+}-H_2O collisions where a pure SEC cross section of $(28 \pm 1.6) \times 10^{-16}$ cm^2 at 1.31 keV/u was obtained. The initial TC-BGM results showed that the main capture channel is $n = 5$, which is inconsistent with Bodewits and Hoekstra [127] where this channel was found to be $n = 4$. It is clear from these comparisons that the TC-BGM capture cross sections for molecular collisions are not reliable for O^{6+} projectiles.

Recall in Sec. 3.4 that the present treatment of molecular collisions makes use of the spectral representation of the molecular Hamiltonian $\hat{h}^{\mathrm{MO}}_{\alpha\beta\gamma}$ (3.18). In practice, this representation of $\hat{h}^{\mathrm{MO}}_{\alpha\beta\gamma}$ is limited to the initially occupied MOs, which means that contributions from excited and continuum states are neglected. It was suspected that the neglect of these states led to the above discrepancies. One approach to include these contributions approximately is by a closure approximation. Starting from the general spectral representation of $\hat{h}^{\mathrm{MO}}_{\alpha\beta\gamma}$ containing all states,

$$\hat{h}^{\mathrm{MO}}_{\alpha\beta\gamma} = \sum_{\Lambda}^{\text{all states}} \epsilon_\Lambda \left|\Lambda_{\alpha\beta\gamma}\right\rangle \left\langle\Lambda_{\alpha\beta\gamma}\right| , \tag{6.5}$$

the summation on the rhs of Eq. (6.5) can be separated into two parts where one represents all occupied states and the other unoccupied states

$$\hat{h}^{\mathrm{MO}}_{\alpha\beta\gamma} = \sum_{\Lambda}^{\text{occupied}} \epsilon_\Lambda \left|\Lambda_{\alpha\beta\gamma}\right\rangle \left\langle\Lambda_{\alpha\beta\gamma}\right| + \sum_{\Lambda}^{\text{unoccupied}} \epsilon_\Lambda \left|\Lambda_{\alpha\beta\gamma}\right\rangle \left\langle\Lambda_{\alpha\beta\gamma}\right| . \tag{6.6}$$

A closure approximation on the second term leads to

$$\begin{aligned} \hat{h}^{\mathrm{MO}}_{\alpha\beta\gamma} &\approx \sum_{\Lambda}^{\text{occupied}} \epsilon_\Lambda \left|\Lambda_{\alpha\beta\gamma}\right\rangle \left\langle\Lambda_{\alpha\beta\gamma}\right| + \bar{\epsilon} \sum_{\Lambda}^{\text{unoccupied}} \left|\Lambda_{\alpha\beta\gamma}\right\rangle \left\langle\Lambda_{\alpha\beta\gamma}\right| \\ &= \sum_{\Lambda}^{\text{occupied}} \epsilon_\Lambda \left|\Lambda_{\alpha\beta\gamma}\right\rangle \left\langle\Lambda_{\alpha\beta\gamma}\right| + \bar{\epsilon} \left(\hat{1} - \sum_{\Lambda}^{\text{occupied}} \left|\Lambda_{\alpha\beta\gamma}\right\rangle \left\langle\Lambda_{\alpha\beta\gamma}\right| \right) , \end{aligned}$$

where $\bar{\epsilon}$ can be viewed as the average energy representing the unoccupied states. After simplifying the above equation the following is obtained

$$\boxed{\hat{h}^{\mathrm{MO}}_{\alpha\beta\gamma} \approx \sum_{\Lambda}^{\text{occupied}} \left(\epsilon_\Lambda - \bar{\epsilon}\right) \left|\Lambda_{\alpha\beta\gamma}\right\rangle \left\langle\Lambda_{\alpha\beta\gamma}\right| + \bar{\epsilon}. \qquad (6.7)}$$

In this way, the unoccupied states are included in a global fashion without introducing additional burden in the computations (e.g., additional basis states). The choice of $\bar{\epsilon}$ is discussed in the following.

The natural starting point of $\bar{\epsilon}$ in Eq. (6.7) is $\bar{\epsilon} = 0$, but this is simply equivalent to carrying out collision calculations without the closure approximation using a minimal-basis set. Varying $\bar{\epsilon}$ in Eq. (6.7) led to changes in the capture cross sections for the two molecular targets. It was found that using a negative $\bar{\epsilon}$ resulted in cross sections that showed no improvements. However, using a small positive $\bar{\epsilon}$ resulted in changes to both the magnitude and distribution of capture cross sections that eventually led to results that are comparable to previous results [59, 127]. Figure 6.2 demonstrates how the pure SEC cross section changes with respect to increasing $\bar{\epsilon}$ from zero for O^{6+}-H_2O and -CH_4 collisions at 1.17 keV/u. The plot shows a minimum at $\bar{\epsilon} \approx 0.15$ for H_2O and $\bar{\epsilon} \approx 0.1$ for CH_4 [2]. Note that these minima also occur around the same $\bar{\epsilon}$ in each respective molecule at 2.33 keV/u.

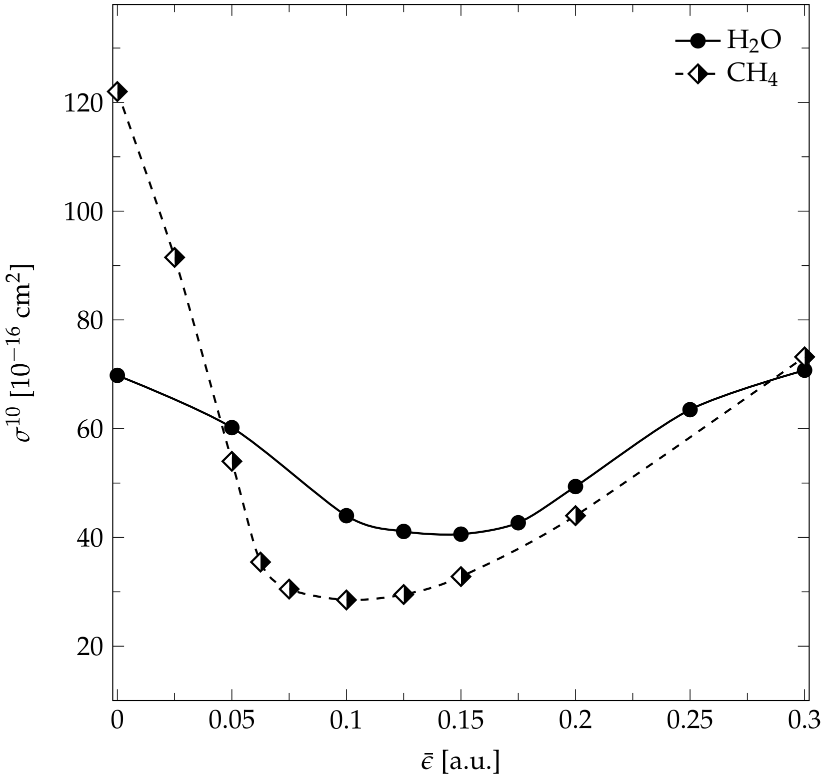

FIG. 6.2: Orientation-averaged pure SEC cross sections of O^{6+}-H_2O and -CH_4 collisions plotted with respect to the average energy of the unoccupied states $\bar{\epsilon}$. Calculations are for $E_P = 1.17$ keV/u.

---

[2] In the original publication of this analysis [56], the minimum for CH_4 was stated to be $\bar{\epsilon} \approx 0.125$. Upon revisiting these calculations for this dissertation, it was found that BGM pseudostates can be included in the L shell, which resulted in slightly different cross sections and thus, a different estimation of the optimal $\bar{\epsilon}$. Although additional pseudostates can also be added for H_2O calculations, this has no significant changes to the cross sections and the optimal $\bar{\epsilon}$ remains the same as in Ref. [58]. It is also important to note that this has no appreciable impact ($< 5\%$) on the radiative spectra results.

Further analysis of varying $\bar{\epsilon}$ reveals how the n-state capture probabilities are affected. This is illustrated using the O^{6+}-H_2O collision system as an example since similar tendencies were also seen for CH_4 collisions. For this analysis, the present basis set had to be extended by including all nlm states in the $n = 7$ and $n = 8$ shells of the projectile. Table 6.2 lists the n-state cross section distributions for various $\bar{\epsilon}$. Starting from $\bar{\epsilon} = 0$, the dominant capture channel is $n = 5$ as mentioned earlier. By setting $\bar{\epsilon} = -0.3$, calculations resulted in a larger total cross section compared to $\bar{\epsilon} = 0$ with the capture population peaking in the $n = 6$ state. Setting $\bar{\epsilon} = 0.15$, the dominant capture state has shifted into a lower energy state of $n = 4$ with a total pure SEC cross section of 39.03×10^{-16} cm^2, which is much closer to the measurements of Bodewits and Hoekstra [127]. Although this dominant capture state remains the same at a larger $\bar{\epsilon}$ of 0.3, the total cross section is overestimated when compared with Bodewits and Hoekstra [127]. In a different view, Figure 6.3 shows the n-state pure SEC impact-parameter profiles at various $\bar{\epsilon}$ from 0 to 0.25. Based on Table 6.2, only capture profiles into $n = 4$ and $n = 5$ of the projectile are shown in Fig. 6.3. These plots illustrate how capture is either enhanced or suppressed due to changes of $\bar{\epsilon}$.

TABLE 6.2: Orientation-averaged n-state pure SEC cross sections (in 10^{-16} cm^2) from O^{6+}-H_2O collisions at $E_P = 1.17$ keV/u.

	$\bar{\epsilon}$			
n state	-0.3	0.0	0.15	0.3
2	<0.001	<0.001	<0.001	<0.001
3	0.001	0.24	2.46	10.79
4	1.25	16.18	35.76	59.64
5	11.88	51.00	0.73	0.01
6	50.01	0.95	0.04	0.06
7	40.89	0.12	0.02	0.04
8	22.83	0.85	0.02	0.09
Total	126.86	69.34	39.03	70.63

From the perspective of sensitivity analysis, $\bar{\epsilon}$ in Eq. (6.7) is viewed as a 'perturbative' parameter in the present numerical problem. This means that a poor choice of $\bar{\epsilon}$ in the model can yield results that are significantly different from the expected solution. Therefore the $\bar{\epsilon}$ at the minimum (Fig. 6.2) would be the natural choice for the optimal solution since small changes of this parameter around this region do not seem to affect the solution significantly. In other words, the solution is the least sensitive to

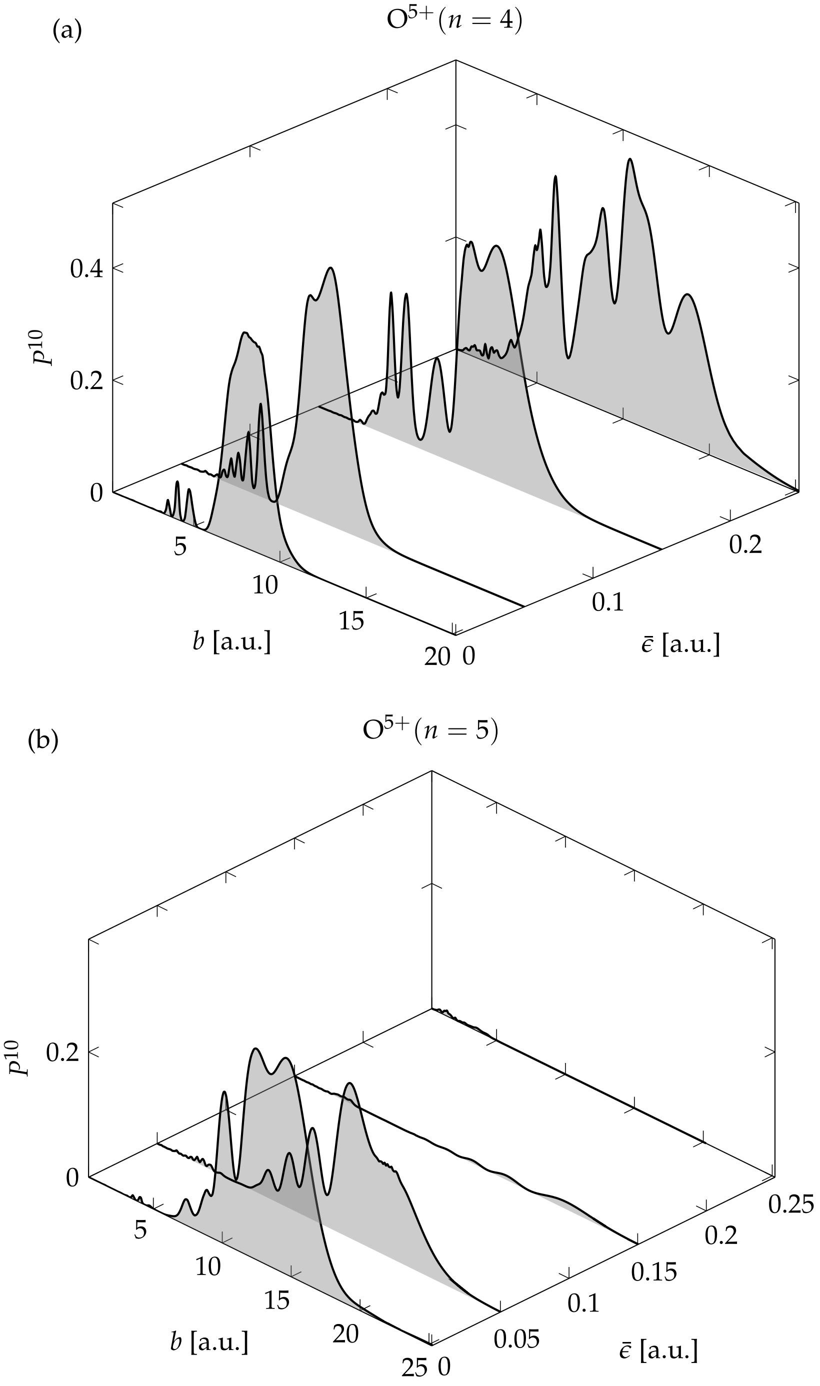

FIG. 6.3: Orientation-averaged pure SEC probabilities plotted with respect to impact parameter and $\bar{\epsilon}$ for O^{6+}-H$_2$O collisions at $E_P = 1.17$ keV/u. Capture probabilities for: (a) $n = 4$, and; (b) $n = 5$.

this particular choice and this was confirmed in the above analysis in which both the total cross section and the corresponding n-state capture distribution do not change significantly. However, it is uncertain whether such a stabilization occurs in another neighbourhood of $\bar{\epsilon}$ since the present method is limited to the interval that is presented in Fig. 6.2. On the other hand, Table 6.2 suggests that the use of any other $\bar{\epsilon}$ outside this interval would produce an n-distribution that is inconsistent with experimental observations [59, 127]. Therefore, the optimal $\bar{\epsilon}$ in Fig. 6.2 is the only choice that is suitable for this problem. From here on, the discussion on the final capture cross sections from collisions with molecular targets is based on results obtained using the optimal $\bar{\epsilon}$ in the closure approximation (6.7).

6.3.2 Total single-, double-, and triple-capture results

Figures 6.4 and 6.5 display the pure SEC probability profiles plotted with respect to the impact parameter at an impact energy of 1.17 and 2.33 keV/u, respectively. Only capture probabilities into $O^{5+}(n = 4)$ are shown since capture into any other states is negligible in comparison. Starting with Ar collisions, there is considerable enhancement in capture between $b = 5$ and $b = 8$ produced from the target-response calculation compared to the no-response results. This observation is somewhat different from what was seen in previous chapters where the enhancement by the response model usually applies to the subdominant capture channels.

For H_2O collisions, there are some similarities in the probability profiles between the two orientations before they deviate considerably for $b > 10$. Recall that when the H_2O molecule is at the $(0, 0, 0)$ orientation, the two hydrogen atoms lie in the scattering plane whereas these atoms are in the azimuthal plane when the molecule is at the $(90, 0, 0)$ orientation. This would then explain the large capture profile for the $(0, 0, 0)$ orientation at large impact parameters. Although the orientation averaging appears crude due to the substantial differences for $b > 10$, it turns out that one obtains a very similar averaged profile when all other possible orientation results are included. This is demonstrated in Appendix E..

Lastly for CH_4 collisions, the probability profiles for each different orientation appear very similar to each other. Given the geometry of this molecule and its orientations considered in this study, there are always two hydrogen atoms that lie in the scattering plane while the other two hydrogen atoms are mirror images with respect to

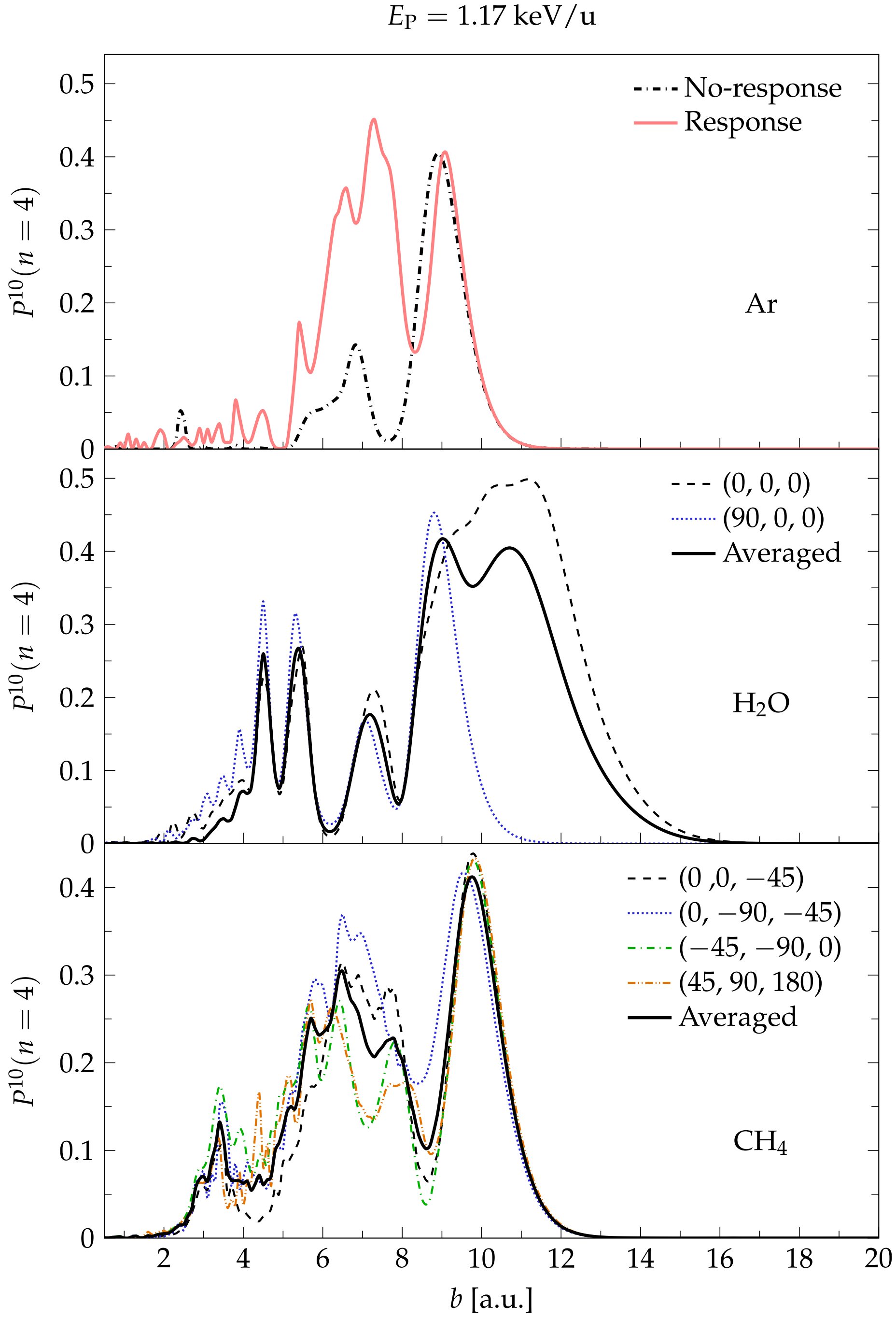

FIG. 6.4: TC-BGM pure SEC probabilities for $O^{5+}(n = 4)$ plotted with respect to the impact parameter at $E_P = 1.17$ keV/u. Calculations are for the following targets: (a) Ar, (b) H_2O, and (c) CH_4.

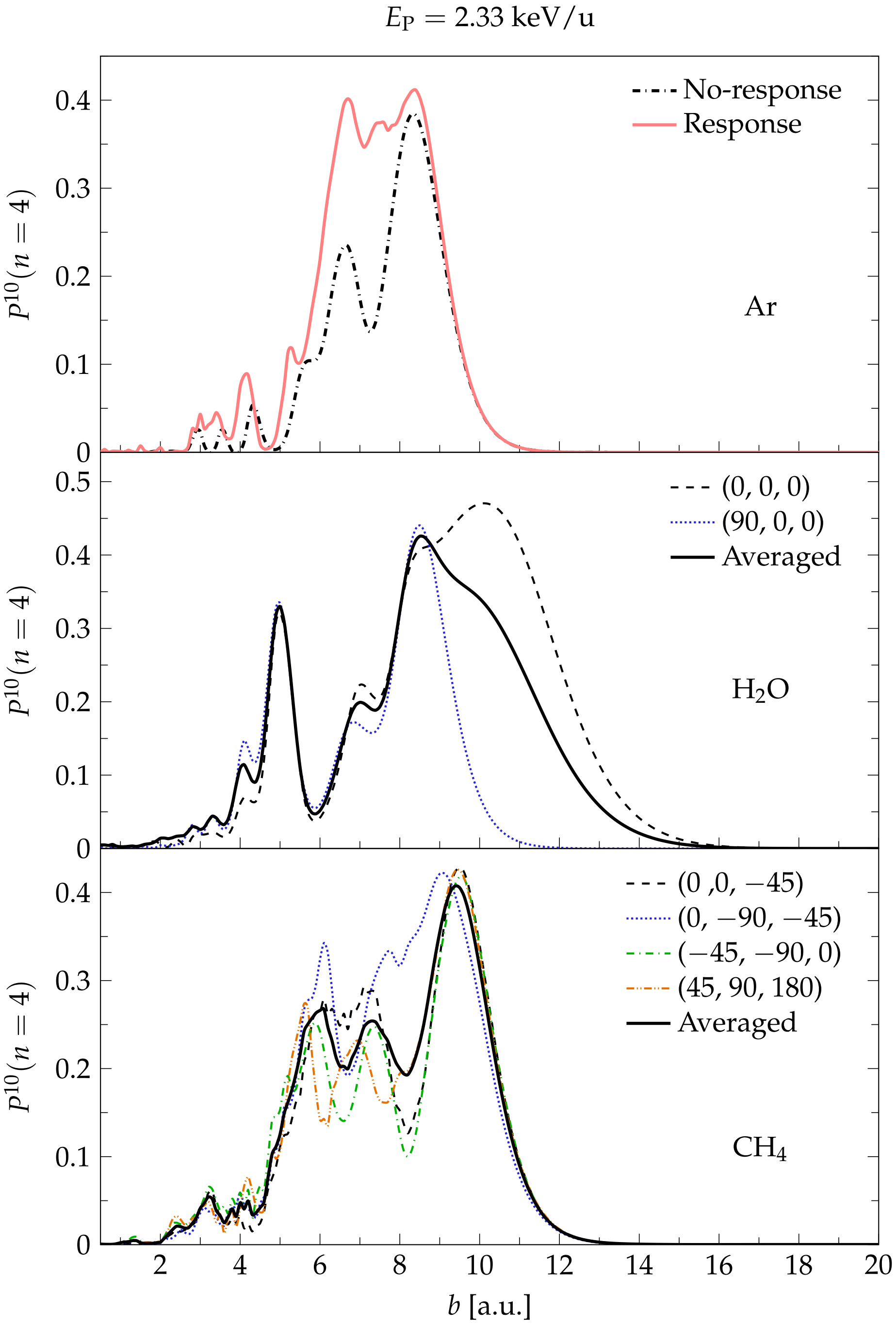

FIG. 6.5: Same as Fig. 6.4 but at $E_\mathrm{P} = 2.33$ keV/u

this plane (cf. Fig. 3.5). The symmetry of this molecule would mostly explain the similarities of these probability profiles of different orientation, more so than in collisions with H_2O.

Total capture cross sections for each collision system are listed in Table 6.3. These cross sections all include contributions from autoionizing multiple-capture events. In the table, the present results are compared with measurements and CTMC results by Machacek *et al.* [59].

TABLE 6.3: Total SEC, DEC, and TEC cross sections (in 10^{-16} cm^2) in O^{6+}-Ar, -H_2O, and -CH_4 collisions. Present TC-BGM results are shown alongside with experimental and CTMC results by Machacek *et al.* [59].

O^{6+}-Ar		TC-BGM			
E_P (keV/u)		No-response	Response	Expt. [59]	CTMC [59]
1.17	SEC	29.6	46.5	49.8 ± 3.4	59.0
	DEC	19.4	10.4	8.4 ± 0.6	5.44
	TEC	5.82	3.47	2.9 ± 0.2	0.126
2.33	SEC	30.3	44.5	46.5 ± 3.1	63.2
	DEC	17.1	8.76	7.1 ± 0.5	5.60
	TEC	6.32	2.64	2.2 ± 0.2	0.138

O^{6+}-H_2O				
E_P (keV/u)		TC-BGM	Expt. [59]	CTMC [59]
1.17	SEC	59.70	47.3 ± 3.2	55.0
	DEC	15.51	8.3 ± 0.6	6.30
	TEC	4.57	3.7 ± 0.3	0.580
2.33	SEC	58.1	45.9 ± 3.1	57.4
	DEC	12.9	7.4 ± 0.5	6.53
	TEC	3.18	2.6 ± 0.2	0.586

O^{6+}-CH_4				
E_P (keV/u)		TC-BGM	Expt. [59]	CTMC [59]
1.17	SEC	52.62	42.9 ± 2.9	54.2
	DEC	26.54	17.8 ± 1.3	6.76
	TEC	4.90	2.7 ± 0.2	0.659
2.33	SEC	50.72	50.2 ± 3.4	56.7
	DEC	22.90	16.3 ± 1.2	6.94
	TEC	4.12	2.3 ± 0.2	0.634

Starting with Ar collisions, the present total cross sections using the response model show very good agreement with the experimental results for both impact energies. In particular, the TEC cross sections show a much closer agreement with the experiment than the no-response and CTMC results. Although not all the present response results fall within the experimental uncertainty, the deviation from the experimental values are no larger than 30%.

For H_2O and CH_4 collisions, one can see the effectiveness of the closure approximation on the molecular-target Hamiltonian (6.7) in producing capture cross sections that are comparable with CTMC and measured results. In close examination, the present results are somewhat larger than the experimental values for all three capture events. This tendency is very similar to the Ar results, with the exception of SEC in the no-response approximation. This tendency could be due to a fundamental issue of the IEM of overestimating cross sections from high-multiplicity capture events, particularly if correlation is important. For instance in SEC, contributions from ADC events to the total SEC cross section can generally be from 10 to 25% [25, 59, 89, 101]. In the present calculations performed within the IEM, it was determined that this contribution is about 30 to 40%, a similar result that was also seen in Ch. 5 involving H_2 collisions. When all the calculated results are assessed, the agreement with the measurements is mixed. CTMC does well in predicting total DEC while the present TC-BGM is more reliable in describing total TEC. Overall though, the present TC-BGM results are consistent with the findings by Machacek *et al.* [59] in that the total capture cross sections do not vary significantly for different target species with similar ionization potentials as well as impact energies.

6.3.3 Partial single-capture cross sections

In this last section on capture cross sections, the focus now turns to the nl-partial cross sections. Because the main interest is in radiative emissions from initial states of $n = 3$ and $n = 4$, Table 6.4 lists only the $3l$ and $4l$ SEC cross section distributions where the former includes ADC contributions. The present post-collision analysis reveals that ADC mainly contributes to the single-capture population in the $n = 2$ and $n = 3$ states of O^{5+} while contributions to all other n-states were found to be negligible. A similar table listing the pure SEC $3l$ distributions is given in Appendix C. to illustrate the role of ADC.

One notable characteristic of the $4l$ cross sections in these collision systems is that there is a strong preference in capture in the lowest l-state (i.e., $l = 0$), which is an observation that is different as seen from previous chapters. Another aspect to this, which was noted earlier, is the enhancement in capture by the response model for Ar collisions. In previous chapters, it was shown that the response model would enhance capture in the maximum l-state whereas here, the enhancement is in the $l = 0$ state. Unlike collision systems discussed in previous chapters, those of the current chapter do not involve a bare projectile ion (i.e., O^{6+} is a dressed ion). Consequently, the energy degeneracy of the l-states is lifted where higher l-states have lower ionization energies than the $l = 0$ state. In the perspective of the CBM, this would explain a stronger preference of capturing into the $l = 0$ state since its corresponding binding energy is the closest match to the ionization potential of the target valence electron. This characteristic in collisions involving dressed projectiles (e.g., O^{6+}, N^{6+}) was also previously observed by others [101, 127] at similar impact energies.

TABLE 6.4: TC-BGM nl SEC cross sections (in 10^{-16} cm^2) for O^{6+}-Ar, -H_2O, and -CH_4 collisions. Results of $3l$ cross section include both pure SEC and ADC.

	Ar			
States (n, l)	No-response	Response	H_2O	CH_4
$E_P = 1.17$ keV/u				
3, 0	0.44	4.04	1.59	0.67
3, 1	0.99	2.54	1.17	1.86
3, 2	2.33	0.99	2.44	4.24
4, 0	6.29	16.3	16.13	6.87
4, 1	4.04	5.95	9.98	7.11
4, 2	1.44	2.13	2.93	3.04
4, 3	3.31	4.73	6.29	5.44

	Ar			
States (n, l)	No-response	Response	H_2O	CH_4
$E_P = 2.33$ keV/u				
3, 0	0.48	3.23	2.21	0.50
3, 1	0.91	1.48	1.54	2.19
3, 2	3.76	1.87	3.10	6.10
4, 0	6.20	8.56	10.2	6.02
4, 1	3.31	4.31	7.90	6.65
4, 2	2.20	2.71	5.41	4.22
4, 3	4.37	5.96	6.38	5.12

6.4 RADIATIVE SPECTRA

Figures 6.6 and 6.7 display the radiative-emission spectra due to total SEC (pure SEC and ADC) from the present TC-BGM and CTMC calculations [59] of all collision systems considered in this study. To compare present results with CTMC [59], the spectral counts from each set of calculations are normalized to unity. To aid this discussion, Fig. 6.8 shows the Grotrian diagram for the O^{5+} ion with all the transitions from Figs. 6.6 and 6.7 included.

By examining the radiative spectra for both impact energies, one sees that they exhibit similar features. For instance, the $3d \rightarrow 2p$ transition line has the largest count. The only exception to this observation is the present result from the response calculation for Ar at 1.17 keV/u [top panel of Fig 6.6]. Looking at the nl capture cross sections for target Ar in Table 6.4, the capture population for $3d$ is relatively small compared to $3s$ in the response calculation. On the other hand, we see the $3d \rightarrow 2p$ transition line is increased for 2.33 keV/u where capture is more probable at the maximum l state for both $n = 3$ and $n = 4$. This tendency was also seen in the measured spectra of Bodewits and Hoekstra [127] for O^{6+}-H_2O collisions.

Continuing with the discussion of the $3d \rightarrow 2p$ transition line, the CTMC results for this line are consistently larger than the present results. Because information of the nl partial cross sections were not reported by Machacek *et al.* [59] and given that no spectral measurements for these collision systems currently exist in the literature, it is difficult to assess these results. In this case, the spectral measurements by Miller *et al.* [14] are utilized to aid this assessment. It is important to note that these measurements are for O^{6+}-CO collisions at an impact energy of 2 keV/u.

Given that the CO molecule has a first ionization energy of 0.51 a.u., the CBM expectation is that the main capture channel is $O^{5+}(n = 4)$. Therefore, it is expected that the resulting spectra due to SEC would be similar to those shown in Fig. 6.7. From the measurements by Miller *et al.* [14], it was found that the normalized spectral count for the $3d \rightarrow 2p$ transition line is 0.43 ± 0.09. Note that Machacek *et al.* [59] have also performed CTMC calculations for the O^{6+}-CO system and their corresponding result for this line at 2.33 keV/u is approximately 0.5. The corresponding TC-BGM results of this line for Ar, H_2O, and CH_4 at 2.33 keV/u are 0.41, 0.28, and 0.38, respectively. If the emission spectra for the O^{6+}-CO collisions measured by Miller *et al.* [14] are a good representation for the three present targets, then this suggests that the spectral

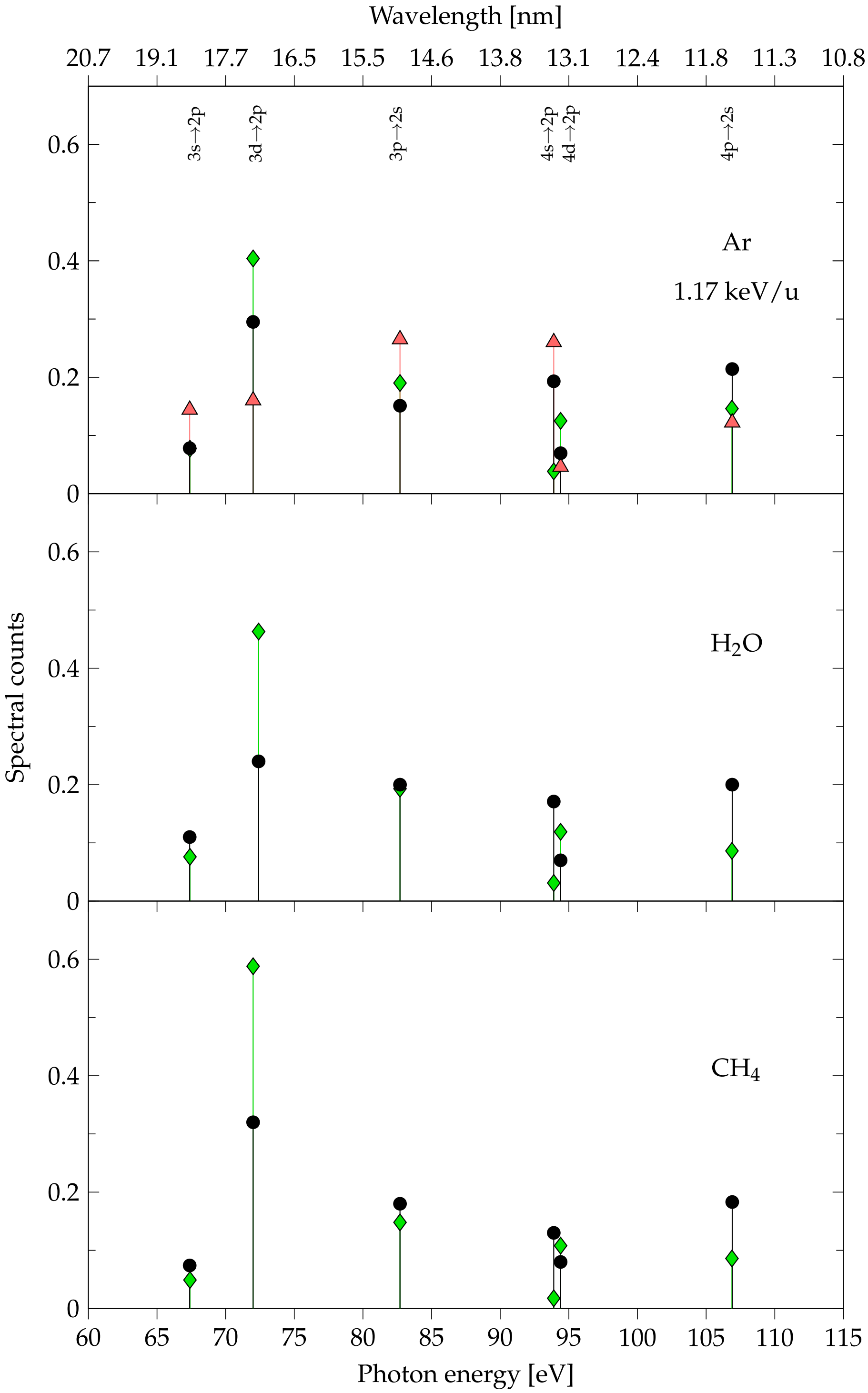

FIG. 6.6: Calculated radiative emission spectra for O^{6+}-Ar, -H_2O, and -CH_4 collisions at 1.17 keV/u. Calculations are CTMC [59] (◆), present TC-BGM in the no-response approximation (●), and TC-BGM in using the target-response model (▲). Note that the wavelength scale shown at the top of the group plot does not scale linearly.

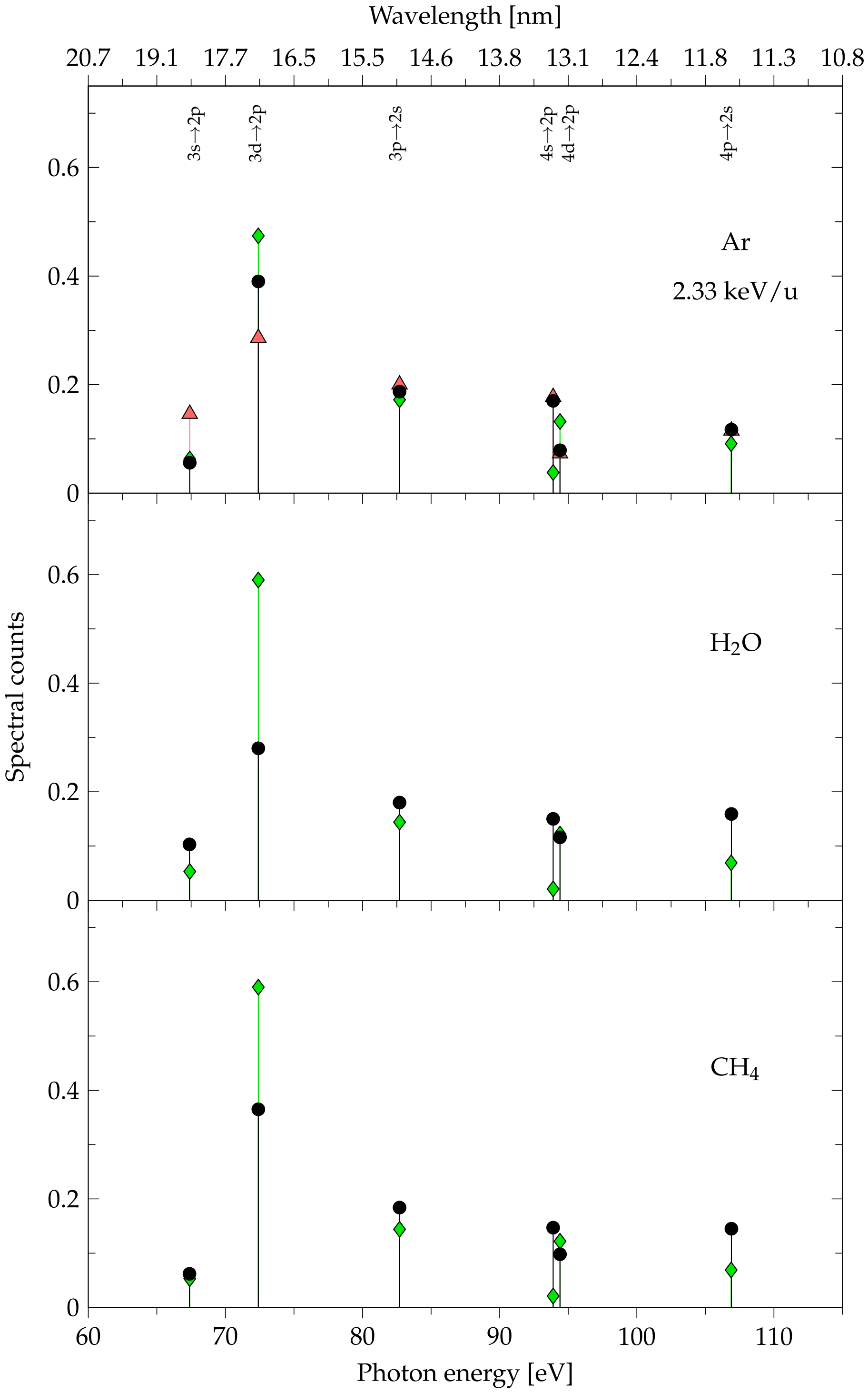

FIG. 6.7: Same as Fig. 6.6 but at $E_\mathrm{P} = 2.33$ keV/u.

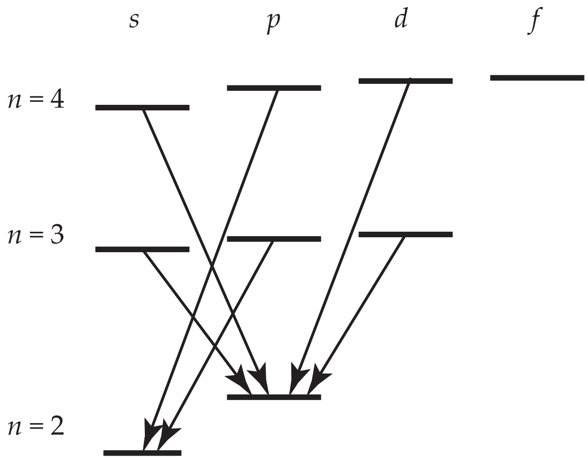

FIG. 6.8: Grotrian diagram for the O^{5+} ion. The arrows from one energy level to another indicate the radiative-decay transitions. The transitions shown in the diagram are those for which spectral counts are shown in Figs. 6.6 and 6.7. Energy widths are not to scale.

count for the $3d \rightarrow 2p$ transition in Ar and CH_4 collisions predicted by the TC-BGM is satisfactory while the spectral count for H_2O collisions is underestimated since it lies outside of the uncertainty range of the measurement. From the Grotrian diagram (Fig. 6.8), one can infer that the capture cross sections for $3d$ are underestimated by the TC-BGM. Since $4f$ can also contribute to this line in the cascade, it is possible that the cross section of $4f$ could be underestimated as well.

There are also other differences that one can spot in the radiative spectra. However, these discrepancies appear less prominent than those for the $3d \rightarrow 2p$ line. One can also carry out similar comparisons with the measurements by Miller *et al.* [14] for the other spectral lines and find that both TC-BGM and CTMC results are mostly within the uncertainty range. As Machacek *et al.* [59] suggested, however, a more appropriate confirmation of these predicted emission spectra would have to come from direct measurements. Nevertheless, the present TC-BGM analysis re-affirms the conclusion by Machacek *et al.* [59] that the total capture cross sections and corresponding emission spectra vary only slightly with the target species considered.

6.5 CONCLUSIONS

Radiative emissions in charge-exchange collisions of O^{6+} with Ar, H_2O, and CH_4 were presented in this chapter. The analysis focused on the two impact energies of 1.17 and

2.33 keV/u. The present TC-BGM results were mainly benchmarked with experimental and CTMC results by Machacek *et al.* [59]. This analysis also provides a first look on the applicability of the molecular TC-BGM in the low energy regime.

The present total electron-capture cross sections for Ar collisions obtained from the target-response model are in very good agreement with the measurements [59]. However, comparisons with Miller *et al.* [14] suggest that the corresponding radiative spectra may not be reliable, particularly at 1.17 keV/u. The present TC-BGM spectra using the no-response approximation, on the other hand, appear to be more consistent in predicting the emission abundances with CTMC and measurements by Miller *et al.* [14]. Furthermore, it was seen in previous TC-BGM analyses that the response model would enhance capture in the maximum l-state. However, that tendency was not seen in this analysis which is most likely due to the projectile involved here not being a bare ion.

For the molecular collision calculations using the TC-BGM, it was initially shown that capture cross sections were inconsistent with previous studies [59, 127]. Specifically, these results were (i) vastly overestimated and (ii) inconsistent in the main capture channel compared to previous studies [59, 127]. For these reasons, a closure approximation in the spectral representation of the molecular Hamiltonian was utilized and this led to more consistent results. With this technique, it was shown that it is possible, at least for H_2O and CH_4, to perform a quantum-mechanical analysis using the IEM TC-BGM for describing capture in slow ion-molecule collisions with satisfactory results.

CHAPTER 7

Collisions of O^{8+} and C^{6+} ions with hydrogen and krypton

---

7.1 OVERVIEW AND BACKGROUND

Following the work on x-ray emissions from C^{6+} collisions with He and H_2 by the collaboration group at the Oak Ridge National Laboratory (cf. Ch. 5), measurements have been performed for collisions of C^{6+} [60] and O^{8+} [61] ions with Kr. These measurements were performed at impact energies from 0.32 to 46 keV/u for C^{6+} collisions and from 0.445 to 8.18 keV/u for O^{8+} collisions.

No theoretical studies of these collision systems existed in the literature when these measurements were reported, which makes the assessment of these results difficult. Instead, experimental Lyman line-emissions were compared with calculated emissions from H collisions by using previously reported cross sections. These results are shown in Figs. 7.1 and 7.2 for C^{6+} and O^{8+} collisions, respectively. The justification of this comparison is that the first ionization potential of the Kr atom (0.51 a.u.) is close to that of the H atom (0.5 a.u.), which suggests the same n-selectivity by the CBM. However, comparisons of the emission ratios revealed that the agreement is not always consistent, particularly with the subdominant ratios, which indicates different l-selectivity between the two targets. In order to obtain better insights into these x-ray measurements, it would be ideal to provide actual calculations of Kr collisions but also compare with H collisions regarding the capture dynamics.

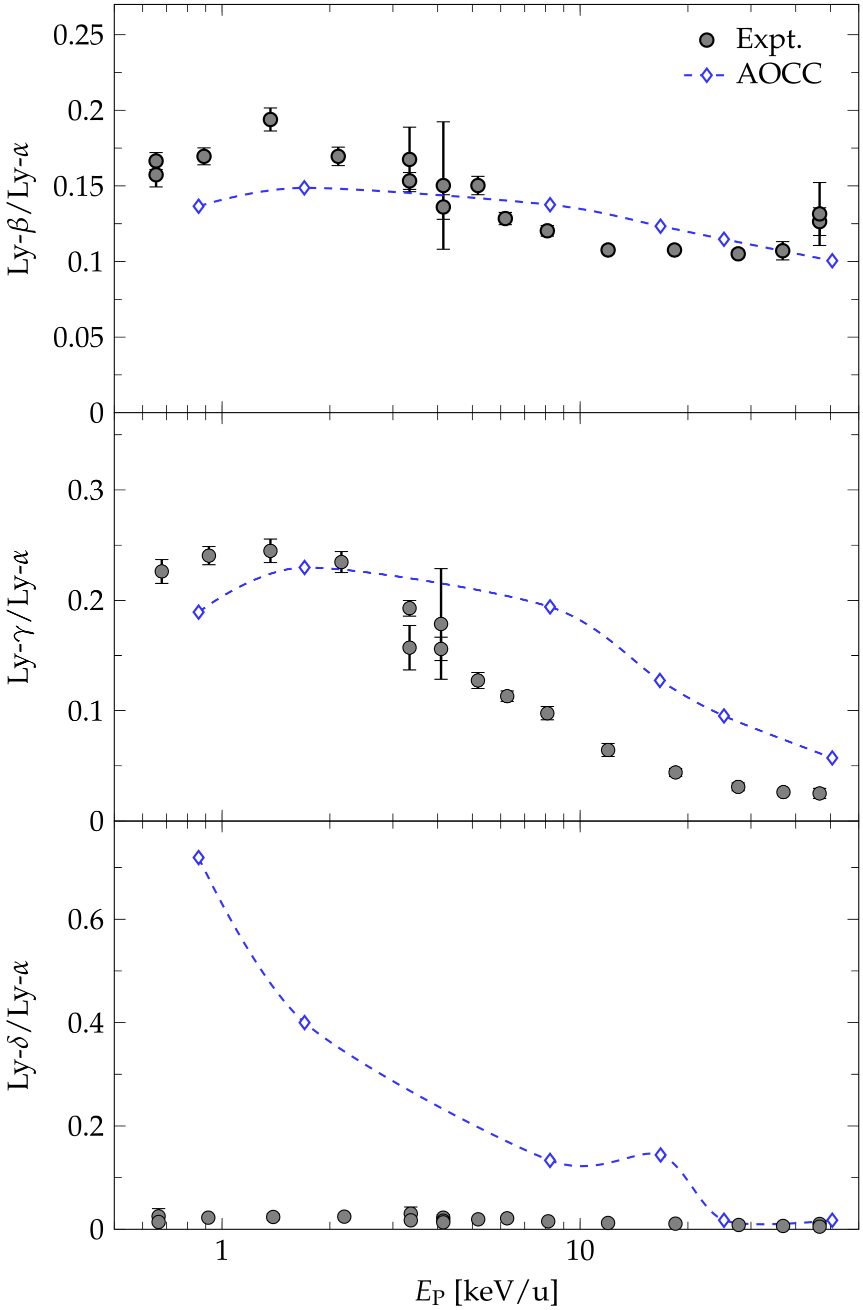

FIG. 7.1: Experimental Lyman line-emission ratios of Ly-β/Ly-α, Ly-γ/Ly-α, and Ly-δ/Ly-α from C^{6+}-Kr collisions [60]. Calculated AOCC ratios (◊) correspond to C^{6+}-H collisions using recommended cross sections from Janev *et al.* [128]. The dashed curve joining AOCC ratios provide visual guidance.

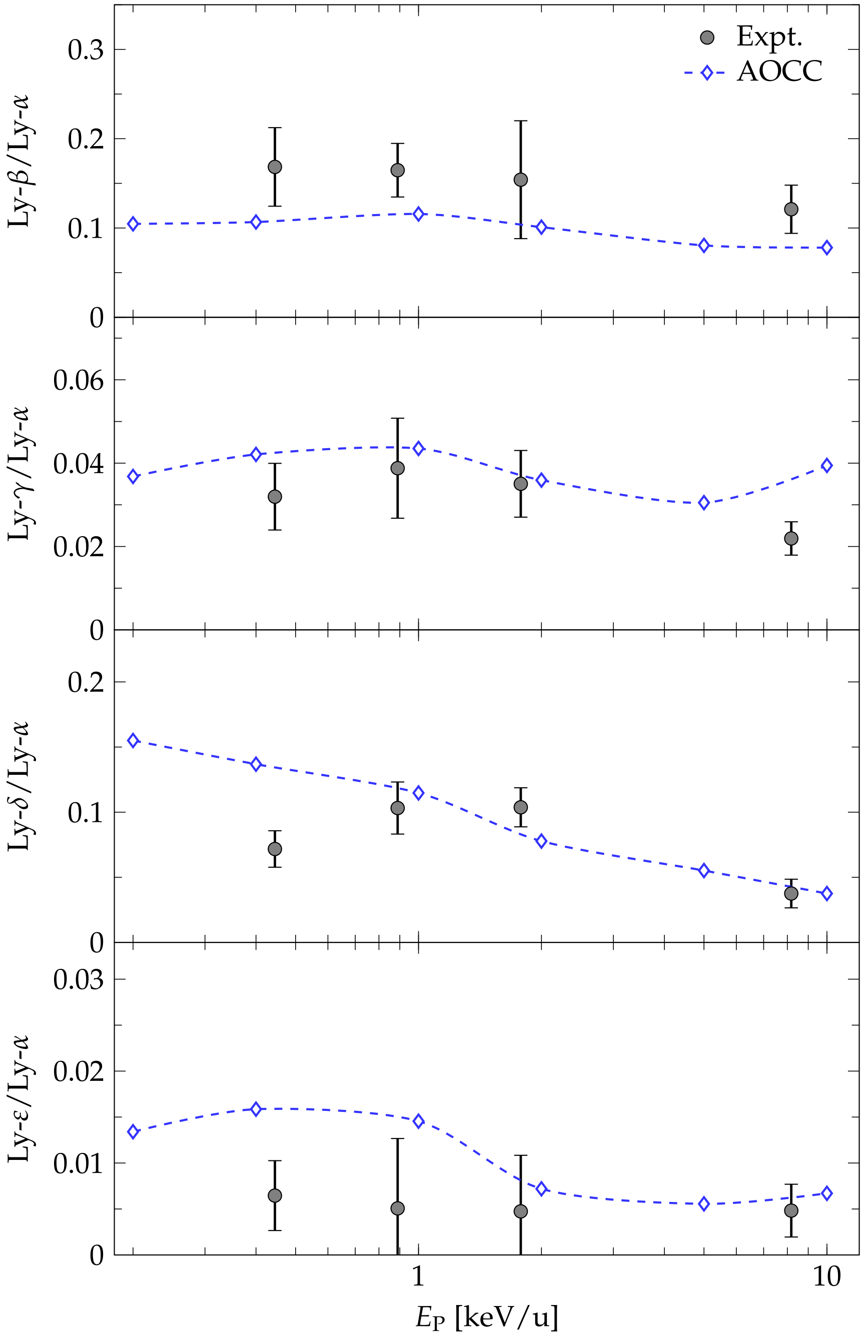

FIG. 7.2: Experimental Lyman line-emission ratios of Ly-β/Ly-α, Ly-γ/Ly-α, Ly-δ/Ly-α, and Ly-ϵ/Ly-α from O^{8+}-Kr collisions [61]. Calculated AOCC ratios ($\diamond$) correspond to O^{8+}-H collisions using recommended cross sections from Fritsch and Lin [82]. The dashed curve joining AOCC ratios provide visual guidance.

7.2 SETUP OF THE PROBLEM

The main focus of this analysis is on C^{6+} and O^{8+} collisions with Kr and H atoms. Calculations were performed at impact energies from 0.5 to 40 keV/u for C^{6+} collisions and from 0.5 to 15 keV/u for O^{8+} collisions. Instead of using previously reported cross sections of H collisions, new calculations are performed using the TC-BGM to compare with Kr collisions. Moreover, new calculations of H collisions also provide a reference of Lyman line-emission ratios for future comparisons[1].

In the single-electron Hamiltonian, the projectile interaction potentials are

$$V_{\mathrm{P}}(t) = \begin{cases} \dfrac{-6}{|\mathbf{r}_{\mathrm{T}} - \mathbf{R}(t)|} & \text{for } \mathrm{C}^{6+}, \\ \dfrac{-8}{|\mathbf{r}_{\mathrm{T}} - \mathbf{R}(t)|} & \text{for } \mathrm{O}^{8+}. \end{cases} \tag{7.1}$$

Interaction with the H atom is straight-forward where a Coulomb potential with nucleus charge $Z = 1$ is used. Obviously the target-response model is not applicable in H collisions. For Kr, the effective ground-state potential was obtained from the OPM [129]. The first ionization potential of Kr generated from the OPM is 0.502 a.u., which is very close to the accepted value of 0.514 a.u. [103].

The basis sets used in the present calculations include: all *nlm* hydrogenlike states from $n = 1$ to $n = 7$ of the projectiles, all states in the *KLMN* shells of the H atom, and all states in the *MNO* shells of Kr. For Kr, test calculations revealed that electron capture from the *M* shell is negligible, and thus, all states in the *K* and *L* shells can be safely neglected in the present calculation. Tables 7.1 and 7.2 list the BGM hierarchies that were used for this study.

To keep the following discussion surveyable, the results of C^{6+} and O^{8+} collisions are examined separately.

7.3 COLLISIONS OF C^{6+}–H AND C^{6+}–Kr

7.3.1 Capture cross sections

Results of total SEC cross sections at impact energies from 0.5 to 40 keV/u are first presented in Fig. 7.3. Figure 7.3(a) shows the results for H collisions from present

---

[1] It was noted in Ref. [32] that experiments on x-ray emissions from C^{6+}-H collisions were left for future work.

TABLE 7.1: BGM hierarchies used in present calculations for C^{6+}-H, -Kr collisions

Target: H

State:	1*s*	2*s*	2*p*	3*s*	3*p*	3*d*	4*s*	4*p*	4*d*	4*f*
Impact energy: $0.5\ \text{keV/u} \leq E_\text{P} < 10\ \text{keV/u}$										
M_v:	0	1	1	2	2	2	2	2	2	2
Impact energy: $10\ \text{keV/u} \leq E_\text{P} \leq 40\ \text{keV/u}$										
M_v:	0	1	2	2	3	3	3	3	3	3

Target: Kr

State:	3*s*	3*p*	3*d*	4*s*	4*p*	4*d*	4*f*	5*s*	5*p*	5*d*	5*f*	5*g*
Impact energy: $0.5\ \text{keV/u} \leq E_\text{P} < 10\ \text{keV/u}$												
M_v:	0	0	0	1	1	1	1	2	2	2	2	2
Impact energy: $10\ \text{keV/u} \leq E_\text{P} \leq 40\ \text{keV/u}$												
M_v:	0	0	1	1	2	2	2	2	3	3	3	3

TABLE 7.2: BGM hierarchies used in present calculations for O^{8+}-H, -Kr collisions

Target: H

State:	1*s*	2*s*	2*p*	3*s*	3*p*	3*d*	4*s*	4*p*	4*d*	4*f*
Impact energy: $0.5\ \text{keV/u} \leq E_\text{P} < 10\ \text{keV/u}$										
M_v:	0	1	1	2	2	2	2	2	2	2
Impact energy: $10\ \text{keV/u} \leq E_\text{P} \leq 15\ \text{keV/u}$										
M_v:	0	1	2	2	2	2	2	2	3	3

Target: Kr

State:	3*s*	3*p*	3*d*	4*s*	4*p*	4*d*	4*f*	5*s*	5*p*	5*d*	5*f*	5*g*
Impact energy: $0.5\ \text{keV/u} \leq E_\text{P} < 10\ \text{keV/u}$												
M_v:	0	0	0	1	1	1	1	2	2	2	2	2
Impact energy: $10\ \text{keV/u} \leq E_\text{P} \leq 15\ \text{keV/u}$												
M_v:	0	0	1	1	2	2	2	2	2	2	3	3

TC-BGM calculations, which are being compared with the recommended values [10]. Recall from Ch. 5 that these recommended values are determined from polynomial fits on data from various experimental and theoretical results and uncertainties were estimated based on the reliability of the experiment and sophistication of the theoretical method. Figure 7.3(b) shows the present results for Kr collisions which are separated by the various present IEM calculations. In addition to pure SEC, the total SEC for Kr collisions includes contributions from ADC. It was found that contributions from higher multiple capture events followed by autoionization are small ($< 10^{-17}$ cm^2), which is qualitatively consistent with the observations from a previous coincidence experiment of triple-electron capture by Martin *et al.* [130] for slow C^{6+}-Kr collisions.

Starting with H collisions [Fig. 7.3(a)], the present cross sections are similar to the recommended values [114]. The cross sections do not vary significantly from 0.5 to 20 keV/u, which is a general behaviour seen in collisions in the low impact-energy regime [10]. Note that there are some discrepancies at 0.5 keV/u between the present results of H collisions and the recommended values. This is likely an indication that the straight-line approximation may not be appropriate at the lowest energies shown for this collision system. Overall, the present cross sections for H collisions are deemed satisfactory for impact energies above 1 keV/u.

Next with Kr collisions [Fig. 7.3(b)], the cross sections shown also do not vary significantly from 0.5 to 20 keV/u. The target-response results are about 5 to 10% greater than the no-response results and total SEC appears to be similar in magnitude to the cross sections of H collisions. Another aspect that is shown is that the no-response profiles show a bit more variation than in the response profiles. Similar to previous studies (cf. Ch. 5), all cross section profiles appear to converge and decrease as impact energy increases towards the intermediate energy regime, which should be expected since ionization becomes more important.

Delving further into the Kr collision cross sections, the present Auger analysis showed that ADC mainly contributes to the single-capture population in the $n = 2$ and $n = 3$ states of the projectile. Furthermore, it was determined from the present IEM calculations using the response model that the ADC to pure SEC ratios are, for example, 0.94, 0.69, and 0.49 at 1, 4, and 10 keV/u, respectively. As for results in the no-response approximation, the respective ratios are 0.84, 0.55, and 0.46. To assess these ratios, comparisons are made with the coincidence collision experiment of two-electron capture by Chen *et al.* [117]. Using results from that study, it can be deduced

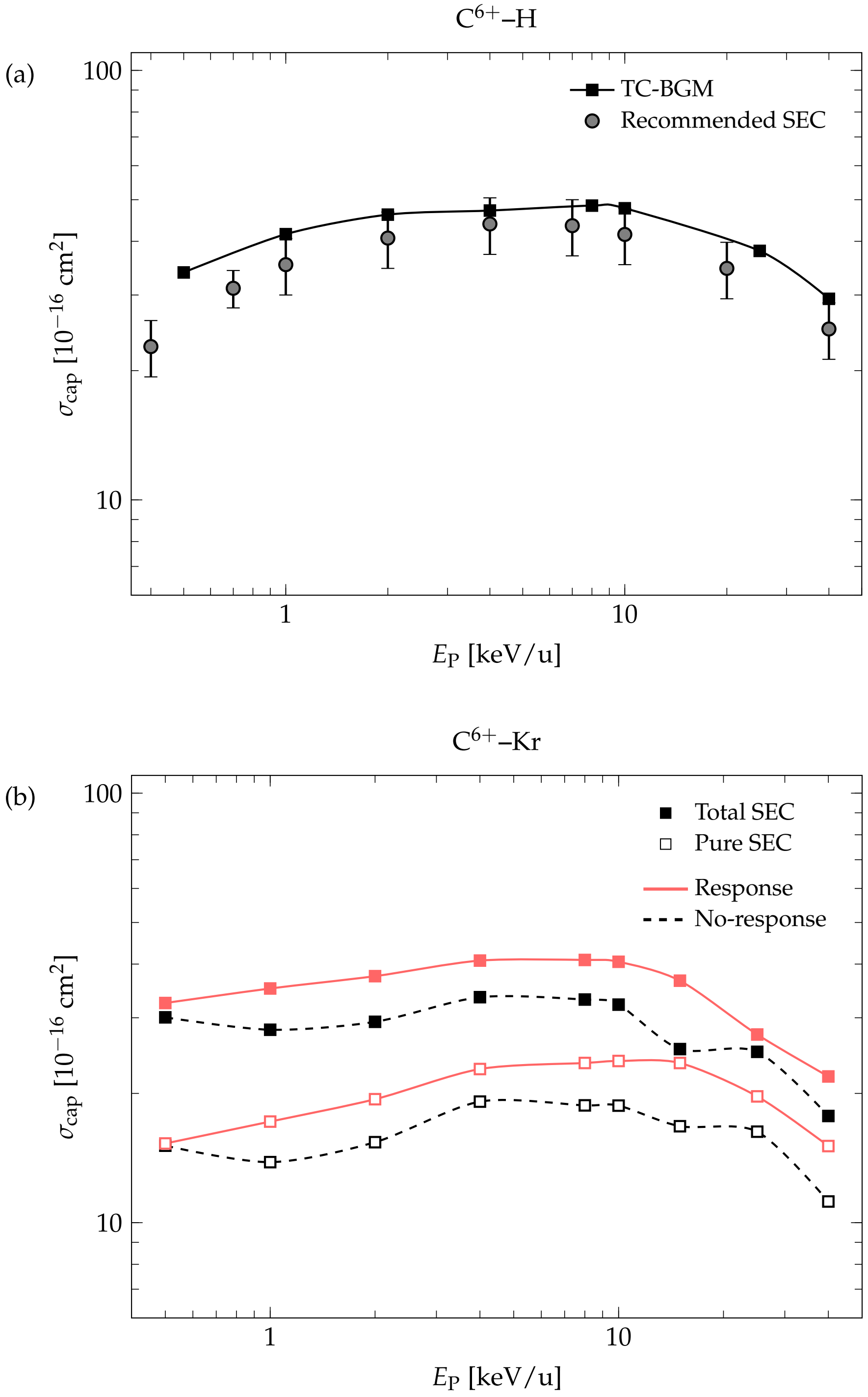

FIG. 7.3: Total SEC cross section plotted with respect to impact energy: (a) C^{6+}-H collisions from TC-BGM and recommended SEC from Janev *et al.* [114]; (b) C^{6+}-Kr collisions from TC-BGM calculations.

that the ratios of ADC to pure SEC for C^{6+}-Kr collisions are 0.53, 0.26, and 0.24 at 1, 5, and 9.5 keV/u, respectively. Although the present calculations appear to produce larger ratios, they are at least consistent with the decreasing velocity dependence from these experimental observations.

The next set of results to examine are the n-state relative capture cross section distributions. Figures 7.4 and 7.5 show the distributions for H and Kr collisions at impact energies of 1, 8, and 25 keV/u. According to the experimental Lyman line-emission ratios from Kr collisions [60], these impact energies approximately represent where the dominant ratios show considerable changes. Furthermore, because another objective in this analysis is to compare Kr and H targets at the true single-electron capture level, only pure SEC results are included in these figures. The complete set of results of the absolute pure SEC and ADC cross sections for the prominent capture states can be found in Appendix D..

For H collisions (Fig. 7.4), the n-distribution at 1 keV/u shows a resonant profile where the relative population peaks at $n = 4$, which is a general feature of capture at this impact energy. Note that this dominant capture state can also be verified by the CBM. As the impact energy increases, the capture distribution broadens.

For Kr collisions (Fig. 7.5), the distribution at 1 keV/u also shows a resonant capture profile with the peak occurring at $n = 4$. However at 8 keV/u, the distribution has a degenerate-like profile, showing a fairly even population in the $n = 4$ and $n = 5$ states. Interestingly at 25 keV/u, the expected broader capture distribution is visible but the population peaks at $n = 5$. This is clearly different from the behaviour in H collisions where the capture population consistently peaks at $n = 4$ at all impact energies that are considered here.

In a different view, Fig. 7.6 shows the pure SEC cross sections in Kr collisions for $n = 4$ and $n = 5$ of the projectile plotted with respect to the impact energy. One subplot shows the results in the no-response approximation [Fig. 7.6(a)] while the other one displays results from calculations using the response model [Fig. 7.6(b)]. A crossing between the two partial cross section profiles is shown for both sets of calculations but at different impact energies. In either case, this is a behaviour that is not seen in H collisions over the same energies and one that is beyond the CBM.

In previous collision studies on O^{8+}-H and Ar^{8+}-H collisions [131–133], a similar crossing of the partial cross section profiles was observed but between $n = 5$ and $n = 6$ at a much lower impact energy of approximately 70 and 150 eV/u, respec-

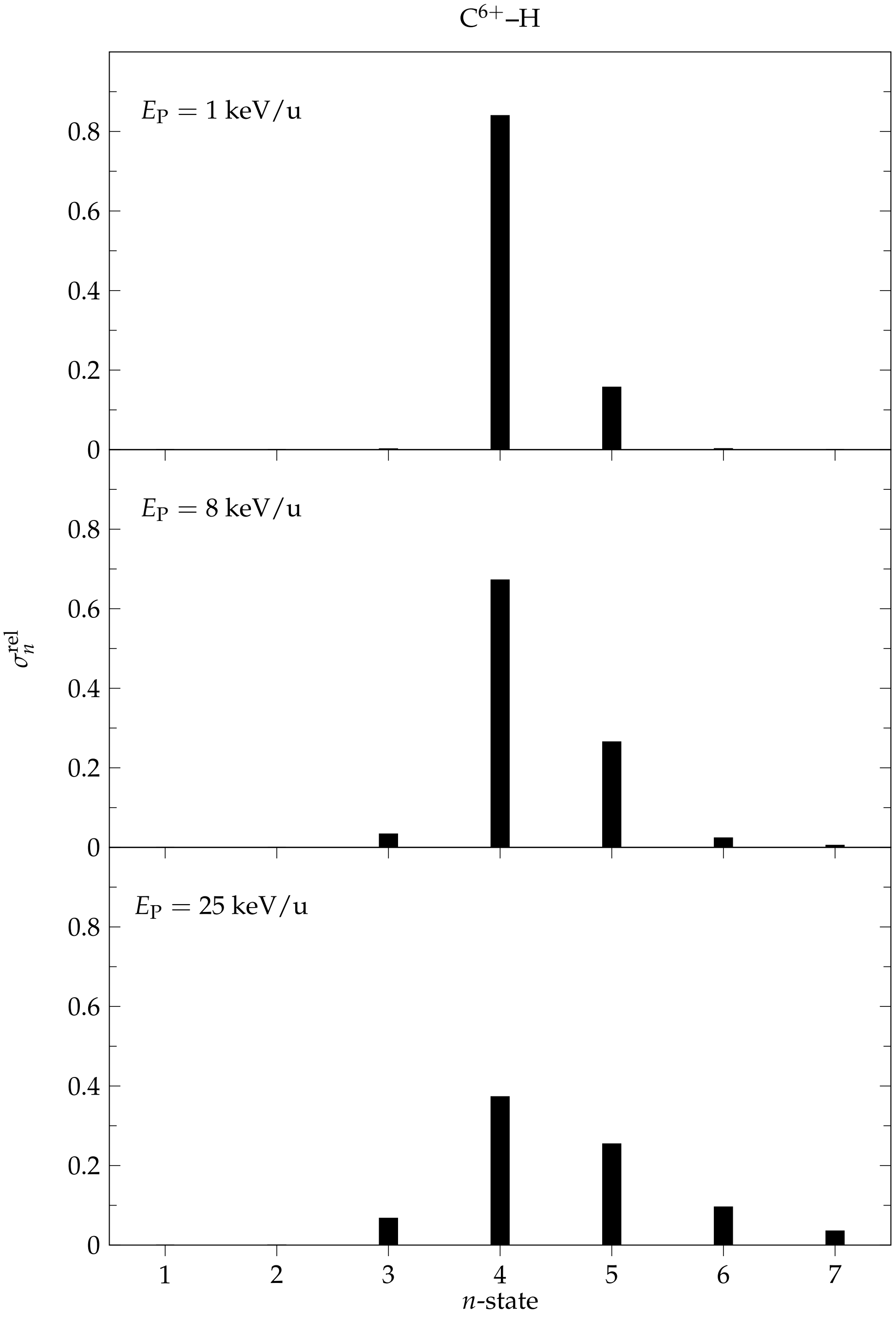

FIG. 7.4: n-state relative SEC cross section distribution for C^{6+}-H collisions at $E_P = 1$, 8, and 25 keV/u from TC-BGM calculations.

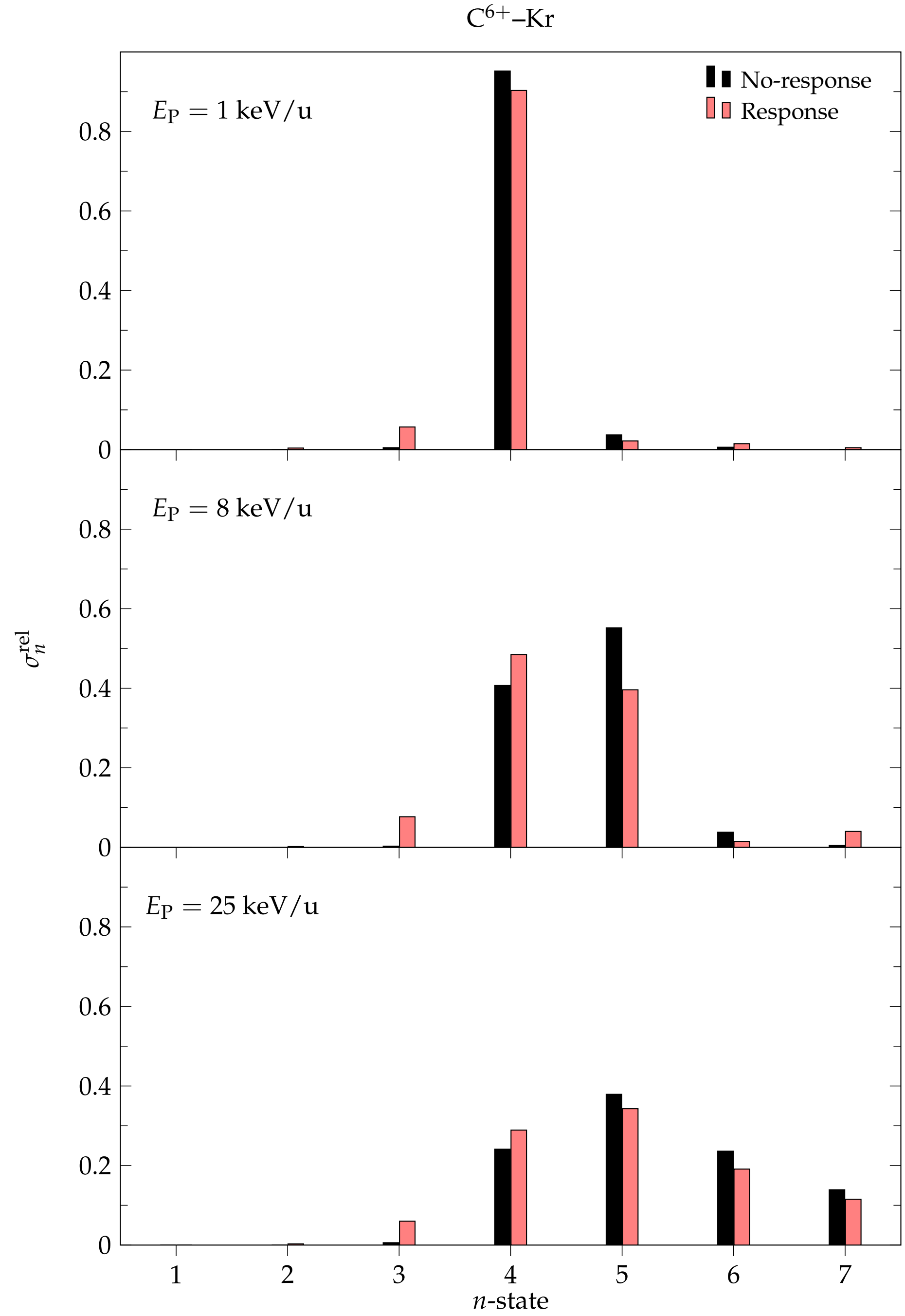

FIG. 7.5: n-state relative pure SEC cross section distribution for C^{6+}-Kr collisions at $E_P = 1$, 8, and 25 keV/u from TC-BGM calculations.

tively. In those collision studies, the situation is 'reversed' where the same target is considered but with different projectile ions having the same charge state. Regardless, it was demonstrated that having different collision species, obviously represented by different effective potentials, has an influence on the capture dynamics. Furthermore, one should also note that capture primarily happens from the $4p$ shell of Kr, which is clearly different from the H atom where capture happens from the $1s$ shell. From the perspective of energy correlation diagrams, one should not expect to see identical avoid crossings from these two collisions. On the other hand, energy correlation diagrams may not fully explain this capture behaviour as it appears to be dependent on the impact energy, which is beyond this type of analysis.

Moving on to the nl-distributions, Fig. 7.7 shows the relative $4l$ and $5l$ distributions for H collisions at 1, 8, and 25 keV/u. Shown alongside with the present results is the statistical l-distribution (4.3) for comparison. Based on the n-distribution results, electron-capture is mainly into the $n = 4$ and $n = 5$ states of the projectile for the impact energies considered here. The present results show that the statistical distribution may be suitable for the $4l$-distribution from 1 to 8 keV/u. At higher energies, the $4l$-distribution becomes over-statistical. As for the $5l$-distribution, capture is much preferred in lower l-states at $E_{\mathrm{P}} = 1$ keV/u while at much higher impact energies (> 10 keV/u) this preference shifts to the maximum l-state. It appears that the statistical distribution is only appropriate for the $5l$ states in a much narrower energy range than for the $4l$ states (i.e., for $1 < E_{\mathrm{P}} < 8$ keV/u).

Similarly, Fig. 7.8 shows the relative $4l$ and $5l$ distributions from present calculations and the statistical model for Kr collisions at 1, 8, and 25 keV/u. There are a few aspects to note which are different from the distributions for H collisions. For the $4l$ distributions between 1 and 8 keV/u, the present no-response results show that the capture population mainly peaks at $l = 2$ and this is evident at 8 keV/u in Fig. 7.8(a). This differs from the response results where the population peaks at $l = 3$, resembling the statistical distribution. For the $5l$ distributions, both no-response and response results at 1 keV/u are very similar to the statistical distribution, which is different from H collisions. However, once the impact energy reaches 8 keV/u, the distributions transitioned to the over-statistical pattern and maintain this distribution at higher impact energies.

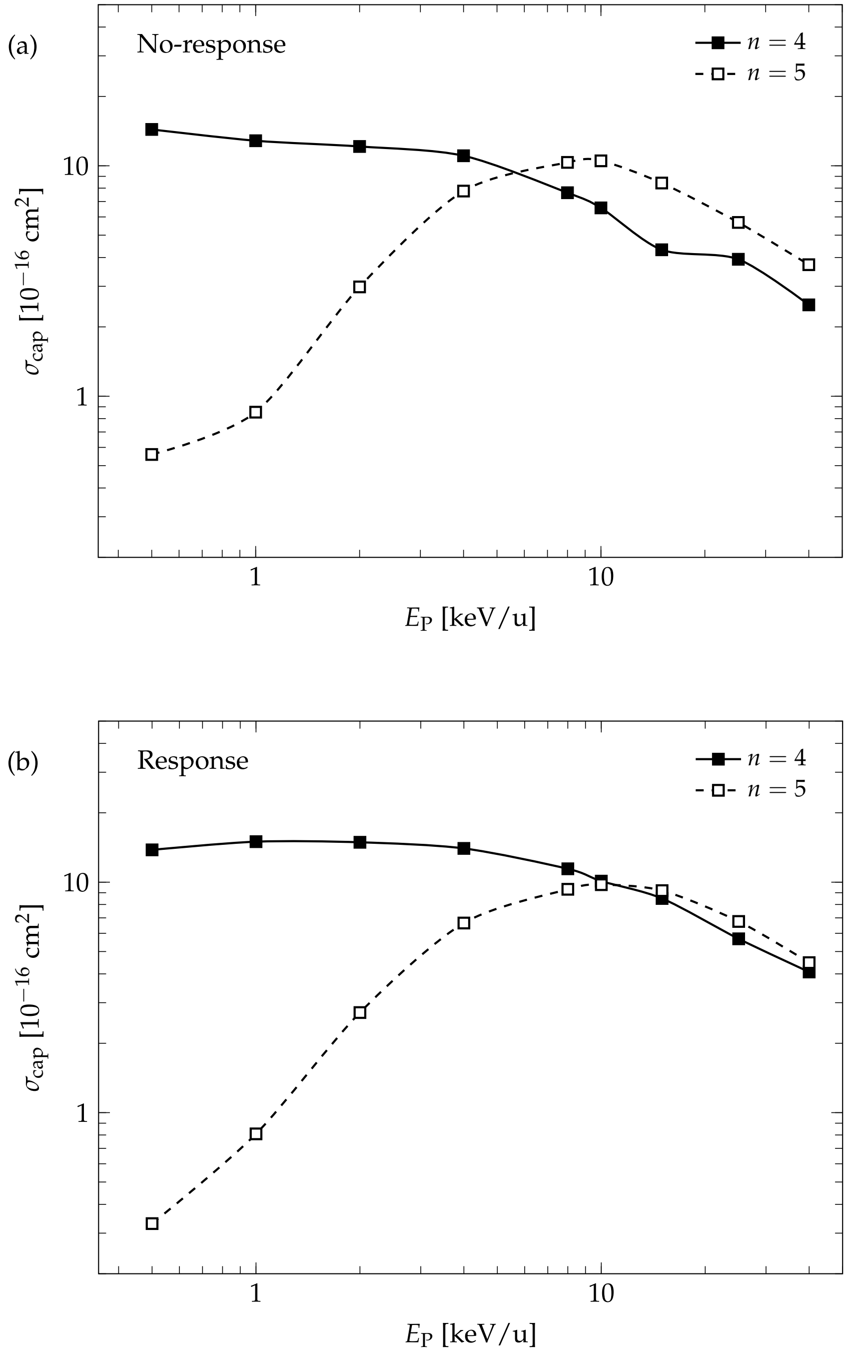

FIG. 7.6: TC-BGM pure SEC cross sections of $n = 4$ and $n = 5$ plotted with respect to the impact energy for C^{6+}-Kr collisions: (a) no-response approximation; (b) target-response model.

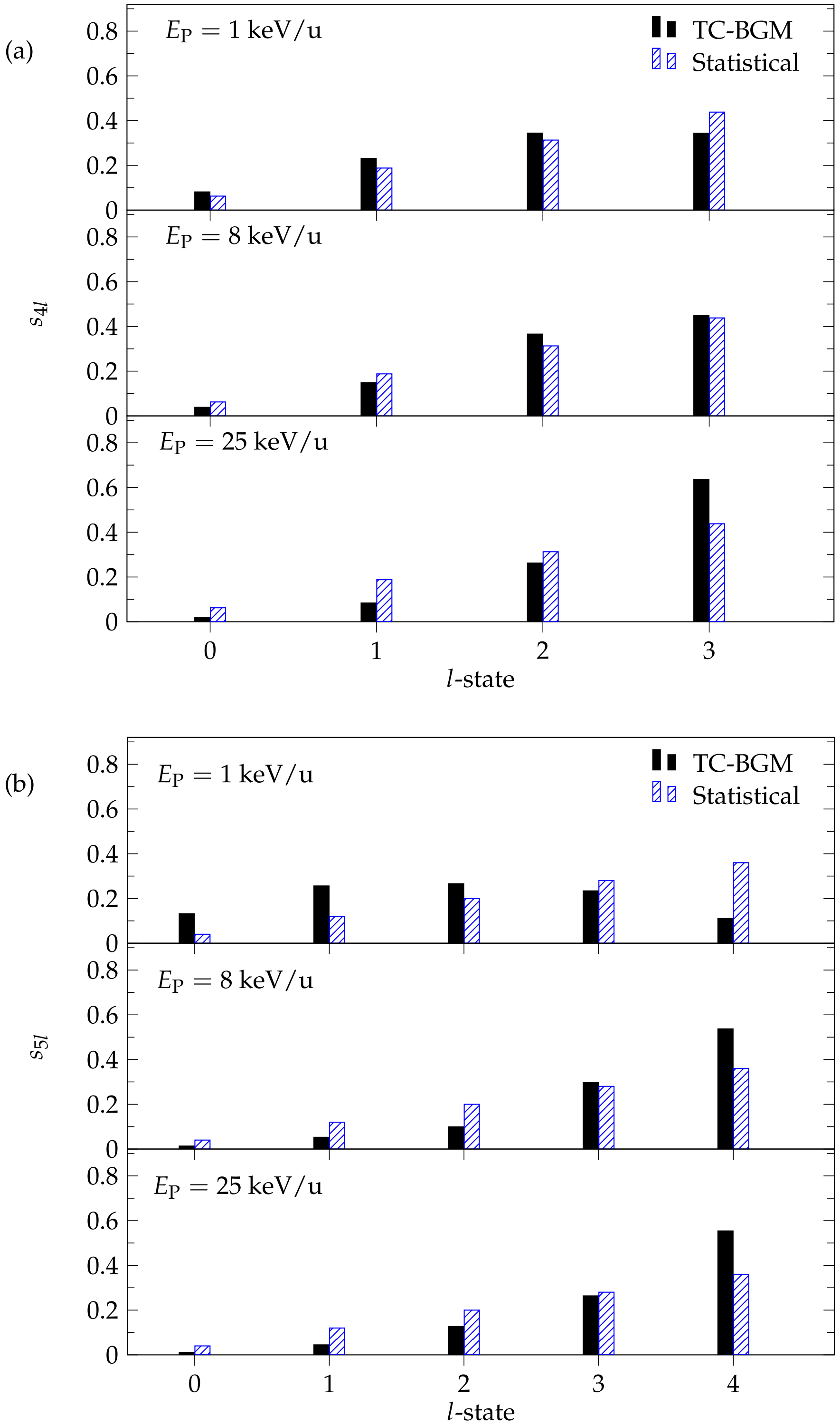

FIG. 7.7: *nl* SEC cross section distributions for C^{6+}-H collisions at $E_P = 1, 8,$ and 25 keV/u: (a) $n = 4$ and (b) $n = 5$. TC-BGM results are compared with the presupposed statistical l-distribution.

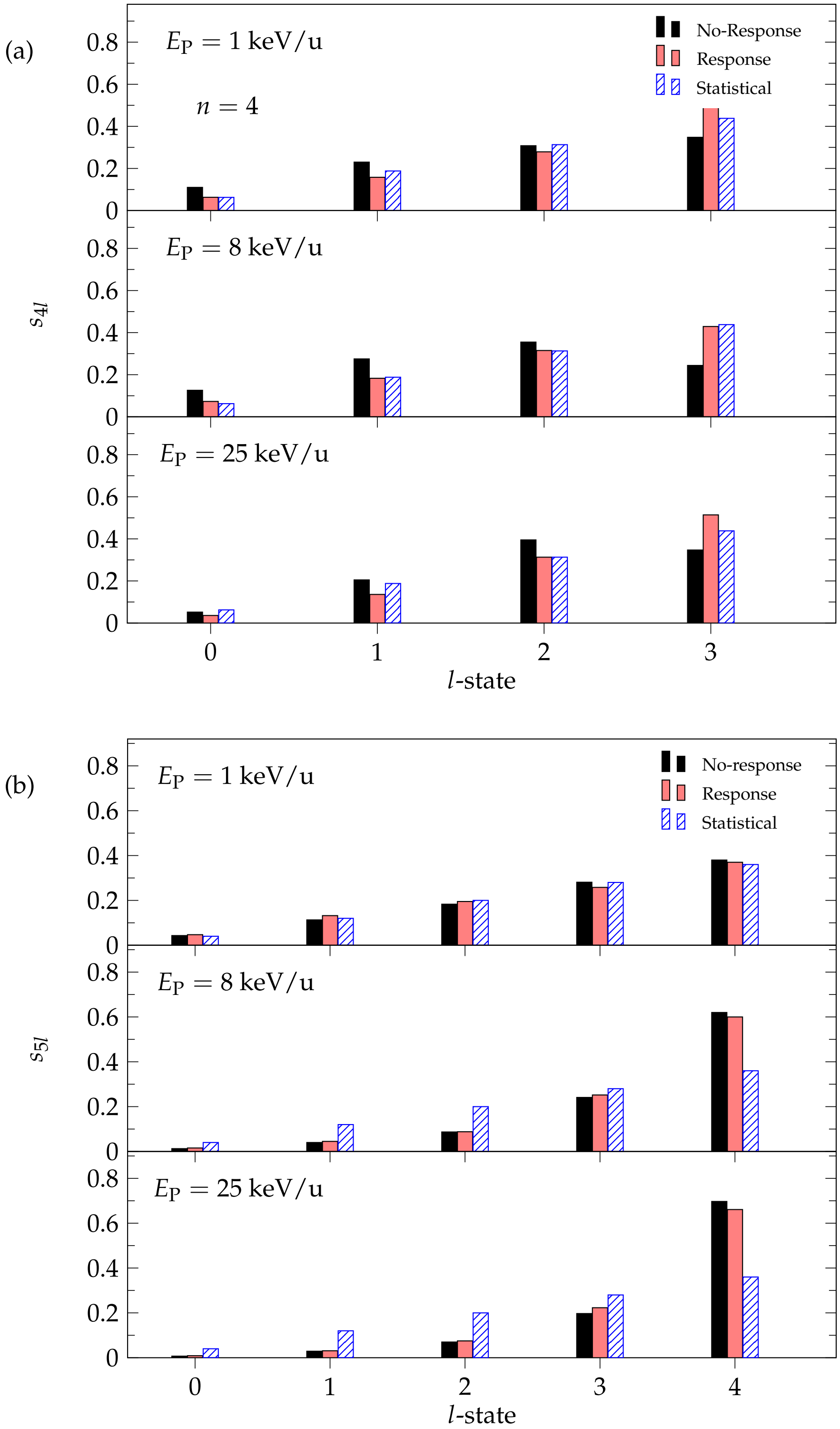

FIG. 7.8: *nl* relative pure SEC cross section distributions for C^{6+}-Kr collisions at $E_P = 1$, 8, and 25 keV/u: (a) $n = 4$ and (b) $n = 5$. TC-BGM results are compared with the presupposed statistical l-distribution.

7.3.2 Lyman line-emission ratios

Figure 7.9 shows the calculated Lyman line-emission ratios from C^{6+}-H and -Kr collisions. All calculated ratios shown in the figure are from the present TC-BGM calculations. For Kr collisions, several variants of the present IEM results are shown separately. Within each of those calculations, they are further separated by pure SEC and total SEC events (i.e, pure SEC + ADC). All calculated ratios are compared with the experimental ratios from Kr collisions [60].

Focusing first on the two dominant ratios of Ly-β/Ly-α and Ly-γ/Ly-α, the results produced by the present calculations for both collision systems are qualitatively consistent with the experimental ratios. Specifically, the ratios appear approximately constant from 0.5 to 4 keV/u and decreases at higher impact energies. This can be understood from the increasing relative capture population in the maximum l-state, thereby increasing the relative Ly-α counts. For the present Kr results, there are some differences between the pure and total SEC profiles. It is apparent that the addition of ADC leads to a profile that is consistent with the experimental profile, demonstrating the importance of ADC. The only exception is the Ly-γ/Ly-α profile produced from the response calculations where no improvements were shown by adding ADC. Despite showing a similar profile as the no-response calculation, the ratio is underestimated relative to the experimental results. This further suggests that the ADC cross sections are slightly overestimated by the present IEM calculations. As for ratios from H collisions, the Ly-β/Ly-α and Ly-γ/Ly-α profiles show very good agreement with the experimental ratios of Kr collisions, even more so than using the recommended cross sections [128] (cf. Fig. 7.1).

For the subdominant Ly-δ/Ly-α and Ly-ϵ/Ly-α ratios, the calculated results for both collision systems also behave consistently with the experimental values. The smallness of these ratios are simply a reflection of the small relative capture populations of nl states for $n > 5$ at all impact energies. For Kr collisions, there are no discernible differences among the various IEM calculations. If one considers the region between the pure SEC and total SEC profiles for Kr collisions in the no-response approximation as the "uncertainty" in the present calculations and notes that the experimental ratios lie within this region, then the present results can be viewed as satisfactory. Finally as for H collisions, the only notable discrepancy shown is the Ly-δ/Ly-α ratio at 1 keV/u. Otherwise, these results appear much closer to the experimental ra-

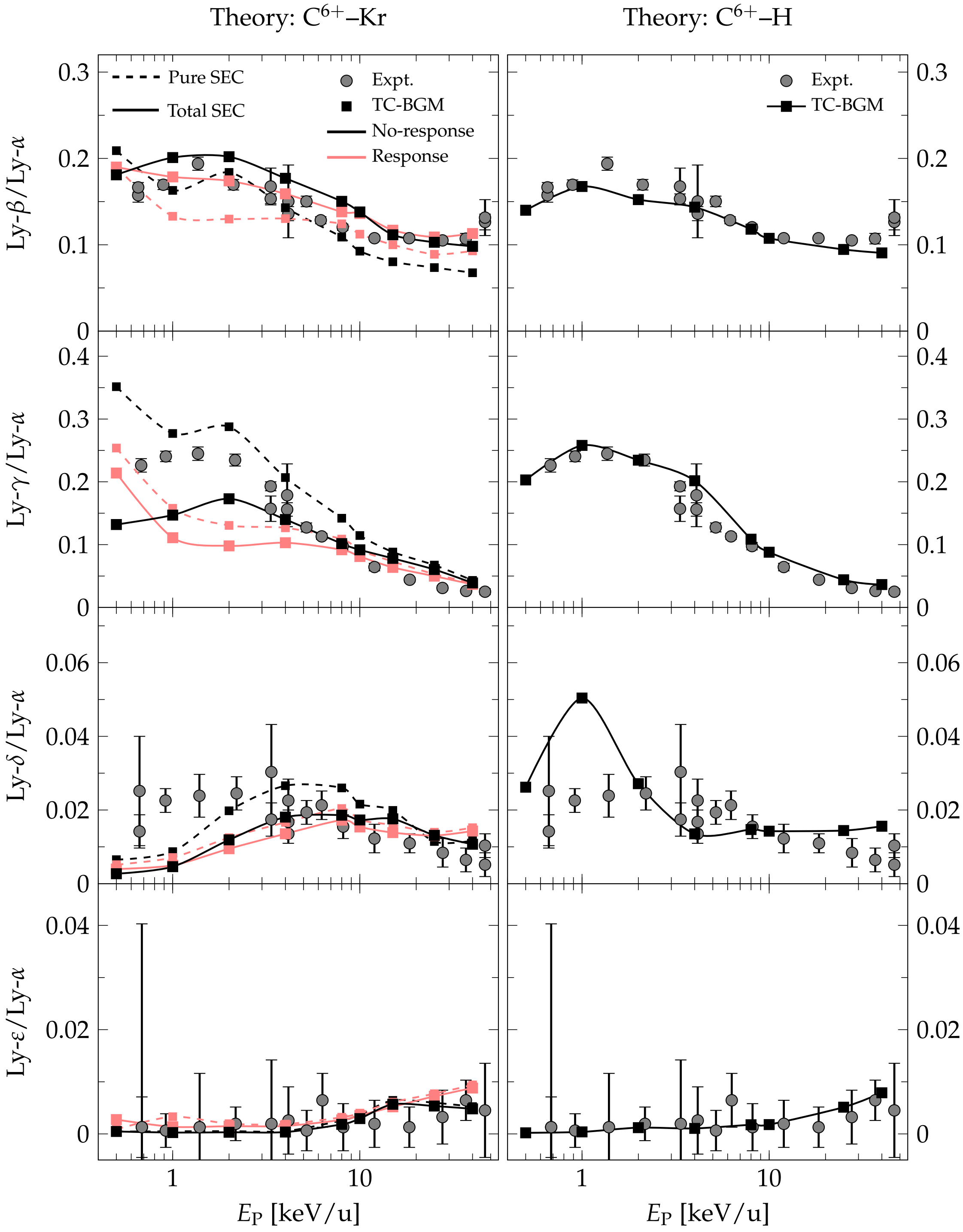

FIG. 7.9: Lyman line-emission ratios of Ly-β/Ly-α, Ly-γ/Ly-α, Ly-δ/Ly-α, and Ly-ϵ/Ly-α. Calculated TC-BGM ratios from C^{6+}-Kr (left column) and C^{6+}-H (right column) collisions. Pure SEC in Kr collisions is represented by dashed curves while total SEC is represented by solid curves. Curves joining the calculated ratios provide visual guidance. Measured ratios [60] in both columns correspond to C^{6+}-Kr collisions.

tios than those based on the recommended cross sections [128]. Overall, despite the differences shown in the partial cross section distributions between Kr and H, they exhibit similar ratios of the Lyman line-emissions from 0.5 to 40 keV/u.

7.4 COLLISIONS OF O^{8+}–H AND O^{8+}–Kr

7.4.1 Capture cross sections

Figure 7.10 shows the total capture cross sections for collisions with the O^{8+} projectile ion between 0.5 and 15 keV/u. Figure 7.10(a) corresponds to results for H collisions that includes the recommended values [114], calculations using the quantum-mechanical hyperspherical close-coupling (HSCC) method by Lee *et al.* [133], and the present TC-BGM calculations. Figure 7.10(b) includes results for Kr collisions from the present calculations only, which are separated into the different variants of the IEM calculations. The total SEC for Kr collisions includes contributions from only ADC since higher-multiple capture events followed by autoionization were found to be negligible.

A few comments are in order in regards to the HSCC method [134]. This approach is based on the so-called perturbed stationary-state approximation [114] of solving the full Schrödinger equation for the collision problem by expanding the electron wavefunction using a MO basis. However, the fundamental problem of the perturbed stationary state approximation is that certain terms in the expansion do not have proper asymptotic behaviours [10, 135], which is problematic in collision problems. In the HSCC method, this problem is addressed by using hyperspherical coordinates and in this way, these asymptotic issues are avoided.

The present TC-BGM cross sections for O^{8+}-H collisions show good, consistent agreement with the recommended values [114] above 1 keV/u. Note the slight deviation of the present cross sections from the HSCC results at 2 keV/u and below. Given the full quantum-mechanical treatment of HSCC, this deviation indicates the limitations of the straight-line approximation at these energies, just as it was pointed out earlier for C^{6+} collisions (cf. Sec. 7.3.1). Overall, because this deviation is less than 10% at 0.5 keV/u and above, the present results are deemed satisfactory for these energies.

For O^{8+}-Kr collisions, the total cross sections that are produced by the various IEM calculations do not change significantly from 0.5 to 15 keV/u. From the various calculations shown in Fig. 7.10(b), the total SEC cross sections produced from the response

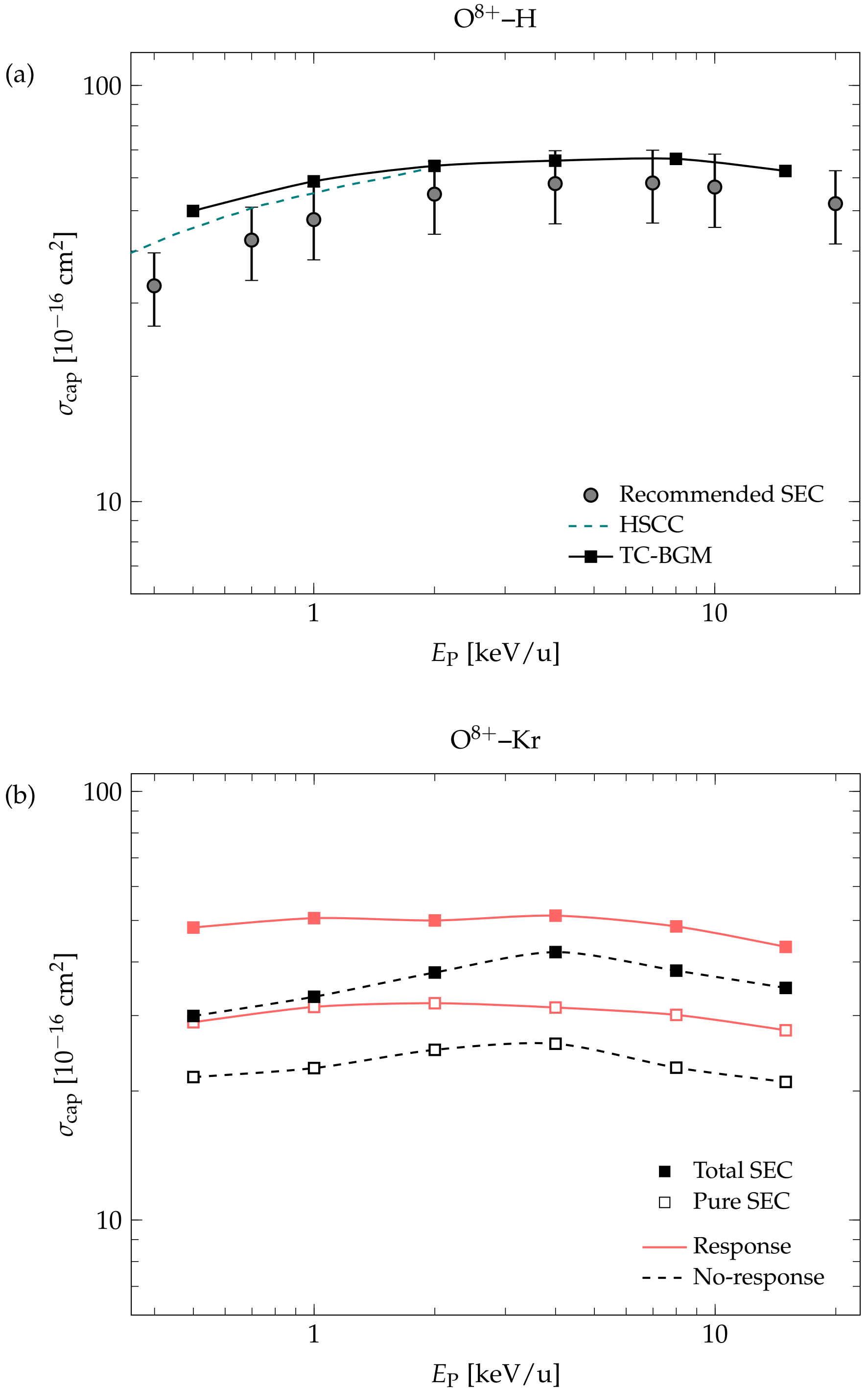

FIG. 7.10: Total capture cross section plotted with respect to impact energy: (a) O^{8+}-H collisions from recommended SEC of Janev *et al.* [114], HSCC calculations [133], and present TC-BGM; (b) O^{8+}-Kr collisions from TC-BGM calculations.

calculation are most similar in magnitude to those in H collisions [Fig. 7.10(a)]. It is also shown that contributions from ADC are not negligible at these energies. The present Auger analyses showed that ADC contributes to the single-capture population in the $n = 3$ and $n = 4$ states of the projectile, but mainly in the former. Moreover, at 1 keV/u, the ratio of ADC to pure SEC is about 0.46 and 0.61 from the no-response approximation and the calculation using the response model, respectively. According to Martin *et al.* [136], a ratio of 0.44 at 1 keV/u can be deduced from their coincidence measurements. It can be inferred that the present ratio from the no-response approximation is satisfactory and that the ratio from the response calculation is overestimated. Since Martin *et al.* [136] did not carry out similar measurements at other impact energies, the velocity dependence of the present ADC results cannot be assessed, but it is expected that ADC would decrease with impact velocity based on the C^{6+} collision analysis (cf. 7.3.1).

Figure 7.11 shows the n-state relative capture cross section distributions for O^{8+}-H collisions at 1, 8, and 15 keV/u. Similar to the C^{6+} collision calculations, absolute partial cross sections at all other impact energies for the dominant capture states can be found in Appendix D.. Starting at 1 keV/u, the dominant capture state is clearly $n = 5$ of the projectile with $n = 6$ being the subdominant channel. As impact energy increases, one sees the broadening of the n-distribution.

The n-state relative capture cross section distributions for O^{8+}-Kr collisions are displayed in Fig. 7.12. Only results from pure SEC are shown for the following discussion. At 1 keV/u, a degenerate-like profile between $n = 5$ and $n = 6$ of the projectile is obtained from the no-response calculation. As for the distribution from the response calculation at 1 keV/u, the maximum capture population of $n = 5$ is more clear. The degenerate-like profile is similar to that of the C^{6+}-Kr collisions except that it occurs at a different impact energy (cf. Fig. 7.5). Continuing with the n-distributions of O^{8+} collisions, the usual broader profile is shown at higher impact energies but the capture population peaks at $n = 6$. This shift in the n-state where the capture population is peaked is further illustrated in Fig. 7.13 where the pure SEC cross sections of $n = 5$ and $n = 6$ are plotted with respect to the impact energy. The plots show a crossing between the two cross section profiles between 0.5 to 15 keV/u. The impact energy at which this crossing occurs is different when analysing the no-response and response results. Comparing these plots with those corresponding to C^{6+}-Kr collisions (Fig. 7.6), this shows that the charge state of the projectile also influences this aspect of capture

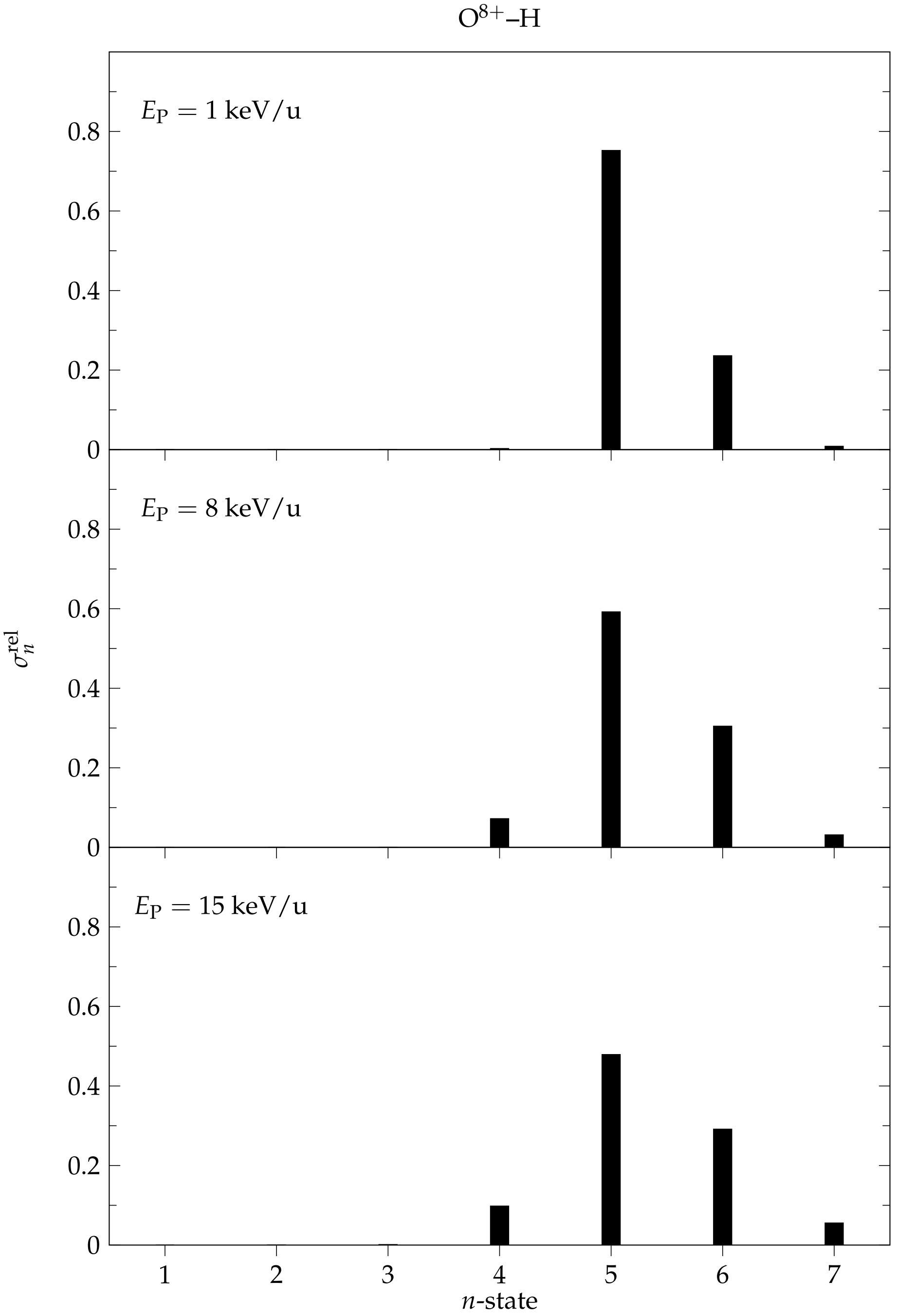

FIG. 7.11: n-state relative SEC cross section distribution for O^{8+}-H collisions at $E_P = 1$, 8, and 15 keV/u from TC-BGM calculations.

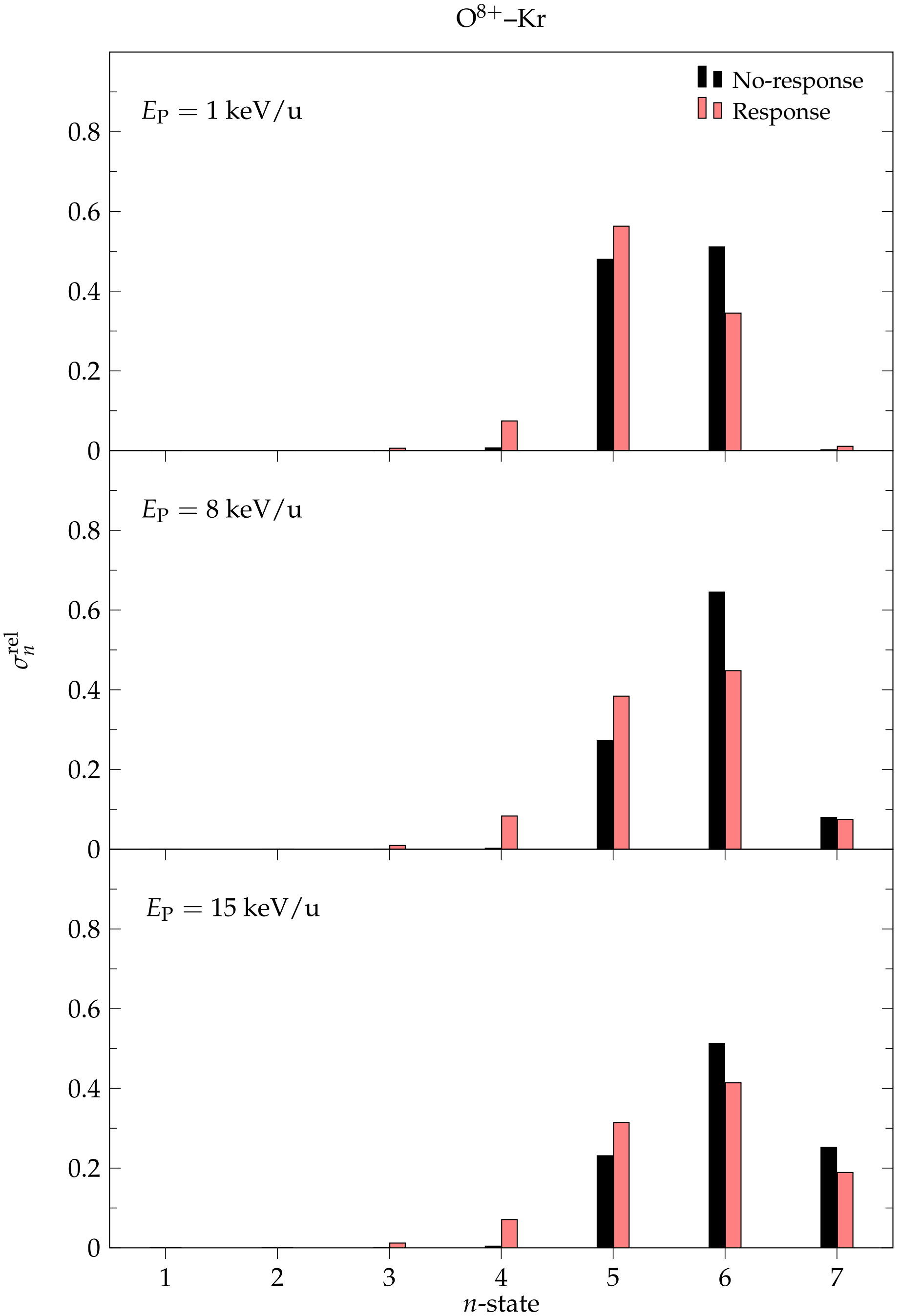

FIG. 7.12: n-state relative pure SEC cross section distribution for O^{8+}-Kr collisions at $E_P = 1$, 8, and 15 keV/u from TC-BGM calculations.

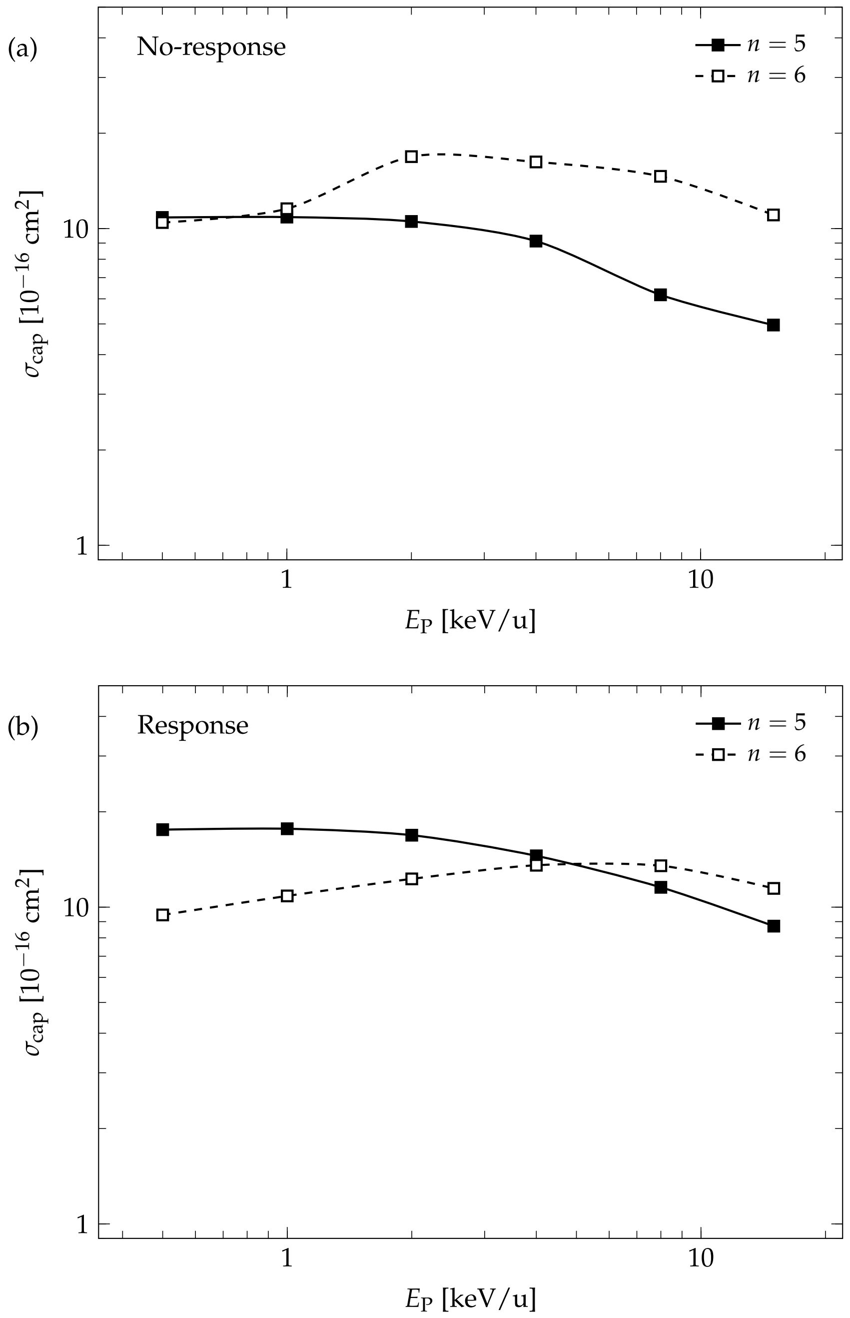

FIG. 7.13: TC-BGM pure SEC cross sections of $n = 5$ and $n = 6$ plotted with respect to the impact energy for O^{8+}-Kr collisions: (a) no-response approximation; (b) target-response model.

dynamics. It is also worth noting that despite these changes in the dominant capture state between 0.5 and 15 keV/u, this does not have a noticeable influence on the total capture cross section [cf. Fig. 7.10(b)].

Next, the relative *l*-distributions are examined. Starting with O^{8+}-H collisions, Fig. 7.14 shows the *l*-distributions at 1, 8, and 15 keV/u. Only the 5*l* and 6*l* distributions at these energies are shown since the capture population is prominent in these states. The complete set of absolute partial SEC and ADC cross sections for the dominant capture states can be found in Appendix D.. Shown alongside with the present TC-BGM results are the presupposed statistical distributions. At 1 keV/u, capture mainly peaks near the maximum *l*-state in both 5*l* and 6*l* distributions. When the impact energy reaches about 8 keV/u, the 5*l* distribution resembles the statistical model. By contrast the 6*l* distribution is over-statistical since the 6*h* state is overpopulated relative to other 6*l* states. The same over-statistical observation also applies to both 5*l* and 6*l* distributions at 15 keV/u.

Figure 7.15 shows the 5*l* and 6*l* relative distributions for O^{8+}-Kr collisions at 1, 8, and 15 keV/u. Only results of pure SEC are shown. From comparisons with H collisions, there are a number of aspects that are worth commenting on. At 1 keV/u, the 5*l* distribution produced from the no-response calculation shows the usual distribution where the capture population peaks near the maximum *l*-state. This is a sharp contrast from the response calculation where the 5*g* state is massively overpopulated relative to lower *l*-states. From this observation, it is apparent that neither of these distributions resemble the statistical model at this impact energy. As impact energy increases, there is a noticeable change in the relative population from the response results while those from the no-response calculations remain the same overall. In either case, the dynamics is somewhat different from H collisions at these energies. For the corresponding 6*l* results, both the no-response and response calculations produced a distribution that closely resembles the statistical model. It is also shown that the 6*l*-distribution behaves in the usual manner where the relative population at the maximum *l*-state increases with respect to the impact energy, which is different from the behaviour of the 5*l*-distribution. From these *l*-distributions, it is clear that the capture behaviour between collisions with H and Kr predicted from the present calculations are different from each other.

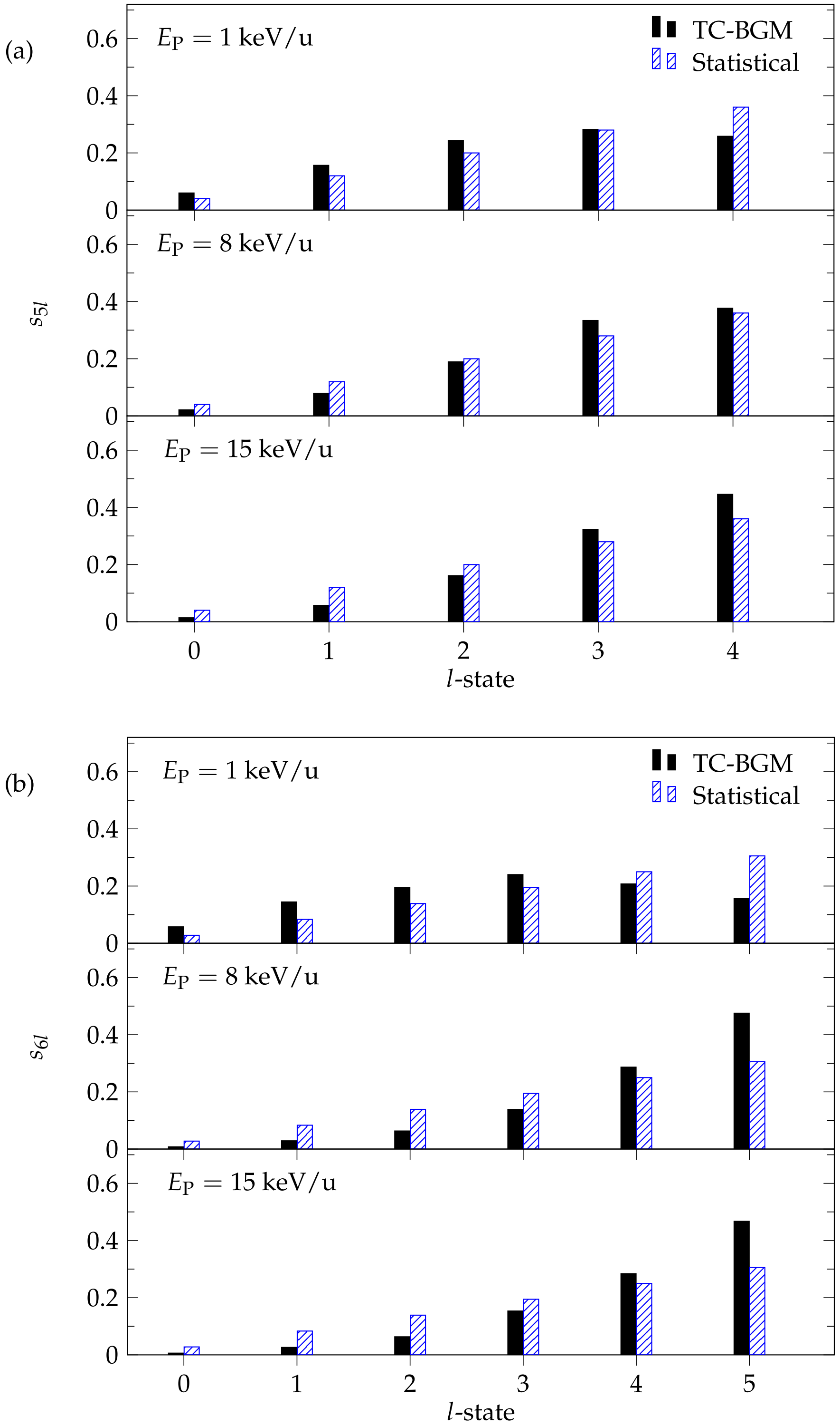

FIG. 7.14: nl relative SEC cross section distributions for O^{8+}-H collisions at $E_P = 1, 8$, and 15 keV/u: (a) $n = 5$ and (b) $n = 6$. TC-BGM results are compared with the presupposed statistical l-distribution.

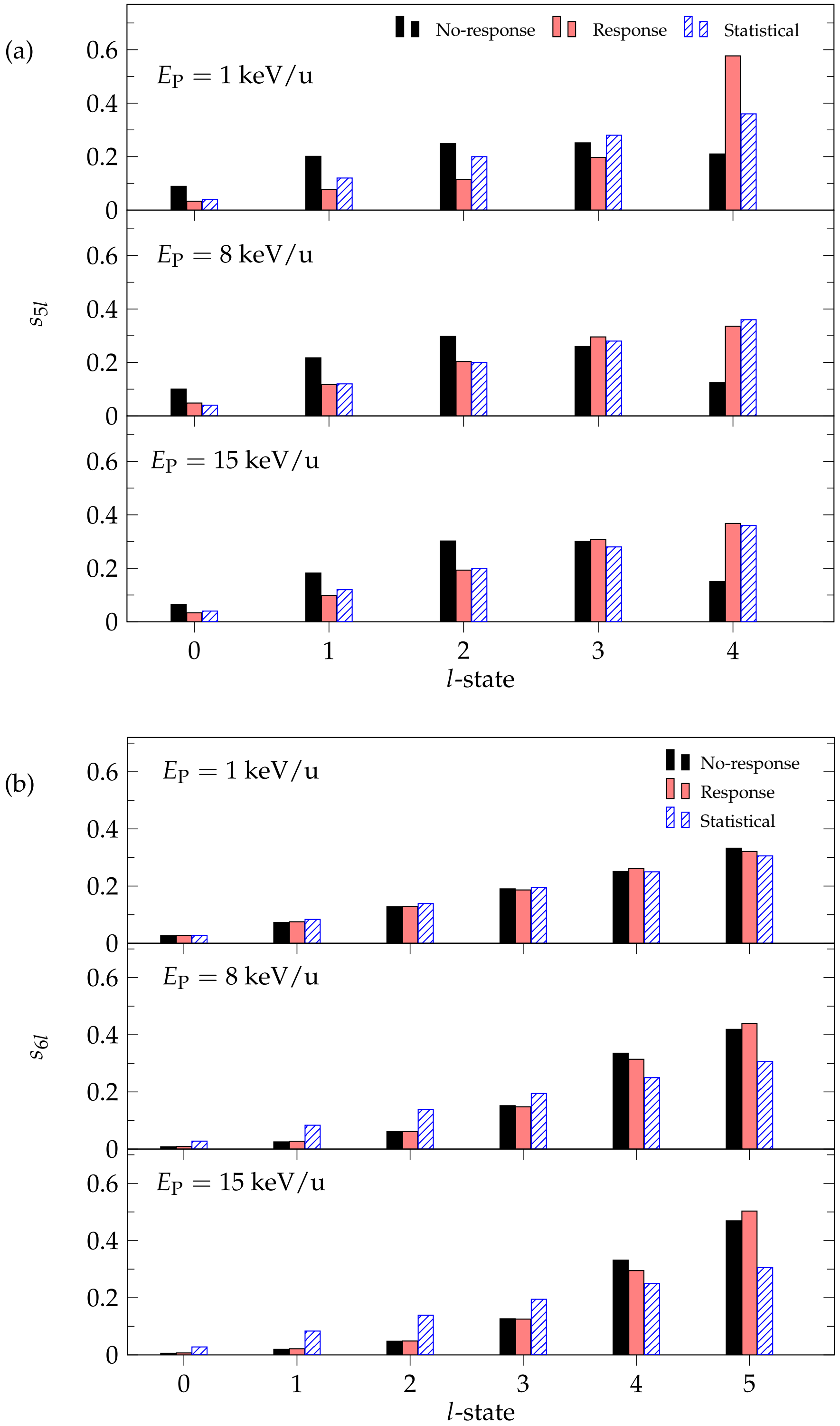

FIG. 7.15: nl pure SEC cross section distributions for O^{8+}-Kr collisions at $E_P = 1$, 8, and 15 keV/u: (a) $n = 5$ and (b) $n = 6$. TC-BGM results are compared with the presupposed statistical l-distribution.

7.4.2 Lyman line-emission ratios

Figure 7.16 shows the Lyman line-emission ratios from O^{8+}-H, and -Kr collisions at impact energies from 0.5 to 15 keV/u. All calculated ratios are from the present TC-BGM calculations. Experimental ratios [61] shown in both columns correspond to O^{8+}-Kr collisions only.

Analysing the present line-emission ratios from Kr collisions, calculations based on the no-response approximation appear to be most consistent with the experimental ratios. Although ratios produced from the combined SEC+ADC processes would be consistent with the experiment of Seely *et al.* [61], it is worth mentioning that the pure SEC ratios also show good agreement with the experimental ratios. The only exception to this are the Ly-ϵ/Ly-α ratios where the results from the response calculations appear closest to the experimental ratios. Even though other response ratios are similar in magnitude at certain impact energies, the overall profiles do not follow the experimental trends. Furthermore, the Ly-ϵ/Ly-α ratios produced from the present calculations are relatively larger than the experimental ratios. The most likely cause for this discrepancy are the Ly-ϵ counts, which correspond to the $6p \rightarrow 1s$ transition, or higher cascades that feed into $6p$, implying that the corresponding cross sections are overestimated. While the Ly-α count might also contribute to this discrepancy, it is unlikely to be the case since a Ly-α count would result in further discrepancies in other line-emission ratios (e.g., Ly-δ/Ly-α).

For the line-emission ratios from O^{8+}-H collisions produced from the present calculations the agreement with the experimental ratios of Kr collisions is overall mixed. Although line-emission ratios of H collisions are similar in magnitude at certain impact energies, the profiles do not necessarily follow the experimental trends, particularly the subdominant ratios involving the Ly-γ and Ly-ϵ lines. This was also shown by Seely *et al.* [61] using the recommended cross sections of H collisions [128] in the radiative cascade calculations (cf. Fig. 7.2). These differences can be attributed to differences in the capture dynamics as shown from the nl-distribution comparisons between the two targets. On the other hand, the present calculations on C^{6+}-H and -Kr collisions also revealed similar differences in capture behaviour between the two targets but show very similar line-emission ratios. This then comes down to differences in the primary capture channels produced by the different projectile ions.

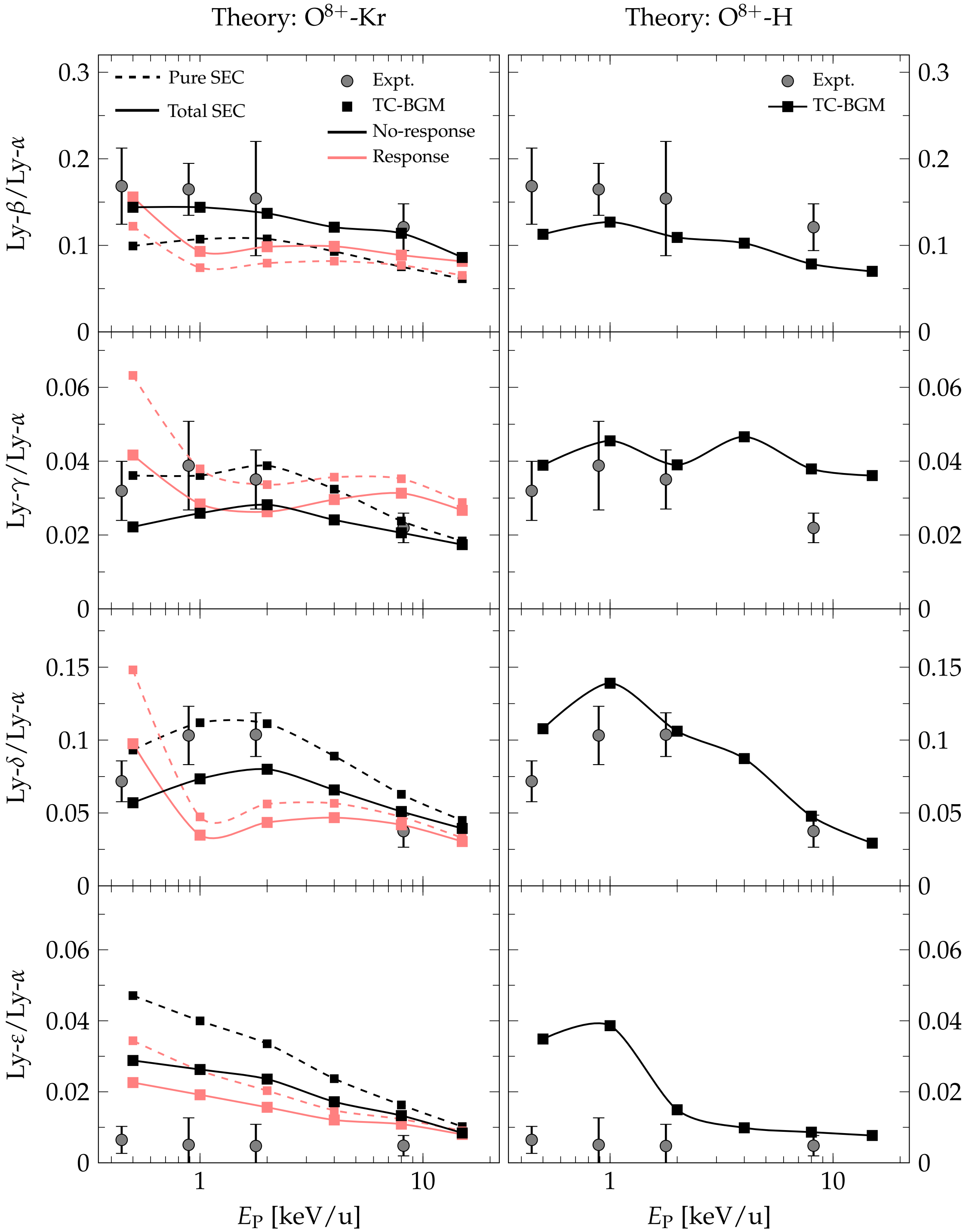

FIG. 7.16: Lyman line-emission ratios of Ly-β/Ly-α, Ly-γ/Ly-α, Ly-δ/Ly-α, and Ly-ϵ/Ly-α. Calculated TC-BGM ratios from O^{8+}-Kr (left column) and O^{8+}-H (right column) collisions. Pure SEC in Kr collisions is represented by dashed curves while total SEC is represented by solid curves. Curves joining the calculated ratios provide visual guidance. Measured ratios [60] in both columns correspond to O^{8+}-Kr collisions.

7.5 CONCLUSIONS

Lyman line-emission ratios from collisions of highly-charged ions with H and Kr were examined using the present TC-BGM performed within the IEM. The experimental studies of Refs. [60, 61] presented an opportunity to provide a set of capture cross sections involving a Kr target using the present analysis. Specifically, collisions of C^{6+}-H and -Kr were analysed from 0.5 to 40 keV/u while collisions of O^{8+}-H and -Kr were analysed from 0.5 to 15 keV/u. The present Lyman line-emission ratios were compared with previous measurements [60, 61].

In the analysis of C^{6+} collisions, the present total capture cross sections of the C^{6+}-H system are in good agreement with the previously reported recommended values [114]. Calculations for C^{6+}-Kr collisions were separated into different variants of the IEM and results using the target-response model describing total SEC (pure SEC and ADC) were very similar to those of C^{6+}-H collisions. However, it was shown that the capture behaviour of partial cross section distributions with respect to impact energy was different between the two targets. Regardless of the distribution behaviour, the corresponding Lyman line-emission ratios from both collision systems showed similar agreement with the experimental ratios [60]. Specifically for Kr collision calculations, the present line-emission ratios using the no-response approximation to describe total SEC are most similar to the measurements, demonstrating the importance of ADC.

Similarly for O^{8+} collisions, the present results of total capture cross sections for O^{8+}-H collisions are consistent with the recommended values [114]. Present calculations using the response model to describe total SEC for O^{8+}-Kr collisions are most similar to the total cross sections of H collisions. Comparisons of partial cross section distributions between the two targets also revealed different behaviours with respect to impact energy. The end result of the Lyman line-emission ratios from Kr collision calculations in the no-response approximation, which included ADC events, showed satisfactory agreement with the experiment while ratios from H collision calculations are overall mixed.

Altogether, the present results indicate that using Kr as a surrogate for H in highly-charged collision experiments should not be treated lightly. Specifically, it was found from present calculations that the capture cross section distributions for Kr collisions revealed behaviours which are different from H collisions. This could restrict certain applications where one may want to use Kr as a surrogate for H.

CHAPTER 8

Summary and outlook

In this dissertation, results of a theoretical study on radiative emissions from slow charge-exchange collisions of highly-charged ions with atoms and molecules have been presented. It is well-known that these collision systems are of significant interest in plasma diagnostics. They are also of significant interest in understanding radiative emissions in astrophysical settings, which has largely inspired the present work. While various experimental studies on these collision systems have been reported, theoretical verifications using quantum-mechanical approaches have been lacking due to practical challenges in obtaining reliable descriptions of capture in slow collisions. This has been the main motivation of this research.

Calculations in this work were carried out using the nonperturbative quantum-mechanical TC-BGM performed within the IEM. It has been thoroughly demonstrated that this approach is capable of describing radiative emissions from SEC in the low-energy regime for various ion-atom and ion-molecule systems. In its current form, the TC-BGM and the various approaches in obtaining the effective ground-state potential of the collision species (i.e., model potentials, OPM) can provide fairly decent total and partial SEC cross sections and subsequent radiative emissions. Although the CTMC approach, which has often been used by various groups to study radiative emissions, can also provide a similar detail on total SEC cross sections, it has its shortcomings when it comes to partial cross sections, which was evident in the comparisons of radiative-emission results discussed in this work.

Successes shown in this work do motivate for new collision studies but not necessarily within the topic of radiative emissions. It should be acknowledged that while the

TC-BGM is adequate for describing electron capture in a variety of collision systems, it relies on models and approximations which do have uncertainties. Future investigations on improved models may benefit the present method. To close this dissertation, a few possible future studies are briefly outlined.

Krypton collisions

The collision study of Ch. 7 is a first attempt to examine electron capture from a Kr target using the TC-BGM. Although no experimental data were available for cross section comparison, the present calculations of the corresponding capture probabilities were found to be well-converged. Given the level of consistency across similar calculations within the noble gas group shown in this work (i.e., He, Ne, Ar), for which the ground-state properties were all obtained from the OPM, it is expected that the cross sections for the Kr results of Ch. 7 are of reasonable accuracy.

Several works on proton and antiproton collisions with noble gases, including Kr, can be found in Ref. [105] (and references therein). Capture and ionization results from the low to nonrelativistic high-energy collisions from these studies serve as an excellent benchmark to study these processes in Kr collisions using the TC-BGM, just as it was done previously for Ar collisions [80]. Net capture in p-Kr collisions is briefly explored here and some preliminary results are shown in Table 8.1; demonstrating that such an analysis is feasible and promising as a future study.

TABLE 8.1: Net capture cross sections (in 10^{-16} cm^2) from p-Kr collisions. TC-BGM results using the no-response approximation and the target-response model. Experimental cross sections are by Rudd *et al.* [106].

E_P (keV/u)	No-response	Response	Expt. [106]
10	27.1	19.4	15.1
20	19.3	14.2	13.1
30	14.5	9.26	8.75
100	1.28	1.20	1.12

Further investigation of time-dependent exchange potential

Through various ion-atom collision studies involving many-electron targets, total capture cross sections from TC-BGM calculations that use a target-response model to describe time-dependent screening on the ground-state (exchange-only) potential consistently showed good agreement with experimental measurements.

As for radiative emissions, results using the TC-BGM in the no-response approximation showed satisfactory agreement with the experimental data while results from using the response model are often mixed. This is an indication that the *nl*-distributions produced by the present model are not always reliable. This could be due to the fact that the current response model is based on a spherical geometry, which may not be sufficient in the presence of a highly-charged projectile ion polarizing the field by a fair amount in close proximity. One could seek an alternative model or attempt a microscopic treatment based on TDDFT. The latter would allow for a more rigorous assessment of the validity and limitations of the IEM since, recall from Ch. 2, the IEM precisely corresponds to the exchange-only limit of the Kohn–Sham scheme. One example is a recent study on He^+-He collisions where a time-dependent exchange potential was obtained by making use of the Krieger-Li-Iafrate approximation to the OPM integral equation in TC-BGM calculations [137].

Radiative stabilization from doubly-excited states

Following the experimental study of Lyman line-emissions from SEC in Ne^{10+} collisions with He, Ne, and Ar, a *K*-shell x-ray spectroscopy study using the COLTRIMS technique was performed on the same collision systems but with a focus on the role of DEC [138]. It was found that radiative stabilization from true double capture is important to the overall x-ray production, possibly due to the projectile being a highly-charged Ne^{10+} ion. These findings provide insight into the high intensity of the $9p \to 1s$ Lyman line observed in P^{15+}-H_2 collisions [139] since energies from radiative decay of $P^{13+}(9l, 9l')$ states are indistinguishable from those of the $9p \to 1s$ transitions [138].

It was shown throughout the present work that DEC cross sections obtained in the IEM tend to be overestimated, particularly involving targets where electron correlation is significant. On the other hand, the collisions studied by Ali *et al.* [138] involve a highly-charged projectile ion, which suggests that correlation may not be important. Regardless, an alternative approach in describing multiple capture on the single-electron level is the IEVM. It was briefly demonstrated in C^{6+}-He collisions that the TC-BGM within this model can yield reliable DEC cross sections (cf. Ch. 5). It would be worthwhile to use the results by Ali *et al.* [138] as a benchmark to further explore the applicability of using the TC-BGM performed within the IEVM for describing radiative emissions from stabilized doubly-excited states in several systems. It may also be useful to compare results from such calculations with those using the IEM to compare and contrast the results between the two models.

Collisions with H_2O and CH_4 at low impact energies

An important insight gained from this research is that the use of a minimal basis set to represent the molecular Hamiltonian of H_2O and CH_4 in spectral representation is not sufficient to reliably describe capture at low impact energies. It was found that the use of a closure approximation to include unoccupied states globally can alleviate this issue. The relative level of success with this approach motivates further exploration of H_2O and CH_4 collisions in the low energy regime. Because slow collisions at only two impact energies were explored in this work, one extension would be to carry out calculations at other energies to explore the extent to which the closure approximation is reliable. Another possible investigation of slow collisions with molecules is fragmentation by electron capture [140, 141]. Such a study may need to rely on empirical branching models to obtain fragmentation cross sections. This approach has been used in previous studies using the TC-BGM in the intermediate and high energy regimes [50, 52] with some level of success.

Role of laser fields in collision-induced radiative emissions

The idea of embedding a laser field in a collision system is one that was first addressed theoretically in the late 1970s [142, 143]. However, because of the absence of experimental investigations and restrictive theoretical models (e.g., limited expansions of the electronic wavefunction), further research on this problem became stagnant for many years. It was only in the early 2000s when this research problem gained new momentum due to the advent of advanced computing power and new numerical methods. This enabled new studies on laser-assisted collisions [144–146], which include calculations using the BGM [47, 147]. Experimental tools and techniques have also advanced considerably to carry out such investigations [148, 149]. In these studies, it was found that the presence of a laser field can enhance or suppress electron capture depending on the laser parameters. If electron capture can be modified with a laser, how would this affect the subsequent radiative emissions? This question is briefly explored here by considering the C^{6+}-H collision system at 1 keV/u following a similar approach as in Refs. [47, 147].

In the IEM framework, the single-electron Hamiltonian of a collision system in an external laser field takes the form

$$\hat{h} = -\frac{1}{2}\nabla^2 + V_{\mathrm{T}} + V_{\mathrm{P}} + \mathbf{r} \cdot \mathbf{E}, \tag{8.1}$$

where $\mathbf{r}$ is the position of the electron with respect to the target centre. For this brief analysis, a uv continuous-wave laser field is considered. The laser field in dipole approximation is given by

$$\mathbf{E}(t) = \boldsymbol{\epsilon}_{\mathrm{pol}} E_0 \sin(\omega t + \delta) \tag{8.2}$$

where $\boldsymbol{\epsilon}_{\mathrm{pol}}$ is the linear polarization, E_0 is the field amplitude, ω is the angular frequency of the field, and δ is the initial phase. A uv laser of moderate field strength, $E_0 = 0.015$ a.u. (corresponding to an intensity of 8×10^{12} W/cm^2) with $\omega = 0.227$ a.u. (corresponding to a wavelength of 200 nm) is chosen. The linear polarization is chosen to be parallel to the projectile beam velocity (i.e., $\boldsymbol{\epsilon}_{\mathrm{pol}} || \mathbf{v}_{\mathrm{P}}$). These parameters ensure that the field ionization in the absence of the projectile ion is negligible. Instead of considering one initial phase of the laser field, a phase-averaged result over $\delta = 0, \pi/2,\ \pi,\ 3\pi/2$ is considered.

Figure 8.1 displays the Lyman line-emission spectra from C^{6+}-H collisions at 1 keV/u comparing photon counts between collisions with and without a laser field. Clearly, there is an enhancement in the Ly-α count due to the laser field. Although enhancements also shown in the Ly-β, Ly-γ, and Ly-ϵ counts, they appear to be minor. Interestingly, the Ly-δ count is shown to be slightly suppressed by this laser field. Obviously, the spectra shown here correspond to only one particular setting as there are a number of parameters in the laser field that can be varied. One may also consider an intense, ultra-fast laser *pulse* as an alternative choice in the calculations as it was done by others [146, 150]. However, such a laser may not be ideal in the lab due to the duty-cycle problem of synchronizing the laser pulse and the collision event. In any case, this brief analysis is merely a demonstration of a possible investigation of collision-induced radiative emissions involving an external laser field.

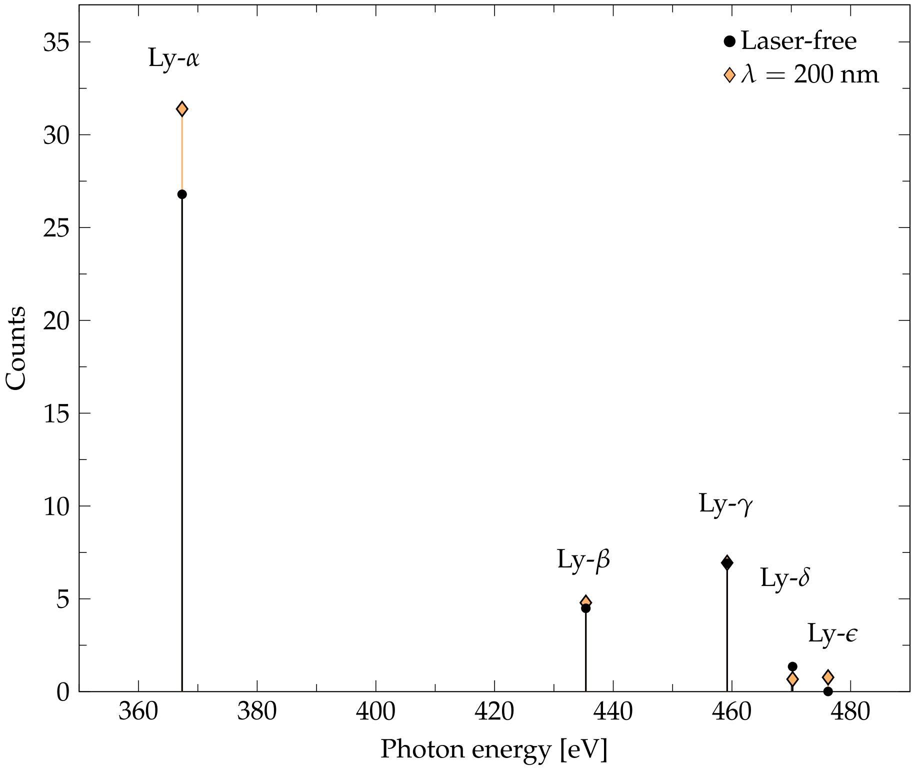

FIG. 8.1: Lyman line-emission spectra from C^{6+}-H collisions at 1 keV/u. TC-BGM results for laser-free and phase-averaged laser-assisted collisions at field strength $E_0 = 0.015$ a.u., at $\lambda = 200$ nm, and longitudinal linear polarization $\boldsymbol{\epsilon}_{\mathrm{pol}} || \mathbf{v}_{\mathrm{P}}$.

Bibliography

[1] C. M. Lisse, K. Dennerl, J. Englhauser, M. Harden, F. E. Marshall, M. J. Mumma, R. Petre, J. P. Pye, M. J. Ricketts, J. Schmitt, J. Trumper, and R. G. West, Discovery of X-ray and Extreme Ultraviolet Emission from Comet C/Hyakutake 1996 B2, Science **274**, 205 (1996).

[2] V. A. Krasnopolsky, Excitation of X rays in comet Hyakutake (C/1996 B2), J. Geophys. Res. **103**, 2069 (1998).

[3] T. E. Cravens, X-ray Emission from Comets, Science **296**, 1042 (2002).

[4] T. E. Cravens, Comet Hyakutake x-ray source: Charge transfer of solar wind heavy ions, Geophys. Res. Lett. **24**, 105 (1997).

[5] R. Wegmann, H. Schmidt, C. Lisse, K. Dennerl, and J. Englhauser, X-rays from comets generated by energetic solar wind particles, Planet. Space Sci. **46**, 603–612 (1998).

[6] P. Beiersdorfer, R. E. Olson, G. V. Brown, H. Chen, C. L. Harris, P. A. Neill, L. Schweikhard, S. B. Utter, and K. Widmann, X-Ray Emission Following Low-Energy Charge Exchange Collisions of Highly Charged Ions, Phys. Rev. Lett. **85**, 5090 (2000).

[7] T. E. Cravens, Heliospheric X-ray Emission Associated with Charge Transfer of the Solar Wind with Interstellar Neutrals, Astrophys. J. **532**, L153 (2000).

[8] D. Koutroumpa, R. Lallement, V. Kharchenko, A. Dalgarno, R. Pepino, V. Izmodenov, and E. Quémerais, Charge-transfer induced EUV and soft X-ray emissions in the heliosphere, Astron. Astrophys. **300**, 18 (2006).

[9] P. Beiersdorfer, C. M. Lisse, R. E. Olson, G. V. Brown, and H. Chen, X-Ray Velocimetry of Solar Wind Ion Impact on Comets, Astrophys. J. **549**, L147 (2001).

[10] R. K. Janev and H. Winter, State-selective electron capture in atom-highly charged ion collisions, Phys. Rep. **117**, 265 (1985).

[11] H. Ryufuku, K. Sasaki, and T. Watanabe, Oscillatory behavior of charge transfer cross sections as a function of the charge of projectiles in low-energy collisions, Phys. Rev. A **21**, 745 (1980).

[12] A. Bárány, G. Astner, H. Cederquist, H. Danared, S. Huldt, P. Hvelplund, A. Johnson, H. Knudsen, L. Liljeby, and K.-G. Rensfelt, Absolute cross sections for multi-electron processes in low energy Ar^{q+}–Ar collisions: Comparison with theory, Nucl. Instrum. Methods Phys. Res. Sect. B **9**, 397 (1985).

[13] A. Niehaus, A classical model for multiple-electron capture in slow collisions of highly charged ions with atoms, J. Phys. B **19**, 2925 (1986).

[14] K. A. Miller, W. W. Smith, T. Ehrenreich, Q. C. Kessel, E. Pollack, C. Verzani, V. A. Kharchenko, A. Chutjian, J. A. Lozano, N. Djuric, and S. J. Smith, X-Ray Emission From Collisions of O^{6+} Ions with CO, Astrophys. J. **742**, 130 (2011).

[15] J. M. Greenberg, Making a comet nucleus, Astron. Astrophys. **380**, 375 (1998).

[16] N. A. Schwadron and T. E. Cravens, Implications of Solar Wind Composition for Cometary X-Rays, Astrophys. J. **544**, 558 (2000).

[17] V. A. Krasnopolsky, CXO X-ray spectroscopy of comets and abundances of heavy ions in the solar wind, Icarus **247**, 95 (2015).

[18] H.-K. Chung, B. J. Braams, K. Bartschat, A. G. Császár, G. W. F. Drake, T. Kirchner, V. Kokoouline, and J. Tennyson, Uncertainty estimates for theoretical atomic and molecular data, J. Phys. D **49**, 363002 (2016).

[19] P. Beiersdorfer, K. R. Boyce, G. V. Brown, H. Chen, S. M. Kahn, R. L. Kelley, M. May, R. E. Olson, F. S. Porter, C. K. Stahle, and W. A. Tillotson, Laboratory Simulation of Charge Exchange-Produced X-ray Emission from Comets, Science **300**, 1558 (2003).

[20] R. E. Olson, Classical Trajectory and Monte Carlo Techniques, in *Springer handbook of atomic, molecular, and optical physics* (Springer New York, New York, NY, 2006), pp. 869–874.

[21] R. E. Olson, n, l distributions in $A^{q+} + H$ electron-capture collisions, Phys. Rev. A **24**, 1726 (1981).

[22] R. L. Becker and A. D. MacKellar, Classical four-body calculations of $^4He^+ + H$ and H+H collisions, J. Phys. B **12**, L345 (1979).

[23] S. Otranto, N. D. Cariatore, and R. E. Olson, X-ray emission produced in charge-exchange collisions between highly charged ions and argon: Role of the multiple electron capture, Phys. Rev. A **90**, 1 (2014).

[24] R. Ali, P. A. Neill, P. Beiersdorfer, C. L. Harris, D. R. Schultz, and P. C. Stancil, Critical Test of Simulations of Charge-Exchange-Induced X-ray Emission in the Solar System, Astrophys. J. **716**, L95 (2010).

[25] M. Fogle, D. Wulf, K. Morgan, D. McCammon, D. G. Seely, I. N. Draganić, and C. C. Havener, X-ray-emission measurements following charge exchange between C^{6+} and H_2, Phys. Rev. A **89**, 042705 (2014).

[26] B. Lippmann and J Schwinger, Variational principles for scattering processes. I, Phys. Rev. **79**, 469 (1950).

[27] E. Schrödinger, An undulatory theory of the mechanics of atoms and molecules, Phys. Rev. **28**, 1049 (1926).

[28] I. B. Abdurakhmanov, A. S. Kadyrov, S. K. Avazbaev, and I. Bray, Solution of the proton-hydrogen scattering problem using a quantum-mechanical two-center convergent close-coupling method, J. Phys. B **49**, 115203 (2016).

[29] B. H. Bransden and M. McDowell, *Charge exchange and the theory of ion-atom collisions* (Oxford: New York: Clarendon Press, 1992).

[30] J. C. Wells, D. R. Schultz, P. Gavras, and M. S. Pindzola, Numerical solution of the time-dependent Schrödinger equation for intermediate-energy collisions of antiprotons with hydrogen, Phys. Rev. A **54**, 593 (1996).

[31] A. Kołakowska, M. S. Pindzola, F. Robicheaux, D. R. Schultz, and J. C. Wells, Excitation and charge transfer in proton-hydrogen collisions, Phys. Rev. A **58**, 2872 (1998).

[32] M. S. Pindzola and M Fogle, Single charge transfer in C^{6+} collisions with H and He atoms, J. Phys. B **48**, 205203 (2015).

[33] W. Fritsch and C. D. Lin, The semiclassical close-coupling description of atomic collisions: Recent developments and results, Phys. Rep. **202**, 1–97 (1991).

[34] J. H. McGuire and L. Weaver, Independent electron approximation for atomic scattering by heavy particles, Phys. Rev. A **16**, 41 (1977).

[35] R. K. Smith and N. S. Brickhouse, Atomic Data Needs for Understanding X-ray Astrophysical Plasmas, in *Advances in atomic, molecular, and optical physics*, Vol. 63, 1st ed. (2014), p. 271.

[36] Y. Wu, P. C. Stancil, Y. Hui, H. P. Liebermann, and R. J Buenker, Theoretical investigation of total and state-dependent charge exchange in O^{6+} collisions with atomic hydrogen, J. Phys. B **45**, 235201 (2012).

[37] V. A. Krasnopolsky, J. B. Greenwood, and P. C. Stancil, X-ray and extreme ultraviolet emissions from comets, Space Sci. Rev. **113**, 271 (2004).

[38] T. R. Kallman and P. Palmeri, Atomic data for x-ray astrophysics, Rev. Mod. Phys. **79**, 79 (2007).

[39] K. Dennerl, Charge Transfer Reactions, Space Sci. Rev. **157**, 57–91 (2010).

[40] H. J. Lüdde, A. Henne, T. Kirchner, and R. M. Dreizler, Optimized dynamical representation of the solution of time-dependent quantum problems, J. Phys. B **29**, 4423 (1996).

[41] O. J. Kroneisen, H. J. Lüdde, T Kirchner, and R. M. Dreizler, The basis generator method: optimized dynamical representation of the solution of time-dependent quantum problems, J. Phys. A **32**, 2141 (1999).

[42] M. Zapukhlyak, T. Kirchner, H. J. Lüdde, S. Knoop, R. Morgenstern, and R. Hoekstra, Inner- and outer-shell electron dynamics in proton collisions with sodium atoms, J. Phys. B **38**, 2353 (2005).

[43] S. Knoop, M. Keim, H. J. Lüdde, T. Kirchner, R. Morgenstern, and R. Hoekstra, State selective single-electron capture in O^{6+} + Na collisions, J. Phys. B **38**, 3163 (2005).

[44] M. Zapukhlyak, T. Kirchner, A. Hasan, B. Tooke, and M. Schulz, Projectile angular-differential cross sections for transfer and transfer excitation in proton collisions with helium, Phys. Rev. A **77**, 012720 (2008).

[45] G. Schenk and T. Kirchner, Multiple ionization of neon atoms in collisions with bare and dressed ions: A mean-field description considering target response, Phys. Rev. A **91**, 052712 (2015).

[46] T. Kirchner, N. Khazai, and L. Gulyás, Role of two-electron excitation-ionization processes in the ionization of lithium atoms by fast ion impact, Phys. Rev. A **89**, 062702 (2014).

[47] T. Kirchner, Laser-field-induced modifications of electron-transfer processes in ion-atom collisions, Phys. Rev. A **69**, 063412 (2004).

[48] S. Knoop, D. Fischer, Y. Xue, M. Zapukhlyak, C. J. Osborne, T. Ergler, T. Ferger, J. Braun, G. Brenner, H. Bruhns, C. Dimopoulou, S. W. Epp, A. J. González Martínez, G. Sikler, R. Soria Orts, H. Tawara, T. Kirchner, J. R. Crespo López-Urrutia, R. Moshammer, J. Ullrich, and R. Hoekstra, Single-electron capture in keV Ar $^{15+...18+}$+He collisions, J. Phys. B **41**, 195203 (2008).

[49] H. J. Lüdde, T. Spranger, M. Horbatsch, and T. Kirchner, Nonperturbative, quantum-mechanical approach to ion collisions from molecular targets, Phys. Rev. A **80**, 060702 (2009).

[50] M. Murakami, T. Kirchner, M. Horbatsch, and H. J. Lüdde, Single and multiple electron removal processes in proton–water-molecule collisions, Phys. Rev. A **85**, 052704 (2012).

[51] M. Murakami, T. Kirchner, M. Horbatsch, and H. J. Lüdde, Quantum-mechanical calculation of multiple electron removal and fragmentation cross sections in He^+-H_2O collisions, Phys. Rev. A **86**, 022719 (2012).

[52] A. Salehzadeh and T. Kirchner, Fragmentation of methane molecules by proton and antiproton impact, Eur. Phys. J. D **71**, 66 (2017).

[53] A. Salehzadeh and T. Kirchner, Strong multiple-capture effect in slow Ar $^{17+}$ -Ar collisions: a quantum mechanical analysis, J. Phys. B **46**, 025201 (2013).

[54] A. C. K. Leung and T. Kirchner, Independent-electron analysis of the x-ray spectra from single-electron capture in Ne^{10+} collisions with He, Ne, and Ar atoms, Phys. Rev. A **92**, 032712 (2015).

[55] L. Liu, J. G. Wang, and R. K. Janev, Charge-transfer-induced x-ray spectra in collisions of Ne^{10+} with He and Ne atoms, Phys. Rev. A **89**, 012710 (2014).

[56] A. C. K. Leung and T. Kirchner, Analysis of x-ray emission spectra in charge-exchange collisions of C^{6+} with He and H_2, Phys. Rev. A **93**, 052710 (2016).

[57] X. Defay, K. Morgan, D. McCammon, D. Wulf, V. M. Andrianarijaona, M. Fogle, D. G. Seely, I. N. Draganić, and C. C. Havener, X-ray emission measurements following charge exchange between C^{6+} and He, Phys. Rev. A **88**, 052702 (2013).

[58] A. C. K. Leung and T. Kirchner, Radiative-emission analysis in charge-exchange collisions of O^{6+} with argon, water, and methane, Phys. Rev. A **95**, 042703 (2017).

[59] J. R. Machacek, D. P. Mahapatra, D. R. Schultz, Y. Ralchenko, A. Moradmand, M. O. A. El Ghazaly, and A. Chutjian, Solar-wind ion-driven x-ray emission from cometary and planetary atmospheres: measurements and theoretical predictions of charge-exchange cross-sections and emission spectra for O^{6+}+H_2O, CO, CO_2, CH_4, N_2, NO, N_2O, and Ar, Astrophys. J. **809**, 75 (2015).

[60] V. Andrianarijaona, D. Wulf, D. McCammon, D. Seely, and C. Havener, Radiance line ratios Ly-β/Ly-α, Ly-γ/Ly-α, Ly-δ/Ly-α, and Ly-ϵ/Ly-α for soft X-ray emissions following charge exchange between C^{6+} and Kr, Nucl. Instrum. Methods Phys. Res. Sect. B **350**, 122 (2015).

[61] D. G. Seely, V. M. Andrianarijaona, D. Wulf, K. Morgan, D. McCammon, M. Fogle, P. C. Stancil, R. T. Zhang, and C. C. Havener, Line ratios for soft-x-ray emission following charge exchange between O^{8+} and Kr, Phys. Rev. A **95**, 052704 (2017).

[62] M. Born and R. Oppenheimer, Zur Quantentheorie der Molekeln, Ann. Phys. **389**, 457 (1927).

[63] E. Runge and E. K. U. Gross, Density-functional theory for time-dependent systems, Phys. Rev. Lett. **52**, 997 (1984).

[64] W. Kohn and L. J. Sham, Self-Consistent Equations Including Exchange and Correlation Effects, Phys. Rev. **140**, A1133 (1965).

[65] R. Daniele, Wave functions and effective potentials of alkalilike ions. I. Lithiumlike ions, J. Chem. Phys. **70**, 3462 (1979).

[66] R. Daniele, Wave functions and effective potentials of alkalilike ions. II. Sodiumlike ions, J. Chem. Phys. **72**, 1276 (1980).

[67] R. Shingal, Charge transfer, target excitation and ionisation in Be 2+ +Li and Li + +Be + collisions, J. Phys. B **21**, 2065–2076 (1988).

[68] D. Elizaga, L. F. Errea, J. D. Gorfinkiel, C. Illescas, L. Méndez, A. Macías, A. Riera, A. Rojas, O. J. Kroneisen, T. Kirchner, H. J. Lüdde, A. Henne, and R. M. Dreizler, Theoretical analysis of electron capture and electron loss in Be^{4+} $+H_2$ and H^{+} $+H_2$ collisions, J. Phys. B **32**, 857 (1999).

[69] L. F. Errea, J. D. Gorfinkiel, C. Harel, H. Jouin, A. Macías, L. Méndez, B. Pons, and A. Riera, Model potential treatment of C^{4+}+H_2 collisions at low impact energies, J. Phys. B **33**, 3107 (2000).

[70] W. Fritsch and C. D. Lin, Atomic-orbital expansion study for the (quasi-)two-electron collision system O^{6+}+He and C^{6+}+He, J. Phys. B **19**, 2683 (1986).

[71] J. D. Talman and W. F. Shadwick, Optimized effective atomic central potential, Phys. Rev. A **14**, 36 (1976).

[72] J. C. Slater, A Simplification of the Hartree-Fock Method, Phys. Rev. **81**, 385 (1951).

[73] R. T. Sharp and G. K. Horton, A Variational Approach to the Unipotential Many-Electron Problem, Phys. Rev. **90**, 317 (1953).

[74] E. Engel and S. H. Vosko, Accurate optimized-potential-model solutions for spherical spin-polarized atoms: Evidence for limitations of the exchange-only local spin-density and generalized-gradient approximations, Phys. Rev. A **47**, 2800 (1993).

[75] E. Engel and R. M. Dreizler, *Density Functional Theory*, Theoretical and Mathematical Physics (Springer Berlin Heidelberg, 2011).

[76] T. Kirchner, L. Gulyás, H. J. Lüdde, A. Henne, E. Engel, and R. M. Dreizler, Electronic exchange effects in p+Ne and p+Ar collisions, Phys. Rev. Lett. **79**, 1658 (1997).

[77] T. Kirchner, L. Gulyás, H. J. Lüdde, E. Engel, and R. M. Dreizler, Influence of electronic exchange on single and multiple processes in collisions between bare ions and noble-gas atoms, Phys. Rev. A **58**, 2063 (1998).

[78] T. Kirchner, M. Horbatsch, H. J. Lüdde, and R. M. Dreizler, Time-dependent screening effects in ion-atom collisions with many active electrons, Phys. Rev. A **62**, 042704 (2000).

[79] T. Kirchner and M. Horbatsch, Nonperturbative calculation of projectile-electron loss, target ionization, and capture in He^++Ne collisions, Phys. Rev. A **63**, 062718 (2001).

[80] T. Kirchner, M. Horbatsch, and H. J. Lüdde, Time-dependent independent-particle model calculation of multiple capture and ionization processes in p-Ar, $\bar{p}$-Ar, and He^{2+}-Ar collisions, Phys. Rev. A **66**, 052719 (2002).

[81] I. M. Cheshire, D. F. Gallaher, and a. J. Taylor, Coupled-state calculations of proton-hydrogen scattering with a pseudo-state expansion, J. Phys. B **3**, 813 (1970).

[82] W. Fritsch and C. D. Lin, Atomic-orbital-expansion studies of electron transfer in bare-nucleus Z ($Z = 2, 4$–8) – hydrogen-atom collisions, Phys. Rev. A **29**, 3039 (1984).

[83] T. Kirchner, H. Lüdde, M. Horbatsch, and R. Dreizler, Quantum-mechanical description of ionization, capture, and excitation in proton collisions with atomic oxygen, Phys. Rev. A **61**, 1 (2000).

[84] T. Kirchner, M. Horbatsch, and H. Lüdde, Nonperturbative calculation of charge-changing processes in C^{4+} scattering from neon atoms, Phys. Rev. A **64**, 1 (2001).

[85] S. Aung, R. M. Pitzer, and S. I. Chan, Approximate Hartree–Fock wavefunctions, one-electron properties, and electronic structure of the water molecule, J. Chem. Phys. **49**, 2071 (1968).

[86] R. M. Pitzer and D. P. Merrifield, Minimum Basis Wavefunctions for Water, J. Chem. Phys. **52**, 4782 (1970).

[87] M. Horbatsch, A semiclassical time-dependent Hartree model calculation of capture and multiple ionization in heavy ion-Ar collisions, Phys. Lett. A **187**, 185 (1994).

[88] M. Mack, Electron spectroscopy in collisions with multiply charged ions, Nucl. Instrum. Methods Phys. Res. Sect. B **23**, 74 (1987).

[89] R. Hoekstra, D. Ciric, F. J. de Heer, and R. Morgenstern, State Selective Electron Capture in Collisions of C^{6+} and O^{8+} on Atomic and Molecular Hydrogen Studied by Photon Emission Spectroscopy, Phys. Scr. **T28**, 81 (1989).

[90] R. Hoekstra, J. P. M. Beijers, A. R. Schlatmann, R. Morgenstern, and F. J. de Heer, State-selective charge transfer in slow collisions of C^{4+} with H and H_2, Phys. Rev. A **41**, 4800 (1990).

[91] R. Ali, C. L. Cocke, M. L. A. Raphaelian, and M. Stockli, Multielectron processes in 10-keV/u Ar^{q+} ($5 \leq q \leq 17$) on Ar collisions, Phys. Rev. A **49**, 3586 (1994).

[92] L. J. Curtis, A Diagrammatic Mnemonic for Calculation of Cascading Level Populations, Am. J. Phys. **36**, 1123 (1968).

[93] J. J. Sakurai, *Modern Quantum Mechanics, Revised Edition* (Addison-Wesley, 1995).

[94] H. Friedrich, *Theoretical Atomic Physics* (Springer-Verlag, Berlin/Heidelberg, 2006).

[95] D. Röhrbein, T. Kirchner, and S. Fritzsche, Role of cascade and Auger effects in the enhanced population of the $C^{3+}(1s2s2p\ ^4P)$ states following single-electron capture in $C^{4+}(1s2s\ ^3S)$-He collisions, Phys. Rev. A **81**, 042701 (2010).

[96] S. Fritzsche, The RATIP program for relativistic calculations of atomic transition, ionization and recombination properties, Comput. Phys. Commun. **183**, 1525 (2012).

[97] S. Fritzsche, Large-scale accurate structure calculations for open-shell atoms and ions, Phys. Scr. **T100**, 37 (2002).

[98] I. Grant, *Relativistic Quantum Theory of Atoms and Molecules* (Springer, New York, NY, 2007).

[99] C. Froese Fischer and G. Gaigalas, Multiconfiguration Dirac-Hartree-Fock energy levels and transition probabilities for W XXXVIII, Phys. Rev. A **85**, 042501 (2012).

[100] S. M. Younger and W. L. Wiese, Theoretical simulation of beam-foil decay curves for resonance transitions of heavy ions, Phys. Rev. A **17**, 1944 (1978).

[101] D. Dijkkamp, D. Ciric, E. Vileg, A. de Boer, and F. J. de Heer, Subshell-selective electron capture in collisions of C^{4+} , N^{5+} , O^{6+} with H, H_2 and He, J. Phys. B **18**, 4763 (1985).

[102] R. Dörner, V. Mergel, O. Jagutzki, L. Spielberger, J. Ullrich, R. Moshammer, and H. Schmidt-Böcking, Cold target recoil ion momentum spectroscopy: a 'momentum microscope' to view atomic collision dynamics, Phys. Rep. **330**, 95 (2000).

[103] J. R. Rumble, ed., *CRC Handbook of Chemistry and Physics*, 98th (CRC Press/Taylor & Francis, Boca Raton, FL).

[104] M. M. Sant'Anna, E. C. Montenegro, and J. H. McGuire, Inversion relations for exclusive and inclusive cross sections within the independent electron approximation, Phys. Rev. A **58**, 2148 (1998).

[105] C. C. Montanari and J. E. Miraglia, Antiproton, proton and electron impact multiple ionization of rare gases, J. Phys. B **45**, 105201 (2012).

[106] M. E. Rudd, R. D. Dubois, L. H. Toburen, C. A. Ratcliffe, and T. V. Goffe, Cross sections for ionization of gases by 5-4000-keV protons and for electron capture by 5-150-keV protons, Phys. Rev. A **28**, 3244 (1983).

[107] S. J. Smith, Electron Impact Excitation of Atoms, Rev. Mod. Phys. **40**, 238 (1968).

[108] D. Vernhet, A. Chetioui, K. Wohrer, J. P. Rozet, P. Piquemal, D. Hitz, S. Dousson, A. Salin, and C Stephan, Alignment of Ne^{8+} $n\ ^1P$ states by collisions of Ne^{9+} with H_2 at 4 keV/amu, Phys. Rev. A **32**, 1256 (1985).

[109] J. B. Greenwood, I. D. Williams, S. J. Smith, and A Chutjian, Experimental investigation of the processes determining x-ray emission intensities from charge-exchange collisions, Phys. Rev. A **63**, 062707 (2001).

[110] I. N. Draganić, D. G. Seely, and C. C. Havener, Low-energy charge transfer between C^{5+} and atomic hydrogen, Phys. Rev. A **83**, 054701 (2011).

[111] D. McCammon, K. Barger, D. E. Brandl, R. P. Brekosky, S. G. Crowder, J. D. Gygax, R. L. Kelley, C. A. Kilbourne, M. A. Lindeman, F. S. Porter, L. E. Rocks, and A. E. Szymkowiak, The X-ray Quantum Calorimeter Sounding Rocket Experiment: Improvements for the Next Flight, J. Low Temp. Phys. **151**, 715 (2008).

[112] M. Kimura and R. E. Olson, Electron capture to (nl) states in collisions of C^{4+} and C^{6+} with He, J. Phys. B **17**, L713 (1984).

[113] M. Kimura, Theoretical investigation of charge transfer in collisions of C^{6+} and N^{7+} ions with H and H_2 targets, Phys. Rev. A **33**, 4440 (1986).

[114] R. Janev, R. Phaneuf, and H. Hunter, Recommmended cross sections for electron capture and ionization in collisions of C^{q+} and O^{q+} ions with H, He, and H_2, At. Data Nucl. Data Tables **40**, 249 (1988).

[115] C. Harel, H. Jouin, and B. Pons, Double capture in C^{6+} -He collisions at low impact energies, J. Phys. B **24**, L425 (1991).

[116] N. Stolterfoht, K. Sommer, J. K. Swenson, C. C. Havener, and F. W. Meyer, Electron-correlation effects in double-electron-capture collisions of 60-keV C^{6+} with He, Phys. Rev. A **42**, 5396 (1990).

[117] L. Chen, J. Bernard, S. Martin, A. Denis, and J. Désesquelles, Two-electron capture and stabilization in collisions of C^{6+} with rare-gas targets at low energy, Phys. Rev. A **54**, 3049 (1996).

[118] R. Shingal and C. D. Lin, Calculations of two-electron transition cross sections between fully stripped ions and helium atoms, J. Phys. B **24**, 251–264 (1991).

[119] Y. D. Wang, C. D. Lin, N. Toshima, and Z. Chen, Ionization and charge transfer in collisions of highly charged ions with helium at low velocity, Phys. Rev. A **52**, 2852 (1995).

[120] M. McCartney, The double ionization of helium by ion impact, J. Phys. B **30**, L155 (1997).

[121] K. M. Dunseath and F. Crothers, Transfer and ionization processes during the collision of fast H^{+} , He^{2+} nuclei with helium, J. Phys. B **24**, 5003 (1991).

[122] J. Burgdofer, R. Morgenstern, and A. Niehaus, Angular momentum distribution in the classical over-barrier model for electron capture into highly charged slow projectiles, J. Phys. B **19**, L507 (1986).

[123] F. W. Meyer, A. M. Howald, C. C. Havener, and R. A. Phaneuf, Low-energy total-electron-capture cross sections for fully stripped and H-like projectiles incident on H and H_2, Phys. Rev. A **32**, 3310 (1985).

[124] D. Sprecher, C. Jungen, W. Ubachs, and F. Merkt, Towards measuring the ionisation and dissociation energies of molecular hydrogen with sub-MHz accuracy, Faraday Discuss. **150**, 51 (2011).

[125] M. Mack, J. H. Nijland, P. v. d. Straten, A. Niehaus, and R. Morgenstern, Correlation in double electron capture in collisions of fully stripped ions on He andH_2, Phys. Rev. A **39**, 3846 (1989).

[126] R. J. Mawhorter, A. Chutjian, T. E. Cravens, N. Djurić, S. Hossain, C. M. Lisse, J. A. MacAskill, S. J. Smith, J. Simcic, and I. D. Williams, Absolute single and multiple charge exchange cross sections for highly charged C, O, and Ne ions on H_2O, CO, and CO_2, Phys. Rev. A **75**, 032704 (2007).

[127] D. Bodewits and R. Hoekstra, Electron capture in collisions between O^{6+} ions and H_2O molecules, Phys. Rev. A **76**, 032703 (2007).

[128] R. Janev, R. Phaneuf, H. Tawara, and T. Shirai, Recommended Cross Sections for State-Selective Electron Capture in Collisions of C^{6+} and O^{8+} Ions with Atomic Hydrogen, At. Data Nucl. Data Tables **55**, 201 (1993).

[129] K. Aashamar, T. M. Luke, and J. D. Talman, Optimized central potentials for atomic ground-state wavefunctions, At. Data Nucl. Data Tables **22**, 443–472 (1978).

[130] S. Martin, J. Bernard, L. Chen, A. Denis, and J. Désesquelles, Double Rydberg States Formed in Stabilized Triple Electron Capture, Phys. Rev. Lett. **77**, 4306 (1996).

[131] E. J. Shipsey, T. A. Green, and J. C. Browne, Modified method of perturbed stationary states. V. Electron-capture cross sections for the reaction O^{8+}+H(1s)→ $O^{7+}(n,l)$ + H^+, Phys. Rev. A **27**, 821 (1983).

[132] E. Edgu-Fry, A. Wech, J. Stuhlman, T. G. Lee, C. D. Lin, and C. L. Cocke, Cold-target recoil-ion momentum spectroscopy studies of capture from atomic and molecular hydrogen by O^{8+} and Ar^{8+}, Phys. Rev. A **69**, 052714 (2004).

[133] T.-G. Lee, M. Hesse, A.-T. Le, and C. D. Lin, Charge transfer in slow collisions of O^{8+} and Ar^{8+} ions with H(1s) below 2 keV/amu, Phys. Rev. A **70**, 012702 (2004).

[134] C. D. Lin, Hyperspherical coordinate approach to atomic and other Coulombic three-body systems, Phys. Rep. **257**, 1–83 (1995).

[135] J. B. Delos, Theory of electronic transitions in slow atomic collisions, Rev. Mod. Phys. **53**, 287 (1981).

[136] S. Martin, J. Bernard, A. Denis, J. Désesquelles, L. Chen, and Y. Ouerdane, True double capture in collisions of bare and hydrogenlike ions with rare-gas atoms ($Z = 7$–13), Phys. Rev. A **50**, 2322 (1994).

[137] M. Baxter, T. Kirchner, and E. Engel, Time-dependent spin-density-functional-theory description of He^+-He collisions, Phys. Rev. A **96**, 032708 (2017).

[138] R. Ali, P. Beiersdorfer, C. L. Harris, and P. A. Neill, Charge-exchange x-ray spectra: Evidence for significant contributions from radiative decays of doubly excited states, Phys. Rev. A **93**, 012711 (2016).

[139] M. A. Leutenegger, P. Beiersdorfer, G. V. Brown, R. L. Kelley, C. A. Kilbourne, and F. S. Porter, Measurement of Anomalously Strong Emission from the $1s$-$9p$ Transition in the Spectrum of H-Like Phosphorus Following Charge Exchange with Molecular, Phys. Rev. Lett. **105**, 063201 (2010).

[140] B. Seredyuk, R. W. McCullough, and H. B. Gilbody, One-electron capture mechanisms in collisions of He-like O and C ions with molecules of astrophysical interest, Phys. Rev. A **72**, 022710 (2005).

[141] B. Seredyuk, R. W. McCullough, H. Tawara, H. B. Gilbody, D. Bodewits, R. Hoekstra, A. G.G. M. Tielens, P. Sobocinski, D. Pesic, R. Hellhammer, B. Sulik, N. Stolterfoht, O. Abu-Haija, and E. Y. Kamber, Charge exchange and dissociative processes in collisions of slow He^{2+} ions with H_2O molecules, Phys. Rev. A **71**, 022705 (2005).

[142] M. H. Mittleman, Atomic charge transfer in the presence of a laser field, Phys. Rev. A **14**, 586 (1976).

[143] D. A. Copeland and C. L. Tang, Photon–assisted nonresonant charge exchange: A simple molecular model, J. Chem. Phys. **67**, 850 (1977).

[144] L. B. Madsen, J. P. Hansen, and L. Kocbach, Excitation in Ion-Atom Collisions Inside Subfemtosecond Laser Pulses, Phys. Rev. Lett. **89**, 093202 (2002).

[145] M. S. Pindzola, T. Minami, and D. R. Schultz, Laser-modified charge-transfer processes in proton collisions with lithium atoms, Phys. Rev. A **68**, 013404 (2003).

[146] F. Anis, V. Roudnev, R. Cabrera-Trujillo, and B. D. Esry, Laser-assisted charge transfer in He^{2+}+H collisions, Phys. Rev. A **73**, 043414 (2006).

[147] T. Kirchner, Laser-field enhanced electron transfer in p-Ne and p-Ar collisions, Phys. Rev. A **75**, 025401 (2007).

[148] Z. Lu, D. Chen, R. Fan, and Y. Xia, Femtosecond laser field induced modifications of electron-transfer processes in Ne^+-He collisions, Appl. Phys. Lett. **100**, 014105 (2012).

[149] Z. Lu, D. Chen, R. Fan, and Y. Xia, Laser-induced quadrupole-quadrupole collisional energy transfer in Xe-Kr systems, Phys. Rev. A **85**, 063402 (2012).

[150] F. J. Domínguez-Gutiérrez and R. Cabrera-Trujillo, Large increase in the electron capture and excitation cross sections for Li^+ colliding with atomic H under UV laser assistance, J. Phys. B **48**, 135202 (2015).

Appendices

A. CROSS SECTIONS FOR Ne^{10+} COLLISIONS WITH He, Ne, AND Ar

The *nl* capture cross sections from the TC-BGM calculation using the target-response model performed in Ch. 4 are listed in Table A1.

TABLE A1: *nl* capture cross sections (in 10^{-16} cm^2) from TC-BGM (with response model).

TC-BGM IEM approximation: Target response						
States	Ne^{10+}-He		Ne^{10+}-Ne		Ne^{10+}-Ar	
(n, l)	Net	SEC	Net	SEC	Net	SEC
$3, 0$	0.04161	0.00712	2.396	0.043	3.131	0.002462
$3, 1$	0.08004	0.01303	5.967	0.099	9.640	0.011226
$3, 2$	0.04956	0.00857	9.332	0.154	12.870	0.031634
$4, 0$	1.640	0.400	1.533	0.2218	2.576	0.0663
$4, 1$	5.129	1.101	4.683	0.4429	8.105	0.1621
$4, 2$	7.494	1.524	8.645	0.7607	12.962	0.2984
$4, 3$	6.168	1.200	14.252	1.3187	14.657	0.3618
$5, 0$	0.946	0.471	0.917	0.7508	2.006	0.319
$5, 1$	2.787	1.618	2.734	1.3718	6.181	0.664
$5, 2$	5.201	3.228	5.808	2.5852	10.269	1.091
$5, 3$	8.466	4.815	10.514	4.0832	17.110	1.586
$5, 4$	7.529	4.610	14.895	5.2729	22.182	1.954
$6, 0$	0.063	0.009	0.099	0.0132	1.579	0.852
$6, 1$	0.147	0.024	0.240	0.0284	4.383	1.593
$6, 2$	0.158	0.026	0.371	0.0609	7.433	2.970
$6, 3$	0.266	0.050	0.439	0.1277	12.325	4.628
$6, 4$	0.447	0.110	0.710	0.2540	19.145	6.463
$6, 5$	0.368	0.129	0.808	0.3755	23.628	6.958
$7, 0$	0.00517	0.00118	0.038	0.0013	0.236	0.054
$7, 1$	0.01367	0.00291	0.098	0.0034	0.577	0.116
$7, 2$	0.02133	0.00400	0.151	0.0054	0.926	0.251
$7, 3$	0.02093	0.00485	0.166	0.0057	1.399	0.492
$7, 4$	0.02831	0.00630	0.151	0.0051	2.037	0.960
$7, 5$	0.02516	0.00600	0.148	0.0047	2.999	1.766
$7, 6$	0.01791	0.00496	0.110	0.0057	4.518	2.357

B. CROSS SECTIONS FOR C^{6+}-He AND C^{6+}-H$_2$ COLLISIONS

The *nl* pure SEC cross sections from C^{6+}-He collisions produced from present calculations in Ch. 5 are shown in Fig. B1. Likewise, *nl* pure SEC cross sections for C^{6+}-H$_2$ collisions are shown in Fig. B2 and partial cross sections of ADC are shown in Fig. B3. Partial cross sections for all other *n*-states were found to be negligible.

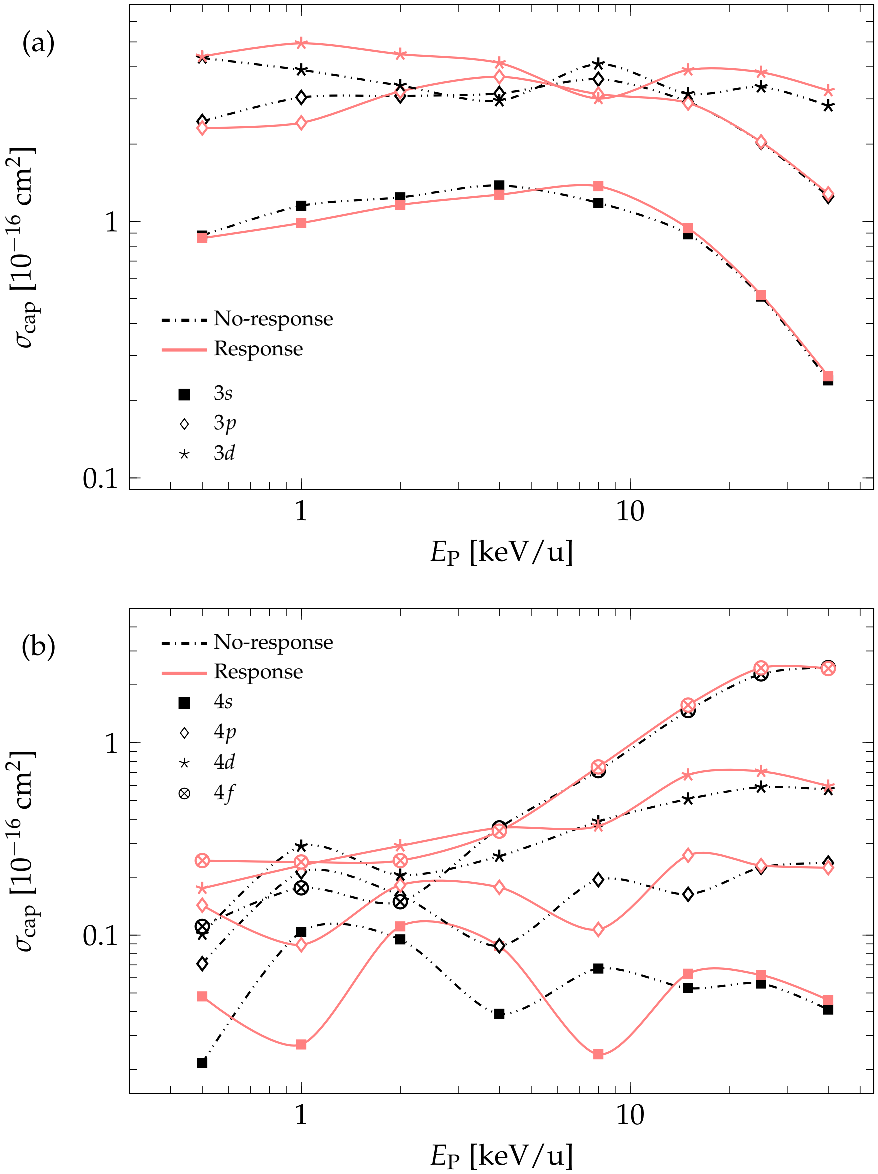

FIG. B1: *nl* pure SEC cross sections for C^{6+}-He collisions with respect to impact energy. Partial cross sections for: (a) $n = 3$, (b) $n = 4$.

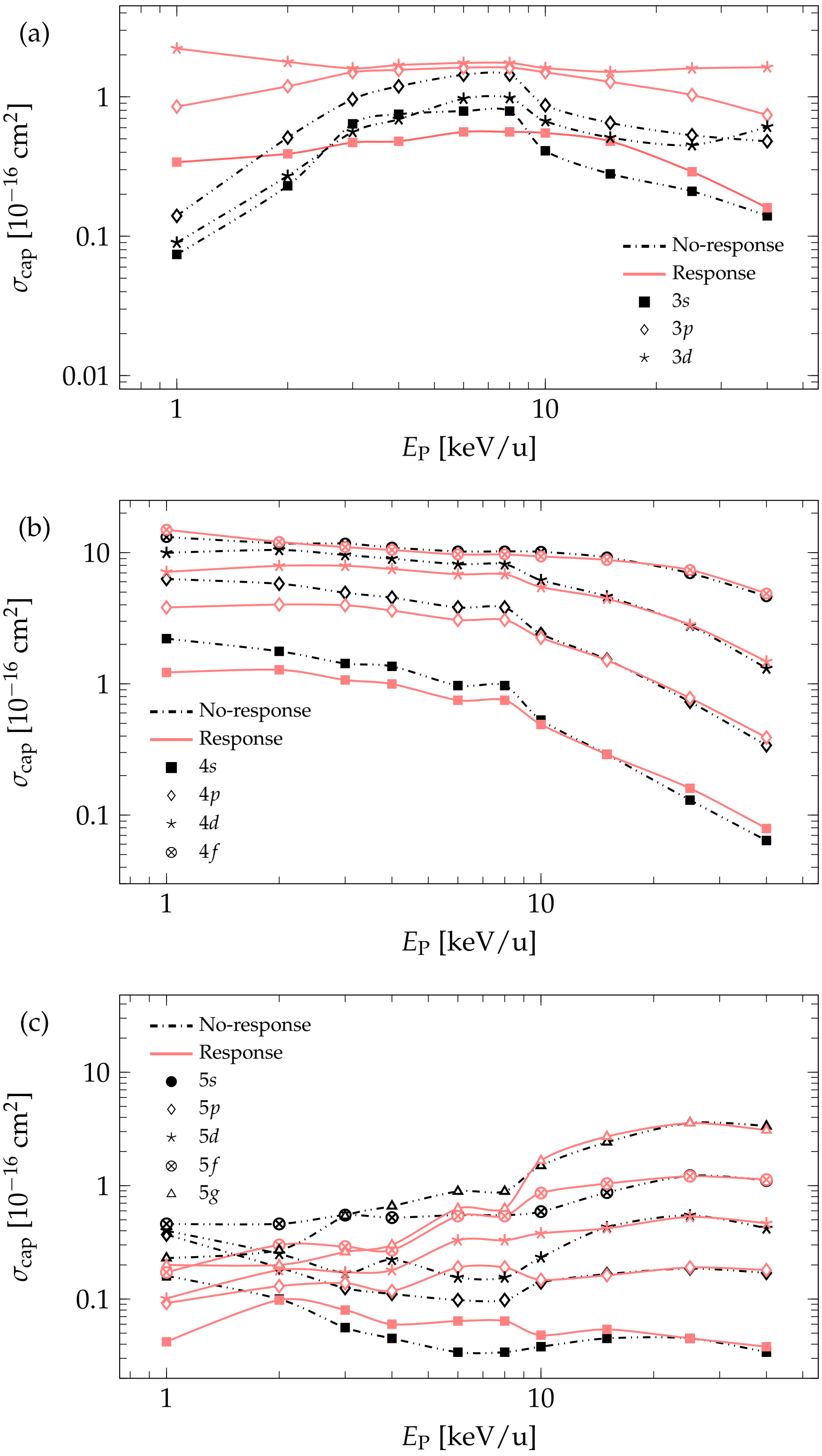

FIG. B2: *nl* pure SEC cross sections for C^{6+}-H_2 collisions with respect to impact energy. Partial cross sections for: (a) $n = 3$, (b) $n = 4$, (c) $n = 5$.

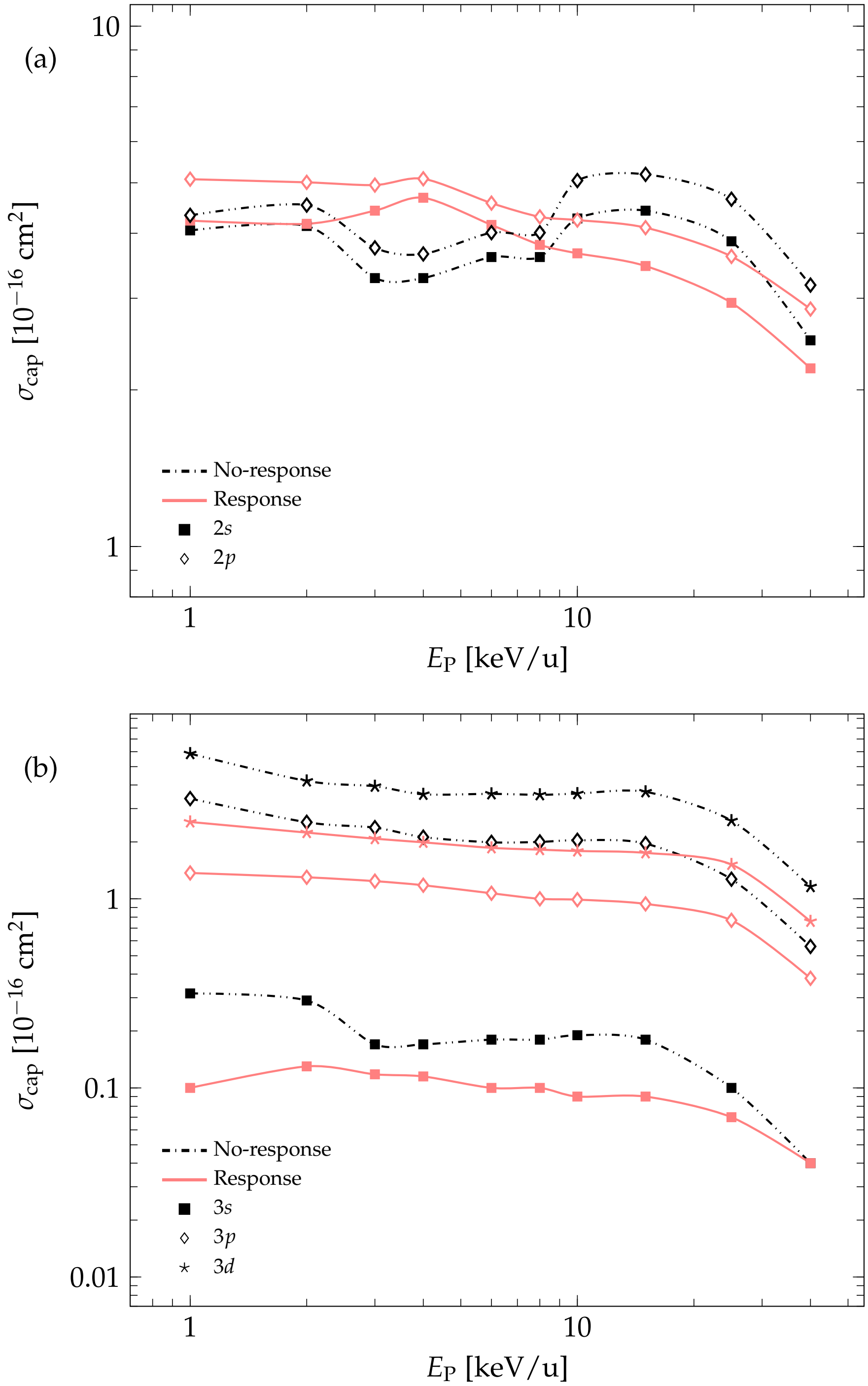

FIG. B3: *nl* ADC cross sections for C^{6+}-H_2 collisions with respect to impact energy. Partial cross sections for: (a) $n = 2$, (b) $n = 3$.

C. CROSS SECTIONS FOR O^{6+}-Ar, -H_2O, AND -CH_4 COLLISIONS

In Ch. 6, results of the *nl* capture cross sections based on contributions from both pure SEC and ADC were discussed. Table C2 lists the corresponding 3*l* cross sections of pure SEC.

TABLE C2: TC-BGM 3*l* pure SEC cross sections (in 10^{-16} cm^2).

	Ar			
States (n, l)	No-response	Response	H_2O	CH_4
$E_P = 1.17$ keV/u				
3, 0	0.07	3.94	1.36	0.11
3, 1	0.27	2.35	0.73	0.81
3, 2	0.10	0.47	0.37	0.40

	Ar			
States (n, l)	No-response	Response	H_2O	CH_4
$E_P = 2.33$ keV/u				
3, 0	0.17	3.10	1.79	0.16
3, 1	0.31	1.21	1.11	0.76
3, 2	0.16	0.52	0.50	0.33

D. CROSS SECTIONS FOR C^{6+} AND O^{8+} COLLISIONS WITH H AND KR

The *nl* capture cross sections for the dominant capture states with respect to impact energy obtained from the present TC-BGM calculations for collisions studied in Ch. 7 are shown in this section. Figure D4 shows the partial cross sections from C^{6+}-H collisions for $n = 4$ and $n = 5$. Partial pure SEC cross sections from C^{6+}-Kr collisions for $n = 4$ and $n = 5$ are shown in Fig. D5 while ADC cross sections for $n = 2$ and $n = 3$ are shown in Fig. D6. Similarly, Fig. D7 shows the partial cross sections from O^{8+}-H collisions for $n = 5$ and $n = 6$. Partial pure SEC cross sections from O^{8+}-Kr collisions for $n = 5$ and $n = 6$ are shown in Fig. D8 while ADC cross sections for $n = 3$ and $n = 4$ are shown in Fig. D9.

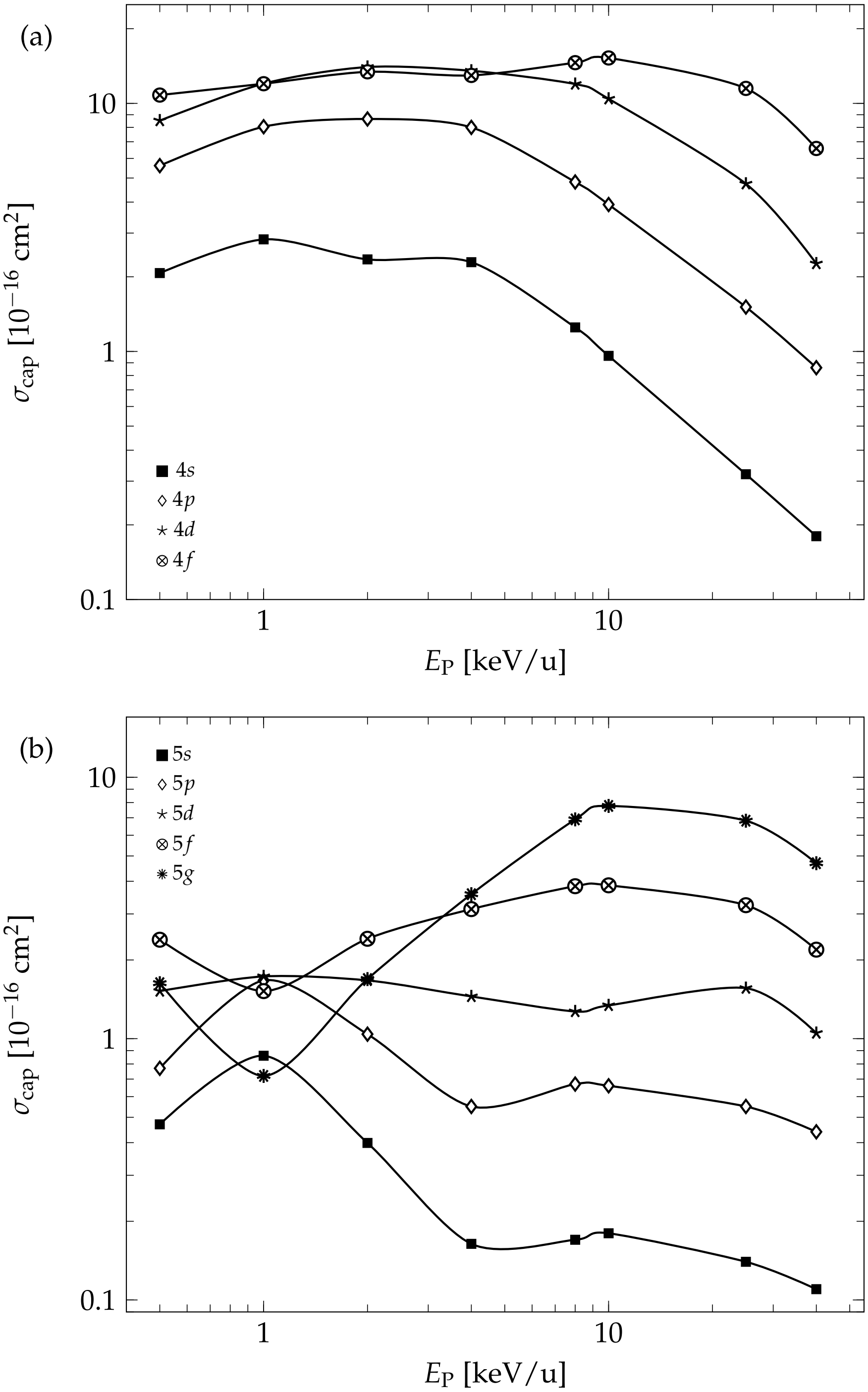

FIG. D4: *nl* SEC cross sections for C^{6+}-H collisions with respect to impact energy. Partial cross sections for: (a) $n = 4$, (b) $n = 5$.

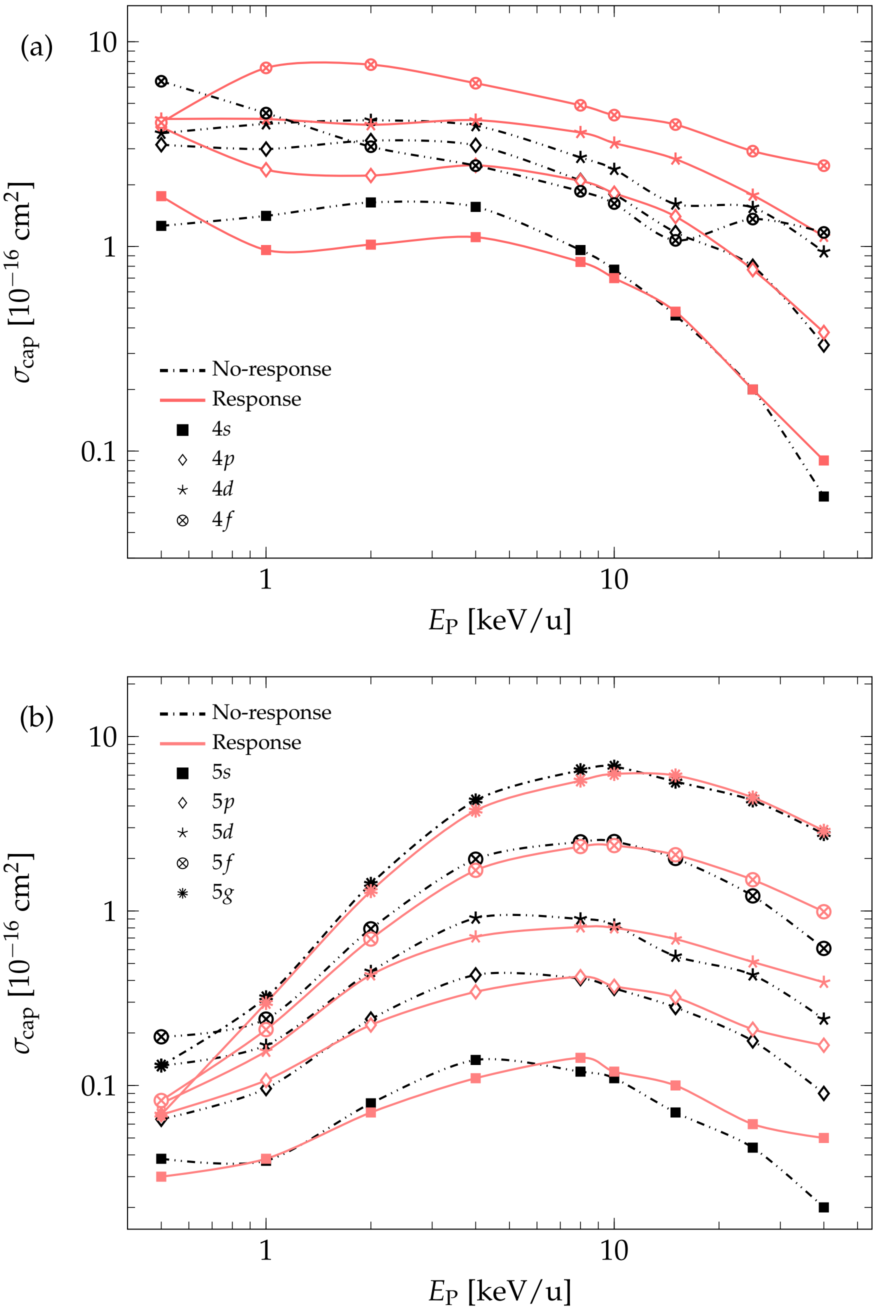

FIG. D5: *nl* pure SEC cross sections for C^{6+}-Kr collisions with respect to impact energy. Partial cross sections for: (a) $n = 4$, (b) $n = 5$.

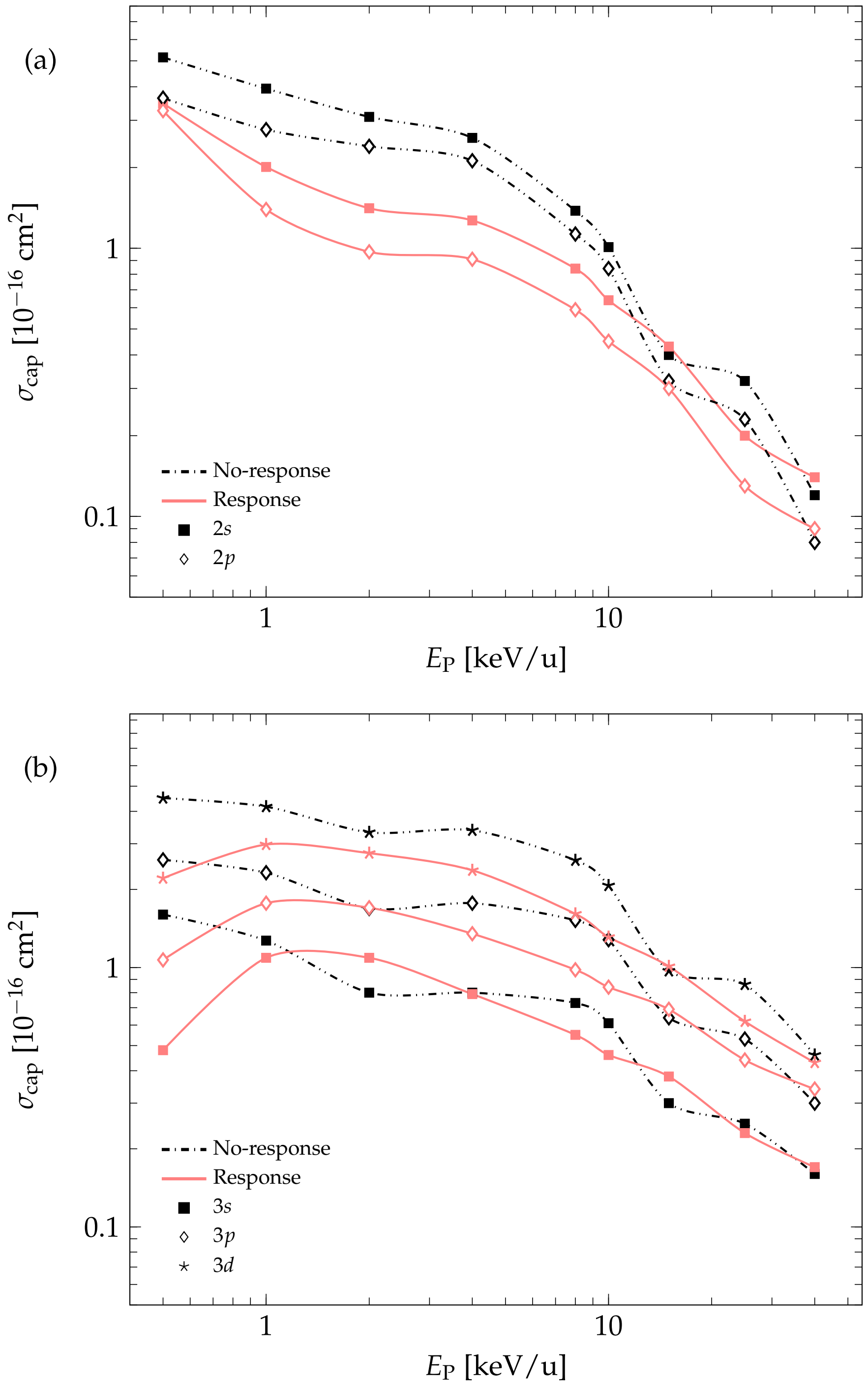

FIG. D6: *nl* ADC cross sections for C^{6+}-Kr collisions with respect to impact energy. Partial cross sections for: (a) $n = 2$, (b) $n = 3$.

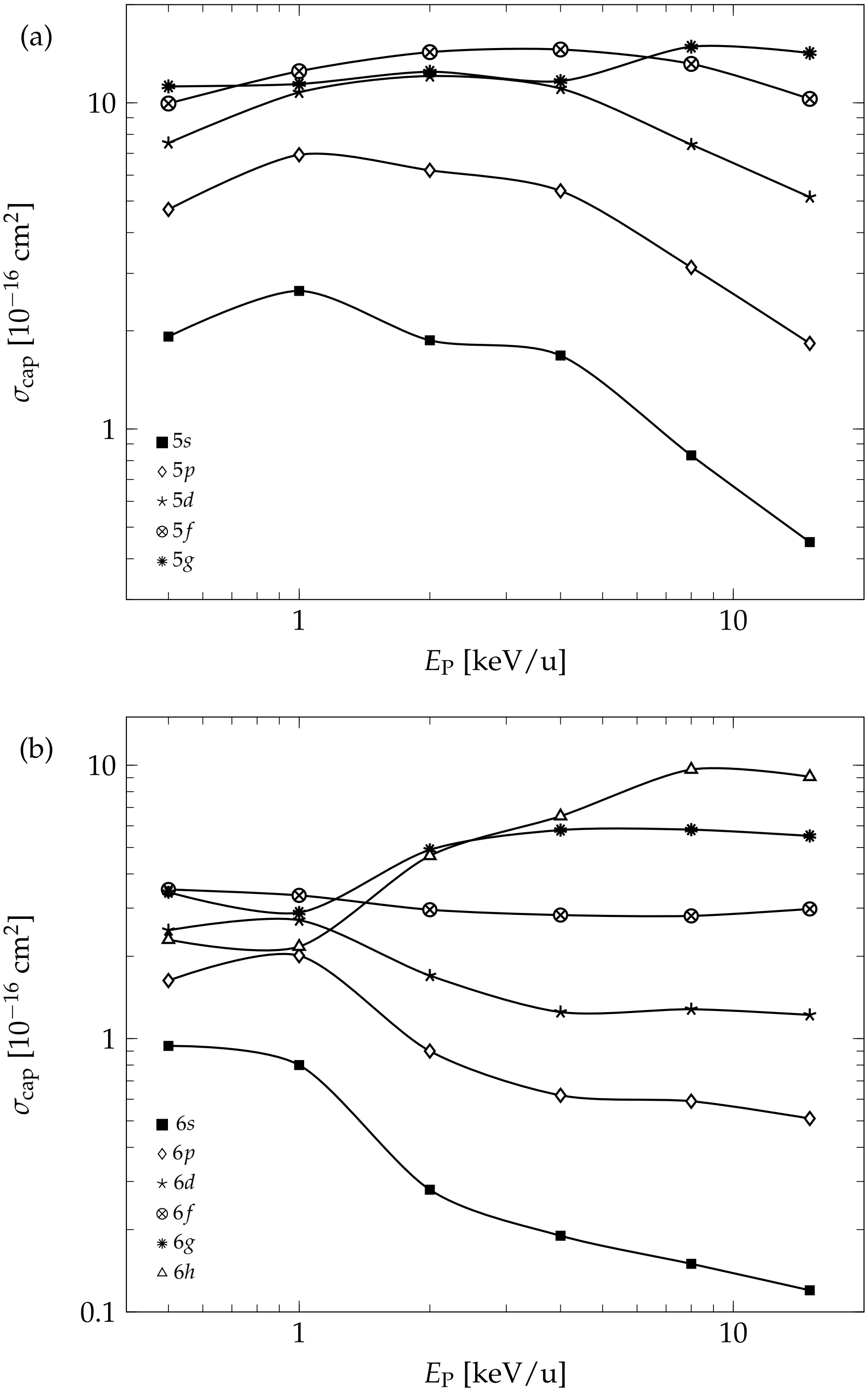

FIG. D7: *nl* SEC cross sections for O^{8+}-H collisions with respect to impact energy. Partial cross sections for: (a) $n = 5$, (b) $n = 6$.

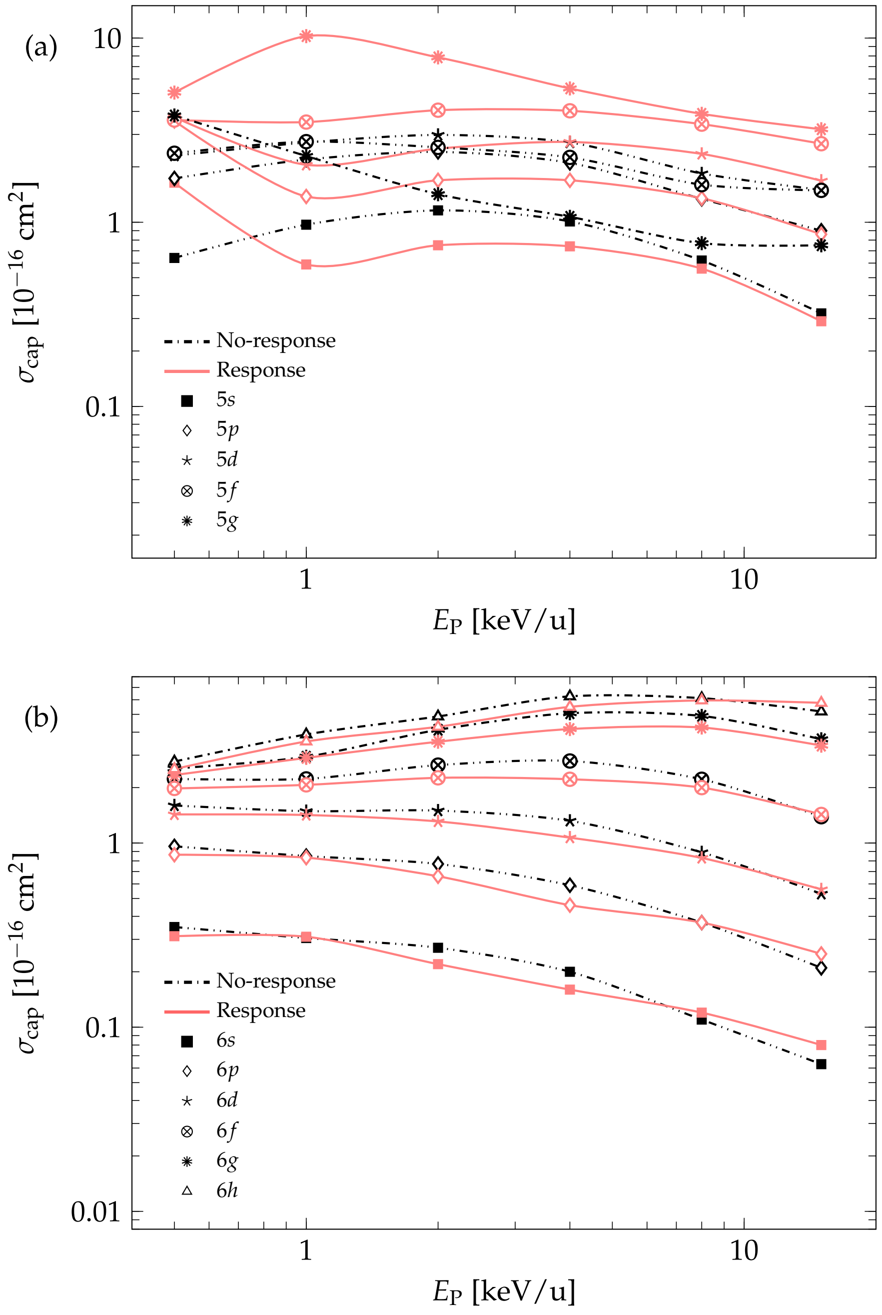

FIG. D8: *nl* pure SEC cross sections for O^{8+}-Kr collisions with respect to impact energy. Partial cross sections for: (a) $n = 5$, (b) $n = 6$.

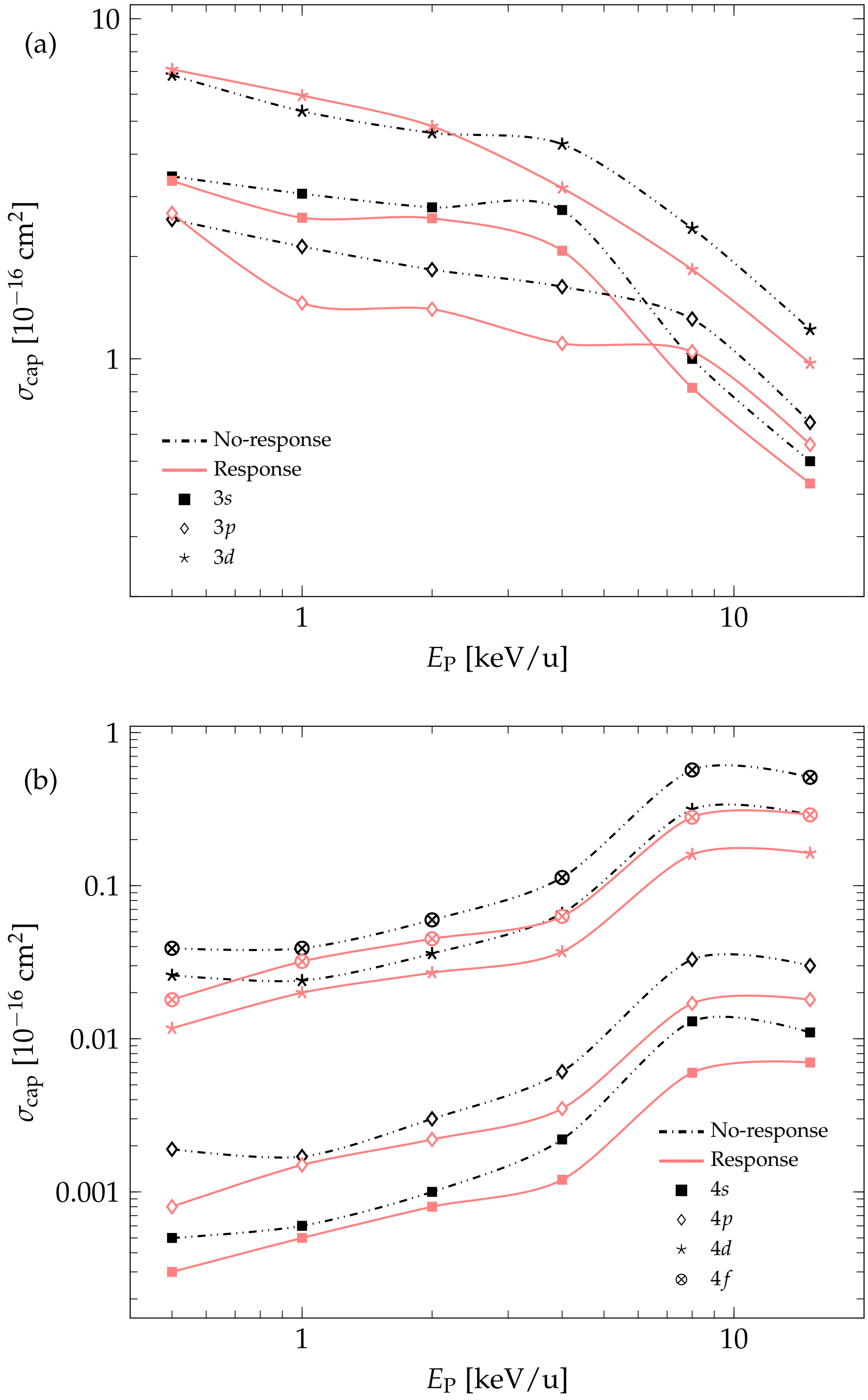

FIG. D9: nl ADC cross sections for O^{8+}-Kr collisions with respect to impact energy. Partial cross sections for: (a) $n = 3$, (b) $n = 4$.

E. ORIENTATION EFFECTS OF H_2O ON CROSS SECTION CALCULATION

In Ch. 6, results of the pure SEC probability as a function of the impact parameter for H_2O collisions at $E_P = 1.17$ keV/u were presented (Fig. 6.4). The plot shows a noticeable difference in capture for the molecular orientations considered in the present study: $(0,0,0)$ and $(90,0,0)$. The purpose of this section is to show that including results from other orientations in the averaging leads to very similar results in the total capture cross section calculation.

Figure E10 shows the pure SEC probability result plotted with respect to the impact parameter for six orientations of H_2O. The plot also shows the averaged results based on these six orientations. From this figure, we see that the curves of $(0,90,0)$ and $(0,180,0)$ have very similar profiles as $(0,0,0)$. This can be understood from the fact that in these three orientations the hydrogen atoms lie in the scattering plane. This is also true for $(0,270,0)$ but the position of the hydrogen atoms for this orientation would be the farthest from the projectile, which likely explains the lower capture probabilities for $b > 10$. Likewise, the $(90,180,0)$ curve has a nearly identical profile as $(90,0,0)$ since the hydrogen atoms lie in the azimuthal plane.

The orientation-averaged result of H_2O in Fig. E10 is now compared with the averaged result in Fig. 6.4. Figure E11 shows these orientation-averaged results for $O^{5+}(n = 4)$ at $E_P = 1.17$ keV/u. Clearly, the two averaged curves have a very similar profile. Calculating the capture cross section for each averaged curve in Fig. E11 results in 36.7×10^{-16} cm^2 for averaging all six orientations compared with a very similar result of 35.5×10^{-16} cm^2 for averaging the two orientations of $(0,0,0)$ and $(90,0,0)$. Although not identical, this shows that averaging results from only the $(0,0,0)$ and $(90,0,0)$ results is just as sufficient as averaging over all six orientations of H_2O.

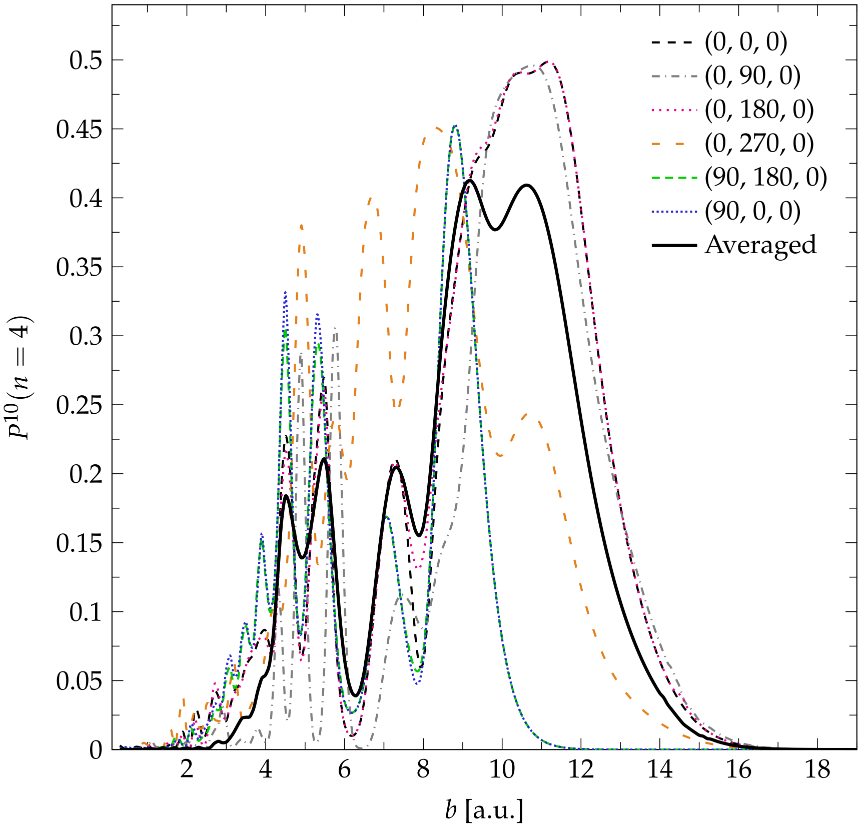

FIG. E10: TC-BGM pure SEC probabilities for $O^{5+}(n = 4)$ from collisions with H_2O plotted with respect to the impact parameter at $E_P = 1.17$ keV/u. Probability curves from six orientations of H_2O.

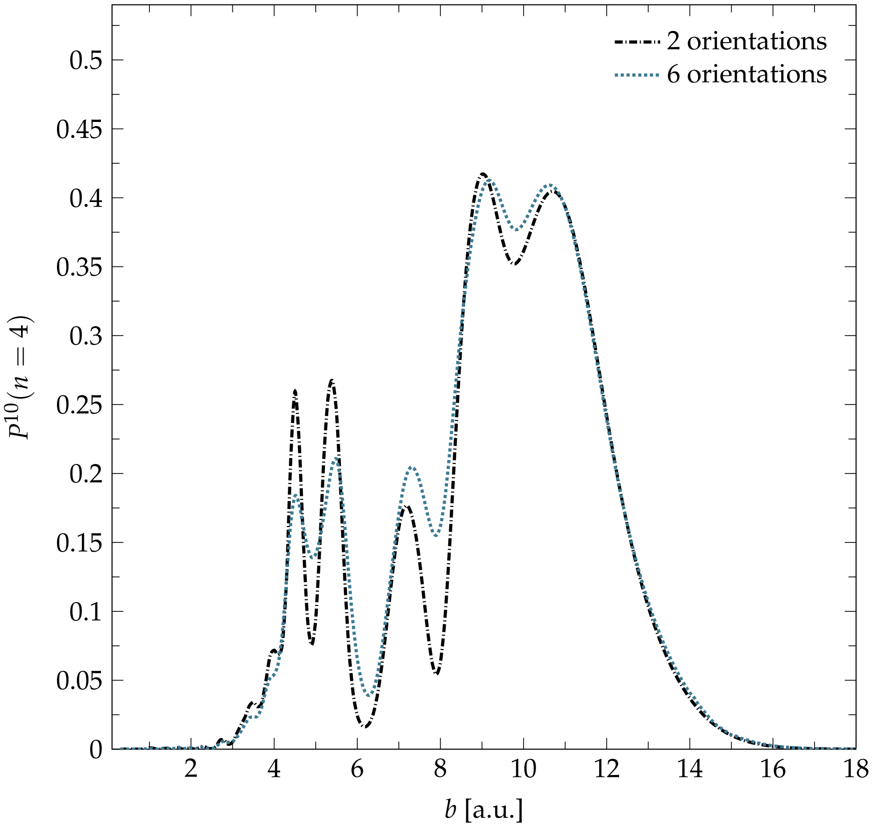

FIG. E11: TC-BGM pure SEC probabilities for $O^{5+}(n = 4)$ from collisions with H_2O plotted with respect to the impact parameter at $E_P = 1.17$ keV/u comparing different orientation-averaging. The '2 orientations' label refers to $(0, 0, 0)$ and $(90, 0, 0)$ while the '6 orientations' label refers to those in Fig. E10.